Bio-inspired Magnetic Systems

Controlled Swimming, Fluid Pumps, and Collective Behaviour

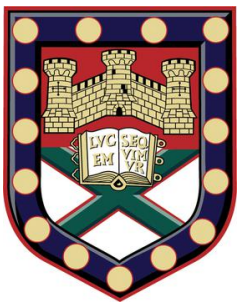

Joshua Kristian Hamilton

Department of Physics

University of Exeter

This dissertation is submitted for the degree of

Doctor of Philosophy in Physics

January 2019

Declaration

Submitted by Joshua Kristian Hamilton to the University of Exeter as a thesis for the degree of Doctor of Philosophy in Physics in January 2019.

This thesis is available for Library use on the understanding that it is copyright material and that no quotation from the thesis may be published without proper acknowledgement.

I certify that all material in this thesis which is not my own work has been identified and that no material has previously been submitted and approved for the award of a degree by this or any other University.

I acknowledge financial support from the Engineering and Physical Sciences Research Council (EPSRC) of the United Kingdom, via the EPSRC Centre for Doctoral Training in Metamaterials (Grant No. EP/L015331/1).

Joshua Kristian Hamilton

January 2019

I would like to dedicate this thesis to Lindsay Geoghegan who has supported me throughout my postgraduate studies…

Acknowledgements

In 2015, I started working towards a Ph.D., and along the way I have had the pleasure of meeting and worked with a number of enthusiastic people. It would be a great task to thank everyone and do it justice, so I will try highlight a few of the key influencers.

First and foremost, I would like to thank my supervisors, Professor Feodor Ogrin and Dr. Peter Petrov for ongoing support throughout my postgraduate studies. Both have been a constant source of inspiration; pushing and guiding me when it was needed. As well as being supportive scientifically, I would also like to thank both Feodor and Peter for all the great laughs and funny stories we have shared. As well as sharing some adventures along the way; including travelling to Grenoble and running between planes and trains with Peter, and being trapped on a "party" boat in Turkey with Feodor.

Now of course being part of a EPSRC Centre for Doctoral Training, means that there was plenty of people have I spend a lot of time with over the past years. I had great fun sharing the office with the people and bouncing off ideas regarding science, as well as frequent trips to the pub on a Friday evening. To highlight a few of the individuals in the CDT, the most impact would have been the students who I had the pleasure of sitting next to. My neighbours throughout my studies changed over the years and included: George Karkera (a close friend from undergrad), Joseph Beadle (a friend that was always a laugh), and finally Miguel Camacho Aguilar (a smart student and a great friend). Being part of the EPSRC Centre for Doctoral Training in Metamaterials, also means I had the joy of having many conversations

with Professor Roy Sambles. I would like to thank Roy for the many encouraging and useful conversations which we have shared over the years.

As well as being part of the EPSRC Centre for Doctoral Training in Metamaterials, my project was also part of the EU joint venture ABIOMATER (Magnetically controlled bio-inspired metamaterials). So, I would like to personally thank the entire consortium: all the members from the University of Oxford, the University of Barcelona, SPINTEC in Grenoble, Platform Kinetics in Leeds, and not forgetting all the members at the University of Exeter. Thank you everyone for the incredibly useful discussions and collaborations.

I would like to especially thank the extremely useful discussions and collaborations with Professor Andrew Gilbert (University of Exeter), Dr. Tom Myers (Platform Kinetics), and Dr. Daiki Matsunaga (University of Oxford). I would like to thank Andrew for all the scientific chats over coffee when they were required, it was always interesting to see the work from a mathematician's point of view. I would like to thank Tom for all the hard work on creating our experimental equipment, as well as all the laughs when you visit Exeter. Daiki has been an amazing collaborator and I am so glad we had the chance to work together. Working with Daiki was a joy, he was always extremely kind and ready to listen. I would also like to thank Dr. Bob-Dan Lechner (University of Exeter) for useful discussions regarding the future investigation focused on lipid monolayers.

During my time in Exeter, I also was given the chance to demonstrate undergraduate physics students. I would like to thank all the undergraduate students I had the joy of demonstrating and wish you all luck in the future.

Finally, I would like to thank my partner Lindsay Geoghegan who I met back in my undergraduate studies in Exeter. Thank you for putting up with me throughout the full roller coaster of the Ph.D. In particular, the difficulty of the long distance relationship, so thank you for always being there for me. The same goes for my family, who have supported me throughout my undergraduate and postgraduate studies.

Thank you everyone for your support, I hope I have made you all proud.

Abstract

This thesis details the original experimental investigations of magnetically actuated and controlled microscopic systems enabling a range of actions at low Reynolds number. From millimetre-robots and self-propelled swimmers to microfluidic and lab-on-a-chip technology applications. The main theme throughout the thesis is that the systems reply on the interactions between magnetic and elastic components.

Scientists often take inspiration from nature for many aspects of science. Millimetre to micrometre machines are no exception to this. Nature demonstrates how soft materials can be used to deform in a manner to create actuation at the microscale in biological environments. Nature also shows the effectiveness of using beating tails known as flagella and the apparent enhancements in flow speeds of collective motion.

To begin with, a swimmer comprised of two ferromagnetic particles coupled together with an elastic link (the two-ferromagnetic particle swimmer), was fabricated. The system was created to mimic the swimming mechanism seen by eukaryotic cells, in which these cells rely on morphological changes which allows them to propel resulting in approximate speeds of up to 2 body lengths per second. The aim of this system was to create a net motion and control the direction of propagation by manipulating the external magnetic field parameters. It was shown that the direction of swimming has a dependence on both the frequency and amplitude of the applied external magnetic field. A key factor discovered was that the influence of a small bias field, in this case, the Earth's magnetic field (100 orders of magnitude smaller than the external magnetic field) resulted in robust control over the

speed (resulting in typical swimming speeds of 4 body lengths per second) and direction of propulsion.

Following this work, swimmers with a hard ferromagnetic head attached to an elastic tail (the torque driven ferromagnetic swimmer) were investigated. These systems were created to be analogous to the beating flagella of many natural microscopic swimmers, two examples would be sperm cells and chlamydomonas cells. These biological cells have typical speeds of 10s of body lengths per second. The main focus of this investigation was to understand how the tail length affects the swimming performance. An important observation was that there is an obvious length tail (5.7 times the head length) at which the swimming speed is maximised (approximately 13 body lengths per second). The experimental results were compared to a theoretical model based on three beads, one of which having a fixed magnetic moment and the other two non-magnetic, connected via elastic filaments. The model shows sufficient complexity to break time symmetry and create a net motion, giving good agreement with experiment.

Portable point-of-care systems have the potential to revolutionise medical diagnostics. Such systems require active pumps with low power (USB powered devices) external triggers. Due to the wireless and localisation of magnetic fields could possibly allow these portable point-of-care devices to come to life. The main focus of this investigation was to create fluid pump systems comprising from the previously investigated two-ferromagnetic particle swimmer and the torque driven ferromagnetic swimmer. Building on the fact that if a system can generate a net motion it would also be able to create a net flow. Utilising the geometry of the systems, it has been demonstrated that a swimmer-based system can become a fluid pump by restricting the translational motion. The flow structure generated by a pinned swimmer in different scenarios, such as unrestricted flow around it as well as flow generated in straight, cross-shaped, Y-shaped and circular channels were investigated. This investigation

demonstrated the feasibility of incorporating the device into a channel and its capability of acting as a pump, valve and flow splitter.

As well as a single pump system, networks of the previously mentioned pump systems were fabricated and experimentally investigated. The purpose of this investigation was to utilise the behaviour of the collective motion. Such networks could also be attached to the walls or top of the channel to create a less invasive system compared to pump based within the channel system. The final investigation involved creating collective motion systems which could mimic the beating of cilia - known as a metachronal wave. Two methods were used to create an analogous behaviour. The first was using arrays of identical magnetic rotors, which under the influence of an external magnetic field created two main rotational patterns. The rotational patterns were shown to be controllable producing useful flow fields at low Reynolds numbers. The second system relied on the magnetic components having different fixed magnetisation to create a phase lag between oscillations. The magnetic components were investigated within a channel and the separation between the components was shown to be a key parameter for controlling the induced flow. In both cases, a simple model was produced to help understand the behaviour.

Finally, a selection of preliminary investigations into possible applications were conducted experimentally. These investigations included, measuring the effective surface viscosity of lipid monolayers, created cell growth microchannels, as well as systems which could be used for blood plasma separation. The properties of lipid monolayers vary with the surface density, resulting on distinct phase transitions. Slight differences in the molecular lattice are often accompanied by significant changes in the surface viscosity and elasticity. The idea was to use a swimmer as a reporter of the monolayer viscosity, resulting in a less invasive method compared to current techniques to monitor monolayer viscosity, for example torsion pendulums and channel viscometers. The reported effective surface viscosity closely matched the typical Langmuir trough measurements (with a systematic shift of approximately 17

Angstrom^2/molecule). The blood plasma separation preliminary work shows the previously investigated two-ferromagnetic particle swimmer mixing a typical volume (100 μm) blood sample with a buffer solution in 21 seconds. The system was also able to create locations with a high population of red blood cells. This resulted in a separation between the blood plasma and red blood cells. Two other preliminary results of future investigations were presented; the collective motion of free swimmers, and the fabrication of ribbon-like structures with fixed magnetic moment patterns.

Table of contents

List of figures

List of tables

Chapter 1

Introduction

1.1 Micro-scaled systems

Controllable swimming devices are miniature devices that can range in size from micrometres (μm) to centimetres (cm). They promise the ability to access small spaces at the micro-scale and manipulate micro/nano-scaled objects, such as within micro-channels (for example fluid sample testing), as well as the human body. Furthermore, due to the nature of their size, multiple devices could be manufactured and large numbers of devices can work synergistically to produce multi-functionalities.

The idea of having such devices has always been a human dream; Richard Feynman speculated that it would be possible to create tiny machines that could perform simple surgical operations [3]. The concept also inspired science fiction films such as *Fantastic Voyage* (1966) and *Innerspace* (1987).

Despite the long standing vision to fabricate these devices, experimental realisation has met several challenges. Similar to their macroscopic counterparts these miniature devices require energy to move. Usual methods used by macro-scale devices - such as single hinged systems like oars - are not particularly useful for micro-scaled devices due to the nature of fluid at this scale [4]. Numerous mechanisms to propel such devices have been proposed,

such as: chemical, acoustic [5], light [6], electric [7], and magnetic [8–10]. Each of these of these methods come with their advantages, but are held back by practical disadvantages.

1.2 Applications and challenges

Micro-scaled swimming devices have been shown to have great potential to be used in various fields, from basic components in lab-on-a-chip technology to transportation devices in targeted drug delivery [11]. These artificially created devices are expected to revolutionise general practices in medicine and medical diagnostics, microfluidic technology, and biophysical applications.

In biomedical applications, such as targeted cell therapy, the devices must be small enough to enter the human body, as well as be bio-compatible with the cells and tissues. Additionally, they must be able to be controlled and tracked in a fashion safe for the human body. Finally, they would need to be functionalised to carry drugs to specific area and interact with the targeted cells. Therefore, a large number of factors need to be taken into account when creating such devices.

In other non-biomedical applications, the devices are required to be cost effective and mass producible. Additionally, they must be reliable when used for microfluidic pump technology, providing robust control over the microfluidic system. Finally, for lab-on-a-chip on-site diagnostics, the system would be required to be transportable and disposable.

There are several challenges to address in order for the devices to achieve their full potential for the desired applications. Suitable methods in micro-fabrication must be identified, since traditional machining methods are insufficient to produce such devices at the desired scale. Another key challenge which must be addressed is how to power these micro-scaled devices, in such a way that is bio-compatible and efficient at the micro-scale. Additionally, when the devices are at the micro-scale, the inertial force associated with swimming be-

comes negligible and the motion is dominated by the drag force of the liquid, resulting in conventional reciprocal methods of propagation to be inadequate.

1.3 Outline

The actuation of this systems using low strength magnetic fields (< 5 mT) is a promising source not only because the energy can be supplied remotely, but is safe for humans as current medical practices use fields up to 7 T, for example magnetic resonance imaging (MRI) [12]. The aim of this thesis is to fabricate and investigate magnetically controlled bio-inspired systems capable of generating propulsion and manipulating fluids. Such systems include low Reynolds numbers swimmers and pumps, as well as collective motion and networks of swimmers to create magnetically controlled membranes. Possible applications of the described systems include using a swimmer as a reporter for effective surface viscosity. This effective surface viscosity measurement could be useful for detecting phase changes in monolayer films. The pump systems could be used for portable point-of-care sample mixing. Such samples could include the mixing of a blood sample with the buffer solution used for medical diagnostics. Following this chapter, a historical background is presented introducing fluid mechanics, along with a review of relevant work on low Reynolds number swimmers, pumps and membranes. Chapter 3 goes on to explain specific experimental methods used throughout the work presented in this thesis. In addition, the fabrication and data analysis tools are also outlined.

Chapter 4 focuses on the fabrication and investigation of two simple bio-inspired magnetic swimmers. The first is a two-ferromagnetic particle swimmer mimicking the deformation of an eukaryotic cell and the second is a single-ferromagnetic particle swimmer mimicking the bending of a flagellum, analogous to sperm cells or bacteria. In both cases, the swimmers are controlled by an external homogeneous magnetic field, however the two systems rely on different magnetic and elastic interactions. The two-ferromagnetic particle swimmer

relies on the dipolar interaction between two ferromagnetic particles (one ferromagnetically hard and the other ferromagnetically soft). In addition to this interaction, the device also experienced a magnetic torque. The single-ferromagnetic particle swimmer only relies on the induced magnetic torque, coupling this with an elastic tail the created bending produced non-reciprocal motion.

Chapter 5 focuses on utilising the controllability of the swimming systems shown in Chapter 4 into fluid pumps and mixers, as well as the fabrication of magnetic materials comprising of interacting networks. The fluid pumps based on the swimmer systems consist of tethering the swimmers in a way allowing the manipulation of various parameters of fluid flow. As well as single pump systems, the fabrication and performance of networks of the previously mentioned systems, are presented. These structures effectively produce magneto-elastic membranes. The focus of the membranes was to integrate the behaviour of the single-ferromagnetic particle systems and create a structure comprising of multiple interacting components. The structure was proposed as a less invasive system which could be used with lab-on-a-chip technology.

Chapter 6 focuses on the fabrication and investigation of collective motion systems. These collective motion systems consist of rotating magnetic rotors and/or rudders which isolated would not produce a net motion. However, collectively would create motion analogues to cilia. Cilia beat with a phase lag with their neighbours, a phenomenon which is known as the metachronal wave. Such systems are shown to have interesting rotational patterns/regimes, which by changing the effectiveness of the dipole-dipole interaction, could extracted from a group of magnetic units.

Finally, Chapter 7 is dedicated to future investigations related to the presented work. This chapter includes ideas and preliminary work on the collective motion of free swimmers and the interacting swimming patterns and novel methods to detect the phase changes in lipid monolayers. Further investigations also include creating applications for the two-

ferromagnetic particle fluid pump system for controlling cell growth within a microchannel and producing blood plasma separation. Finally, the fabrication of a ribbon-like membrane structure is presented, which could be used as a fluid pump or to be built into a microchannel. The actuation method for this system is controlled now the magnetisation of the structure.

Chapter 2

Background

2.1 Fluid mechanics

Micro-scaled swimmers show promise for a number of applications in both medical and biological fields. In all the desired applications, micro-scaled swimmers will interact with a surrounding fluid. Therefore, it is important to study the environment that these swimmers reside in, to understand how they move. The basic physics of locomotion changes in the transition from the macro-scale to the micro-scale, thus it is important to understand which effects dominates; viscous or inertial. To gain an understanding of the limitations of motion at the micro-scale, it is useful to first derivate the equations commonly used within fluid dynamics [13].

At a microscopic scale, a fluid comprises of many individual molecules and the physical properties (for example: density, and velocity) are non-uniform - due to the fluctuating Brownian motion. However, it is convenient to describe fluids as a continuum, i.e. not to take this molecular detail into account. This assumption breaks down only when the mean free path of the molecules (the average distance travelled by a fluid particle between two successive collisions) becomes the same order of magnitude as the typical characteristic lengths of the problem (for example gas flow in the atmosphere). At this level the fluid is

considered as a collection of fluid elements containing a large number of molecules. One can assign a locally averaged density $\rho(\mathbf{x},t)$ to an element at point $\mathbf{x}$. One can also define a local bulk flow velocity $\mathbf{u}(\mathbf{x},t)$.

Consider a volume V bounded by a given surface S. The mass inside the volume will be given by $\int_V \rho dV$. So, the rate of decrease of mass in V is

$$-\frac{d}{dt}\int_V \rho dV = -\int_V \frac{d\rho}{dt} dV. \tag{2.1}$$

If mass is conserved in the system, Equation 2.1 must equal the total rate of mass flux out of V. The rate of outward mass flux across a element $d\mathbf{S}$ is $\rho\mathbf{u}\cdot d\mathbf{S}$. Integrating over the whole surface will give the rate of mass flux out of V

$$\int_S \rho\mathbf{u}\cdot d\mathbf{S} = \int_V \nabla\cdot(\rho\mathbf{u}) dV. \tag{2.2}$$

For the mass to be conserved everywhere, Equations 2.1 and 2.2 must be equal for any volume, so finally arriving at the continuity equation:

$$\frac{d\rho}{dt} + \nabla\cdot(\rho\mathbf{u}) = 0. \tag{2.3}$$

For an incompressible Newtonian fluid, ρ is constant, independent of space and time. Thus, the continuity equation may be written as

$$\nabla\cdot\mathbf{u} = 0. \tag{2.4}$$

To derive a similar relationship for the conservation of momentum; consider a volume V bounded by a *material* surface S which moves with the flow. For any physical quantity $q = q(\mathbf{x},t)$, there are two different types of time derivatives. The first is given by $\partial q/\partial t$, which is the rate of change of q at a particular point, which is fixed in space. The second

derivative (Dq/Dt) is described as rate of change of q in a given element of fluid as it moves along a trajectory $\mathbf{x} = \mathbf{x}(t)$. This time derivative is known as the material derivative

$$\begin{aligned}\frac{Dq}{Dt} &= \frac{d}{dt}q(x(t),y(t),z(t),t) \\ &= \frac{\partial q}{\partial t} + \frac{dx}{dt}\frac{\partial q}{\partial x} + \frac{dy}{dt}\frac{\partial q}{\partial y} + \frac{dz}{dt}\frac{\partial q}{\partial z} \\ &= \frac{\partial q}{\partial t} + u\frac{\partial q}{\partial x} + v\frac{\partial q}{\partial y} + w\frac{\partial q}{\partial z} \\ &= \frac{\partial q}{\partial t} + \mathbf{u}\cdot\nabla q.\end{aligned} \tag{2.5}$$

Now the volume V will have a momentum given by $\int_V dV\rho\mathbf{u}$. Using this momentum and Equation 2.5, the rate of change of the momentum can be given by

$$\frac{d}{dt}\int_V dV\rho\mathbf{u} = \int_V dV\rho\frac{D\mathbf{u}}{Dt}. \tag{2.6}$$

This must be equal to the net force on an element. Two types of forces act on a fluid: body forces - that act on the whole mass at the centre of mass (e.g. gravity, $\rho\mathbf{g}dV$), and surface forces - that act on the boundaries. For any element, the net effects due to interactions with other elements acts as a thin surface layer. This forms the stress tensor T_{ij}, defined with the force exerted per unit area across a surface element $d\mathbf{S} = \hat{\mathbf{n}}dS$, $\mathbf{f} = T_{ij}\cdot\hat{\mathbf{n}}$. In T_{ij} the i-direction is normal to the surface, and j-direction is which the stress acts on - i and j can equal 1, 2, and 3. Thus, the total net force acting on the fluid can be taken as

$$\int_V dV\rho\mathbf{g} + \int_S T_{ij}\cdot d\mathbf{S} = \int_V dV(\rho\mathbf{g} + \nabla\cdot T_{ij}). \tag{2.7}$$

Finally, by using Newton's second law and equating equations 2.6 and 2.7 the equation known as the *Cauchy equation* is found

$$\rho\frac{D\mathbf{u}}{Dt} = \rho\mathbf{g} + \nabla\cdot T_{ij}. \tag{2.8}$$

Similar to the continuity equation (Equation 2.4), the incompressible restrictions can be applied to the Cauchy equation. At this point, it is possible to take the stress tensor as

$$T_{ij} = -P\delta_{ij} + \mu\left(\frac{\partial u_j}{\partial x_i} + \frac{\partial u_i}{\partial x_j}\right), \tag{2.9}$$

where P is pressure, μ is the dynamic viscosity of the fluid, and δ_{ij} is the Kronecker delta. The dynamics viscosity is the measure of a fluid's resistance to flow when an external force is applied. The viscosity of a fluid can also be described using the kinematic viscosity, $\nu = \mu/\rho$. The kinematic viscosity is the measure of the resistive flow of a fluid under the weight of gravity. Notably, the stress tensor is symmetric, i.e. $T_{ij} = T_{ji}$, meaning the tensor reduces to six unique equations.

By substituting Equation 2.9 into Equation 2.8, for the case of constant viscosity μ

$$\begin{aligned}\rho\frac{D\mathbf{u}}{Dt} &= -\frac{\partial P}{\partial x_i} + \mu\frac{\partial}{\partial x_j}\left(\frac{\partial u_j}{\partial x_i} + \frac{\partial u_i}{\partial x_j}\right) + \rho\mathbf{g} \\ &= -\frac{\partial P}{\partial x_i} + \mu\frac{\partial}{\partial x_i}\left(\frac{\partial u_j}{\partial x_j}\right) + \mu\frac{\partial^2 u_i}{\partial x_j^2} + \rho\mathbf{g}.\end{aligned} \tag{2.10}$$

As the fluid is incompressible, it can be stated that $\partial u_j/\partial x_j = \nabla\cdot\mathbf{u} = 0$, thus Equation 2.10 becomes

$$\rho\frac{D\mathbf{u}}{Dt} = -\nabla P + \mu\nabla^2\mathbf{u} + \rho\mathbf{g}. \tag{2.11}$$

This is known as the Navier-Stokes equation, which was derived by Claude-Louis Navier in 1822 and later worked on by George Gabriel Stokes in 1845 [14]. Using Equation 2.5, the system as the rate of change of velocity of a given point can be described as

$$\rho\frac{\partial\mathbf{u}}{\partial t} + \rho(\mathbf{u}\cdot\nabla\mathbf{u}) = -\nabla P + \mu\nabla^2\mathbf{u} + \rho\mathbf{g}. \tag{2.12}$$

It is useful to convert the Navier-Strokes equation to a non-dimensional form. By defining the appropriate scales for length L, flow velocity U, and time L/U, the following dimensionless variables can be stated

$$\mathbf{x}^* = \frac{\mathbf{x}}{L}, \quad \nabla^* = L\nabla, \quad \mathbf{u}^* = \frac{\mathbf{u}}{U}, \quad t^* = \frac{Ut}{L}, \quad P^* = \frac{PL}{\mu U}.$$

There are two ways of non-dimensionalisation pressure, here P^* is defined for dominant viscous effects i.e. *creeping flows*. If the dynamic effects were assumed to be dominant i.e. *high velocity flows*, $P^* = P/\rho U^2$.

Using the defined dimensionless variables, the terms of the Navier-Stokes equation (Equation 2.12) become

$$\rho\frac{\partial \mathbf{u}}{\partial t} = \frac{\rho U^2}{L}\frac{\partial \mathbf{u}^*}{\partial t^*}, \quad \rho(\mathbf{u}\cdot\nabla\mathbf{u}) = \frac{\rho U^2}{L}(\mathbf{u}^*\cdot\nabla^*\mathbf{u}^*),$$

$$\nabla P = \frac{\mu U}{L^2}(\nabla^* P^*), \quad \mu\nabla^2\mathbf{u} = \frac{\mu U}{L^2}(\nabla^{*2}\mathbf{u}^*),$$

thus - assuming the absence of gravitational effects - the Navier-Stokes equation can be stated as

$$\frac{\rho UL}{\mu}\left[\frac{\partial \mathbf{u}^*}{\partial t^*} + (\mathbf{u}^*\cdot\nabla^*\mathbf{u}^*)\right] = -\nabla^* P^* + \nabla^{*2}\mathbf{u}^*. \tag{2.13}$$

Finally, introducing the dimensionless number known as the Reynolds number (Re), the non-dimensionalised Navier-Stokes becomes

$$\left[\frac{\partial \mathbf{u}^*}{\partial t^*} + (\mathbf{u}^*\cdot\nabla^*\mathbf{u}^*)\right]\mathrm{Re} = -\nabla^* P^* + \nabla^{*2}\mathbf{u}^*. \tag{2.14}$$

The Reynolds number (Re) was introduced by George Gabriel Stokes in 1851 and popularised by Osborne Reynolds in 1883. The quantity is defined by the ratio between the

inertial and viscous forces when an object moves through a fluid. The Reynolds number can be expressed in terms of the dynamics viscosity μ as well as the kinematic viscosity ν

$$\mathrm{Re} = \frac{\rho UL}{\mu} = \frac{UL}{\nu}. \tag{2.15}$$

There are generally two main divisions which describe fluid flow. The first is for the when $\mathrm{Re} \gg 1$, this regime is called the inviscid flow (also known as Euler flow). In this regime, the viscous friction can be neglected. As a result, in this limiting case Equation 2.12 - assuming the absence of gravitational effects - would become

$$\rho \frac{\partial \mathbf{u}}{\partial t} + \rho(\mathbf{u} \cdot \nabla \mathbf{u}) + \nabla P = 0. \tag{2.16}$$

This is known as the Euler equation. Assuming an inviscid flow is useful for simplifying many fluid dynamics problems, in which the viscous forces are insignificant. Some examples include ocean currents and the flow around an airplane wing.

Another condition that leads to the elimination of the viscous force is when $\nabla^2 \mathbf{u} = 0$, and results in an *inviscid flow arrangement*. Such flows are found in vortex-like structures and may be key in the formation of tornadoes and tropical cyclones.

The second main division is the case where the Reynolds number is very small (i.e. $\mathrm{Re} \ll 1$). In this regime the viscous friction dominates and is known as Stokes flow (or creeping flow). This regime is the typical situation for flows where the fluid velocities are very slow, viscosities are larger, or the length scales associated with the flow are small. Some examples of these creeping flows include the swimming of microorganisms, and the flow of lava. This viscous dominated regime will be the focus of the systems presented in this thesis.

2.1.1 Life at low Reynolds numbers

Typically, living micro-organisms live in the low Reynolds number regime (Re $\sim 1 \times 10^{-3}$). This is due to the Reynolds number scaling by scale, not only viscosity. For example, take a 1 mm particle, assuming it could self-propel at 1 mm s^{-1}. If this particle was propelling through water (μ = 1 mPa s) the Reynolds number would be Re = 1, therefore not in the low Reynolds number regime. However, if the fluid was switched to Glycerol ($\mu = 1.4 \times 10^{-3}$ Pa s), the Reynolds number would now become Re = 1×10^{-3}).

Therefore, one can mimic the low Reynolds number environment which a micro-organism lives in by creating a millimetre device and using a high viscosity fluid. In this regime the viscous forces dominate the flow, thus any dynamic contribution of the system can be disregarded, and the Navier-Stokes equation (Equation 2.14) reduces to

$$\nabla^* P^* = \nabla^{*2} \mathbf{u}^*. \tag{2.17}$$

This is known as the Stokes equation. Such a system with a very low Reynolds number results in the inertia of a body being completely negligible. Thus, the movement of a body depends only on the instantaneous force acting on it and not the velocity it previously had. Since Equation 2.17 is linear, hence all flows are in the 'creeping flow' limit and are kinematically reversible. This means that if a fluid element is displaced by a forward stroke motion and subsequently displaced by the mirror reverse stroke, the fluid will return to its original position at the end of one swimming cycle, with zero net fluid motion.

For an organism to propel in this regime, the body requires a motion which can break time symmetry. Such a situation is best explained by Edward M. Purcell in the 1977 paper entitled *"Life at Low Reynolds Number"*, in which he introduced the scallop theorem [4]. According to Purcell, a scallop cannot propel itself in viscous liquids by opening its shell slowly and closing quickly – the strategy that works perfectly in water. In a low Reynolds number

environment, the scallop has only one degree of freedom and is confined by reciprocal motion. Thus, a 'microscopic scallop' attempting to swim in water will fail.

The theorem states that to achieve propulsion in a low Re environment, a swimmer must deform its shape in such a way that would make it variant under time-reversal. The simplest system that could propel at a low Reynolds number would comprise of two hinges, thus offering two degrees of freedom, that beat out of phase. Figure 2.1 shows a schematic of such a swimmer for which, the two paddles of the swimmer can move with angles θ_1 and θ_2 relative to the hinges. For the case where the arms moves in sync ($\theta_1 = -\theta_2$, Figure 2.1b) the swimmer is bound by reciprocal motion. Figure 2.1b shows that in configurational space for the configuration $R_A R_B R_C$, the motion is completely symmetric. This can be shown with a simple comparison of forces. If ξ_i is let to be a constant (for simplicity) for either the paddles or the body, the drag forces (between configuration R_A and R_B) can be defined as

$$F_{\mathrm{PAD}} = \xi_{\mathrm{PAD}}(v_{\mathrm{PAD}} - u_{\mathrm{BOD}}), \tag{2.18}$$

$$F_{\mathrm{BOD}} = \xi_{\mathrm{BOD}} u_{\mathrm{BOD}}, \tag{2.19}$$

where v_{PAD} is the velocity of the paddles, and u_{BOD} is the velocity of the body. Assuming that the forces are balanced and the displacement is $\Delta x = u_{\mathrm{BOD}} t$

$$\Delta x = v_{\mathrm{PAD}} \left(\frac{\xi_{\mathrm{PAD}}}{\xi_{\mathrm{PAD}} + \xi_{\mathrm{BOD}}} \right) t. \tag{2.20}$$

In the reverse motion (between configuration R_B and R_C), using the same analysis

$$\Delta x' = v'_{\mathrm{PAD}} \left(\frac{\xi_{\mathrm{PAD}}}{\xi_{\mathrm{PAD}} + \xi_{\mathrm{BOD}}} \right) t'. \tag{2.21}$$

In reciprocal motion, the paddles will return to their original location, so $v_{\mathrm{PAD}}t = v'_{\mathrm{PAD}}t'$

$$\Delta x' = u'_{\mathrm{BOD}}t' = v'_{\mathrm{PAD}}\left(\frac{\xi_{\mathrm{PAD}}}{\xi_{\mathrm{PAD}}+\xi_{\mathrm{BOD}}}\right)t' = v_{\mathrm{PAD}}\left(\frac{\xi_{\mathrm{PAD}}}{\xi_{\mathrm{PAD}}+\xi_{\mathrm{BOD}}}\right)t. \tag{2.22}$$

Equation 2.22 shows that $\Delta x' = \Delta x$, therefore with this configurational sequence, there will be no net motion.

If the swimmer was to use the configurational sequence shown in the Figure 2.1c, where the paddles move out of phase from each other, there will be a net motion produced. This is shown in the configurational space, via a loop - as there is an asymmetry in the motion. The asymmetry shown produces non-reciprocal motion and propels the swimmer to the right (visualised with an arrow), for as long as it moves through the configuration shown.

Many biological organisms adapted these rules by using intricate ways of deforming their bodies, an example of this is the *Eutreptiella* [15]. Another biological organisms use cilia and rotating flagella [16, 17] to self-propel. Figure 2.2 shows schematics of real micro-organisms that propel themselves at these low Reynolds numbers. *Escherichia coli* (*E. coli*) use multiple flagella oriented along the cells body to propel along the cells long axis, achieved by rotation of the flagella and bunching of the filaments together.

2.1.2 Propulsion mechanisms of micro-scaled swimmers

There has been a great amount of interest in adapting such mechanisms for the construction of artificial micro-scale devices that can propel in these environments. Such devices promise a number of potential applications such as the transportation and delivery of drugs or cells [18–20] and active pumps in microfluidic technology [21–23].

Since the inspiring work by E. Purcell [4] there have been large variety of models proposing different mechanisms for time-irreversible motion. This also includes a number of experimental prototypes.

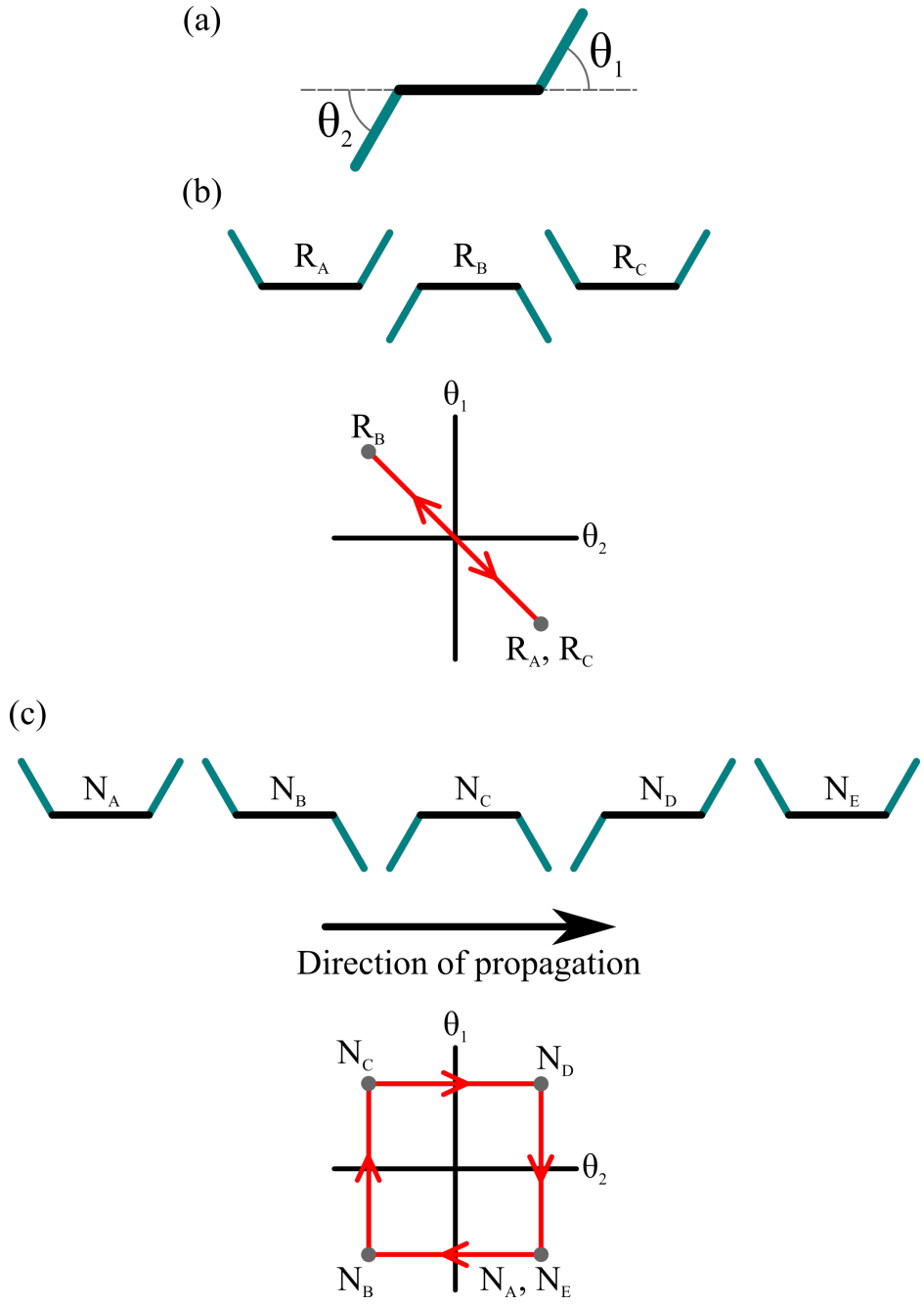

Fig. 2.1 The two hinge swimmer proposed by E. Purcell [4]. (a) Shows the two dimensions in configurational space, θ_1 and θ_2. (b) For the configurational sequence $R_A R_B R_C$, there will be no net displacement after one cycle. (c) For the configurational sequence $N_A N_B N_C N_D N_E$, there will be a net displacement after one cycle. The closed loop in configurational space is shown by red arrows. The direction of propagation for this configuration is shown.

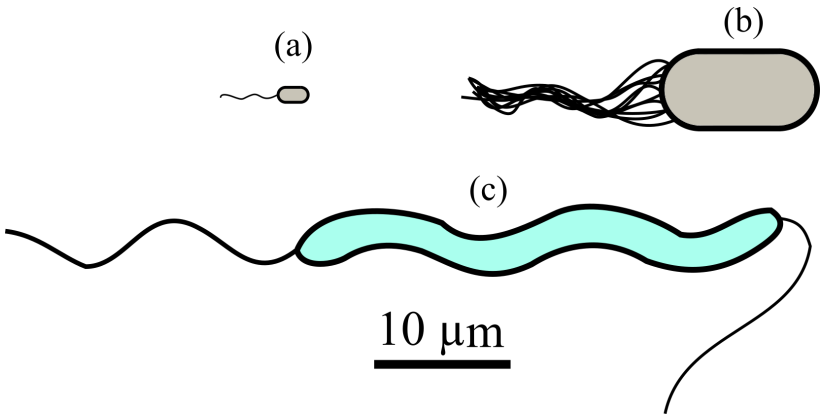

Fig. 2.2 Scale drawings of various bacteria. (a) *Escherichia coli.* Approximately six filaments on the sides of the cell form a bundle at one end of the bacteria propelling the cell moving in unison. (b) *Chromatium okenii.* Approximately forty filaments arise at one end of the bacteria. (c) *Spirillum volutans.* Shown swimming from left to right, the body is helical and has approximately twenty-five filaments at each end of the bacteria, those on the right are in the "head" configuration. Figure adapted from [17]

Kinematics

One simple low Reynolds number swimmer was proposed based on Purcell's original idea [4] (Figure 2.1) which consisted of three identical spheres that were linked by a rod [24]. It was shown that the swimmer would propel by manipulating the separation between the spheres in a particular sequence of 4 motions. Starting from the initial condition shown in 2.3a, motion starts with (1) the left arm increases in length, (2) the right arm decreases in length. Following this (3) the left arm decreases in length and finally to return to the initial configuration (4) the right arm increases in length. By completing one cycle it is shown that the central sphere has moved a distance Δx_a.

A similar swimmer consisting of a pair of spheres that change their volumes and mutual distance has been shown theoretically to propel at low Reynolds numbers [25]. When one sphere expands it acts as a source pushing away the shrinking sphere – which acts as a pull – thus giving the swimmer the name *"Pushmepullyou"*. It was shown that the *"Pushmepullyou"* (Figure 2.3b) was more intuitive – due to its simpler design – and more efficient than the three linked spheres - as $\Delta x_b > \Delta x_a$ [25].

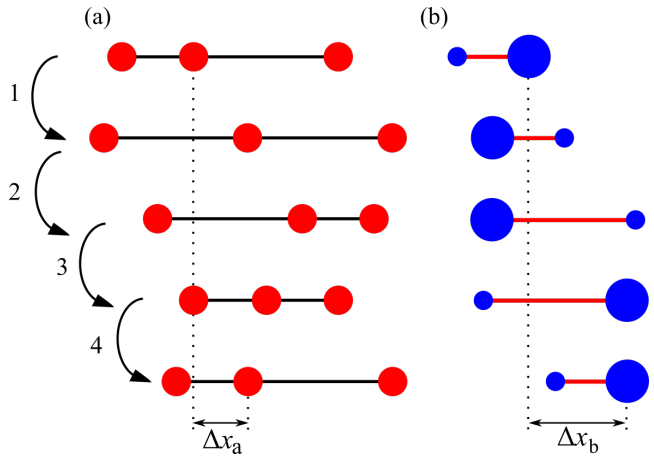

Fig. 2.3 Schematic diagram of the simple three sphere swimmer and the *"Pushmepullyou"*. In both cases, the sequence starts from the top image to the bottom. One complete cycle of the proposed swimmer, showing non-reciprocal motion. (1) The left arm increases in length. (2) The right arm decreases in length. (3) The left arm decreases in length, and finally (4) the right arm extends back to its original length. By completing one cycle it is shown that the central sphere has moved a distance Δx_a. Figure adapted from [24]. (b) Schematic diagram showing five snapshots of the *"Pushmepullyou"* swimming stroke. After a full cycle the swimmer has returned to its original configuration but has been displaced to the right, with a distance Δx_b. Figure adapted from [25].

Chemical propellers

The first type of experimental prototypes discussed will be micro-scale swimmers that are powered by a chemical reaction between the swimmer itself and the surrounding medium. The chemical reactions typically use hydrogen peroxide (H_2O_2). During this reaction oxygen is produced on the surface of the swimmer providing the driving force for propulsion through the medium. One type of swimmers proposed were striped platinum/gold (Pt/Au) nano-rods [26–28] ($\sim$ 370 nm in diameter and $\sim$ 1 µm long). The platinum was used because it is an active catalyst for the decomposition of H_2O_2, and gold is not. Although these swimmers displayed movement (2 – 10 body lengths per second), the direction of motion was subject to random fluctuations due to the nature of the chemical reaction. An example of the trajectories of such devices is shown in Figure 2.4a.

Another example of chemically propelled swimmers are known as Janus spheres [29, 30]; typically polystyrene spheres (with a diameter of μms), coated one side with platinum. At short time scales (compared to the rotational diffusion time) the propulsion of the spheres was directed with speed in the μm s^{-1} range, but at longer time scales the trajectories became randomised. An example of the trajectories of such Janus spheres is shown in Figure 2.4b.

The random propulsion direction can lead to difficulties in applications, such a precise drug transport and delivery. The main issue with chemical reaction powered swimmers is that they required H_2O_2, which is toxic to the human body, thus any bio-medical application would not be feasible.

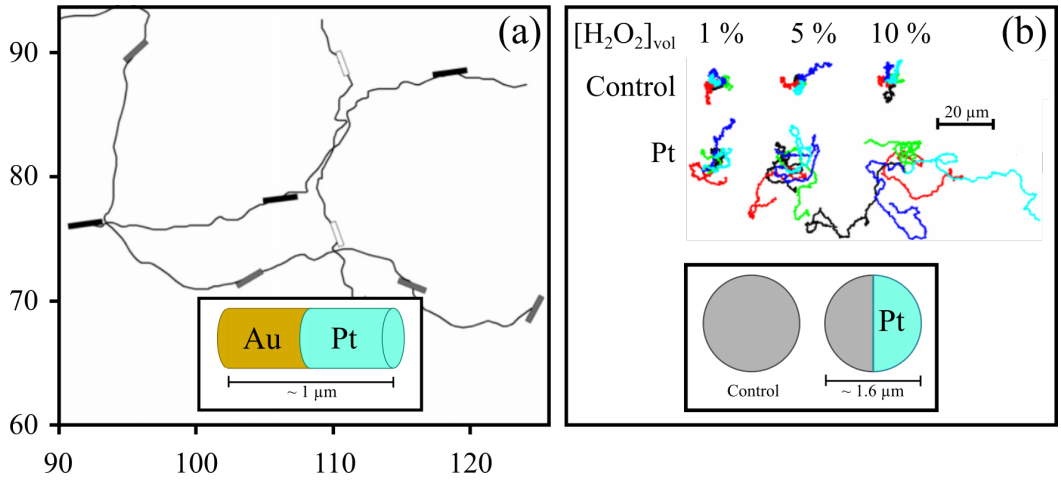

Fig. 2.4 Trajectory plots of two different types of catalytic swimmers. (a) Trajectory of three platinum/gold rods in 2.5% aqueous hydrogen peroxide. The axes show x and y position in μm, the inset shows a schematic of the catalytic rod. Figure adapted from [26]. (b) Trajectories of the control microsphere (polystyrene only) and half platinum coated microspheres, for different concentrations of hydrogen peroxide. The inset shows a schematic of the catalytic Janus sphere. Figure adapted from [30].

More recently, a range of chemical propellers which rely on non-hazardous levels of H_2O_2 or even complete alternatives to H_2O_2 have been investigated to varying levels of success [31, 11]. Hollow Pt-coated Janus particles (diameters of 8 μm) have been shown to be able to propel at concentrations as long as 0.1% H_2O_2 [32]. As well as these hollow Janus particles, nano-scaled particles (diameters < 100 nm) have been shown to propel at

concentrations lower than 3% [33]. Water-based bubble-propelled micro-motors were first shown in 2012 [34]. These Janus devices comprised of a titanium half and an aluminium-gallium (Al-Ga) half. When submerged in water the Al-Ga section would react and hydrogen bubbles were created, resulting in speeds of up to 150 body lengths per second.

Other examples of fuel alternatives include glucose and urea. However, these fuels also come with their drawbacks related to the required concentrations, as well as much lower velocities compared to other stated chemicals [35–37]. Other alternatives include the use for materials such as zinc or manganese. These materials decompose in acidic environments, thus making them ideal for operating inside the stomach or other environments where the pH level is below 7 [38–42].

Ultrasound driven propellers

Acoustic energy has been used for many applications such as detecting objects and measuring distances, as well as diagnostic sonography. Ultrasonic acoustic waves are an interesting method of propelling micro-scaled swimmers, as high frequency sound waves – in particularly in the MHz regime – are known to have minimal effects on biological systems [43, 44]. One pioneer in this field used pulsed or continuous ultrasound to propel micro-scaled metallic rods [45, 46]. It was shown that ultrasound standing waves in the MHz range, could levitate, propel (at speeds of $\sim 200\,\mu m\ s^{-1}$), rotate, align, and assemble gold (Au) and gold-ruthenium (AuRu) segmented micro-rods (2 µm long and 330 nm diameter). A plausible mechanism for the directional motion of the micro-rods is based on the asymmetric shape of the rods, leading to an asymmetric distribution of the acoustic pressure (Figure 2.5). These systems are appealing due to the apparent lack of limitations other than the directionality. A common approach with ultrasound devices is to use the ultrasound as the propulsion device and use a magnetic material in the swimmer and use a magnetic field for guidance [47, 5]. This then

creates the question why not create a similar system which only relies on the magnetic field for both the propulsion and guidance.

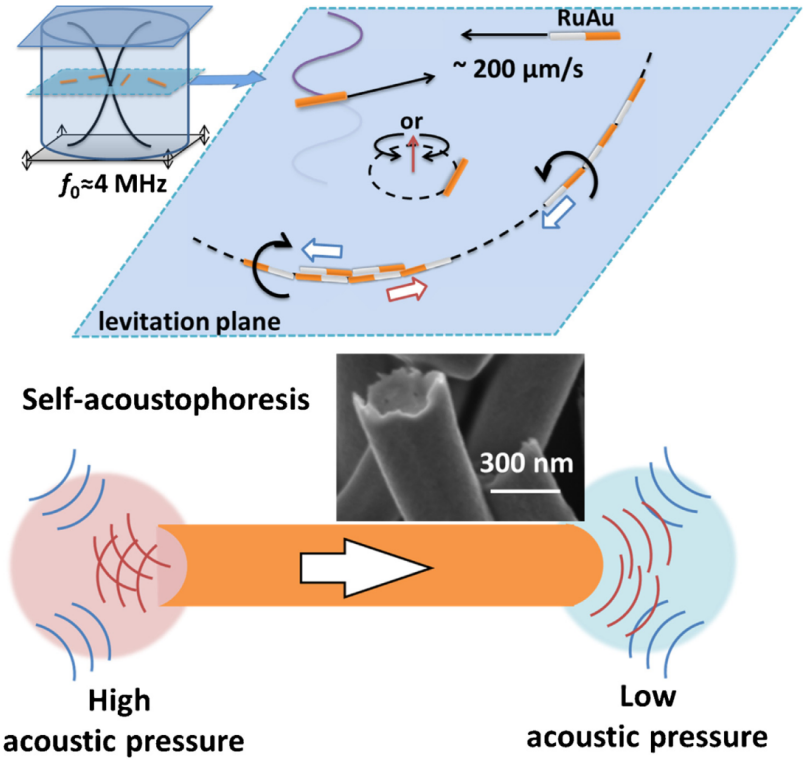

Fig. 2.5 Ultrasonically powered Au and segmented AuRu micro-rods. Asymmetrically shaped metallic micro-rods are activated in an ultrasonic standing wave at MHz frequency through an acoustic pressure gradient along the length of the micro-rod, resulting in directional motion. Figure from [45, 46].

Light driven propellers

Liquid-crystal elastomers, whose constituent molecules are orientationally ordered, have a strong coupling between their mechanical strain and alignment of the molecules. The order can be affected by external stimuli, in this case light, which lead to strains and change in the shape (Figure 2.6a). It has been shown that by dissolving azo dye into the network of the liquid-crystal elastomers [48], the deformation in response to visible light is more than 60° of bending. The interaction of elastomers with fluids was also studied, and remarkably it was shown that a disk (diameter 5 mm and thickness 0.32 mm) of the material would swim

away from the external light source. More recently, a swimmer (2.6 cm) has been fabricated using polymer film containing the azobenzene chromophore – acting as a motor – attached to an artificial flagellum [49]. The azobenzene chromophore is sensitive to ultra-violet (UV) light; periodically switching between UV and white light will create an oscillation of the artificial flagellum, resulting in an average swimming speed of 142 µm s^{-1}. A schematic of the artificial flagellum is shown in Figure 2.6b. A possible limitation of these devices is the fact that system relies on an optically transparent environment for the actuation to occur. Therefore, these devices may encounter issues when externally controlling through a human body, however, could be useful for components in transparent lab-on-a-chip systems.

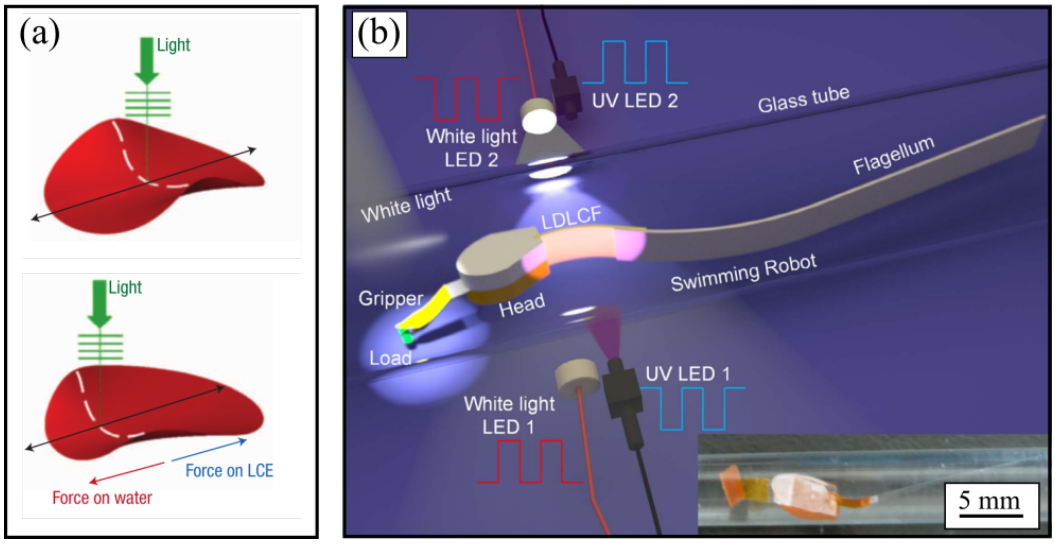

Fig. 2.6 Illustrations to visualise the induced deformation of the liquid-crystal elastomers. (a) Illustration of how the sample shape changes and hence interacts with the fluid below it. Figure adapted from [48]. (b) Schematic diagrams of the micro swimming robot and light irradiation system. Figure from [49].

Recent work from P. Fischer's group has focused on creating soft micro-robots utilising these liquid-crystal elastomers [50]. The micro-robots were cylindrical in shape with diameter 200 µm and length 1 mm. By manipulating the applied light pattern, travelling waves were able to be created along the surface of the device, and propel at 200 µm s^{-1}. These micro-

robots were designed to mimic the body deformations of microorganisms such as annelids and ciliated protozoa.

Electric actuation

Electro-osmosis and electro-phoresis are the two key processes for transporting charged micro-scaled objects through a fluid [7]. Electro-osmosis is the bulk motion of a fluid over a charged surface, due to the presence of an electric field. The second process, electro-phoresis, is the drift velocity of a charged object due to the electric force $\mathbf{F_E} = q\mathbf{E}$ from an applied electric field $\mathbf{E}$. Micro-diodes have been shown to act as self-propelling particles when exposed to an external electric field, due to the effects of the electro-osmotic process [51]. The micro-diodes travelled with speeds in the mm s^{-1} range and the direction of motion depends on the orientations of the anode and cathode.

Magnetic swimmers

Magnetically actuated swimmers have attracted a considerable interest in the recent decade. The direction of their propulsion is normally related to the orientation of the bias/oscillating field that can be controlled via simple rotation of the principle axes of the magnetic system. Expanding on this appeal, other methods of actuation, such as chemical [46, 52] and ultra-sound [47, 5] have adapted magnetic components to control the propagation direction of swimming. Magnetically driven micro-scaled swimmers will be expanded on in the following section.

2.2 Magnetic actuation

The influx and appeal of magnetically controlled swimmers is due to the fact that magnetic fields are bio-compatible and have good penetration into human tissue (for example: MRI used in current medical diagnostics). Such controllability makes these devices attractive for a number of biomedical and technological applications.

The basic principle that governs the majority of magnetically actuated swimmers is magnetic torque $\mathbf{T_M}$ due to an applied magnetic field. When a magnetic object is subject to a constant external magnetic field $\mathbf{H}$ (i.e. not a gradient), the magnetic torque is given by

$$\mathbf{T_M} = \mu_0 \mathbf{m} \times \mathbf{H}, \tag{2.23}$$

where μ_0 is the permeability of free space ($4\pi \times 10^{-7}$ Hm^{-1}). The magnetic moment $\mathbf{m}$ of the object is defined as

$$\mathbf{m} = \int_V \mathbf{M} dV. \tag{2.24}$$

Here, $\mathbf{M}$ is the magnetisation of the object and dV is the volume element. It is clear from Equation 2.23 and 2.24 that the torque experienced by the object is dependent on its orientation (from the angle between parameters $\mathbf{m}$ and $\mathbf{H}$), the strength of the external field, as well as the magnetisation and volume of the object. The magnetisation of a magnetic material is in turn a function of $\mathbf{H}$, depending on the class of magnetic material.

In magnetism, a key equation is the magnetic flux density between two magnetic dipoles. A magnetic dipole is the magnetic analogue of an electric dipole. A point to note about this analogy, is that magnetic monopoles – the equivalent of an electric charge – are yet to be observed. The magnetic flux density produced by a magnetic dipole moment is defined by $\mathbf{B} = \nabla \times \mathbf{A}$, where $\mathbf{A}$ is the magnetic vector potential. Finally, the magnetic flux density in

tesla is

$$\mathbf{B} = \frac{\mu_0}{4\pi}\left(\frac{3(\mathbf{m}\cdot\mathbf{r})\mathbf{r}}{r^5} - \frac{\mathbf{m}}{r^3}\right), \tag{2.25}$$

where r is the radial distance from the dipole [53].

Magnetic materials can be classified into three main types according to the response of materials in an external magnetic field: ferromagnetic materials, paramagnetic materials and diamagnetic materials. The three classifications are shown in Figure 2.7

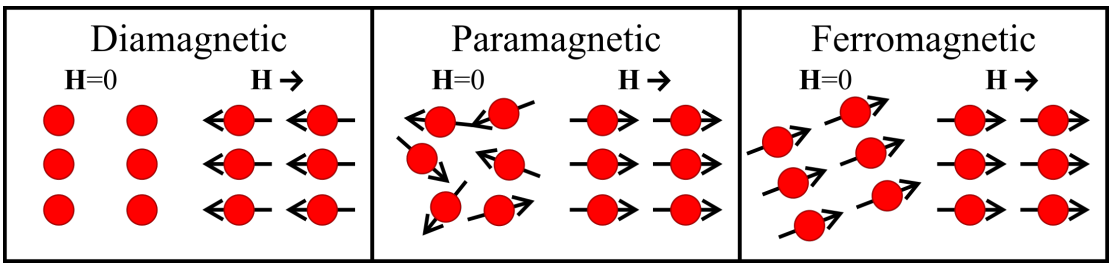

Fig. 2.7 Schematic representation of diamagnetic, paramagnetic, and ferromagnetic materials microscopic structures at rest and in the presence of a magnetic field **H**

A diamagnetic material has no net atomic or molecular magnetic moment. A magnetic response derives from the change in the movement of electrons in the presence of an external magnetic field. The electrons move in such a way that they produce a magnetic dipole moment anti-parallel to the external magnetic field. The magnetic response does not remain when the external field is removed. Most elements are diamagnetic, a couple of examples include; copper (Cu), silver (Ag) and gold (Au).

Paramagnetic materials have a net magnetic moment at the atomic level, with random orientation when no external magnetic field is applied. When an external magnetic field is applied, the moments tend to align parallel with it. Materials which exhibit this response include magnesium (Mg), platinum (Pt), and aluminium (Al).

Ferromagnetic materials such as iron (Fe), cobalt (Co), and nickel (Ni) have a net magnetic moment at the atomic level, but show a strong coupling between magnetic moments. The

magnetic moments align in the same direction and parallel to each other. This coupling gives rise to macroscopic regions of aligned moments, known as domains. The magnetic domains undergo further alignment when a ferromagnetic material is subjected to an external magnetic field. Ferromagnetic materials can be permanently magnetised since they are able to retain a residual magnetisation - even with the removal of the external magnetic field.

In general, the magnetisation of paramagnetic and diamagnetic materials have a linear dependence on the applied magnetic field **H**. The magnetisation is defined as

$$\mathbf{M} = \chi_{\mathrm{m}}\mathbf{H}, \tag{2.26}$$

where the quantity χ_{m} is the magnetic susceptibility. If $\chi_{\mathrm{m}} > 0$, the magnetic field is increased by the material, and this corresponds to a paramagnetic material. If $\chi_{\mathrm{m}} < 0$, the magnetic field is decreased by the material, this corresponds to a diamagnetic material. The main feature of a ferromagnetic material is that their magnetisation is nonlinear in **H**, a phenomenon known as magnetic hysteresis (Figure 2.8).

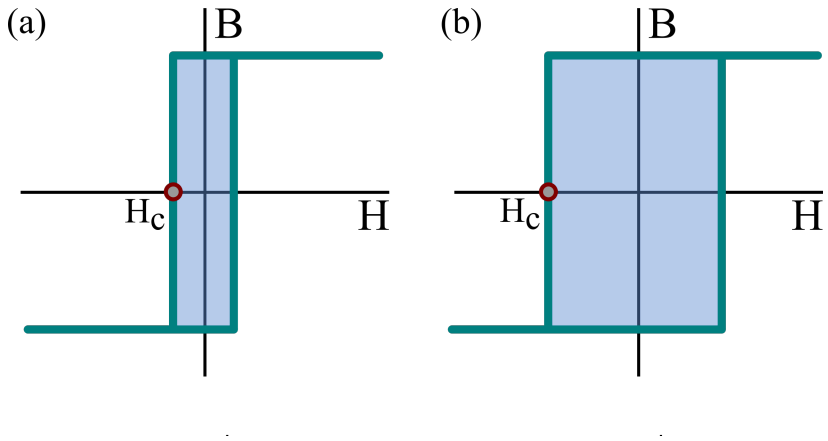

Fig. 2.8 Ideal representation of hysteresis loops for ferromagnetic materials. The magnetic coercivity is shown as H_c. (a) A material with a typical soft ferromagnetic response. (b) A material with a typical hard ferromagnetic response.

Ferromagnetic materials have been very important in modern technology and are the basis for many electrical devices, including motors and transformers, as well as magnetic storage devices such as hard disks and tape recorders.

The behaviour of ferromagnetic materials is based on the coercivity (H_c) of the material. Coercivity is the intensity of the applied magnetic field required to reduce the magnetisation of the material to zero, after saturation. The saturation is the state at which the applied magnetic field can no longer increase the magnetisation of the material, shown as the plateaus with no area on Figure 2.8. Typically, ferromagnetic materials with a high coercivity are known as ferromagnetically hard, as after saturation the material will keep its magnetisation. Practically, this means materials with an intrinsic coercivity greater than $\sim 10\ \mathrm{kAm}^{-1}$. A material with a low coercivity will demagnetise on small time scales and are known as ferromagnetically soft. Such materials, typically have an intrinsic coercivity less than $\sim 1\ \mathrm{kAm}^{-1}$. An example of a hard ferromagnetic material is neodymium iron boron (NdFeB) and a soft ferromagnetic material, iron (Fe) - these are the magnetic materials investigated in this work. Ferromagnetic materials are typically used for the fabrication of magnetic swimmers, since they have larger magnetisation compared to paramagnetic and diamagnetic materials. The large magnetisation results in a stronger magnetic force and torque experienced. Although some micro-scale swimmers - where rely on collective interactions - have been fabricated using paramagnetic materials [54, 55, 20, 56, 57].

2.2.1 Magnetically actuated swimmers

Two main types of magnetic fields have been used to manipulate the propulsion of magnetic micro-scaled swimmers, rotating field and oscillating fields. A rotating magnetic field has a flux density **B**, which rotates around a central axis. In an oscillating field, the flux density **B**, changes direction in the plane. There are three main types of magnetic swimmers that have been investigated over the years. The first that will be discussed will be swimmers that

are based on spiral or helical structures. In the case of these helical strictures, a rotating magnetic field rotates around the axis of the length of the swimmer. The second type are known as "surface walkers" and rely on the magnetic field interactions of many magnetic colloidal particles bound to a surface. The final type are flexible magnetic swimmers, which have been shown to be actuated using both rotating and oscillating magnetic fields. These swimmers rely on the interactions of both the magnetic and flexible components present. The swimmers shown in this sections are the closest of interest to the work presented in the following chapters.

Spiral and helical magnetic swimmers

One of the first magnetically actuated swimmer was shown in the work produced by K. Ishiyama *et al*. The swimmer consisted of a screw-shaped structure and a NdFeB magnet (Figure 2.9a) of total length 12 mm [8] and was controlled by using a rotating magnetic field. The mechanism of propulsion of the device showed great potential for being used for micro-scaled swimmers, as it could swim under conditions of a Reynolds number of 10^{-7}. The authors later worked on a similar device, in which an endoscope capsule was incorporated [58]. The device comprised of a NdFeB magnet inside of the capsule and a spiral shape outside (Figure 2.9b). It was demonstrated that the device could move at a maximum speed of 5 mm s^{-1}. A popular method used to utilise the induced magnetic torque are micro-scaled helical swimmers actuated via rotating magnetic fields [59–61, 18, 62, 63, 19]. These magnetic helical swimmers mimic the flagella propulsion mechanism used by *E. coli* and other micro-organisms. First proposed by Honda *et al*, the device (Figure 2.10a) was composed of a small samarium–cobalt (SmCo) magnet (1 mm $\times$ 1 mm $\times$ 1 mm) attached with a spiral Cu wire with length 21.7 mm [59]. The swimmer was submerged in silicone oil and actuated using a rotating magnetic field, causing the magnet to rotate due to the induced magnetic torque. As a result, the swimmer was able to propel in a low Reynolds number

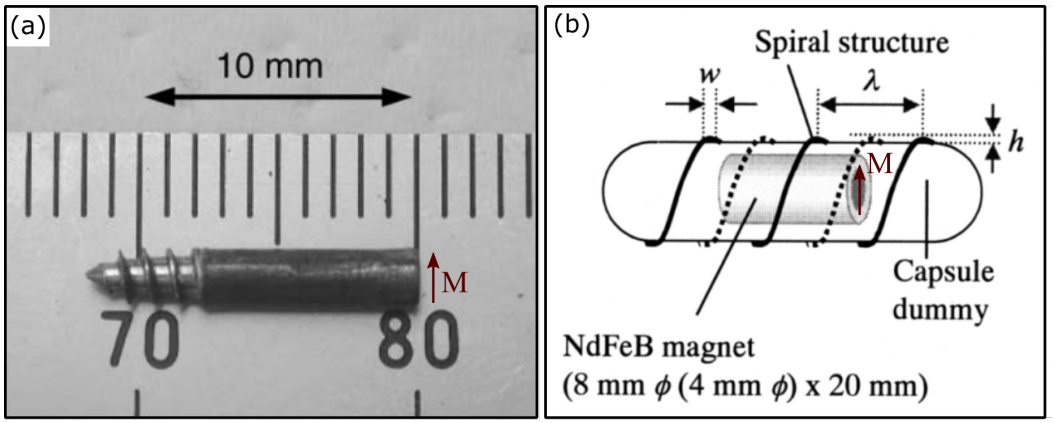

Fig. 2.9 Examples of the simple designs of magnetic torque devices. (a) Photograph of the spiral-type magnetic device consisting of a 7.5 mm long (2 mm diameter) NdFeB magnet - magnetised along the diameter - and a 4 mm spiral cone tip. Figure adapted from K. Ishiyama *et al* [8]. (b) Schematic of the device comprising of a NdFeB magnet - magnetised along the diameter - encased in an endoscope capsule, with a spiral structure on the outside. Figure adapted from M. Sendoh *et al* [58].

environment and the velocity of the swimmer increased linearly with frequency. In 2005, the same group developed a smaller version of the swimmer, with a total length of 5.55 mm [60]. The swimmer (Figure 2.10b) was composed of a SmCo magnetic cylinder and a Cu tube attached to a spiral tungsten wire. It was shown that the swimmer was able to trail a thin wire and change direction within a narrow fluidic channel. Using silicone oil (the viscosity is much greater than that of water) this system mimicked propulsion through a blood vessel, resulting in the propulsion method showing great potential for navigating medical catheters. In 2007, the first micro-scaled helical swimmer was reported [64]. The flagella of living bacteria can range in size from 2 - 20 µm, thus the swimmer was of comparable size to what is observed in nature (Figure 2.10c). The swimmer consisted of a soft magnetic head and a helical tail with the diameter of 3 µm and a length of 30 - 40 µm. The swimming properties of these artificial bacterial flagella (ABF) were characterised by Zhang *et al* [65]. It was shown that the ABFs could be propelled and steered precisely in water by a low-strength (2.0 mT) rotating magnetic field. The directional control of the ABFs was achieved by the translational motion and rotation directions of the applied field (Figure 2.10d). It was stated

by the authors that the tracking and navigation of the ABFs in a dynamic fluid environment would be challenging.

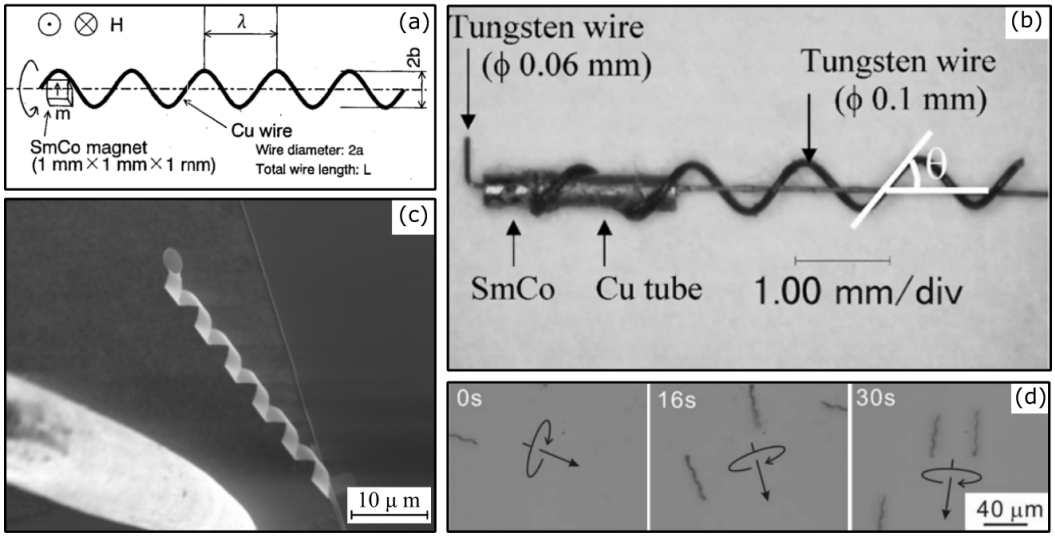

Fig. 2.10 An overview of magnetic helical swimmers. (a) The first prototype of a magnetic helical swimmer. Figure from [59]. (b) Millimetre scaled magnetic helical comprising of a SmCo magnet attached to a tungsten wire. Figure from [65]. (c) The first micro-scaled prototype of a helical swimmer. Figure from [64]. (d) Characterised motion of the micro-scaled prototype shown in Figure 2.10c. The arrows indicate the translational motion and rotation direction of the applied magnetic field.

In 2009, P. Fischer's group was working a different fabrication method which allowed a large number of micron sized colloidal screw-propellers to be created in a single evaporation run [66]. The method was based on a deposition technique known as "glancing angle deposition" (GLAD). During the deposition of the material (SiO_2), the substrate was at an angle to the vapour flux and was rotated, resulting in the fabrication of a screw-like structure between 1 to2 μm in length. The structures were then coated with a 30 nm layer of cobalt to create a magnetic swimmer (Figure 2.11a). Under the actuation of a 6.0 mT rotating magnetic field, the propellers were able to propel at 20 body lengths per second.

An alternative fabrication method was proposed by W. Gao *et al* in 2014 [67]. This method involved creating plant-based helical swimmers (typically 50 μm). The proposed method simply consisted of depositing a thin magnetic coating on isolated spiral xylem

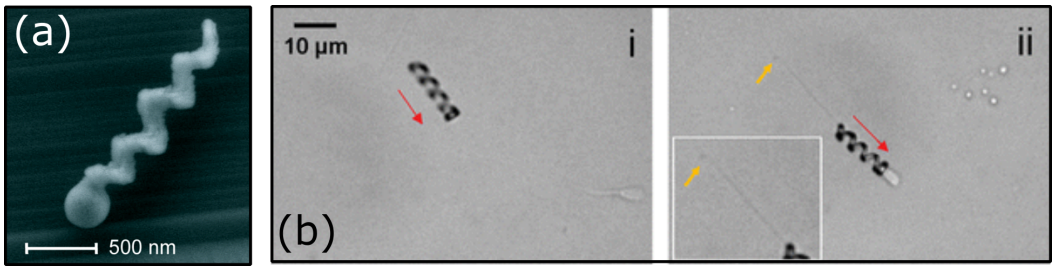

Fig. 2.11 Further examples of magnetic helical swimmers. (a) Scanning electron microscope image of an individual glass screw with nanostructured helicity, fabricated by P. Fischer's group using the GLAD technique. Figure from [66]. (b) The so-called spermbot was able to propel, capture an immobile sperm cell and transport the cell. Figure from [19].

vessel planet fibres. This method created mover a million individual helical swimmers (biocompatible) from a single segment of the plant stem. These novel plant-based swimmers were able to propel at speeds of approximately 5 body lengths per second.

Spiral and helical swimmers have been a large focus for many groups [61, 18, 62, 63]. Most recently, in the work by M. Medina-Sanchez *et al* the swimmers were shown [19] a transportation devices for sperm cells. The so-called spermbots (approx. 20 µm) were fabricated using Direct Laser Writing and were coated with a soft-magnetic NiTi layer. These swimmers were shown to have a peak speed of 70 µm s^{-1}. Most interestingly, the swimmers were able to capture, transport, and release a single immotile living sperm cell without damaging the cell (Figure 2.11b).

Surface interaction swimmers

Devices that rely on surface interactions are known as "surface walkers" and require an air-fluid or fluid-fluid to propel. A large amount of these devices have been proposed, in which micro-scaled magnetic colloidal particles self-assemble into structures induced by an alternating magnetic field [54, 55, 20, 56, 68–71]. The work produced by A. Snezhko *et al*, is based on the formation of snakelike structures (Figure 2.12a) from nickel micro-particles, via an out-of-plane oscillating magnetic field [68]. In addition, an in-plane DC magnetic field was applied to probe the magnetic properties of the structure. It was later shown, that

these nickel micro-particles could be used to produce a magnetic surface swimmer [69], by attaching a bead to one end of the snakelike structure (Figure 2.12b). The bead used for the head was either glass or polystyrene (1 - 2 mm) and would self-attach itself to one end of the snake structure. The authors state that the control over the direction of the swimmer could be gained through use of spatially inhomogeneous fields. Such structures are of great interest, but the main concern with these "surface walkers" is that they rely on the surface interactions, making them impractical for many of the desired bulk fluid applications.

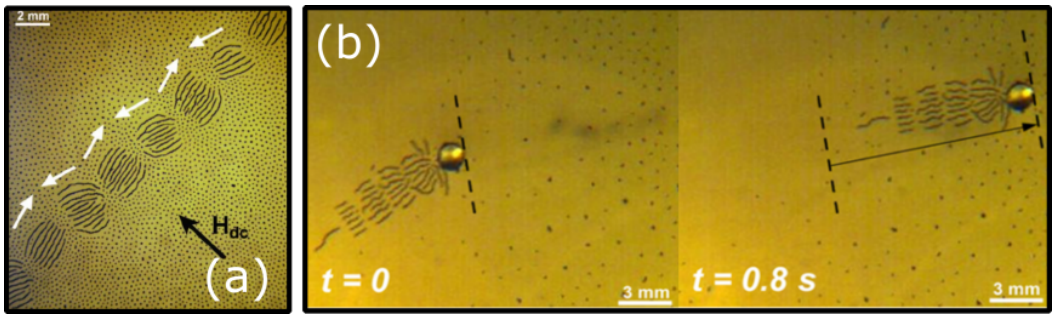

Fig. 2.12 Examples of magnetic surface swimmers. (a) Formation of the snake-like self-assembly structure due nickel micro-particles subject to an out-of-plane magnetic field. Figure from [68]. (b) Surface swimmer consisting of a snake-like self-assembly structure and a glass bead. Figure from [69].

More recently, work has been conducted to be investigate the flocking behaviour of colloidal particles [72]. In this work, the global behaviour of ferromagnetic particles actuated by a vertical alternating magnetic field were investigated. It was shown that large-scale collective motion could be observed: spontaneous clockwise/counter-clockwise rotation, and alignment of particle velocities. This work was shown to be useful for understanding coherence in large-scale active systems.

Flexible magnetic swimmers

An early simple example of a flexible device that is actuated by an oscillating field, is two permanent magnets coupled together [73]. In this work, two NdFeB magnets (0.7 mm $\times$ 0.7 mm $\times$ 2 mm) attached by a rubber film, swim in water in parallel to the applied magnetic

field (Figure 2.13a). The motion is induced by the magnetic torque and the repulsive force yielded on the magnets.

An elegant example of a device using this method, is the artificial micro-scaled swimmer produced by R. Dreyfus *et al* [9]. This swimmer had a red blood cell which acted as the head of the device, and a linear chain of magnetic particles linked by DNA serving as a flexible artificial flagellum (Figure 2.13b). The chain would align with an external uniform magnetic field and would be actuated by an oscillating transverse field. They found that the actuation induced a beating pattern that was able to propel the structure, and that by varying the external fields, the velocity and direction of motion could be controlled.

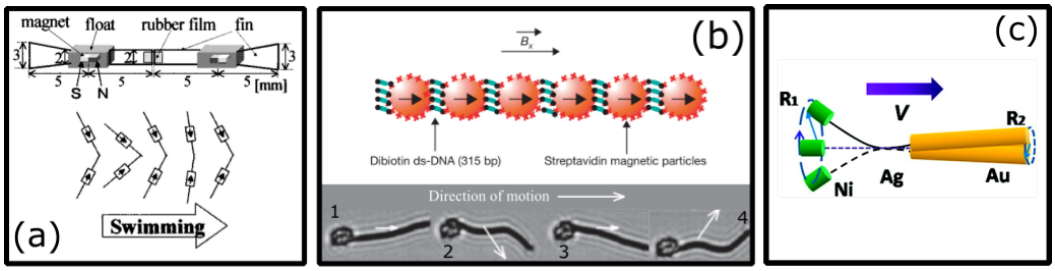

Fig. 2.13 Examples of flexible magnetic swimmers that use oscillating magnetic fields. (a) Structure of the device comprising of two NdFeB magnets coupled together. Schematic of the motion of the device in the presence of an oscillating magnetic field. Figure from [73]. (b) Schematic representation of a flexible magnetic filament. Beating pattern of the motion of a magnetic flexible filament - comprising of DNA connected magnetic particles - attached to a red blood cell. The white arrow represents the direction of motion. The magnetic field at time steps is represented by the red arrows. ($B_x = 8.3$ mT, $B_y = 13.7$ mT, $f = 10$ Hz). Figure from [9]. (c) Schematic diagram of the flexible Au/Ag/Ni nano-wire device. Figure from [74].

In 2010, a device comprised of flexible Au/Ag/Ni nano-wires utilised rotating magnetic fields [74]. This device comprised of a gold head and a nickel tail coupled by a partially weakened silver link (Figure 2.13c). The flexible link promoted cyclic mechanical deformations under an external rotating magnetic field. In such a field the nickel tail would start to rotate, causing the gold head to rotate at a different amplitude. The authors concluded that this simple design obviates the requirement for the complex helical micro-structures, as previously stated. Similarly, to the helical swimmers, by changing the direction of the

rotational axis of the applied field, these swimmers can navigate in three dimensions in the bulk of the fluid.

More recently, I.S.M Khalil *et al.* fabricated a device that mimicked the motion of a sperm cell [75]. The device known as MagnetoSperm (Figure 2.14a) comprised of SU-8 photoresist (epoxy based photoresist), in the shape of a sperm cell, with length 322 µm, and a 200 nm CoNi layer on the head of the cell. The CoNi layer provided a dipole moment, and allowed the flexible structure to align with the oscillating magnetic field, hence generating propulsion, with an average speed of 0.1 – 0.5 body lengths per second. The direction of propulsion was controlled by directing the oscillating magnetic field towards a reference position.

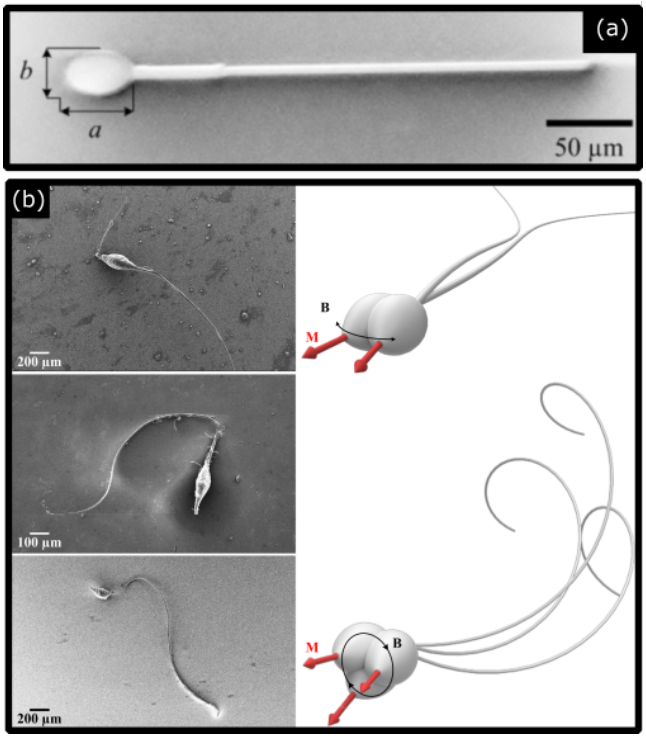

Fig. 2.14 Examples of flexible magnetic swimmers that were developed by I.S.M Khalil *et al.*. (a) Image of the SU-8 and CoNi device known as MagnetoSperm. Figure from [75]. (b) The robotic sperm consisting of a magnetic head and a flexible flagellum. The Planar flagellar propulsion was achieved by applying in-plane uniform field along direction of motion with a sinusoidally varying orthogonal component. The helical flagellar propulsion was created by rotating the magnetic field as shown in the figure. Figure from [75].

As well as the creation of the MagnetoSperm, I.S.M Khalil *et al.* also developed a magnetic sperm-like device made from an ultra-thin polymer material (Figure 2.14b) [76]. The device was able to switch between two modes of propulsion, by manipulating the out-of- and in-plane components of the applied magnetic field. The two modes were a planar motion and a helical flagellar propulsion. They showed that the device could increase the swimming speed by a factor of 1.4 when transitioning between the modes, such a behaviour would not be possible with more rigid materials.

2.3 Pump technology for microfluidic devices

Pumps and valves are basic components in virtually every microfluidic platform. In laboratory conditions, pumps often are external to the microfluidic assembly, which allows for easy and accurate control over every aspect of fluid flow. Lab-on-a-chip devices, however, impose a number of design restrictions that stem from the basic requirement for packing complex functionality in a restricted space. In response to this demand, recent years have seen a number of original design solutions for pumps (both passive and active), valves, mixers and other components that could be incorporated into lab-on-a-chip devices, having various levels of performance and complexity and different actuation mechanisms [77, 78].

2.3.1 Mechanical actuation of micropumps

A main consideration when designing micropumps is the nature of the fluid flow. Typical microfluidic systems (channel widths and height on length scales of tens of micrometres) operate under low Reynolds number conditions, i.e. viscous forces dominate over inertia - as previously discussed. Thus, the systems are under the same restrictions as micro-scaled swimmers. In order to create overall displacement of the liquid, such a pump must execute asymmetric strokes, i.e. the backward stroke must not be a mirror image of the forward stroke, otherwise the liquid volume will oscillate with no net displacement. Stroke asymmetry can be achieved using a system of valves, but at the expense of increased complexity, footprint and cost.

All mechanical micropumps require an actuation source to provide the asymmetric stroke. Some actuation sources include; piezoelectric, pneumatic, and electromagnetic mechanisms.

Piezoelectric actuation

Piezoelectric actuation has been produced by utilising the properties of piezoelectric materials (for example lead zirconate titanate). When a voltage is applied to a piezoelectric material, a

strain and mechanical deformation is produced. By coupling a piezoelectric material - for example a disk - to a pump membrane, the membrane would flex and produce an asymmetric stroke [79–81].

Pneumatic actuation

Pneumatic actuation relies on using a high pressure gas source. The gas chamber is controlled by a two valve system, which either open to pressurise the chamber or closed to depressurise. Coupling this interaction with a flexible membrane, produces a flexing on the membrane and an asymmetric stroke [82–84].

Electromagnetic actuation

The main electromagnetic actuation works using a small-scale electromagnet (a solenoid). The plunger is produced from a ferromagnetic material, and coupled to a membrane. When the electromagnet is powered the ferromagnetic plunger displaces and creates a deformation of the membrane. When the electromagnet is switched off the ferromagnetic plunger returns to its original rest position. Usually such structures are large compared to the other mentioned actuation methods - due to the size of the solenoid [85–87]. However, this system can be quite controllable by tailoring the coil current, and winding number of the coil for the desired application.

2.3.2 Utilising microswimmers as micropumps

Production of a valve-free pump is a non-trivial problem, and requires the identification and implementation of a set of physical interactions that introduce asymmetry to the stroke cycle.

Microfluidic flow generation is the reciprocal of the problem identified for swimming under low Reynolds number conditions, summarised succinctly by the scallop theorem [4]: a swimmer under low Reynolds number conditions will not be able to self-propel unless the

forward swimming stroke is geometrically different from the backwards stroke. Swimming and pumping in this context are two sides of the same coin: a low Reynolds number swimmer can be turned into a micropump by a simple "change of reference", i.e. a spatially restricted swimmer will be able to drive fluid flow. Such an approach has been demonstrated by several groups [88, 89, 22, 90, 91] who implemented methodologies for assembling artificial magnetic cilia which can be used to induce fluid flow.

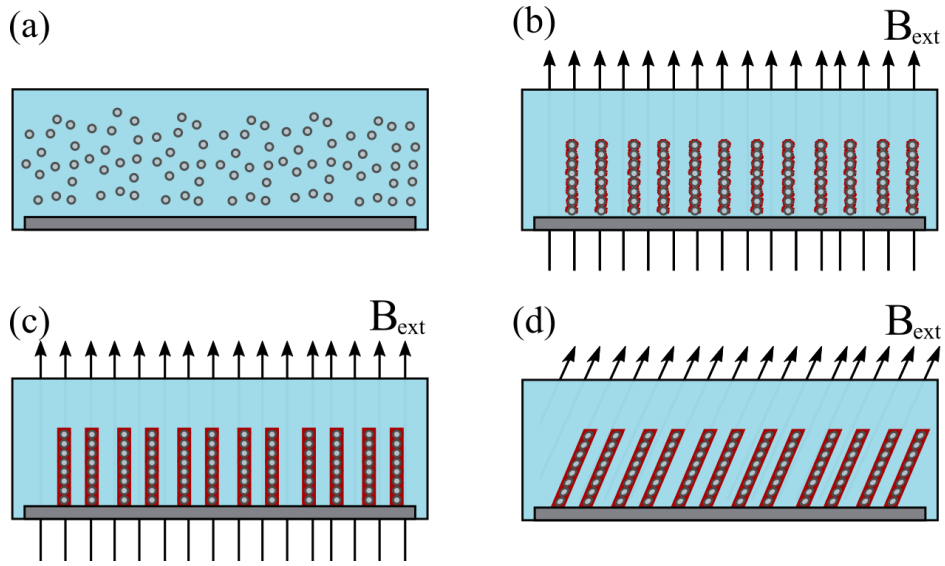

Fig. 2.15 Fabrication of the artificial cilia created by Y. Wang *et al.* (a) A mixture of 2.7 µm spherical polystyrene spheres with embedded magnetic nanoparticles and latex particles are placed within a fluid cell. (b) The magnetic beads are linked into chains and attached to the surface in the presence of an external magnetic field B_{ext}.(c) The latex particles attach to the beads by electrostatic attraction and create chains after heating. (d) Actuation of the artificial cilia by an external field. Figure recreated from [91].

Y. Wang *et al.* created a cost-effective *in situ* fabrication method for magnetic cilia-like structures [91]. The cilia structures ($\sim$ 3 µm) were constructed by self-assembly of micro sized magnetic beads (polystyrene spheres with embedded magnetic nanoparticles) and were encapsulated with soft polymer (latex) coatings. The artificial cilia were actuated using a rotating magnetic field, and a frequency of 5 Hz, created a non-reciprocal motion and a net flow velocity of 3 µm s^{-1}.

The magnetic approach for activating such systems is desirable due to the wireless capabilities and the simplicity of generating the field as small field (< 5 mT) only requiring a small amount of power to generate. Other magnetically controlled valves, pumps, and stirrers have also been demonstrated by other groups [92–95].

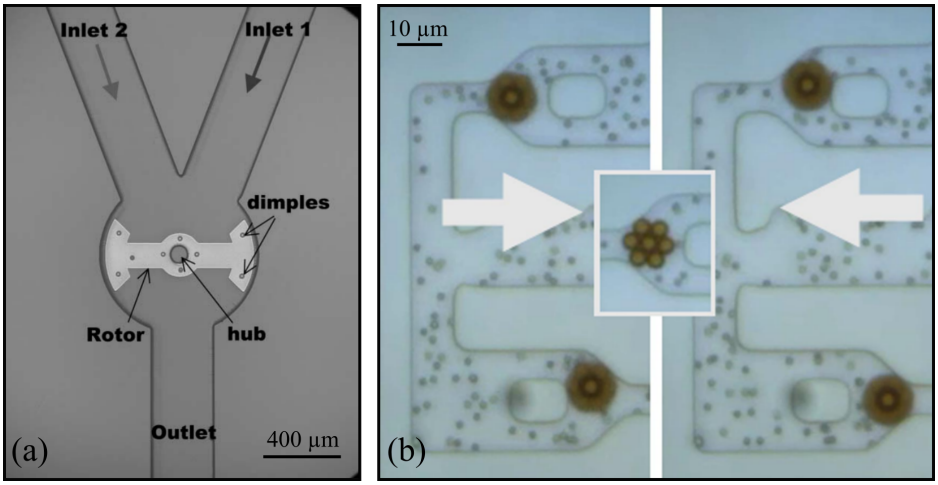

Fig. 2.16 (a) Optical image of a magnetic stir bar inside a microchannel. Two streams of fluid join in the rotor and mix. The rotor diameter is 400 µm. Figure from [92]. (b) Check valve position as a function of applied flow. The colloidal assembly composes of 4.5 µm particles. Note that 1.5 µm particles are used here as flow tracers, the white arrows indicate flow direction. Figure from [93]

2.3.3 Magnetically controlled membranes

Another system of interest consists of creating magnetic-elastic membranes which can be used as valves and fluid pumping systems [96–98]. These membranes can be attached to the top surface of the channel or even built into the walls of the channel. The interest in these is due to them being less intrusive compared to pumps and mixers placed within the channel.

The work by P. Tseng *et al.* shows a method of integrating varying size permalloy features (4 µm to 5 mm) into PDMS (photographs of the structure are shown in Figure 2.17) [98]. Application of an external magnetic gradient led to a deformation of the permalloy

array embedded into PDMS. The structure showed potential to generate new applications in magnetic droplet control, magnetophoresis, bio-patterning, and self-assembly.

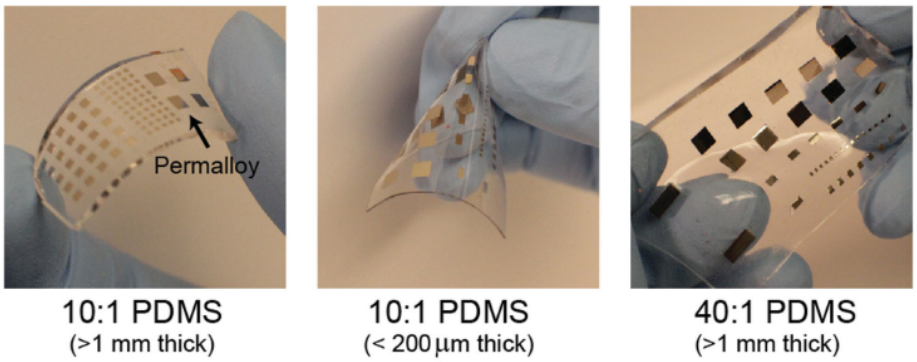

Fig. 2.17 Optical images of a magnetic PDSM membranes of different thicknesses. Thin PDMS membranes can be folded, while metal structures on 40:1 PDMS can be morphed in x and y dimensions. Figure from [98].

2.4 Conclusion

The underlining issue of swimming at a low Reynolds number has been discussed, showing the derivation in fluid mechanics. The history of swimming in this regime was discussed leading onto a number of different propulsion mechanisms.

As has been demonstrated in a number of cases, a typical approach to tackling the problem would be by mimicking the natural microscopic swimmers in one way for another. Nature finds a way of overcoming the challenges of the microscopic world by deforming their bodies or employing cilia and rotating flagella.

The idealise models showing the volume and separation between spheres is analogous to deformations employed by the eukaryotic cells. However, the creation of such systems has been mainly limited to light driven systems. Light driven systems are shown to be elegant, although such a system could be described as problematic for applications. As this actuation method requires a UV light pulse, the system could not be used in an opaque environment. In addition to this if the system was to be used for a lab-on-a-chip system, addition components will be required, for example a miniature light source and power supply. Many other different methods of propulsion at a low Reynolds number have been discussed including: chemical, ultrasound, electric and magnetic.

The catalytic chemical method creates random propulsion direction can lead to difficulties in applications, such a precise drug transport and delivery. For these random propulsion directions to be controlled, magnetic components are added to the structures. The addition of the magnetic components adds another layer of complexity to the system – when other systems rely only on a magnetic field. The main issue with these systems being used for bio-medical applications or use inside the human body is the requirement of H_2O_2 for the reaction, which is toxic. Similar to that of the chemical propellers, ultrasound actuated systems have also been adapted with magnetic components to improve the control over the system. Actuation via electric fields shows promise for applications as pumps and

components in a lab-on-a-chip. However, such a method may be troublesome when involving a human body.

Magnetic actuation will be the focus of the work presented in this thesis, thus a section was dedicated to the understanding of the relevant magnetic theory with a focus on ferromagnetism. Magnetic actuation is a popular method due to the relative safety of magnetic fields, as well as the ease of fabrication of structures. The vast majority of magnetic controlled devices rely on three dimensional or rotating magnetic field structures to produce either the guidance and/or propulsion. For the systems to be portable, this would require the magnetic field to be as simple as possible to have a low power required to generate the field. As a result of this, all presented work in this thesis is focused on one dimension weak (< 5 mT) magnetic fields. The common method used to create a motion is to mimic the beating of cilia or rotation of flagella. This has been studied using the combination of flexible and magnetic materials, as well as fully magnetic materials. Such structures typically have a complex fabrication process.

The underpinning physics behind microfluidic pumps was also discussed, showing how the restrictions due to the Scallop theorem not only apply to micro-scaled swimmers, but also to applications which involve the manipulation of millilitre to microlitre volumes of fluid. The magnetic approach for activating such systems is desirable due to the wireless capabilities and the simplicity of generating the field. Portable devices could be created using the magnetic approach as long as low field strengths are used (< 5 mT), as these fields can be locally generated using the power from a USB. The elegant method of creating a pump by restricting the transitional motion of a micro-scaled swimmer has shown to be an area of interest, however the field is currently still in its infancy. In this thesis, there will be a focus on creating fluid pumps for different application (examples include: possible cell sorting channels and blood plasma separation) using a range of different elastic-ferromagnetic swimmers.

The collective interactions of natural flagella as well as artificial flagella has been shown to create a motion – be it propulsion or fluid flow – greater than a single beating system. Building upon the fabrication techniques outlined in this thesis, collective arrays of magnetic components were created. Unlike the previously discussed flagella systems, these systems are comprised of components that on their own are bound by reciprocal motion. Therefore, do not create a net flow, until they are allowed to magnetically interact with each other, resulting in rotational patterns not possible before.

Chapter 3

Experimental methods

This chapter will describe the experimental methods which were commonly used over the course of the work. This includes the fabrication of magnetic and elastic components, the main experimental system used, as well as the data collection and analysis.

3.1 Swimmer, pump, and membrane fabrication

The fabrication of all presented devices follows a similar methodology, comprising of different combinations of magnetic and elastic components. This section focuses on the creation of the different ferromagnetic and elastic components used within this work.

3.1.1 Fabrication of magnetic components

A key ingredient in the presented devices are the magnetic components. All systems created in this work rely on having at least one hard ferromagnetic particle, and in some cases a mixtures of hard ferromagnetic and soft ferromagnetic particles. Hard ferromagnetic materials have a high coercivity and thus retain their magnetisation in the absence of an applied field (for example permanent fridge magnets). In contrast soft ferromagnetic materials have a low coercivity, thus demagnetise on small timescales in the absence of an applied field (for

example a paper clip). The creation of the soft ferromagnetic particles size and geometry has remained the same throughout all presented work, and will be discussed first.

In this work, iron (Fe) was used as the soft ferromagnetic material, because it is an intrinsically soft ferromagnetic material, that is relatively easy to magnetise and demagnetise in weak magnetic fields. 99.5% pure Fe wire (diameter 0.5 mm) was purchased from Advent Research Materials. The material was cut using a diamond dicer (LoadPoint Micro Ace 3 Dicing Saw) to produce the soft (0.7 mm long with diameter 0.5 mm) particles.

The hard ferromagnetic material used throughout this work was neodymium iron boron (NdFeB), however this material has taken different forms during the work. Initially, the creation of the hard ferromagnetic particles consisted of using a method similar to that of the soft ferromagnetic particles. For example, 5 mm $\times$ 2 mm $\times$ 0.45 mm rectangle NdFeB magnets were purchased from First4Magnets. These magnets were cut once again using the diamond dicer (LoadPoint Micro Ace 3 Dicing Saw) to produce hard ferromagnetic particles with dimensions 0.6 mm $\times$ 0.6 mm $\times$ 0.45 mm. A better option used in later work was the use of hard ferromagnetic particles, purchased from SuperMagnetMan. Cube magnets with the dimensions 0.5 mm $\times$ 0.5 mm $\times$ 0.5 mm.

The hard ferromagnetic particles used in the presented investigations was further improved in order to have a greater control over the geometry and strength of the particles. The method used to create these magnetic components were based on the production of the elastic components. The method will be discussed in the following subsection.

3.1.2 Fabrication of elastic components

The second component present in all the fabricated systems was the elastic material. The presented work focuses on the interaction of different magnetic forces, with different geometries of elastic materials. Thus a high control over the geometry and dimensions was required. The initial prototypes used a brass based mould to create the elastic component (discussed in

Chapter 4), however this method had little control over the geometry and could not be used for rapid prototyping or mass production.

To create the control over the geometry a stereolithography 3D printer was used (Formlab Form 2). This method can be used to create structures with layers as fine as 0.05 mm, resulting in a minimum feature size of 0.2 mm. To create the desired geometries a commercial computer-aided design software (Autodesk AutoCAD) was used to design a mould. As a result of combining 3D printing and AutoCAD the ability to easily produce a large range of elastic shapes was achieved. Once the mould was printed, it was placed in a bath of isopropyl alcohol for 20 minutes to remove any uncured material. After this process, the mould could be used to create the elastic components.

The elastic material of choice was a silicone based rubber. Other elastomers were also tested. Dow Corning 781 silicone sealant cured at room temperature for 4 hours produced a large number of air bubble defects. Liquid latex cured at room temperature for 6 hours also produced components with a large number of visible defects. Polycraft silicone rubber and fast cure catalyst (GP-3481-F) were purchased from MBFibreglass. The two components were mixed with a weight ratio of 1:10 (catalyst:silicone) and placed into the 3D printed mould cured at room temperature for 6 hours, with minimal defects.

3.1.3 Controlling geometry and magnetic properties

As previously mentioned, the final improvement for the magnetic components relied on the 3D printing methods used for the elastic components. Using AutoCAD and the 3D printer resulted in a high degree of control over the geometry and dimensions. This method was latter used for the magnetic components; mixtures of silicone based rubber and magnetic powder were created.

The liquid silicone rubber was once again mixed with the curing catalyst in a 1:10 ratio (by weight). NdFeB powder (average diameter $< 10\,\mu m$) was added to the rubber mix.

By mixing different volumes of NdFeB powder to the rubber, the desired control over the magnetic properties of the components is obtained. Once the magnetic rubber mixture was cured, the component would need to be magnetised. To magnetise the components, a MicroSense Vibrating Sample Magnetometer (VSM) was used, shown in Figure 3.1.

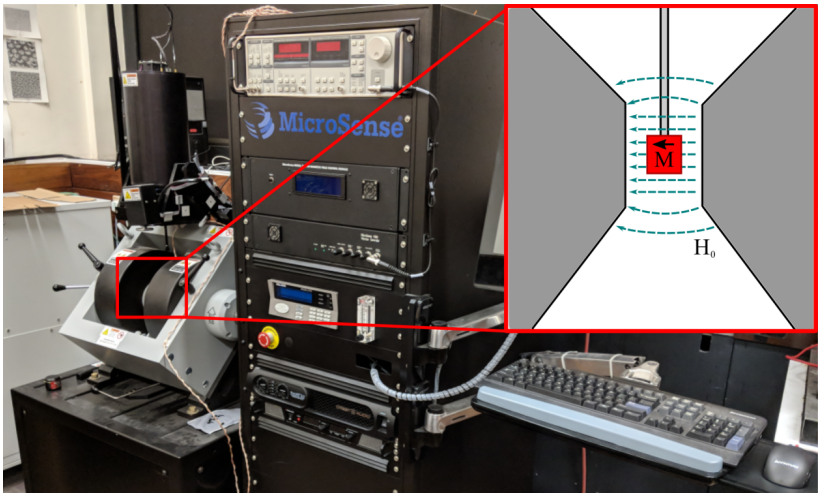

Fig. 3.1 Photograph and schematic diagram of a Vibrating Sample Magnetometer.

Vibrating Sample Magnetometry is based on Faraday's law which states that an electromagnetic force is generated in a coil when there is a change in flux through the coil [53]. When measuring a magnetic response with a VSM, a magnetic sample is moved in the proximity of two pickup coils. The sample is fixed to a sample holder and vibrated vertically via a sinusoidal signal. The sample is placed in the centre of the two poles of an electromagnet which generates a homogeneous magnetic field $\mathbf{H}_0$.

Pickup coils are mounted on the end of the poles of the electromagnets, with the symmetry centre in line with the static location of the sample. As the sample is displaced vertically, the magnetisation of the sample induces a voltage difference U_{ind}. Using this induced voltage, according to Faraday, the magnetic properties of the sample can be found. However, in the presented work, the VSM is used to saturate the hard ferromagnetic components.

The VSM used is capable of generating magnetic field strengths up to 1.8 T. NdFeB has a saturation of is $\sim$ 1.6 T, thus the VSM it was able to fully magnetise the NdFeB magnetic

component in the direction of the applied magnetic field strength. This provided a complete control over the fixed magnetic moment direction of the magnetic components.

Using the combination of the high resolution 3D printer, elastic materials, magnetic powder and the VSM, it was possible to have a high control over the parameters of the magnetic components. These parameters include the geometry, the dimensions (sizes down to 0.2 mm), the volume fraction of magnetic material, and the fixed magnetic moment direction.

3.2 Experimental systems

This section will describe the experimental setup commonly used in all the presented work. All magnetic systems investigated rely on an external magnetic field to be actuated. This work was focused on producing a uniform oscillating magnetic field, who's the frequency and amplitude can be varied. In this work, two coil Helmholtz systems were used to create a one dimensional uniform field; however, three different versions of two coil systems were used.

The basic idea of a Helmholtz coil system is to create a region of nearly uniform magnetic field. A Helmholtz coil system consists of two identical circular magnetic coils on the same axis, shown in Figure 3.2. The coils of radius R_{Helm} are separated by a distance h. In the case of a Helmholtz pair, $h = R_{\text{Helm}}$, which minimises the non-uniformity of the produced magnetic field.

The strength of the magnetic field B_{Helm}, is controlled by the winding of the coils n, the coil current I, and radius R_{Helm}. Starting from Biot-Savart law, for a single wire loop [53], of radius R_1 will in induced magnetic field, which is defined as

$$B_1(x) = \frac{\mu_0 I R_1^2}{2(R_1^2 + x^2)^{3/2}}, \tag{3.1}$$

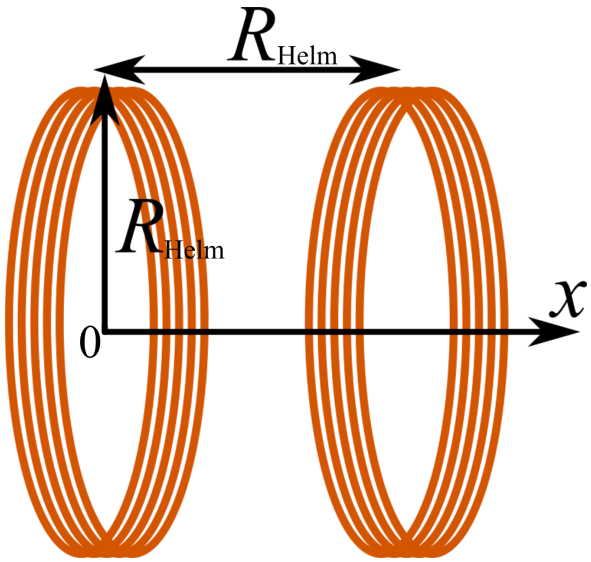

Fig. 3.2 Schematic diagram of a Helmholtz pair.

where μ_0 is the permeability of free space, and x is the distance from the wire loop. As a Helmholtz coil consists of n turns of a wire, the equivalent current is nI

$$B_1(x) = \frac{\mu_0 n I R_1^2}{2(R_1^2 + x^2)^{3/2}}. \tag{3.2}$$

Halfway between two loops the field strength will be twice as high - due to there being two coils

$$\begin{aligned} B_{\text{Helm}}(R_{\text{Helm}}/2) &= 2\text{B}_1(R_{\text{Helm}}/2) \\ &= \frac{2\mu_0 n I R_{\text{Helm}}^2}{2(R_{\text{Helm}}^2 + (R/2_{\text{Helm}})^2)^{3/2}} \\ &= \left(\frac{4}{5}\right)^{3/2} \frac{\mu_0 n I}{R_{\text{Helm}}} \end{aligned} \tag{3.3}$$

3.2.1 Initial Helmholtz coil system

The initial experimental setup consisted of a large area Helmholtz coil system. Each coil of the magnetic system had approximately 560 turns with a width of 61 mm, inner bobbin

diameter 155 mm and height 37 mm. A large area Petri dish (148 mm diameter) was placed in the centre of the system. A magnetic field was produced by a signal generator using a sinusoidal signal, that was connected to a power amplifier to increase the voltage of the signal. The fields generated had a frequency range of 1 - 200 Hz, with a maximum field strength of 4.0 mT. A 1080p HD camera was attached to the top of the coils to monitor the Petri dish. The camera was connected to a computer for video analysis. A photograph of the initial system is shown in Figure 3.3.

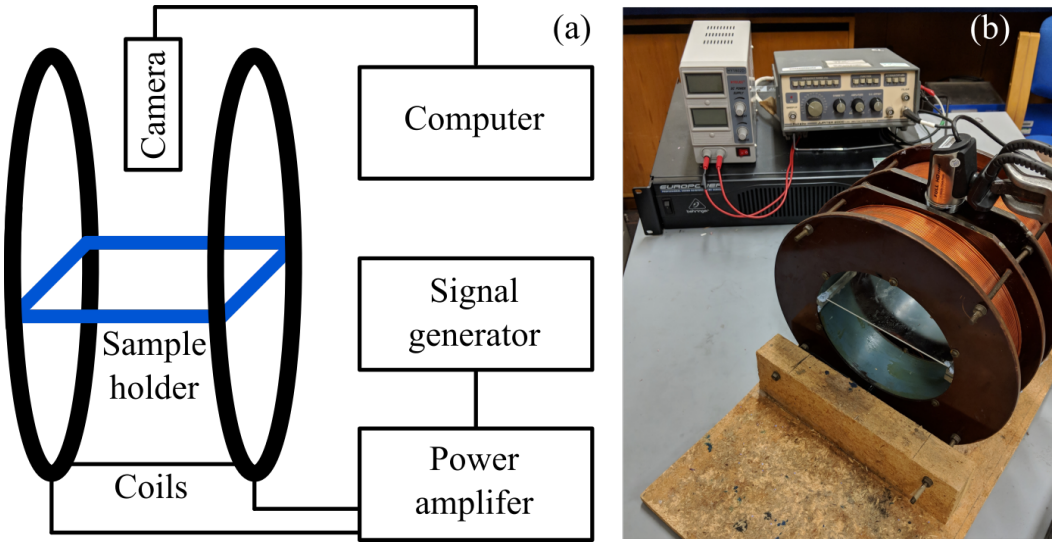

Fig. 3.3 (a) A schemetic diagram and (b) a photograph of the large area Helmholtz coil system, with a camera for particle tracking. The signal is produced by a signal generator attached to a power amplifier. A DC power supply is also shown for creating static magnetic fields.

3.2.2 High-speed camera system

To improve on the first experimental setup, Dr. Tom Myers from Platform Kinetics collaborated with the University of Exeter to create a new system. This system also was required to create a uniform AC electromagnetic field. In this case, the system was created as a 3 axis coil system, however in the presented work, only the x component was used. The x and y axes were based on a rectangular Helmholtz geometry and the z axis on a circular geometry. A photograph of the system is shown in Figure 3.4

The produced magnetic field strengths ranged up to 25 mT for frequencies of 1 - 300 Hz, with an observation area of 50 mm $\times$ 50 mm. A PC interface was created to control the frequency, amplitude and phase of the three magnetic fields. A microscope was built around the coil assembly with an extended optical path to reach into the centre of the coils. A high-speed camera was also attached to the microscope system (Mikrotron Motionblitz), which could achieve a frame rate up to 1700 fps.

Due to the smaller area, this system was useful for observing the internal motion of the devices (rather than net motion), and fluid pumps. This system was also very useful for creating high field strengths (up to 6.0 mT) at 1 Hz. These high fields at such a low frequency were very useful for some of the collective motion systems discussed in this work.

Fig. 3.4 Photograph of the inside of the 3 axis Helmholtz coil system. Photograph of the optical system in use, produced by Platform Kinetics.

3.2.3 Portable Helmholtz coil system

In addition to the other two Helmholtz coil systems, Dr. Tom Myers from Platform Kinetics also created a smaller, portable (approximately 15 cm x 15 cm x 25 cm), all-in-one system. This system (shown in Figure 3.5) comprised of a single axis Helmholtz pair, connected to a Raspberry Pi and touch screen. The system also had a built-in camera, thus it was completely self-contained. The user friendly interface to control the frequency and amplitude of the magnetic field made the system perfect for quick initial exploratory tests (before a full investigation), as well as for the undergraduate physics laboratory.

Fig. 3.5 Photograph of the portable system, produced by Platform Kinetics.

3.2.4 Controlling the viscosity of the fluids

Due to the nature of the experiments, a range of viscous fluids were required to test the capability of the devices in different Reynolds number regimes. To do this, sucrose (reagent grade) and sodium azide were purchased from Sigma-Aldrich and were dissolved in water using a heating magnetic stirrer to produce sucrose solutions with concentrations of 30%, 40%, 50%, 60%, and 70%. The trace amount of sodium azide (30 mg per 100 ml) was added to prevent bacterial growth. The viscosity of these solutions have been well studied in the literature [99, 100]. Other fluids used in the experiments were water (for the lowest viscosity) and glycerol (for the highest viscosity). Table 3.1 shows all viscous fluids used.

Viscous fluid	Kinematic viscosity [m^2s^{-1}]
Water	8.96×10^{-7}
30% Sucrose	2.48×10^{-6}
40% Sucrose	4.41×10^{-6}
50% Sucrose	1.01×10^{-5}
60% Sucrose	3.45×10^{-5}
70% Sucrose	2.40×10^{-4}
Glycerol	7.20×10^{-4}

Table 3.1 List of viscous fluids produced in the experiments.

3.3 Data analysis

This section will focus on the collection and analysis of data. In all experiments, the raw data was videos. However, depending on the system, the analysis was different. The two main analysis methods were particle tracking and particle image velocimetry (PIV).

3.3.1 Analysis of migration characteristics

When the magnetic device of interest is free to execute translational motion on the surface of the fluid, a particle tracking software is required to analyse its migration characteristics. In this work, the linear net motion of the device is known as the swimming speed. The Open Source software - Tracker was used to obtain the resulting swimming speeds.

Tracker has manual and automated object tracking with position, velocity and acceleration. The automated object tracking worked by assigning a 'region of interest', and saved the pixels within this region. The area has an allowed evolution rate (typically set to 10%) which allows variation in the pixels over the frames.

The video of interest was then split into frames and the software searched for the pixels of the 'region of interest' over the length of the video. An examples of this is shown in Figure 3.6. For calibration, a known distance is specified and the time was taken from the frame rate of the video.

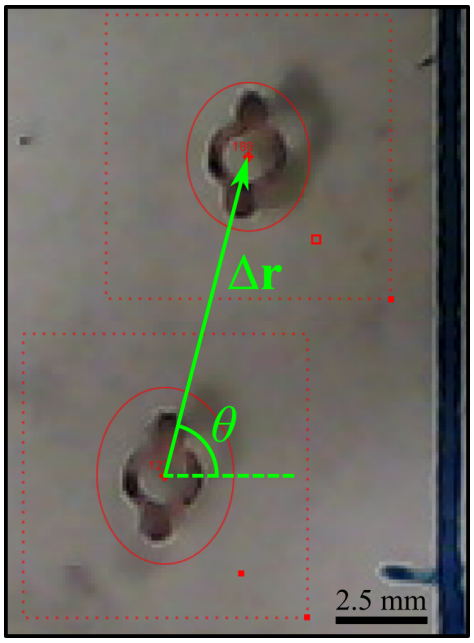

Fig. 3.6 Visualisation of the particle tracking software, showing the position vector, $\Delta\mathbf{r}$, and angle θ between two frames of the video. The long axis of the shown swimmer is 3.6 mm.

The timescale was set to $\Delta t = \frac{1}{framerate}$, and the velocity was found by taking the position of the pixels between each frame, $\Delta\mathbf{r}$ and dividing by the timescale. Using trivial trigonometry, the angle could be found. This method was applied over the total length of the video and the velocity is averaged over all the values. The software was found to be very useful for the cases where the magnetic system was free to propel. In the cases where a fluid flow was being induced, a slightly different method was required - particle image velocimetry.

3.3.2 Particle image velocimetry (PIV)

Digital particle image velocimetry is a common technique used for both qualitative and quantitative flow visualisation [101–104]. The software used in this work (PIVLab), was developed by W. Thielicke [105, 106] and is an open source tool in Matlab. In PIV, typically the motion of a fluid is visualised by illuminating a thin sheet of fluid containing buoyant tracer particles which reflect the light. However, in this work, the surface flows are investigated, thus by placing light the tracer particles (in this case, a fine graphite powder) on the

surface of the fluid. Due to the surface tension of fluid (water and water/sucrose mixtures) and the buoyancy of the particle, they were restricted to the two-dimensional plane of the fluid surface. The sample was illuminated from the top and the videos are captured at 240 frames per second.

In most cases of PIV analyses, two images are created (A and B) at times t_0 and $t_0 + \Delta t$. The distance that the particles have travelled between image A and B is known as the particle displacement. The particle displacement is typically calculated for groups of particles by evaluating the correlation of many small sub-regions of the images. These correlations give the most probable displacement of the group of particles, assuming they travel in straight lines between image A and image B. The velocity of the area of interest can then be evaluated from the particle displacement and Δt.

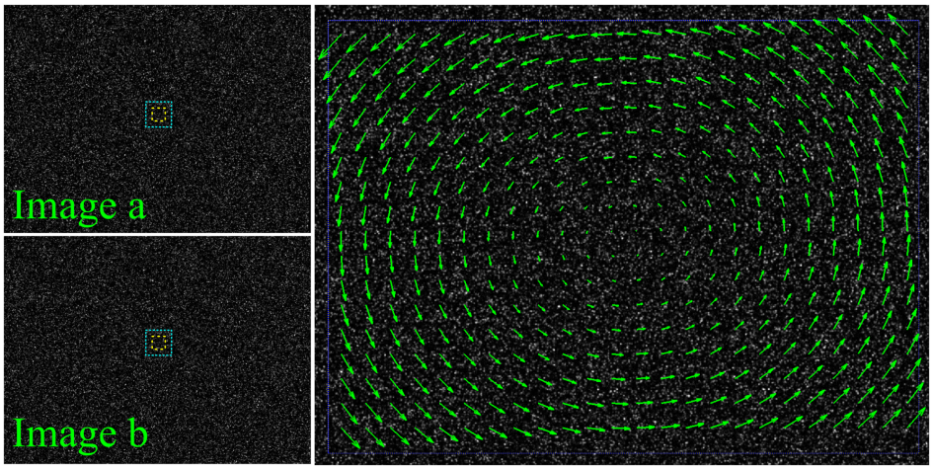

Fig. 3.7 Visualisation of the process used in particle image velocimetry. The boxes on Image A and Image B show the typical sized of the sub-regions. The final image shows the velocity field calculated from the time step and particle displacement.

Figure 3.7 visualises the PIV process, for a computer generated rotational flow (an example created by the software). In reality, the flow fields were more complex and the vectors were vectored over multiple frames of the video. This process was very useful for analysing the flow fields generated by the magnetic systems.

3.3.3 Error analysis

Generally, the intrinsic error of the measurements arises from uncertainties in the measured position and speed of the particle (or swimmer) and the speed of the fluid flow. The speed and position were measured using particle tracking and particle image velocimetry (PIV) between two subsequent frames of the video footage. As an example, a 30 second video (filmed at 30 frames per second) would have created 450 values for the speed for the swimmer, from which the mean and standard deviation are calculated.

For the case of a PIV analysis, an average flow speed over the frame area was created. For example, similar to that of the particle tracking, for a 30 second video, 450 values would be created, however each value in this case contained the flow profile for the measured area. The mean and standard deviation of each point (direction and speed, i.e. 408 white arrows on Figure 3.7). A mean flow speed of the whole area of interest was calculating using the produced flow profile.

The standard deviation was used as a measure of the experimental error. This type of error analysis was used for in all experiments presented in the thesis, unless stated otherwise (for example multiple devices or systems).

Chapter 4

Magnetically controlled swimmers

This chapter focuses on the fabrication and experimental investigation of magnetic millimetre-scaled swimmers. There are two main swimming system that will be focused on. The first is a new class of autonomous ferromagnetic swimming devices, actuated and controlled solely by an oscillating magnetic field. These devices are comprised of a pair of interacting ferromagnetic particles (one NdFeB and one Fe) coupled together by a silicone rubber link. Due to the difference in magnetic properties of the two particles, the application of an external magnetic field leads to time varying dipolar gradient force between the particles (resulting in a relative radial motion) as well as time-dependent torque (causing an oscillatory rotational motion of the whole system). The deformation of the elastic link caused by the two interaction reminiscent of the deformation that many biological organisms, for example the amoeboid movement of eukaryotic cells [107].

The second focus will be on a torque driven ferromagnetic swimmer. This swimmer comprises of a magnetically hard ferromagnetic material attached to a flexible elastic tail. Once actuated by an external magnetic field, the swimmer experiences a torque and creates bending modes that successfully create an asymmetric motion. The swimmer showed a motion which is analogous to the beating flagellum of many natural microscopic swimmers.

4.1 Two-ferromagnetic particle swimmers

This section will demonstrate the experimental and theoretical understanding of the two-ferromagnetic particle swimmer. These swimmers are based on a pair of interacting ferromagnetic particles - of different size and different anisotropic properties - joined by an elastic link. The swimmers are actuated and controlled by the manipulation of the parameters of the external magnetic field - resulting in a robust control over the speed and direction of propulsion.

4.1.1 The theoretical model

In the simplest case, the proposed swimmer utilises two types of interactions, the dipolar gradient forces between the magnetic particles and the torque exerted by the external magnetic field. A schematic representation of the system consisting of a hard and soft magnetic particles is shown in Figure 4.1. To investigate the plausibility of such a system F. Ogrin *et al.* [1, 2]

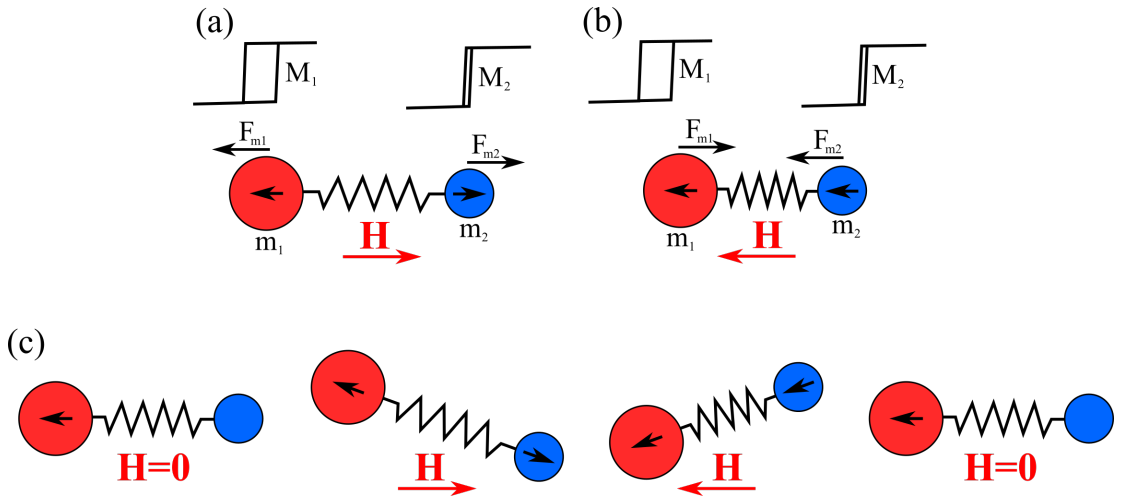

Fig. 4.1 Schematic representation of the system consisting of a hard (red) and a soft (blue) particle connected with an elastic link. The magnetic forces experienced by each particle are shown for two orientations of the external magnetic field: (a) anti-parallel to the magnetic moment of the hard particle, (b) parallel to the magnetic moment of the hard particle. (c) Shows the effects of the magnetic torque when the system is subject to an oscillating magnetic field.

developed a computational model, which calculates the trajectories of the two magnetic particles. The model assumes that both magnetic particles are point dipoles, therefore, for a dipole magnetic field, Equation 2.25 will become

$$\mathbf{B}_{\mathrm{k}} = \frac{\mu_0}{4\pi}\left(\frac{3(\mathbf{m}_{\mathrm{k}}\cdot\mathbf{r}_{\mathrm{k}})\mathbf{r}_{\mathrm{k}}}{r_{\mathrm{k}}^5} - \frac{\mathbf{m}_{\mathrm{k}}}{r_{\mathrm{k}}^3}\right), \tag{4.1}$$

where $\mathbf{B}_{\mathrm{k}}$ is the flux density generated by the particle k, $\mathbf{m}_{\mathrm{k}}$ is the magnetic moment of particle k, and $\mathbf{r}_{\mathrm{k}}$ position vector of the particles j and k (indices denote the particle number, $j = 1$ or $j = 2$ and $k = 3 - j$). The resulting force of attraction or repulsion between the particles is given by

$$\mathbf{F}_{\mathbf{Mj}} = \nabla(\mathbf{m}_{\mathrm{j}}\cdot\mathbf{B}_{\mathrm{k}}). \tag{4.2}$$

The force of attraction or repulsion resulted in a physical displacement of the two magnetic particles relative to each other. This interaction gave the first degree of freedom for the system. To determine the orientation of the dipole moments in the external field $\mathbf{H}$ the model used a standard magnetostatic approach [108] in which the interaction energy is minimised to find the local minima with stable positions of both moments. For simplicity, the magnetostatic energy density for each particle was represented by

$$E_{\mathrm{mag}} = -\mathbf{M}\cdot\mathbf{H} + K\sin^2\alpha. \tag{4.3}$$

The first term is the Zeeman energy representing the interaction of the magnetic moments with the applied magnetic field. The second term is the uniaxial magnetic anisotropy term. This describes the combined effects of shape and crystalline anisotropy, with α being the angle between the magnetic moment of the particles and the orientation of the easy axis respect to the vector $\mathbf{M}$. K is the effective anisotropy field constant. The soft particle was

given a zero value of K, whereas for the hard particle K was chosen so that the effective anisotropy field was higher than the applied magnetic field.

As the system is in the presence of an external elliptical magnetic field, it experiences a magnetic torque. The hard particle (with higher anisotropy) will rotate to align its easy axis with the direction of the applied field. If the particles were rigidly connected with each other, the whole system would experience a mechanical torque, resulting in a rotation of the whole dipole pair. This mechanical torque provided the second degree of freedom in the configuration space required to propel.

As well as the magnetic interactions, both particles were subject to elastic forces (from the elastic link) and hydrodynamics friction. The elastic force $\mathbf{F}_{\mathrm{el}}$ results from compression and extension of the elastic link connecting the particles

$$\mathbf{F}_{\mathrm{el}} = k_{\mathrm{spr}}[(\mathbf{r}_2 - \mathbf{r}_1) - \mathbf{r}_0]. \tag{4.4}$$

Here k_{spr} is the effective spring constant and $\mathbf{r}_0$ is the vector representing the natural length of the spring. In the model the bending modulus of the spring was assumed to be infinitely large.

The hydrodynamic interactions between the two magnetic particles has a decisive contribution for the symmetry breaking and generation of translational displacement. The hydrodynamic interactions were derived by considering the flow past a moving sphere in a viscous fluid, by taking the leading order term from the greens function shown in [109]

$$\tilde{m}_{\mathrm{j}}\mathbf{a}_{\mathrm{j}} = \mathbf{F}_{\mathrm{j}}^{\mathrm{ext}} - \gamma_{\mathrm{j}}\left[\mathbf{v}_{\mathrm{j}} - \frac{3}{4}\frac{R_{\mathrm{k}}}{L_{\mathrm{jk}}}(\hat{\mathbf{n}}_{\mathrm{jk}}\hat{\mathbf{n}}_{\mathrm{jk}} + \mathbf{I}) \cdot \mathbf{v}_{\mathrm{k}}\right], \tag{4.5}$$

where j, k = 1, 2 and $j \neq k$ denotes each magnetic particle, $\mathbf{v}_{\mathrm{j}}$ is the particle velocity, R_{k} is the particle radius, L_{jk} is the inter-particle separation, $\tilde{m}_{\mathrm{j}}$ is the particle mass, $\mathbf{a}_{\mathrm{j}}$ is the acceleration, $\mathbf{F}_{\mathrm{j}}^{\mathrm{ext}}$ is the sum of the external forces, $\hat{n}_{\mathrm{jk}}$ is the unit vector in the direction

connecting the particles, $\mathbf{I}$ is the identity matrix, and $\gamma_j = 6\pi\nu R_j$. The left-hand side could be neglected as, as the motion of the swimmer was over-damped.

In the simulation, an elliptical oscillating magnetic field is applied in the *xy* plane, with $H_x = H_x^0 \cos(\omega t)$ and $H_y = H_y^0 \sin(\omega t)$. Here H_x and H_y are the amplitudes of the field, ω is the angular frequency of the field and t is time.

Parameter	Value
Horizontal magnetic field amplitude	$H_x^0 = 500$ Oe
Vertical magnetic field amplitude	$H_y^0 = 10$ Oe
Magnetic properties of hard particle	$M_1 = 1.4 \times 10^{-6}$ Am^{-1}, $2K_1/M_1 = 1$ kG
Magnetic properties of soft particle	$M_2 = 1.4 \times 10^{-6}$ Am^{-1}, $2K_2/M_2 = 0$ kG
Radius of hard particle	$R_1 = 3.2$ µm
Radius of soft particle	$R_2 = 6.4$ µm]
Natural spring length	$r_0 = 6.4$ µm
Effective spring constant	$k_{spr} = 0.05$ Nm^{-1}
Dynamic viscosity of fluid	$\mu = 0.1$ Pa s
Reynolds number	Re $\sim 1 \times 10^{-3}$

Table 4.1 Simulated parameter values for the two-ferromagnetic particle swimmer [1, 2].

The motion of the system was calculated for realistic parameters, shown in Table 4.1. Figure 4.2 shows the trajectories of the centre of reaction (black), as well as the particles themselves (hard particle - red, soft particle - blue). The simulation shows a linear displacement of the centre of reaction, with a net motion of approximately 8 µm s^{-1}. Thus, the conditions for swimming at a low Reynolds number are fulfilled allowing a net translational motion. For the size of the swimmer this would correspond to a speed of 0.7 body lengths per second. Eukaryotic cells are able to create a swimming speed of up to 2 body lengths per second. This proposed system showed promise for a reliable method to propel a swimming at a low Reynolds number.

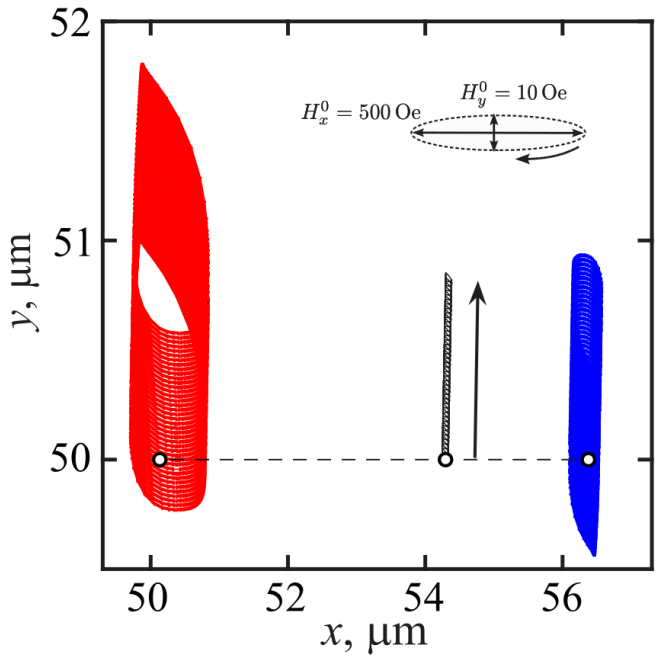

Fig. 4.2 Trajectories of the centre of reaction (black), hard particle (red), and soft particle (blue), after application of an elliptically rotating external field. The black arrow shows the direction of the linear displacement of the system. The circles show the initial position of the two particles and their centre of reaction. Simulation parameters are shown in Table 4.1. Figure taken from F. Orgin *et al.* [2].

The direction of propagation was shown to also depend on the parameters of the external magnetic field. Two main regimes of the system were identified. The first is the case when the magnetic torque of the system dominated; in this case the model predicted that the swimmer would move along its principal axis. For this regime the magnetic particles would exhibit large amplitude undulations, the internal motion would resemble a pendulum-like motion (Figure 4.3a). In contrast, the second regime was present when the magnetic dipolar force between the particles dominated. For this regime the swimmer mainly rocked about a mean angle with large compressions and extensions of the elastic link. In this case the swimmer would propel perpendicular to its primary axis and this regime was termed "locomotive" (Figure 4.3b).

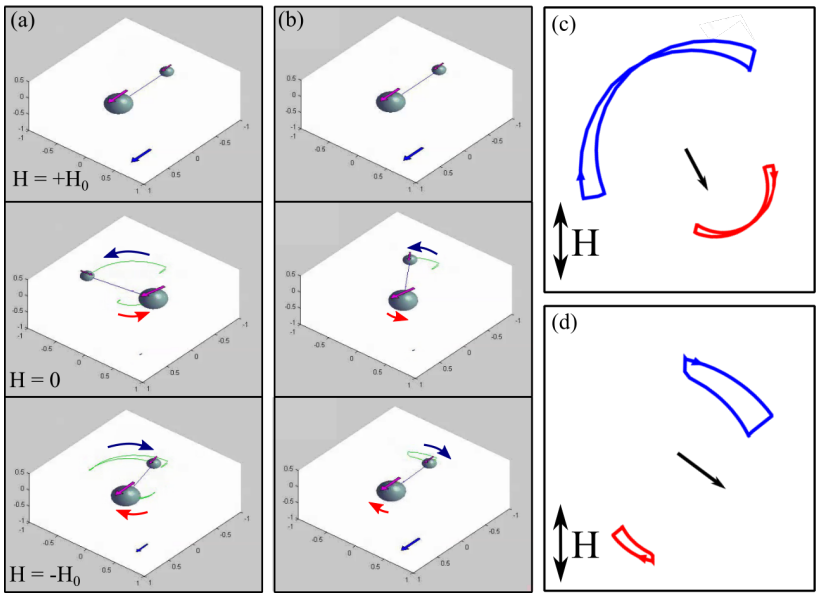

Fig. 4.3 Trajectories of the hard particle (red), and soft particle (blue) after one cycle. The black arrow shows the direction of the linear displacement of the system after multiple cycles. (a) Particle trajectory when the system is in the pendulum regime. (b) Particle trajectory when the system is in the locomotive regime. Figure adapted from A. Gilbert *et al.* [110, 111].

4.1.2 The first prototype

This section will focus on the fabrication and investigation of the first prototype based on the model system proposed by F. Ogrin *et al.* [1, 2]. The initial prototypes were fabricated using a brass mould built in-house to create the elastic links. The mould comprised of two brass disks. The first had a pin - producing the inner diameter of the link - and the second had a hole - producing the outer diameter. A schematic of the described brass mould is shown in Figure 4.4a. Once a uncured liquid rubber was added to the mould and cured, the mould could be disassembled.

This fabrication process created elastic ring structures which were the building blocks for the first prototypes (Figure 4.4b shows a cured silicone gel ring, of outer diameter of approximately 2 mm and depth 0.6 mm). Once a ring was fabricated, the magnetic particles could be attached using superglue. To create a soft ferromagnetic particle 0.5 mm diameter iron wire was cut to a length of approximately 2 mm. The hard ferromagnetic particle was

created by cutting cube-like fragments with pliers from a 1 cm cubic neodymium iron boron (NdFeB) magnet (approximately 2 mm x 1 mm x 1 mm). Figure 4.5 shows two of the first prototype created. Figure 4.5a shows a photograph of a prototype where the elastic link is created from a silicone gel, and Figure 4.5b shows a photograph of a prototype where the link is created using a latex based rubber.

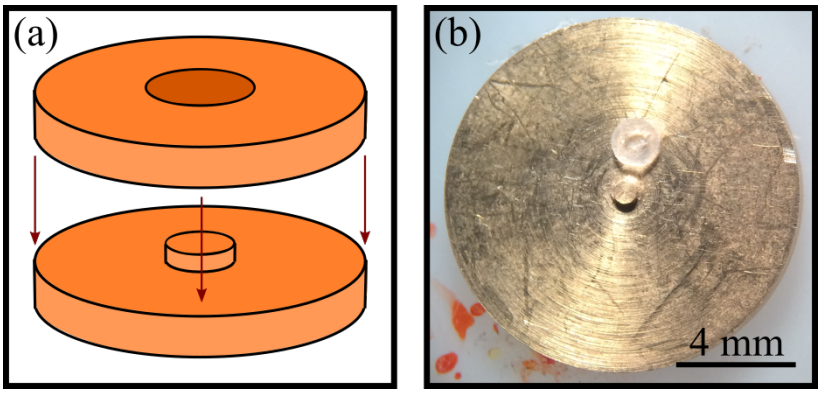

Fig. 4.4 (a) Schematic diagram of the two brass disks of the mould. (b) A fabricated silicone gel ring - with approximate diameter of 2 mm on top of the base disk of the mould.

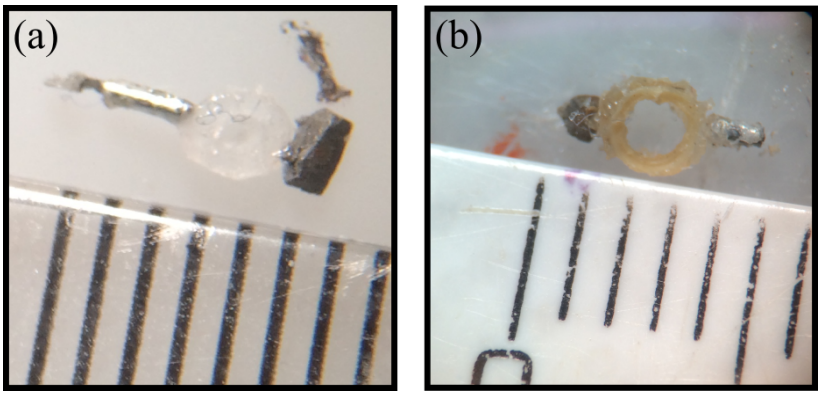

Fig. 4.5 Photographs of the first fabricated two-ferromagnetic particle prototypes, (a) with a silicone gel link and (b) a latex-based link. A millimetre scaled ruler is shown for scale.

To systematically investigate the swimming capabilities of the initial swimmers, the swimmers mobility was examined at the fluid-air interface, so they were restricted to the surface. The swimmers were placed in the centre of a large area (148 mm diameter) Petri

dish, which ensured that it was not affected by the curved meniscus near the edges of the Petri dish (the capillary length for water is a few millimetres).

To create the actuating magnetic field for the initial swimmers, a Helmholtz coil system was powered with a sinusoidal signal via a standard audio amplifier. An open-source particle tracking software was used to determine both the average speed and direction of migration of the swimmers. A full description of the experimental method can be found in the Experimental Methods Chapter.

Figure 4.6 shows data collected from the swimmer with the latex-based ring (Figure 4.5b). The figure shows the swimming speed as a function of the frequency of the external magnetic field for different field strengths. For all shown field strengths, there is an observed drop in swimming speed as the frequency is increased apart from a peak at 100 Hz. The peak occurs due to a small bias (25 to 65 μT) perpendicular to the external magnetic field - the Earth's magnetic field. The presence of the Earth's magnetic field perpendicular to the external field creates additional regimes, not originally shown in the model. The effects of the Earth's magnetic field will be discussed further later in this chapter. The maximum speed observed for this swimmer was $\sim 15.82 \pm 0.13$ mm s^{-1} (approximately 3 body lengths per second), but quickly falls off with frequency (a change of 20 Hz) to < 5 mm s^{-1} (1 body lengths per second). This device showed good comparison to the speeds of eukaryotic cells (2 body lengths per second), however it would be desirable for the system to be stable over a broader band frequency range, so that the different propulsion regimes could be explored. As well as the fall off with frequency, this swimmer also exhibited a poor directional control, despite the fact that the model predicted different propulsion direction at different frequency and strength of the external magnetic field, due to a switching and mixing of the dominating swimming regime.

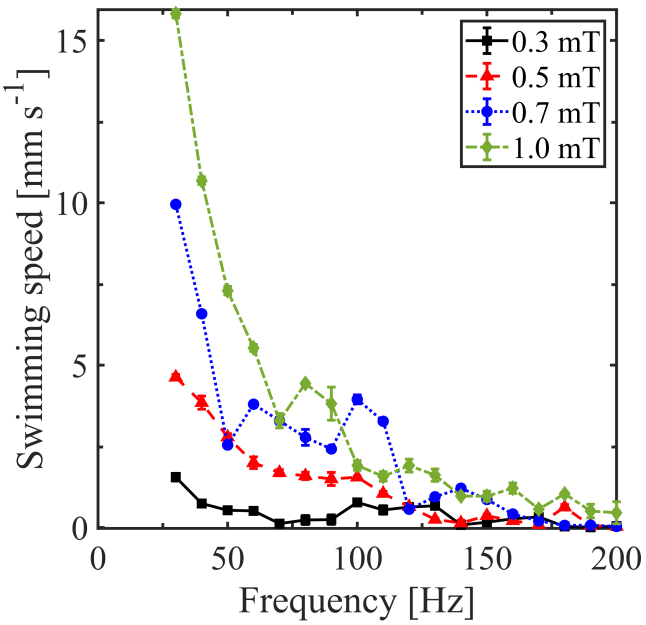

Fig. 4.6 Swimming speed as a function of frequency for the initial prototype for different external magnetic field strengths. Black solid line (squares) - 0.3 mT, red dashed line (triangles) - 0.5 mT, blue dotted line (circles) - 0.7 mT, and green dot-dashed line (diamonds) - 1.0 mT.

I proposed that the issue of directional control was arising from the fabrication process. Although these swimmers showed that the model by F. Ogrin *et al.* [1, 2] could experimentally create the motion required for low Reynolds number swimming, it needed to be improved. The most likely reason for this was that the superglue used to attached the ferromagnetic particles to the elastic link was altering the elastic properties of the link. This was causing the link to become more rigid. Another issue in the fabrication was the creation of hard NdFeB particles, as they were quite irregular with their shape as can be seen in Figure 4.5.

4.1.3 Improving the two-ferromagnetic particle swimmer

This section focuses on the optimisation of the two-ferromagnetic particle swimmer. The optimisation includes the improvement of the mould, elastic properties and ferromagnetic particle production. All these variables improved the reproducibility and reliability of the fabricated two-ferromagnetic particle swimmers.

To reduce the effect on the elastic properties due to the superglue, I proposed and designed a new mould. Once again this mould comprised of two brass disks, but in this case the top disk was altered. In this mould two regions were milled with width 0.6 mm, and length 0.8 mm (shown in Figure 4.7a). These regions were created so that the ferromagnetic particles could be placed in the mould when the elastic material was in its liquid form. The depth of the ferromagnetic swimmer fabricated was kept the same as previously stated (0.6 mm). This alteration means that the particles were encapsulated within the elastic material once cured, so the material would keep the same elastic properties. To further improve the mould, screws and dowels were added so that the two sections of the mould could be compressed tightly together (shown in Figure 4.7b). Ensuring that the two halves of the mould were tightly bound reduced the leakage of liquid elastic material into the joins. This small alteration helped improve the uniformity of the fabrication of the two-ferromagnetic particle swimmers as well as their swimming behaviour.

To further improve the uniformity of the two-ferromagnetic particle swimmers, a diamond blade dicer was used to cut 2 cm diameter, 0.6 mm thick disk NdFeB magnetic into 0.6 mm $\times$ 0.6 mm $\times$ 0.45 mm. The diamond blade dicer was also used to cut the length of the iron wire to 0.7 mm. Using this method to cut the desired dimensions of the ferromagnetic particles increased the similarities between different fabricated swimmers.

To improve the performance of the swimmer for the range of external magnetic field parameters, I investigated how the material would affect the operating range. As previously shown (Figure 4.6) the swimming performance fell off quickly with the frequency of the

external magnetic field. Three materials were investigated, silicone gel (4.7c), silicone rubber (4.7d), and a latex-based rubber (4.7e).

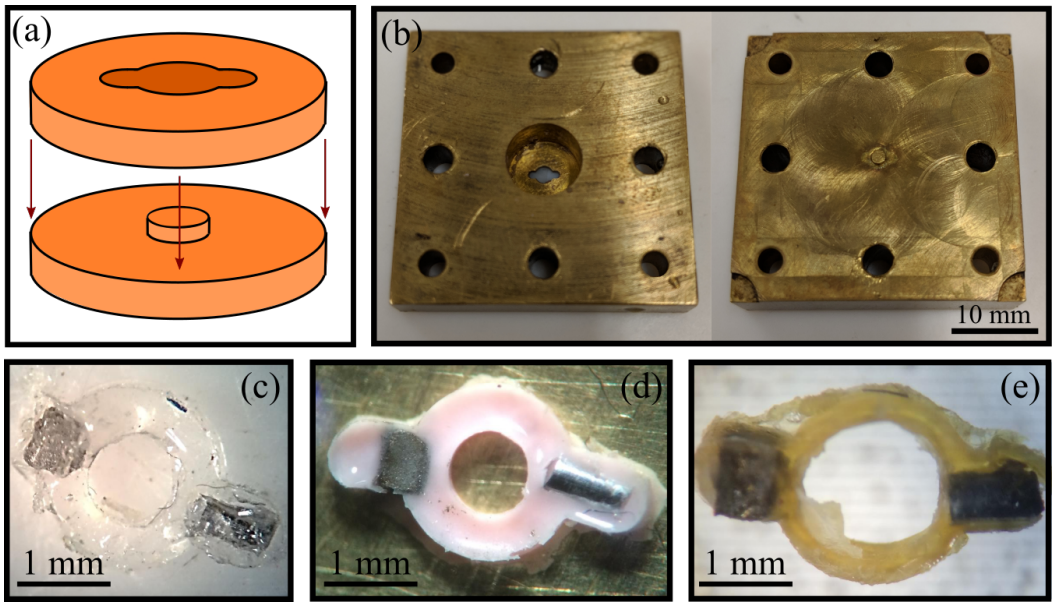

Fig. 4.7 (a) Schematic diagram showing the improved two brass disks of the mould. (b) Photograph of the final improved mould - with holes for screws and dowels. The photographs show the swimmers produced from this mould for different materials: (a) silicone-based gel, (b) silicone rubber, and (c) latex.

The swimming performance of the different material two-ferromagnetic particle swimmers were investigated for a frequency sweep of 60 Hz to 260 Hz at a field strength of 1.0 mT (Figure 4.8a). The different material swimmers were also tested for a magnetic field strength sweep of 1.0 mT to 4.0 mT at a frequency of 100 Hz (Figure 4.8b). As a control a swimmer was fabricated with two soft iron particles and its behaviour is shown with the green dot-dash line. Figure 4.8 shows that its swimming speed is very low. These low speeds were to be expected due to the minimal magnetic torque experienced by the soft particles which interact only via a small dipolar force. This would result in the moment being reciprocal and therefore no overall propulsion.

The swimming speed of all swimmers fall off with increasing frequency, a peak is also shown for all materials between 80 Hz - 110 Hz (similar to the peaks shown in Figure 4.6).

The latex based swimmer exhibited a large maximum (approximately 6.2 ± 0.3 mm s^{-1}), followed by a quick drop to swimming speeds similar to those for the silicone gel swimmer. The silicone rubber swimmer has the steadiest decrease in swimming speed.

In the magnetic field strength investigation, the speed of the silicone rubber swimmer (red dashed) and the latex swimmer (black solid) both increased with increasing field strength. The latex based swimmer had a steeper gradient and higher swimming speeds but the device has a tendency to became unstable on the surface of the fluid. This was thought to be due to the deflect and air bubbles seen in the structure (no two swimmers ever showed the same swimming behaviour). On the other hand, the silicone gel swimmer's speed decreased as the magnetic field strength was increased.

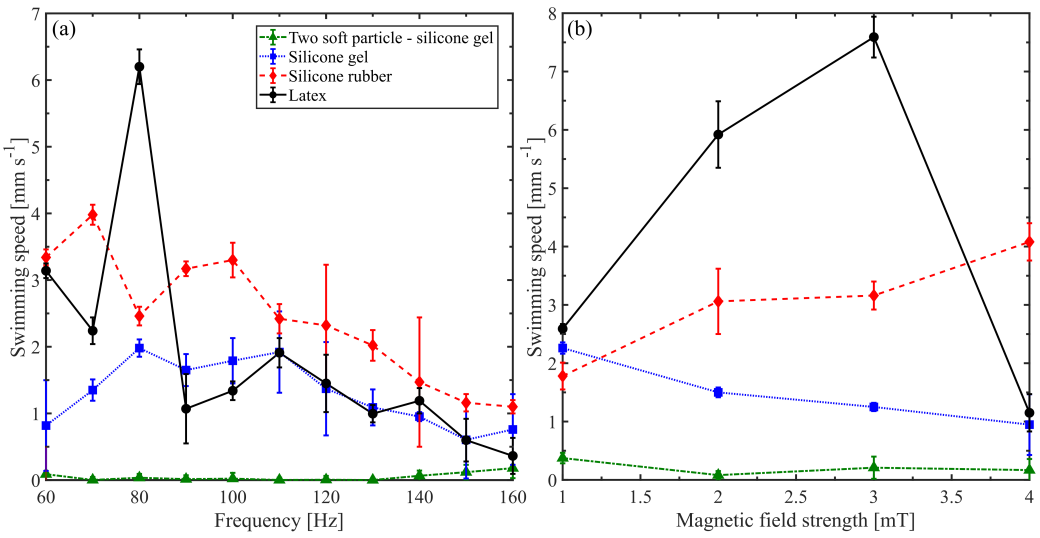

Fig. 4.8 Swimming speed as a function of (a) frequency (60 Hz - 160 Hz) at 1.0 mT and (b) magnetic field strength (1.0 mT - 4.0 mT) at 100 Hz for the improved swimmer prototype for different materials. Black solid line - latex, red dashed line - silicone rubber, blue dotted line - silicone-based gel. Green dot-dashed line shows a control swimmer which has two soft (iron) particles.

Following the elastic material tests, I decided that the most stable and interesting elastic material to use for all two-ferromagnetic particle swimmers would be the silicone rubber (Fig-

ure 4.7d). The swimmers design and materials had now been finalised and the investigation of the full swimming performance and directional control could start.

4.1.4 Magnetically controlled two-ferromagnetic particle swimmers

In this section, I will discuss the investigations of the dynamic performance of the two-ferromagnetic particle swimmer in fluids of different viscosity as a function of the external field parameters (frequency and magnetic field strength) and demonstrate stable propulsion over a wide range of Reynolds numbers. The publication on this work can be found in J.K. Hamilton *et al.* [112].

Swimming speed

As noted previously, the systematic investigation of the frequency and viscosity dependencies of the average propagation speed of the silicone rubber two-ferromagnetic particle swimmer revealed that the orientation of the system relative to a small bias field - in this case the Earth's magnetic field - is an important parameter. Figure 4.9a shows the average propagation speed of a two-ferromagnetic particle swimmer as a function of the applied frequency at three different field strengths (1.0 mT, 1.5 mT, and 2.0 mT). In this case the Helmholtz coil system is aligned parallel to the Earth's magnetic field. To clarify in this orientation, the line joining the geometrical centres of the two coil loops is parallel to the direction of the Earth's magnetic field. In this configuration a maximum is observed followed by a steady decrease in swimming speed with increasing frequency, ω. For the case of the strongest magnetic field investigated a maximum is present at 60 Hz. For the same orientation, Figure 4.9b shows the swimming speed as a function of the viscosity for three different frequencies (50 Hz, 100 Hz, and 150 Hz). For all cases, the swimming speed falls off with increasing kinematic viscosity. The swimmer's swimming behaviour was investigated over a range of viscosity start from

water ($\nu = 1.0 \times 10^{-6}$ m^{2}s^{-1}) to a mixture of 30% water and 70% sucrose ($\nu = 2.4 \times 10^{-4}$ m^{2}s^{-1}).

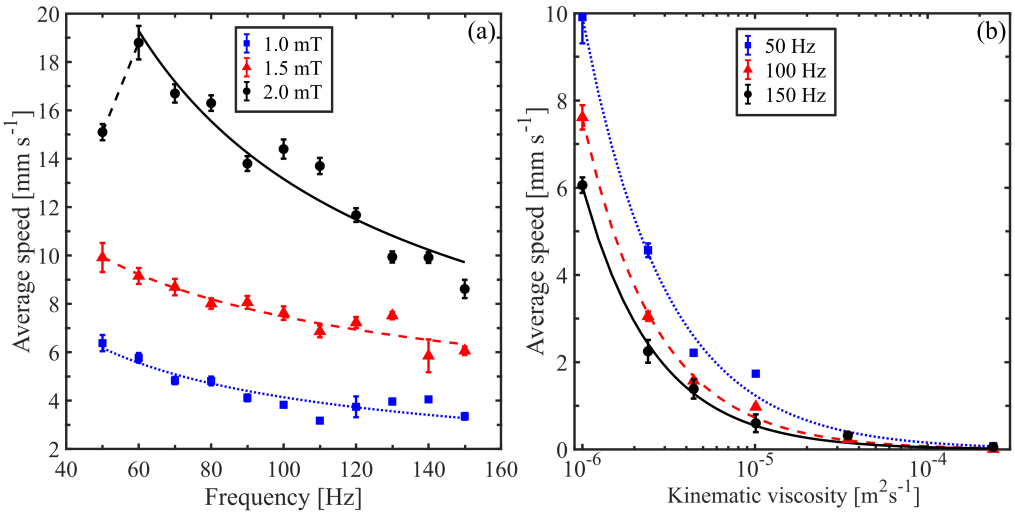

Fig. 4.9 (a) Swimming speed as a function of frequency (50 Hz - 150 Hz) for different magnetic field strengths. Black circles - 2.0 mT, red triangles - 1.5 mT, and blue squares - 1.0 mT. (b) Swimming speed as a function of fluid viscosity, for different frequencies. Black squares - 150 Hz, red triangles - 100 Hz, and blue circles - 50 Hz, with an external magnetic field of 1.5 mT. The lines shown are power law fits with the colour corresponding to the fitted data.

In Figure 4.9a frequencies lower than < 50 Hz are not shown in the investigation. At these frequencies (< 50 Hz) the swimmer would experience a full rotation and would result in no net motion or incoherent swimming. This motion is due to that fact that the magnetic torque felt by the external magnetic field has time to fully rotate the swimming in one cycle. As previously defined within the Methods Chapter, the swimming speed as linear motion and therefore this motion was defined as not swimming. Figure 4.10 shows a typical trajectory of a swimmer in this spinning regime, a schematic shows a full rotation.

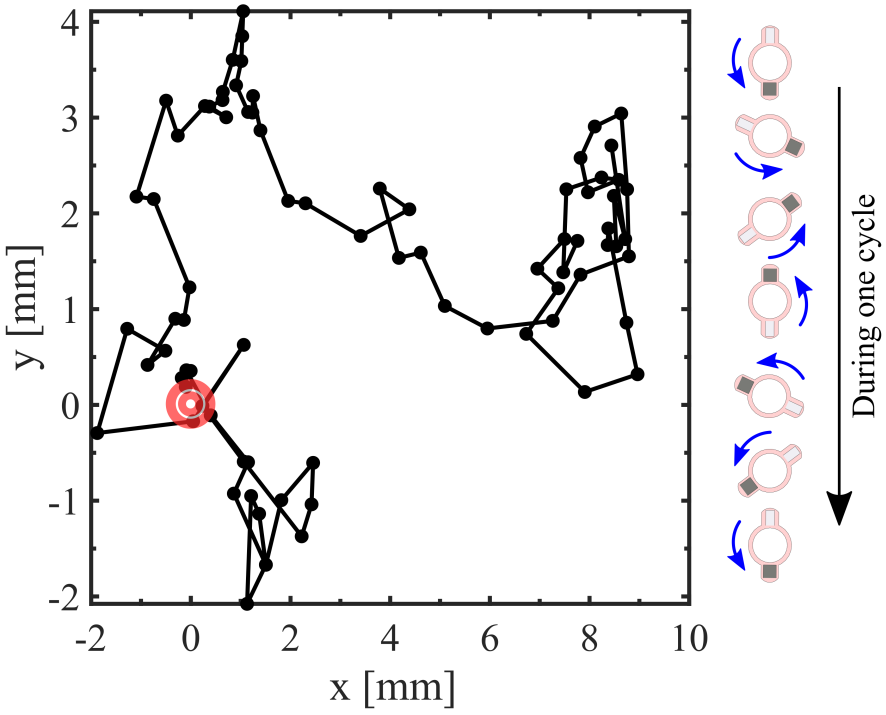

Fig. 4.10 Trajectory plot of a swimmer in the presence of a 1.5 mT field with a frequency of 40 Hz. In this regime the swimmer undergoes a full rotation (within a period) creating incoherent swimming. A schematic depicts the motion within one cycle.

Using Figure 4.9a, Figure 4.9b, and a power law fitting tool, one can deduce an experimental dependence of swimming speed on frequency and fluid viscosity. For the case shown in these figure, $u \propto \omega^a \nu^b$, with $a \approx -0.6$ (-0.6 ± 0.2 at 1.0 mT,-0.4 ± 0.1 at 1.5 mT, and -0.7 ± 0.2 at 2.0 mT) and $b \approx -1$ (-0.9 ± 0.2 at 50 Hz,-1.0 ± 0.1 at 100 Hz, and -1.0 ± 0.1 at 150 Hz).

These power law dependencies are in qualitative agreement with the current theoretical model [110] which predicts the reduction in swimming speed with the increase of both frequency and fluid viscosity. . In the model, an equation of motion was created by solving a Lagrangian, which balanced the forces in the system: hydrodynamic interactions, dipolar gradient force, magnetic torque, and the elastic restoring force. From the equation of motion, the key parameters that effect the swimming speed can be extracted. Here, the parameters of interest are the external stimuli (field strength B^{ext}, viscosity ν, and frequency ω), resulting

in

$$u \propto \frac{B_{\text{ext}}^2}{\nu\omega}. \tag{4.6}$$

The dependency on viscosity is to be expected, as in the Stokes regime the velocity is proportional to $\frac{1}{\nu}$ (as shown in Equation 4.5). The dependence on frequency is a result of the two magnetic interactions (dipolar gradient force between the two particles and the magnetic torque felt by the hard particle) as well as the hydrodynamic interactions. By comparing the magnetic response time to the frequency of the field, as the frequency is increased the system would have less time to react to the forces within a cycle. It would result in a decrease in velocity increasing frequency. The viscosity sets an additional time scale in the system. For example, it is important when discussing the frequency response. For low frequencies, the system will be able to rotate, however has the viscosity is increased the motion is supressed by the viscous friction, this result in shown in Figure 4.9b.

As previously stated the applied magnetic field in the theoretical model comprised of an elliptical field, with no bias. Following the experimental investigation, the effects of a constant bias field - parallel to the applied magnetic field - was added to the model. Figure 4.11 shows the theoretical prediction and has similarities to the experimental findings shown for 2.0 mT in Figure 4.9a. Figure 4.11 reveals the presence of a maximum (approximately 3 body lengths per second) at low dimensionless frequencies (ϖ is the dimensionless magnitude of the viscous drag compared with elasticity, at a frequency ω), followed by a monotonic decrease in swimming speed for increasing field dimensionless frequency. The two other main dimensionless parameters in the model are: A_{mag} which is the measure of the dipole attraction between the two ferromagnetic particles (compared with the elastic force), which varies as the ferromagnetically soft particle dipole direction follows the external magnetic field, and A_{ext}, which gives the torque on the ferromagnetically hard particle due to the external magnetic field (compared with the elastic force). The parameters are defined as follows

$$\varpi = \frac{6\pi\omega\mu}{k}\frac{R_1R_2}{(R_1+R_2)}, \tag{4.7}$$

$$A_{\text{mag}} = \frac{3\mu_0 m_1 m_2}{4\pi k r_0^5}, \tag{4.8}$$

$$A_{\text{ext}} = \sqrt{m_1 m_2}\frac{B_{\text{ext}}}{k r_0^2}. \tag{4.9}$$

Recalling the variables [110], R_{i} the radii of the particles, m_{i} the magnetic moments of the particles (where i = 1 or 2), k the string constant, r_0 the natural length, external magnetic field strength B_{ext}, and frequency ω, and ν the fluid viscosity. Using these parameters, the experimental system can be tested to verify that the regime would be similar to that for the model.

Parameter	Experimental value
M_1	1.39×10^{-4} Am^{-1}
M_2	2.45×10^{-5} Am^{-1}
R_1	0.30×10^{-3} m
R_2	0.25×10^{-3} m
r_0	1.6×10^{-3} m
μ	1.0×10^{-3} Pa s
B_{ext}	2.0×10^{-3} T

Table 4.2 Simulated parameter values for the two-ferromagnetic particle swimmer model, based on the experimental device.

The values of the dimensionless parameters can be found using the experimental values in Table 4.2 and assuming the elastic force for an elastic ring with a rectangular cross-section

can be evaluated by using the Castigliano theorem

$$F_{\mathrm{el}} = 4.55\frac{he^3E}{D^3}y, \tag{4.10}$$

where y is the extension, h is the cross-sectional height (0.6 mm), e is the width (0.2 mm), D is the diameter of the ring (1.8 mm), and E is the Young's Modulus of the material. Assuming that the system obeys Hooke's Law ($F_{\mathrm{el}} = ky$), an expression for a predicted k can be obtained. In the literature, the value of E (for silicone rubber) is known to be 0.001 GPa.

Parameter	Model	Experiment
ϖ	0.0503	0.00043
A_{mag}	0.0403	0.026
A_{ext}	0.207	0.012

Table 4.3 Comparison between the simulated and experimental dimensionless parameter for the two-ferromagnetic particle swimmer.

The theoretical values of the dimensionless quantities are for a micrometre-sized swimmer (total length of 11.2 μm) activated in an external field of 0.05 T and frequency 2500 rad s^{-1}. The agreement between the experimental and theoretical values (all values less than 1.0) imply that the system is scalable and results in the swimmer remaining in the same regime.

It is worth noting that the region marked in red on Figure 4.11 indicates a region of incoherent swimming. In this region the motion of the swimmer is not a linear and this can be compared to the experimental findings. In the experiment, for frequencies lower than shown ($<$ 40 Hz), the torque experienced by the swimmer by the external magnetic field is too large. When the swimmer experiences a large torque, the swimmer fully rotates resulting in non-linear motion.

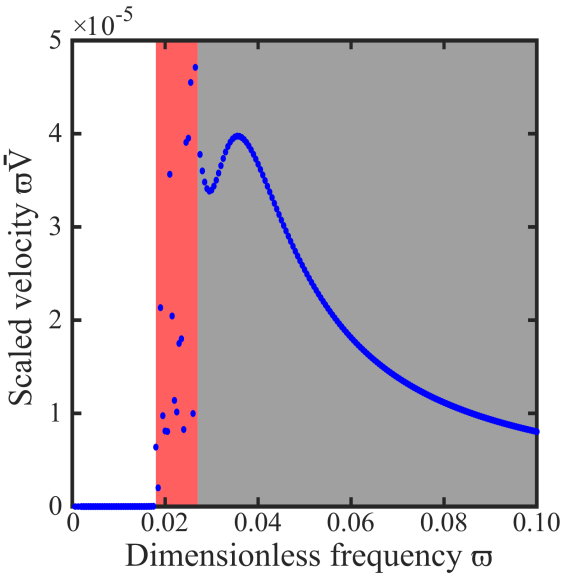

Fig. 4.11 Simulated dependencies of the average speed of the swimmer on frequency (dimensionless) for a parallel bias field. Three distinct swimming behaviours are observed (depicted in different colours): no or very slow swimming (white), incoherent swimming (red) and stable swimming (grey). The externally applied oscillating field is almost uniaxial (1% aspect ratio) to mimic the uniaxial field in experiment and the bias field is 0.5% of the maximum external field. The rest of the parameters are the same as the model by A. Gilbert *et al.* [110]. Initially, the swimmer is aligned with its primary axis along the bias field as in the experiments.

The quantitative differences between the model and experiment are to be expected since the model employed a simplified geometry (previously described as two spherical magnetic particles joined with a linear spring of zero volume). Another difference between the two is that the model assumed the swimmer to be placed within the bulk of the fluid, whereas in reality the experiments were conducted on the air-fluid interface.

A range of Reynolds numbers can be deduced from the viscosity experiments. Basing the Reynolds number on the maximum average speed achieved by a swimmer, the overall length of the swimmer and the viscosity of the fluids, Re is between 6×10^{-5} and 20. This shows that these two-ferromagnetic particle swimmers are capable of self-propulsion at low to moderate Reynolds numbers.

In addition to the investigation of the frequency and viscosity dependence, further experimental studies were conducted. Figure 4.12 shows the dependence of the magnetic field strength on the swimming speed. In this investigation the frequency was kept at 50 Hz, 100 Hz, and 150 Hz, respectively, and the coil system is in the parallel alignment to the Earth's magnetic field. An increase in swimming speed is observed for increasing magnetic field strength (for 50 Hz and 100 Hz). However, at the higher frequency (150 Hz) the swimming speed reaches a saturation at high magnetic field strength (1.25 mT) and plateaus.

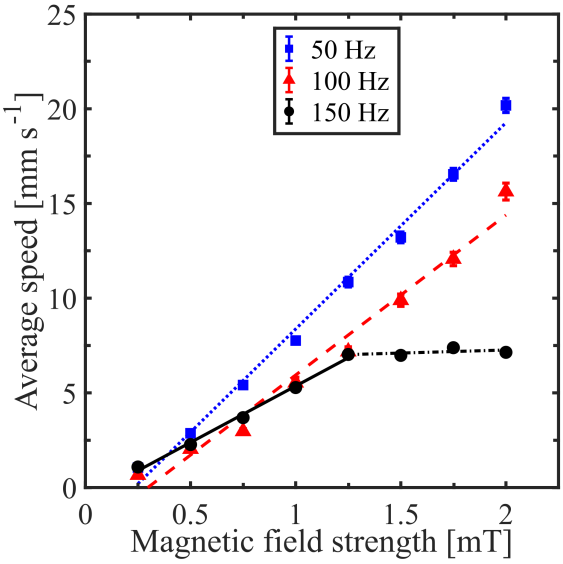

Fig. 4.12 Swimming speed as a function of magnetic field strength (0.25 mT - 2.0 mT) for different frequencies. Black circles - 150 Hz, red triangles - 100 Hz, and blue squares - 50 Hz. The lines shown are linear fits with the colour corresponding to the fitted data.

Figure 4.13a and Figure 4.13b show the same dependencies but in this case the coil system was placed perpendicular with respect to the Earth's magnetic field. In this orientation, the swimming performance is significantly modified. In this case the frequency dependence is no longer shown to be monotonically decreasing and exhibits more than one maximum even at low field strengths. At higher field strengths, there is a tendency of fast decrease in the speed with increase of frequency up to ca. 110 Hz, after which the speed begins rising again.

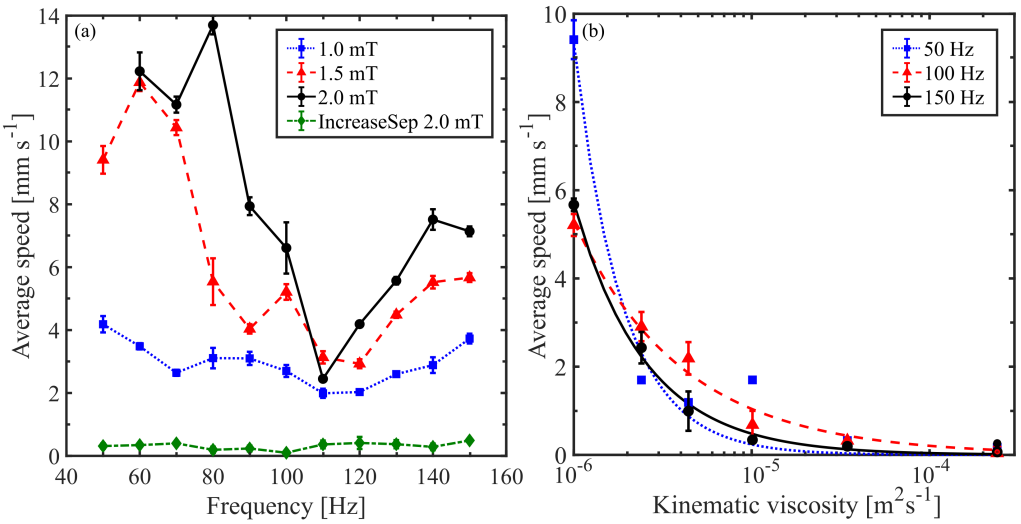

Fig. 4.13 (a) Swimming speed as a function of frequency (50 Hz - 150 Hz) for different magnetic field strengths. Black circles - 2.0 mT, red triangles - 1.5 mT, and blue squares - 1.0 mT. The green diamonds show the swimming performance of a swimmer with an increased particle separation of 3.0 mm for a field strength of 2.0 mT. (b) Swimming speed as a function of fluid viscosity, for different frequencies. Black squares - 150 Hz, red triangles - 100 Hz, and blue circles - 50 Hz, with an external magnetic field of 1.5 mT The lines shown are power law fits with the colour corresponding to the fitted data.

It is evident that the presence of a constant bias field (even as small as the Earth's magnetic field) is an important factor that could be used to control the performance of the swimmers. The bias field provided an additional symmetry axis and contributed to the torque affecting the swimmer's speed. I predicted that, depending on the frequency, it would lead to switching between the different propulsion regimes previously described. This switching of regimes results in a complex frequency dependence. To test this prediction, a small bias field was added in the theoretical model perpendicular to the main applied magnetic field. In this configuration of the model, for increasing frequency, there are two maxima (shown in Figure 4.14), qualitatively similar to the experimental findings. The two maxima have speeds of approximately 2.6 body lengths per second and 3.4 body lengths per second, respectively.

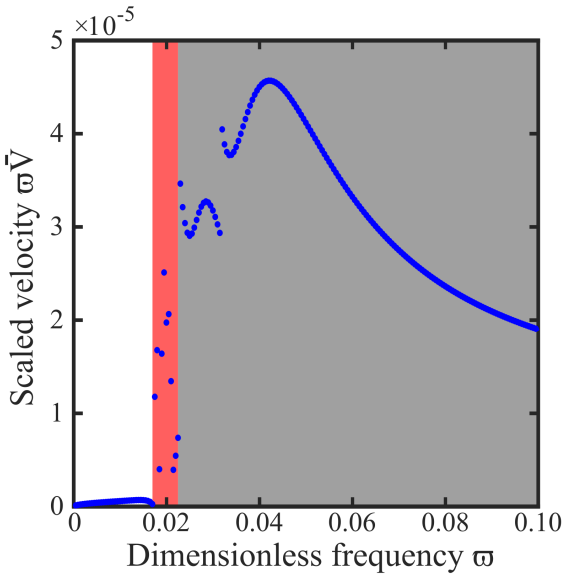

Fig. 4.14 Simulated dependencies of the average speed of the swimmer on frequency (dimensionless) for a perpendicular bias field. Three distinct swimming behaviours are observed (depicted in different colours): no or very slow swimming (white), incoherent swimming (red) and stable swimming (grey). The externally applied oscillating field is almost uniaxial (1% aspect ratio) to mimic the uniaxial field in experiment and the bias field is 0.5% of the maximum external field. The rest of the parameters are the same as the model by A. Gilbert *et al.* [110]. Initially, the swimmer is aligned with its primary axis along the bias field as in the experiments.

Small variations in the geometrical parameters of the swimmer were shown to drastically affect the swimming performance. One parameter investigated was the equilibrium distance between the magnetic particles, which has a strong effect due to the dependence of the magnetic particle-particle interaction forces on the particle separation. Figure 4.13a illustrates this with the green diamonds (IncreaseSep) - where the separation was increased by $\sim 36\%$. This increase in separation was shown to reduce the swimming speed by almost two orders of magnitude. The dynamics of the system depends on the gradient forces generated by the magnets, the elasticity of the coupling and thus the strain in the elastic coupling over the oscillation cycle.

The magnetic force between the two particles can be analytically estimated if the geometry of the particle is known [113]. Figure 4.15 shows the magnetic gradient forces between the

particles (estimated using the geometry and magnetic response of the particles) as a function of particle separation. The standard separation (2.2 mm) for the swimmers is shown, as well as the increased separation of the IncreaseSep swimmer (green diamonds on Figure 4.13a), shown with the grey dashed line. Assuming the strongest attraction force between the particles (the anti-parallel alignment of the magnetization), an external field of 2.0 mT and an equilibrium particle-particle separation of 2.2 mm, the elastic and magnetic forces can be balanced. The maximum extension of 0.25 mm is obtained (a deformation of $\sim 7\%$) from this balancing of forces. Characterising the deformation of the single parameter of longitudinal strain, the model would have predicted a deformation of $\sim 13\%$ of the total length. In the case of the swimmer with the increased particle separation (IncreaseSep) ($\sim 36\%$), the resulting extension would decrease to 0.13 mm. This reduction in elastic deformation produces the reduction in the speed of motion seen in Figure 4.13a (green diamonds).

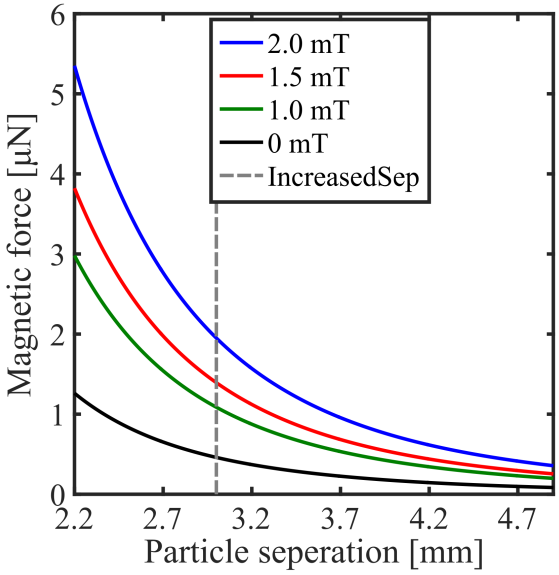

Fig. 4.15 Analytical estimate of the magnetic force between the hard and soft ferromagnetic particles as a function of the separation between them in the presence of external magnetic fields of different strength (green: 1.0 mT, red: 1.5 mT and blue: 2.0 mT) and zero external magnetic field (black). The vertical dashed line corresponds to increased particle separation of $\sim 36\%$, as for a swimmer with an increased particle-particle separation.

Both experiments and simulations reveal rich dynamics which has implications for the control of the swimming motion - not only speed but also direction of motion. The rich behaviour of the swimmer under the actuation of the external magnetic parameters will be discussed in the following section.

Directional control

One of the main advantages of the two-ferromagnetic particle swimmer presented in this work is the directional control of the swimmer. The direction of motion can be easily controlled by adjusting the frequency and strength of the external magnetic field without spatial repositioning of the coil system. Figure 4.16 illustrates the effects of altering the frequency of the external magnetic field on the orientation of the swimmer as well as the trajectory (for parallel alignment with respect to the Earth's field), Figure 4.16a, and the perpendicular alignment, Figure 4.16b.

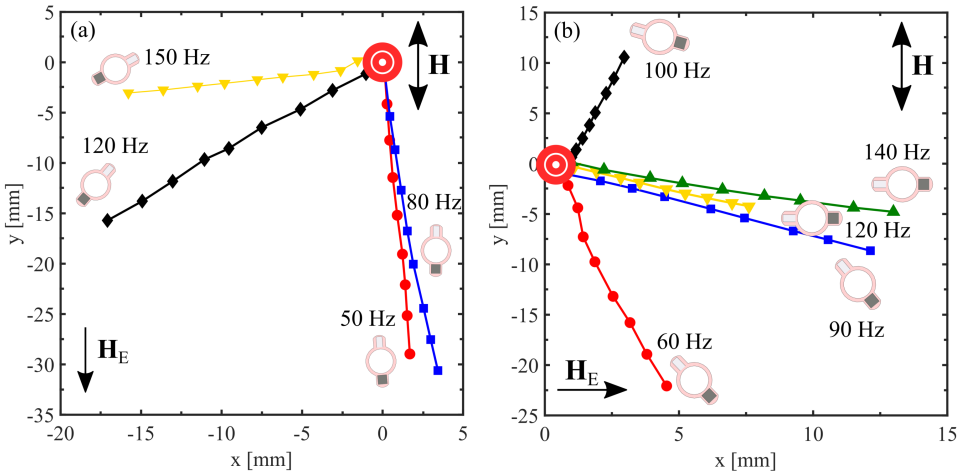

Fig. 4.16 Effects of the frequency of the external magnetic field on the direction of migration. The direction of the external magnetic field, $\mathbf{H}$, and the Earth's magnetic field, $\mathbf{H}_E$ (~ 0.02 mT) are indicated. (a) Direction of motion as a function of frequency at 2.0 mT for a parallel alignment between $\mathbf{H}$ and $\mathbf{H}_E$. The mean orientation of the swimmer is shown schematically for each frequency. The final point on each trajectory is at 1.9 seconds. (b) Direction of motion as a function of frequency at 2.0 mT for a perpendicular alignment between $\mathbf{H}$ and $\mathbf{H}_E$. The mean orientation of the swimmer is shown schematically for each frequency. The final point on each trajectory is at 1.9 seconds.

In the parallel alignment between the coil system and the Earth's magnetic field the direction of propagation of the swimmer could be controlled within a 95° angle. In this orientation, the swimmer would either travel parallel, or perpendicular to the external magnetic field. . This is expected due to the swimmer's motion either in one of the two extremes: the previously discussed pendulum and locomotive regimes. In the pendulum regime (when the magnetic torque is the dominate interaction), the swimmer would rock on its major axis and travel parallel to this major axis. In the case of the locomotive regime (when the dipolar gradient force is the dominate interaction), the swimmer would experience a greater attraction and repulsion force between each cycle. This interaction created a 'rolling' motion, which typically resulted in the swimmer propelling perpendicular to its major axis. In the intermediate frequencies where no interaction dominates ('sub-regimes'), the swimmer could propel at angles between the two extremes. The regimes are illustrated via the schematic of the swimmer on the figure. Examples of the two regimes can be seen in Figure 4.16a: 50 Hz and 80 Hz show a pendulum like regime and 120 Hz and 150 Hz show a locomotive regime.

In the perpendicular alignment between the coil system and the Earth's magnetic field the direction of propagation of the swimmer can be controlled within a 115° angle. As the frequency of the external magnetic field is increased, the swimmer had the tendency to migrate in the direction of the Earth's magnetic field. The effect of this migration is suspected to be due to the initial conditions of the swimmer. Initially, the swimmer is aligned with its primary axis along the bias field (similar to a compress pointing north with the Earth's magnetic field). At rest the swimmer is free to rotate in the presence of the Earth's magnetic field; the swimmer will align along the direction of this small bias. Once the external magnetic field is applied - at larger frequencies - the swimmer does not have enough time to physically rotate the swimmer, thus the swimmer would oscillate about the direction of the Earth's field. As a result, there is a new regime - resembling the pendulum one - created when the small bias is perpendicular.

In Figure 4.16, the only manipulated external parameter was the frequency of the external magnetic field. In Figure 4.17, both the strength and frequency of the external magnetic field were varied. In this case, the system was once again in the perpendicular alignment relative to the Earth's magnetic field. The three discussed regimes are clearly shown in Figure 4.17: 50 Hz shows the regular pendulum, 90 Hz shows the locomotive, and 130 Hz shows the bias-based pendulum. The trajectories shown in this figure show a control over the direction of propagation in over 270°, only by manipulating the frequency between 50 Hz and 150 Hz, and strength of 2.5 mT to 0.9 mT.

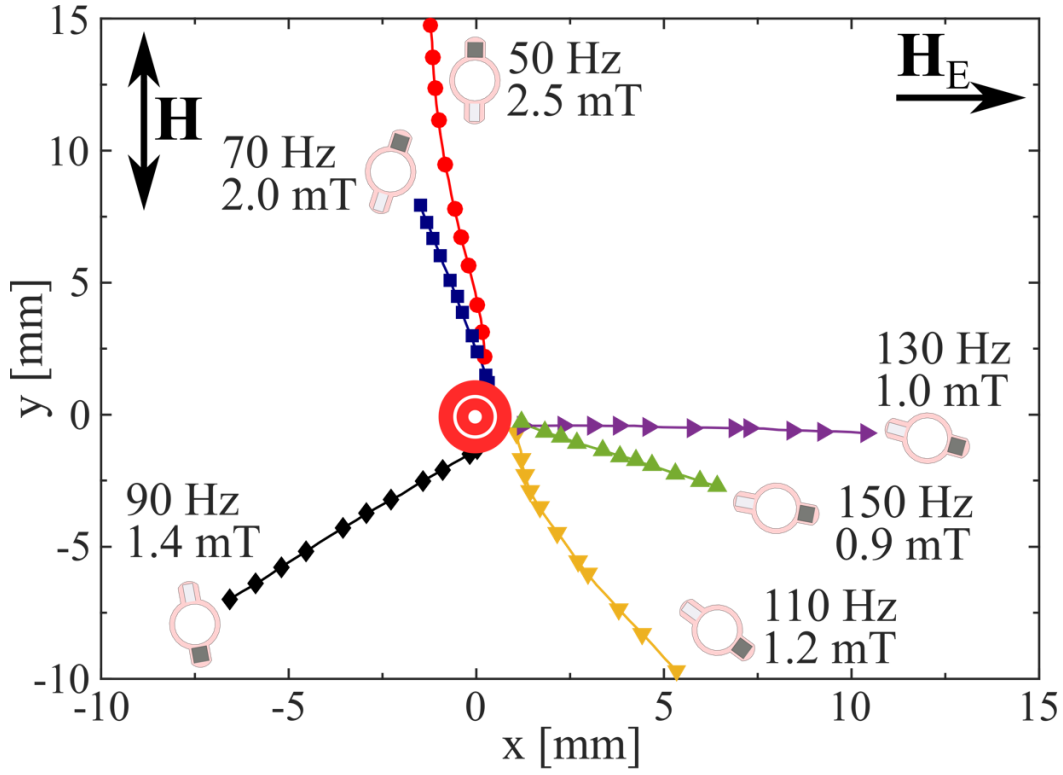

Fig. 4.17 Direction of motion as a function of different frequencies and magnetic field strengths (ranging between 50 – 150 Hz and 2.5 – 0.9 mT, respectively) for a perpendicular alignment between **H** and $\mathbf{H}_E$. The mean orientation of the swimmer is shown schematically for each frequency. The final point on each trajectory is at 2.7 seconds.

Figure 4.17 shows that when the frequency and amplitude are adjusted simultaneously, one can achieve virtually any direction. This addition control of the swimmer is due to the

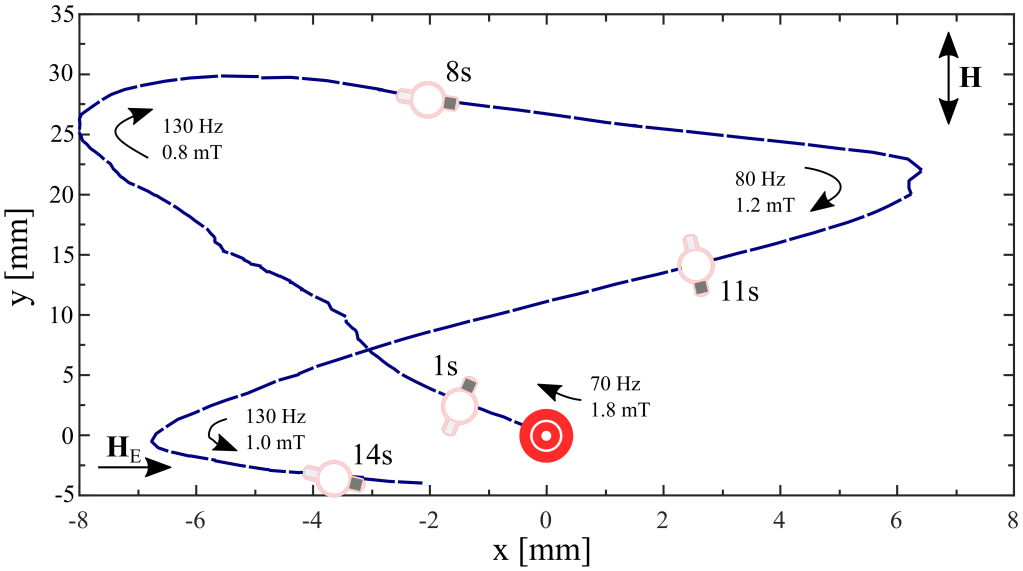

Fig. 4.18 A figure of eight trajectory produced by varying the frequency and amplitude. The four sketches of the swimmer show its orientation at the respective time points.

dependencies that the swimmer has on both frequency and field strength. By systematically controlling these external parameters, and utilising the small bias field (the Earth's magnetic field) different 'sub-regimes' could be used to control the swimmer. To further demonstrate this, Figure 4.18 shows the trajectory of the swimmer while both the frequency and strength of the external magnetic field were manipulated. The figure-of-eight trajectory shown, was achieved by only varying the frequency and amplitude within the ranges 50 – 150 Hz and 0.5 – 2.0 mT, respectively. The orientation of the swimmer is also illustrated for different time points along the trajectory.

The results from this investigation show how a high level of control over the speed and direction of propagation can easily be achieved by tuning the frequency and amplitude of the external magnetic field. With the addition of a very small constant bias to it (in this case the Earth's field, ~ 0.02 mT) the control can be tailored for the requirements. This would be highly advantageous in technological applications requiring robust actuation and control.

4.1.5 Final improvements to the two-ferromagnetic particle swimmer

To further improve the reproducibility of the swimmers in the fabrication, NdFeB cube magnets were purchased from SuperMagnetMan, these magnets have dimensions of 0.5 mm $\times$ 0.5 mm $\times$ 0.5 mm. Using these magnets, the swimmers could be fabricated reliably with the same geometry and magnetic properties. To improve the fabrication of multiple swimmers, a Formlabs Form 2 resin based 3D printer was used (resolution of 25 µm) example of a 3D printed mould is shown in Figure 4.19. Further information can be found in Experimental Methods Chapter.

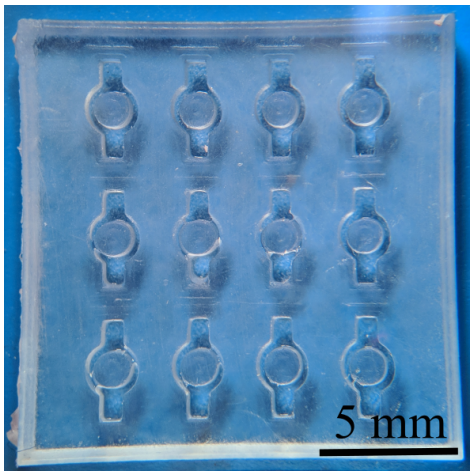

Fig. 4.19 An example of a mould recreated using Autodesk AutoCAD and the Formlabs Form 2 3D printer

4.2 Torque driven ferromagnetic swimmers

This section will focus on torque driven ferromagnetic swimmers. The publication on this work can be found in J.K. Hamilton *et al.* [114] in collaboration with A. Gilbert. The theoretical framework and all simulations were developed by A. Gilbert (shown in Appendix A), and the experimental findings were produced by myself. After the previously highlighted drawbacks with the micrometre-sized two-ferromagnetic particle swimmer (small magnetic

forces compared to the elastic force), an investigation into fabricating a new system was proposed.

As has been demonstrated in a number of cases, a typical approach to create non-reciprocal propulsion cycle would be by mimicking the natural microscopic swimmers, such as sperm cells or bacteria. One way to achieve this is by including magnetic particles for actuating and driving the swimmer in the liquid with an external magnetic field. The mechanism of motion in this case relies on the collective response of all particles. Even though the individual torques created on each bead is small the overall mechanics of the system is sufficient to generate a non-zero displacement [115, 9].

Other approaches take advantage of the elastic properties of the tail, while applying the torque only to a single particle [75, 116–123]. For example, in a recent study by F. Box *et al.* [124] a centimetre-scale system of elastically linked spheres was investigated, comprising of three spheres connected by elastic struts of unequal length. One of the spheres contained a fixed magnetic moment and the field was applied perpendicular to the moment.

In this section, the properties and external responses of a self-propelled millimetre-scaled ferromagnetic swimmer based on only one ferromagnetic particle are presented. Experimentally, this is implemented by using a high anisotropy magnetic particle - the head - attached to a flexible elastic filament - the tail - to mimic the structure of a beating flagellum. In order to describe this system, a simplified model based on multiple particles, in which the effect of the tail is represented by non-magnetic particles linked with massless elastic links was developed. Further information regarding the model can be found in Appendix A.

4.2.1 Experimental investigation of the torque driven single ferromagnetic particle swimmer

The initial prototype

To show experimentally, that such a system could indeed propel in the low Reynolds environment, a prototype was fabricated (shown in Figure 4.20). The first prototype was fabricated by using a thin strip (0.09 mm thick, 0.25 mm wide, and 7.1 mm long) of silicon rubber and attaching a 0.5 mm $\times$ 0.5 mm $\times$ 0.5 mm cubic NdFeB ferromagnetic on the top of one end.

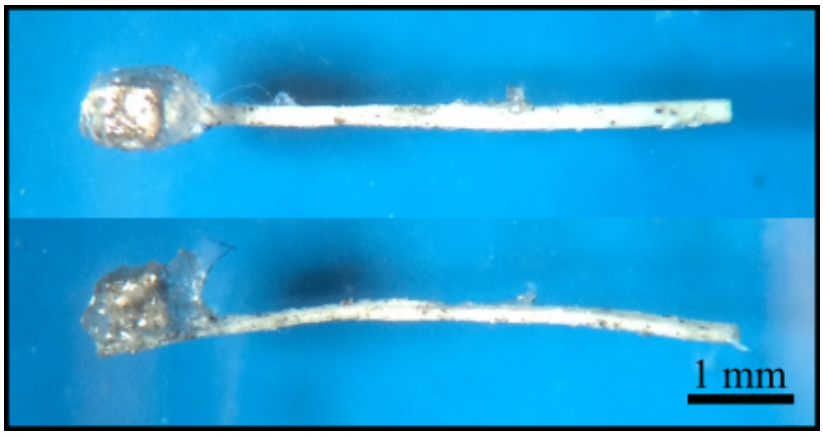

Fig. 4.20 Photograph of the first torque driven ferromagnetic swimmer prototype.

Initially, how the swimming speeds depended on the frequency investigated, using the same experimental setup as previously described. The swimming behaviour of the millimetre scaled swimmers were studied by examining their mobility on an air-fluid interface of a large area Petri dish (148 mm diameter). The experimental setup comprised a Helmholtz coil system, powered with a sinusoidal signal, providing a uniform magnetic field to actuate and control the swimmers. Further information can be found in the Experimental Methods Chapter.

Figure 4.21 shows the initial data for the torque driven ferromagnetic swimmer. The figure shows the frequency dependence of the swimmer for the range of 20 Hz - 200 Hz, for three external magnetic field strengths: 0.5 mT - blue squares, 1.0 mT - red triangles, and 1.5

mT - black squares. The typical trends of the swimming speed remain similar for all external field strengths, only an increase in swimming speed with field strength is observed, similar to that shown in Figure 10.4. This increase in swimming speed would be expected as the torque experienced by the swimmer would be greater for larger external field strengths and was predicted in the model. For all external field strengths, the swimmer speed gradually decreases with increasing frequency until a cut-off frequency (shown in the orange region). The gradual decrease in swimming speed was also shown in the model (Figure 10.4), however the cut-off frequency was not present. At the cut-off frequency the swimming speed quickly falls off. The cut-off frequency is expected to be due to the external magnetic field oscillating too fast for the beating of the swimmers tail. This cut-off frequency is shown in other torque driven swimmers when the device cannot keep up with the rotation of the magnetic field [19, 65].

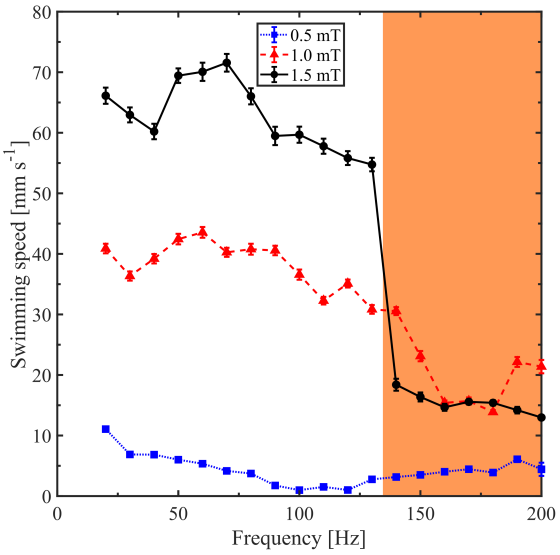

Fig. 4.21 Frequency dependence of the swimming speed of the first torque driven ferromagnetic swimmer prototype for different external magnetic field strengths: blue squares - 0.5 mT, red triangles - 1.0 mT, and black circles - 1.5 mT. The orange region indicates the region beyond the cut-off frequency for the swimmer.

Figure 4.22 shows the trajectory of the torque driven ferromagnetic swimmer for different external magnetic field frequencies. The orientation of the swimmer is also shown, the end point of each trajectory is after 1 second of actuation. The typical migration is approximately perpendicular to the external magnetic field, as expected from the model and previous work [116, 120]. At the largest frequency shown (200 Hz), the swimmer starts to swim almost parallel to the external magnetic field, this is suspected to be due to additional asymmetries in the experiment - compared to the models.

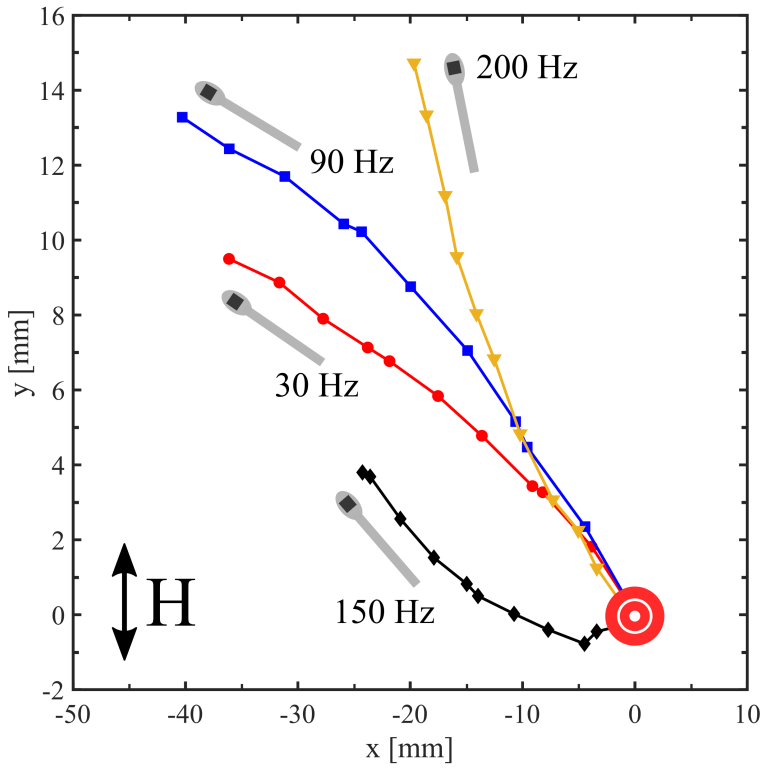

Fig. 4.22 Trajectory plots of the first torque driven ferromagnetic swimmer prototype actuated by a 1.0 mT external magnetic field for different frequencies. Frequencies are shown on the figures, as well as a schematic of the swimmer.

Optimising the single ferromagnetic particle swimmer

To improve the initial prototype so that a systematic investigation could be conducted, 3D printing was used. The 'tails' were constructed using a 3D printed mould to produce the

desired overall swimmer geometry (shown in Figure 4.23a). The mould was designed using Autodesk AutoCAD and 3D printed using a Formlabs Form 2. The hard ferromagnetic material (NdFeB) used was cubic with dimensions of 0.5 mm $\times$ 0.5 mm $\times$ 0.5 mm, with the anisotropy axis along the tail axis of the swimmer. Silicone rubber was used to create the flexible elastic tail (shown in Figure 4.23b). The length of the tail was varied in the range of $L = 1 - 12$ mm, while keeping the head cubic ($h = 0.7$ mm) and tail width ($b = 0.4$ mm) constant. For all produced swimmers, the depth was kept at 0.7 mm, to ensure the complete encapsulation of the magnetic particle.

In previous investigations, the swimming behaviour of swimmers with flexible tails have been shown to have a dependence on the length of the tail, frequency of the applied field, the bending stiffness of the filament and the tail's fluid dynamic interactions [121, 125]. This investigation focused on the effects of the external parameters of the magnetic field - frequency ω and field strength B_{ext} - on the swimmers, as well as tail length L. To find the optimum length of the swimmer's tail, swimmers of different tail lengths were created and the change in swimming performance for different field strengths and frequencies were investigated.

Figure 4.24a shows the range in performance of the swimming speed (scaled by $L\omega$) as a function of tail length for different frequencies. The magnetic field strength is fixed at 1.5 mT. There is a clear peak for all frequencies at $L = 4$ mm. When the tail length is increased past the peak, the swimming speeds start to decrease for all frequencies. A maximum dimensionless speed of 0.18 is observed, corresponding to a real speed of 57.8 ± 0.1 mm s^{-1} (approximately 12 body lengths per second), with an external field of 1.5 mT and 80 Hz and a tail length of 4 mm.

Figure 4.24b shows a similar trend, but in this case for different field strengths, with a fixed frequency of 50 Hz. As the field strength is increased the overall speed of the swimming increases - due to the increased torque effects - as well as a peak at L = 5 mm

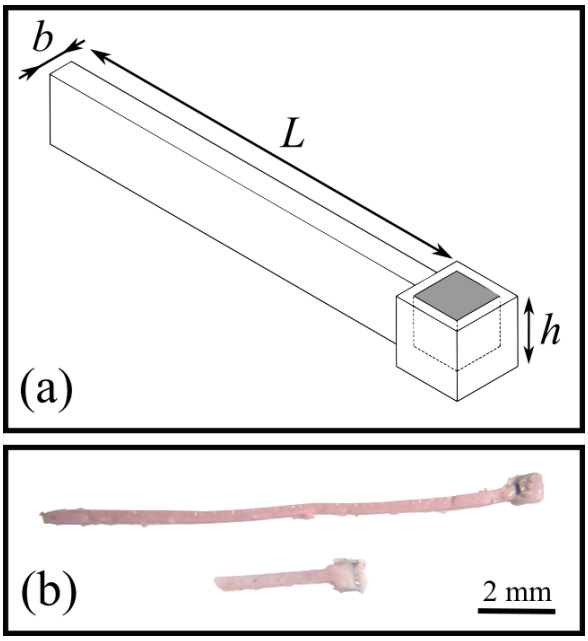

Fig. 4.23 (a) Schematic and (b) Photograph of the improved torque driven ferromagnetic swimmer. The length of the tails were varied in the range of $L = 1 - 12$ mm, while keeping the head cubic ($h = 0.7$ mm) and tail width ($b = 0.4$ mm) constant. The two swimmers shown have length of 12 mm and 3 mm, respectively.

manifesting at the higher field strengths. The maximum dimensionless speed in this case is 0.3 corresponding to a speed of 74.6 ± 0.1 mm s^{-1} (approximately 13 body lengths per second), with an external field of 3.2 mT and 50 Hz and a tail length of 5 mm.

Figure 4.24 shows that as the length of the tail becomes shorter ($L < 3$ mm), the swimming performance begins to reduce; this is expected, due to the tail becoming effectively more rigid. For such conditions, the device becomes similar to a single degree of freedom reciprocal system and the scallop theorem will apply [4]. On the other hand, as the tail length is increased ($L > 10$ mm), the elastic deformation or beating patterns become irregular, resulting in another reduction of swimming speed.

From the theoretical model shown in Appendix A, the predicted swimming speed can be obtained and written as:

$$\frac{\dot{X}}{l_0 \omega} = \varepsilon \frac{21 A_{\text{ext}}^2}{16\varpi(\varpi^2 + 36)}. \tag{4.11}$$

The velocity, $\dot{X}$, here has been normalised in terms of body lengths per radian of the magnetic field cycle $l_0\omega$. The dimensionless frequency is shown as ϖ and A_{ext} is known as the magnetoelastic number. The following experimental parameter values were used for the developed theory,

Parameter	Value
R	1.25×10^{-3} m
k	1.67×10^{-2} N m^{-1}
l_0	5×10^{-3} m
$\ell = kl_0^2$	4.2×10^{-7} J
m	1.2×10^{-4} A m^2
B_{ext}	3×10^{-3} T
ω	$100 \times 2\pi$ s^{-1}
μ	1×10^{-3} Pa s

Table 4.4 Simulated parameter values for the torque driven ferromagnetic swimmer model, based on the experimental device.

The theory developed (in Appendix A) and the parameters shown in Table 4.4 the above gives an approximation to the swimming speed yields,

$$\dot{X} = \varepsilon l_0 \omega \frac{21A_{\text{ext}}^2}{16\varpi(\varpi^2+36)} \simeq 2.4 \times 10^{-2} \text{ m s}^{-1}. \tag{4.12}$$

The value for the swimming speed shown in Equation 4.12 ($\simeq 2.4 \times 10^{-2}$ m s^{-1}) can be compared with the typical value of speed shown experimentally. Comparing to the experimental data, the velocities range ~ 5 mm s^{-1} - 70 mm s^{-1}. This comparison gives good order of magnitude agreement and provides support for the model, despite its idealised nature - simplified geometry and elastic properties.

Differences between the model and the experiment could also arise from the swimmer being modelled within the bulk of the fluid. In the experiment the simmer is mainly confined to the interface, with only part of the body submerged into the liquid.

An important observation is that there is an obvious optimum length at which the swimming speed is maximised. This behaviour can be linked to previous work, [116, 120] - as

well as the three-particle model and the initial prototype - which show a rapid decrease in swimming performance and irregular beading trajectories at large tail lengths. It also appears that there is also a second peak at L = 8 mm (Figure 4.24). It may be due to the second harmonic beating pattern, as the tail is twice the length of that for the first peak.

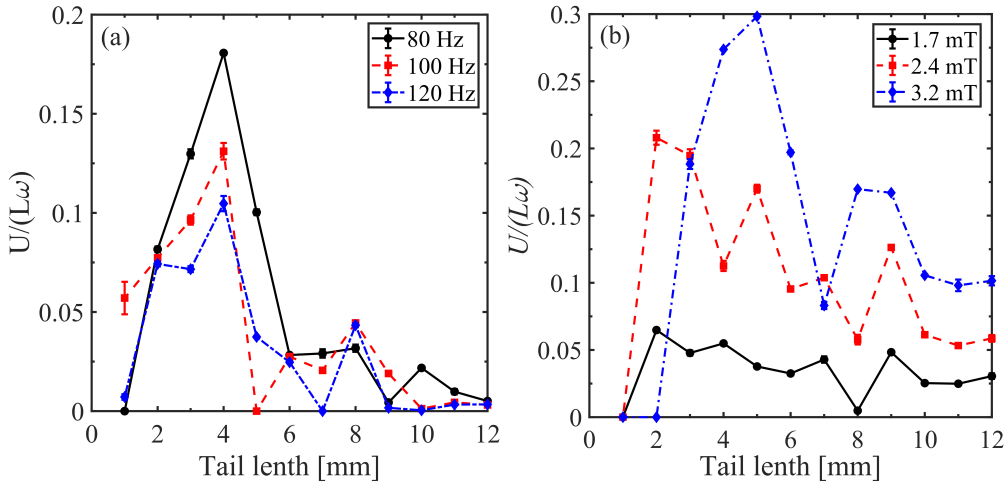

Fig. 4.24 Dimensionless speed (by $L\omega$) as a function of tail length for (a) different frequencies - 80 Hz (black circle), 100 Hz (red square) and 120 Hz (blue diamond) with an external magnetic field strength of 1.5 mT, (b) different magnetic field strengths - 1.7 mT (black circle), 2.4 mT (red square) and 3.2 mT (blue diamond) with a fixed frequency of 50 Hz.

Directional control of the single ferromagnetic particle swimmer

Figure 4.25 shows a trajectory plot to visualise the direction of motion of the swimmer for different tail lengths and frequencies. The field direction is given in the last panel. The trajectories for four frequencies are shown: 30 Hz (black circle), 80 Hz (red triangle), 130 Hz (blue square) and 170 Hz (green diamond). If the trace for a given frequency is not present, this is due to unstable propulsion of the swimmer for this combination of tail length and frequency.

Figure 4.25 clearly shows that as the frequency is increased for all tail lengths, the swimmer can be controlled for a range of propagation angles. The maximum angle of control $\sim 90^{o}$, can be observed for L = 12 mm. The trajectories also visualise the variations of

swimming speed with tail length, as the distance between the two points on the trajectories increases (the time between two points is kept constant at 0.2 seconds). For the swimmer with tail length less than 6 mm, the trajectories tend to be parallel to the applied magnetic field.

Typically, as the length of the tail is increased ($L > 6$ mm), at low frequencies, the trajectories become more perpendicular to the applied field. This mix of parallel and perpendicular behaviour is unexpected, as one would expect the trajectories to be perpendicular to the applied field [116, 120]. This could be due to irregular beating patterns created at large tail lengths, but could also be caused by additional degrees of freedom. These extra degrees of freedom could be caused in fabrication: there may be a small out-of-plane magnetic component, resulting in a rocking in the z-plane when the external field is applied. As the devices are placed on the surface of the fluid, this could also cause extra asymmetries in the motion, due to boundary effects. At the air-liquid interface, the force arising from the surface tension confines the swimmer to the liquid surface as it acts against swimmer's motion in the z-direction (i.e. in the direction normal to the liquid surface). This behaviour could also be explained by the increased Reynolds number for the larger values of L, resulting in inertia effects being present.

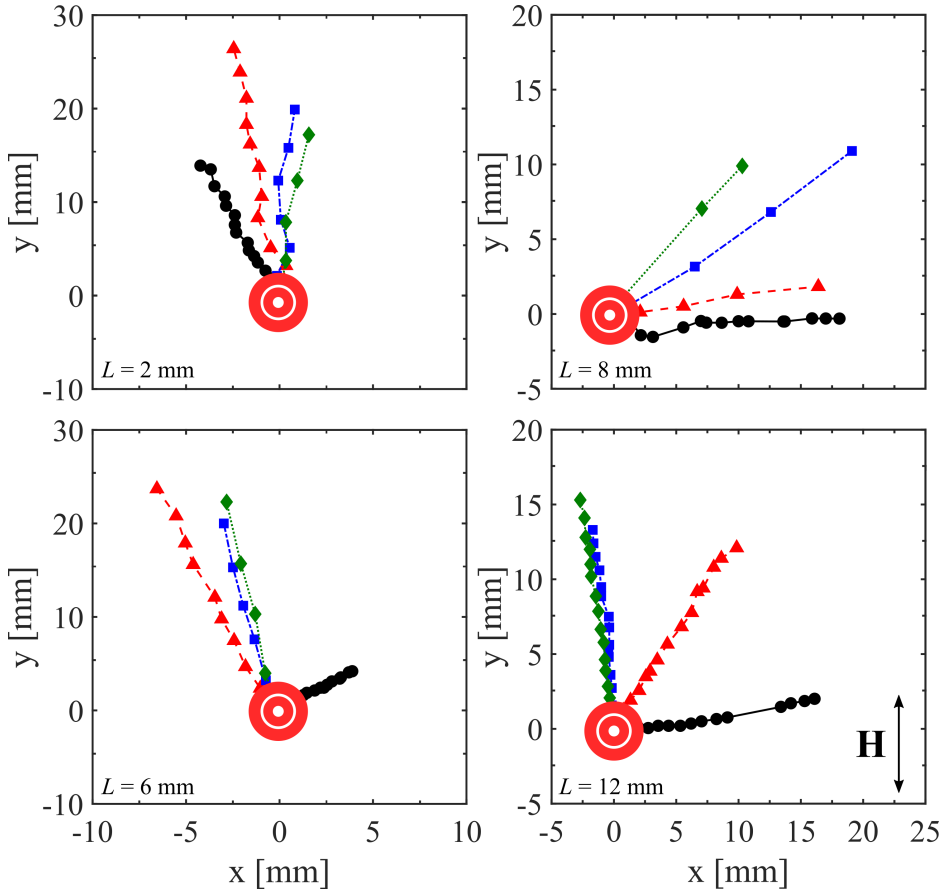

Fig. 4.25 Trajectory plots for tail lengths, 12 mm, 10 mm, 8 mm, 6 mm, 4 mm and 2 mm. The field has a strength of 1.5 mT and frequencies shown are 30 Hz (black circle), 80 Hz (red triangle), 130 Hz (blue square) and 170 Hz (green diamond). The swimmer is recorded for 20 seconds and the time between two points on a trajectory is 0.2 second.

Viscosity dependency of the single ferromagnetic particle swimmer

Figure 4.26 shows the swimming speed of a single particle swimmer with $L = 3$ mm for fluids of different viscosities. The dynamic viscosity ranges from 1×10^{-3} Pa s (100% water) to 1.4 Pa s (100% glycerol). The external magnetic field has a frequency of 50 Hz and strength of 3.0 mT. The predicted velocities are shown with the solid red line - using the experimental parameters with no fitted parameters and Equation 4.11. The experiment and theory show good agreement, expect for the most viscous data where the experiment is out performing the theoretical prediction. The differences between the theory and experiment

may arise from the simplifications made in the theory. Figure 4.26 shows that the swimmer can successfully propel at both low and moderate Reynolds number - given the Reynolds number range of $\sim 3 \times 10^{-6} - 90$.

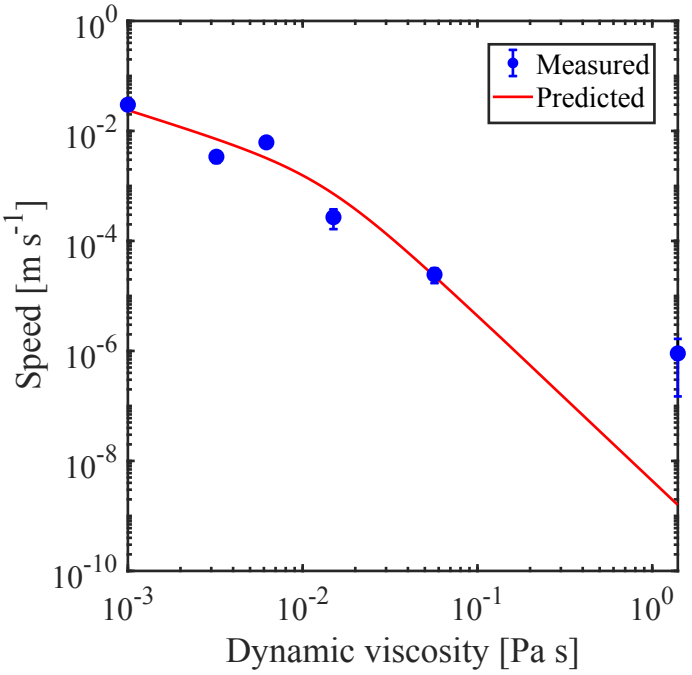

Fig. 4.26 Swimming speed of the improved torque driven swimmer as a function of dynamic viscosity. The solid red line indicates the predicted values from the theory (Equation 4.11). The external magnetic field has strength 3.0 mT and frequency 50 Hz. The Reynolds numbers shown here are: 90 (for $\eta = 1 \times 10^{-3}$ Pa s), 0.53 (for $\eta = 1 \times 10^{-2}$ Pa s), 1.6×10^{-4} (for $\eta = 0.1$ Pa s) and 2.5×10^{-6} (for $\eta = 1$ Pa s).

4.3 Conclusion

In summary this chapter focused on the fabrication, optimisation and the experimental investigation of two types of ferromagnetic elastic swimmers.

The first was the two-ferromagnetic particle swimmer. This swimmer was based on magnetic, elastic and hydrodynamic interactions of a pair of particles (a hard ferromagnetic particle NdFeB and a soft ferromagnetic particle Fe), controlled by an external oscillating magnetic field. Due to the different anisotropic properties of the two particles, the application of an external magnetic field leads to time varying dipolar gradient force between the particles (resulting in a relative radial motion) as well as time-dependent torque (causing an oscillatory rotational motion of the whole system). Another key factor for the propulsion is the particles having different sizes leading to the hydrodynamics interactions which breaks the symmetry of the motion.

The swimming performance of the first millimetre scaled prototype was shown, as well as the improvements made to the swimmer, including the materials used and the fabrication process.

The swimmer's response to changes in the external magnetic field (frequency and amplitude) as well as fluid viscosity was investigated. How its speed and direction of motion can be controlled using the magnetic field parameters was also demonstrated. It was shown that the inclusion of a small constant bias to the external field could be advantageous for establishing tighter control over both the direction of motion of the device and its speed. Swimmers on a micrometre-scale were also shown to have similar trends to the millimetre-scale system. However, a ferromagnetic material which has a larger coercivity would be required to overcome the proportionally greater elastic force [126].

The second system was a millimetre scaled single ferromagnetic particle swimmer based on the bending of a flexible tail. The swimmer was actuated and controlled by an oscillating magnetic field (< 3.5 mT), which created a torque on the swimmer, creating bending modes

of the tail. This investigation involved the fabrication and optimisation of the swimmer and its characterisation by device and external parameters (tail length, field strength and frequency). The frequency and tail length response showed that there is an optimum tail length of 4 mm, corresponding to swimming speed and control of direction. The single ferromagnetic particle swimmer was shown to successfully propel at a range of Reynolds numbers $\sim 3 \times 10^{-6}$ – 90.

This investigation of macroscopic swimmers helps to understand the swimming behaviour of artificial flagella-based swimmers and paves the way for fabricating optimum microscopic magnetic flagella-based swimmers. As well as helping understand the behaviour of the micro-scale swimmers, this presented work also helps blends into the applications of milli fluidic pumps. In the world of fluid mechanics, a swimmer and a pump can be thought of one in the same. The only different between swimming and pumping the fluid is the reference frame. If a human was kicking their legs in a swimming pool they would propel themselves. However, if that same human was holding onto the edge of a swimming pool and kicking their legs, they would induce a flow in the fluid. Even when the system is scaled down (resulting in a low Reynolds number) this same principle stands. The focus of the following chapter will be using the actuation methods described in this chapter to create fluid pump systems rather than swimming devices.

Chapter 5

Magnetically controlled fluid pumps and mixers

This chapter focuses on magnetically controlled fluid pumps, valves, and mixers. Pumps and valves are basic components in virtually every microfluidic platform. In laboratory conditions, pumps often are external to the microfluidic assembly, which allows for easy and accurate control over every aspect of fluid flow. Lab-on-a-chip devices, however, impose a number of design restrictions that stem from the basic requirement for packing complex functionality in a restricted space. In response to this demand, recent years have seen a number of original design solutions for pumps (both passive and active), valves, mixers and other components that could be incorporated into lab-on-a-chip devices, having various levels of performance and complexity and different actuation mechanisms. Details on these developments can be found in the thorough reviews by J. Zahn [78], D. Nikitopoulos and A. Maha [127], and K. Au *et al.* [77].

Typical microfluidic systems (channel width and height on length scales of tens of micrometres) operate under low Reynolds number conditions, thus are bound by the same restrictions as the micro-scaled swimmers. Therefore, a popular approach has been to utilise low Reynolds number swimmers as microfluidic pumps [88, 89, 22, 90, 91]. These

pumps formed from swimmers have been shown to be effective in their pumping mechanics. However, most rely on complex fabrication methods or collective behaviour to generate a flow. An ideal pump system would be to utilise a highly efficient swimmer (in this case large swimming speeds compared to body length) which can be fabricates simply.

In this chapter the two previously described magnetically controlled swimmers are converted to pumps and valves. As well as single pump systems, the fabrication and performance of networks of the previously mentioned systems, are presented. These networks are known as active membranes. The focus of the membranes is to utilise the collective behaviour of multiple simple single-ferromagnetic particle systems and create a less invasive system for lab-on-a-chip technology.

5.1 Two-ferromagnetic particle based fluid pumps

In the present work, the previously described two-ferromagnetic particle swimmers are re-purposed to control fluid flow in microfluidic systems. By tethering the swimmer, a variety of flow patterns could be elicited remotely, via manipulating parameters of the applied magnetic field. Depending on the channel geometry, a single swimmer was able to serve as a pump, valve or mixer, demonstrating its versatility for self-contained lab-on-a-chip applications. The publication on this work can be found: J.K. Hamilton *et al.* [128].

5.1.1 Tethering the two-ferromagnetic particle swimmer

The swimmer was converted into a pumping device by making use of the ring geometry of the elastic link. A thin (0.25 mm diameter) non-magnetic rigid post was mounted to the bottom of the channel, and the swimmer was loosely threaded through it as shown in Figure 5.1a. This restricts the translational motion of the swimmer when actuated, but it is still free to rotate and oscillate, which are essential requirements for inducing and sustaining fluid flow.

In this configuration, the pinned swimmer rests gently on the surface of the fluid (supported by surface tension forces) and the fluid flow it generates can conveniently be investigated. Experiments were conducted using several different channel geometries (5.1).

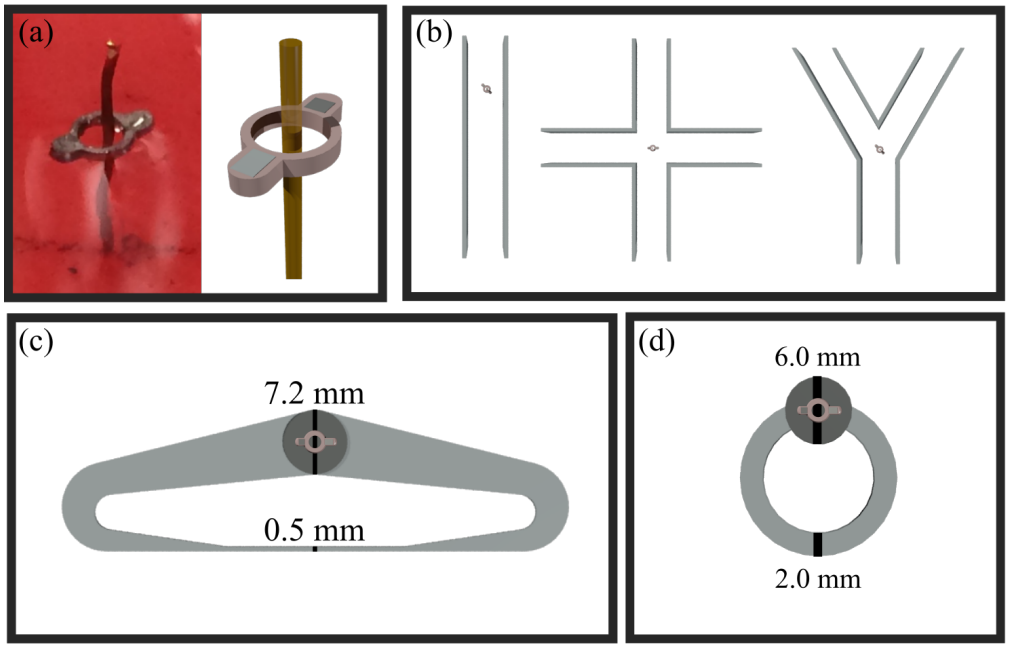

Fig. 5.1 (a) Photograph and schematic of a two-ferromagnetic particle swimmer pinned on a non-magnetic rod. (b) Diagrams (made to scale) of channel geometries with the pinned swimmer shown within: a straight channel of width 10 mm, a cross-shaped channel of width 11 mm, and a Y-shaped channel of width 10 mm. (c) Diagram showing a closed circuit channel with a cross-section of 7.2 mm wide close to the swimmer well tapering down to 0.5 mm. (d) Diagram showing a closed circuit channel with a uniform cross-section of 2 mm $\times$ 1.1 mm.

First, the fluid flow around a swimmer pinned in the middle of a large Petri dish (148 mm diameter) was investigated. Then the flow behaviour was investigated when the pinned swimmer was placed in 3D-printed straight channels (5.1b) of different width (between 4 and 13 mm), a cross-shaped channel, a Y-shaped channel (all with a depth of 13 mm but only partly filled with liquid to ca. 8.7 mm) and closed channels of different geometry containing the swimmer as shown in Figure 5.1d. The circular channel shown in Figure 5.1c was 1.1

mm deep, and 2 mm wide, with a well containing the swimmer with depth 1.5 mm. The other closed circuit shown in Figure 5.1d was shallower (0.5 mm) with the same depth of the well (1.5 mm), with a width tapering from 7.2 mm to 0.5 mm.

Fluid flow around a pinned swimmer

First, the flow around a pinned swimmer on the surface of a fluid contained in a large Petri dish was investigated. The flow that developed under the action of the swimmer was investigated at different frequencies and amplitudes of the external magnetic field. Figure 5.2 shows a typical flow pattern around a pinned swimmer actuated on the surface of the fluid (in this case water). The external magnetic field used to actuate the swimmer had a frequency of 60 Hz and strength of 2.0 mT.

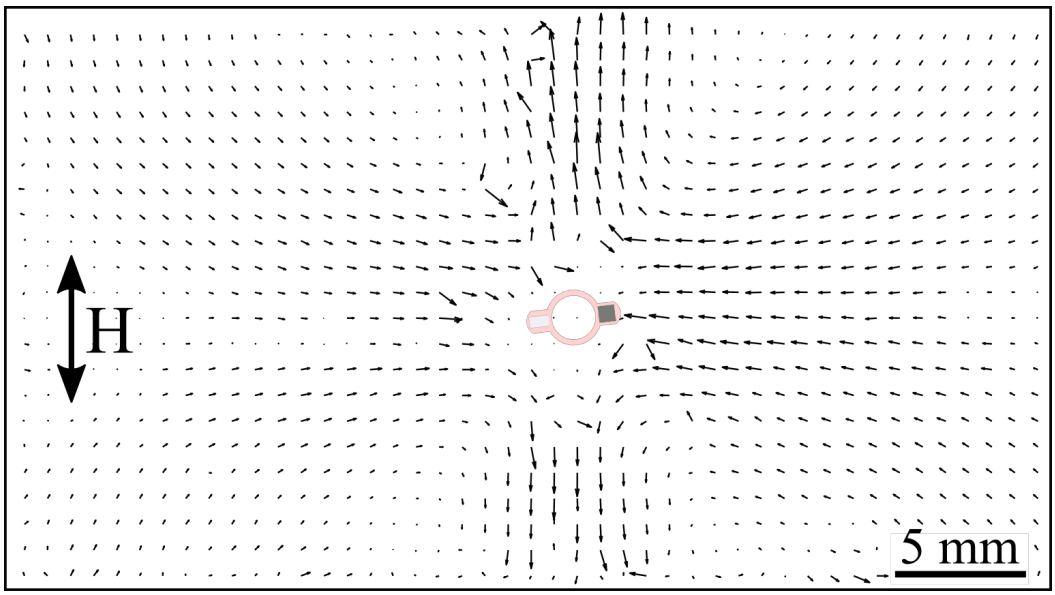

Fig. 5.2 Typical surface flow generated by a pinned swimmer actuated by an external magnetic field of strength 2.0 mT and frequency 60 Hz. The overlay of the schematic swimmer in the middle indicates its mean orientation around which it oscillates (radially and tangentially). The amplitude of the radial and tangential oscillations is on a sub-mm length scale. The swimmer is prevented from translation by a thin post protruding through the elastic circular link (not shown in the picture). The arrows indicate the direction and magnitude of flow, and were generated using particle image velocimetry (PIV).

The cross-shaped steady-state flow pattern that developed had a structure with four vortices around the swimmer, which extended over large distances compared to the size of the swimmer. The resulting net flow was pulled towards the swimmer along its major axis and ejected in the perpendicular direction. As discussed and presented previously, the swimming behaviour of a free, unrestricted two-ferromagnetic particle swimmer greatly depends on the frequency and amplitude of the external magnetic field. Therefore, the effect of these two parameters on the flow features around a pinned swimmer was investigated.

The main flow feature, namely its cross-shaped structure and four vortices, occurred at all frequencies and amplitudes investigated. However, the orientation of the cross varied for different values of the field parameters, enabling the flow pattern to be 'rotated' by merely changing the frequency and amplitude, without spatially repositioning the two Helmholtz coils. This effect is illustrated in Figure 5.3. At field strength of 1.5 mT, the cross-shaped pattern of the flow is rotated by $+25^\circ$ (i.e. clockwise) relative to the applied oscillating magnetic field axis for a frequency of 90 Hz, whereas changing the frequency to 130 Hz rotates the pattern to -30° (anticlockwise).

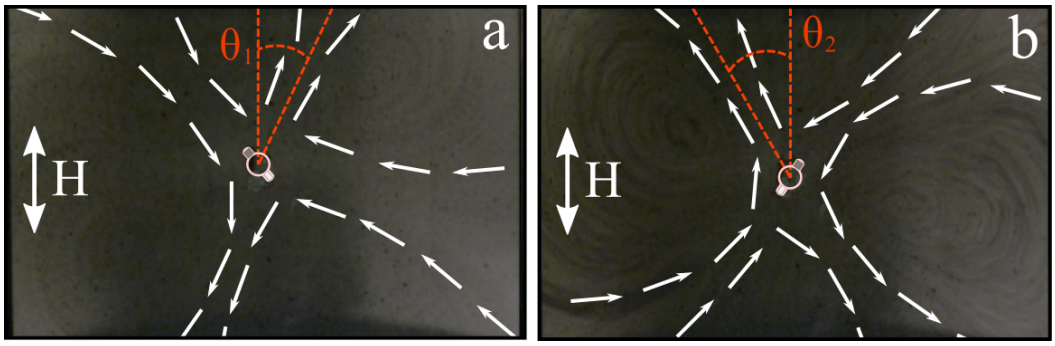

Fig. 5.3 Fluid flow around a pinned swimmer under a magnetic field of strength 1.5 mT and frequency of (a) 90 Hz ($\theta_1 = +25^\circ$ relative to the applied magnetic field) and (b) 130 Hz ($\theta_2 = -30^\circ$ relative to the applied magnetic field). The overlay of the schematic swimmer shows the mean orientation of the pinned swimmer, different at the two frequencies. The arrows represent the direction of flow (but not the magnitude of the velocity).

Note also that the mean orientation of the swimmer with respect to the applied magnetic field is different at the two different frequencies, which is a distinct feature of the swimmer

as discussed previously and relates to its propagation mechanism. The results of these initial experiments indicate the possibility of controlling the direction and speed of flow by varying the parameters of the externally imposed magnetic field. This has clear implications for the behaviour of a pinned swimmer in narrow channels, as reported below.

5.1.2 Production of the fluid pump

Typical microfluidics applications involve fluid flow in narrow channels, a situation that is very different from unrestricted flows due to the effect of nearby boundaries. In principle, the pumping performance of a pinned swimmer (measured as the volumetric flow rate that is generated) is related to the swimming velocity of the equivalent free swimmer. Thus, investigating the swimming performance of a free swimmer in a channel can bring a great deal of understanding of the range of behaviours exhibited by a pinned swimmer

Two-ferromagnetic swimmer within a straight channel

In this investigation, the behaviour of the two-ferromagnetic particle swimmer within a straight channel - of different widths - were tested. For the same channel width and field strength, increasing the frequency leads to variation in swimmer's speed, a change in its mean orientation (due to change of the propagation mechanism) and reversal of direction of propagation, as illustrated in Figure 5.4. At 40 Hz, the swimmer travels with the axis joining the two particles perpendicular to the direction of travel. Increasing the frequency to 130 Hz results in direction reversal and change in the propulsion mode, with the hard particle leading and a much higher speed (from 9.7 ± 0.3 mm s^{-1} to 35.5 ± 0.1 mm s^{-1}). A further increase in frequency to 140 Hz forces another switch in direction of travel, and now the swimmer propels with its soft particle leading and a reduction in speed (12.6 ± 0.2 mm s^{-1}).

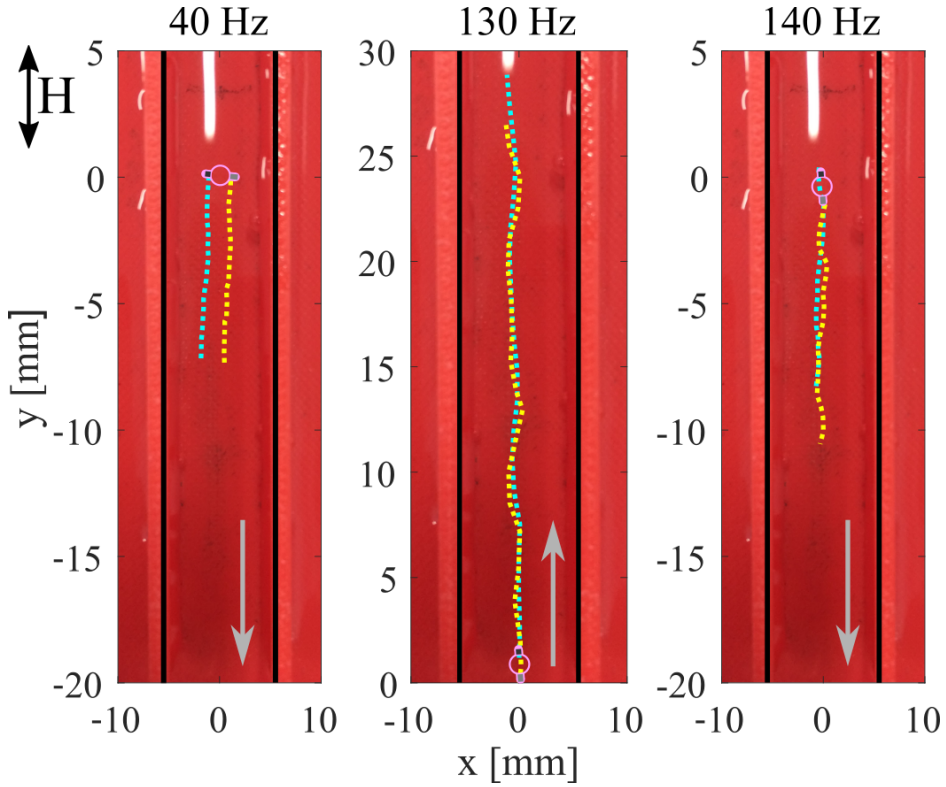

Fig. 5.4 Free two-ferromagnetic particle swimmer in a straight channel of 11 mm width. Trajectories of the hard particle (blue dots) and the soft particle (yellow dots) are overlaid on the image of the channel. The three panels show different propagation modes of the swimmer at a constant magnetic field strength of 1.5 mT and varying frequency (40, 130 and 140 Hz) for a period of 0.8 s. The external magnetic field is aligned along the main axis of the channel. The grey arrows indicate the direction of swimming.

Varying the channel width also affects the swimming performance. Figure 5.5 shows that at 1.5 mT and 40 Hz, the speed of swimming gradually decreases with the increase in the channel width. In principle, the speed of the swimmer is affected by a combination of factors, e.g. channel width, swimming regime, field parameters, orientation etc. [129]. The main factor is expected to be the boundary conditions associated with the channel width. As the width of the channel is decreased the swimmer will start to experience an increase in speed due to the boundary conditions of the channel forcing the swimmer into different regimes. For the case of the smallest channel width, the swimmer is physically forced into the locomotive regime and must propel parallel to the channel.

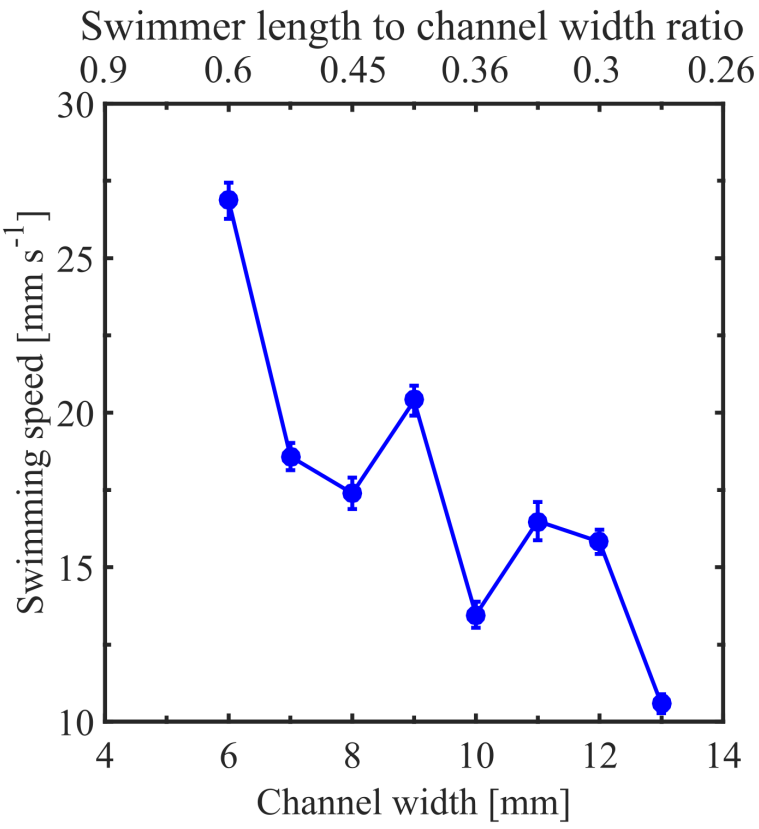

Fig. 5.5 Swimming speed as a function of channel width at field strength of 1.5 mT and frequency of 40 Hz. The upper horizontal axis is the ratio between the swimmer's size (3.6 mm) and the channel width.

Pinned swimmer in a straight channel

The results of the previous section suggest that one could expect a set of varying but controllable flow responses when the swimmer is pinned in a channel. Therefore, the fluid flow induced by a pinned magnetic swimmer in channels of different width and as a function of the external field parameters, fluid viscosity and channel orientation with respect to the external magnetic field was investigated. The experiments were conducted with a range of Reynolds numbers from $\sim 6 \times 10^{-5}$ to ~ 20.

Figure 5.6a shows the frequency dependencies of the flow speed on the surface of the liquid (measured in the middle of the channel) taken at a distance of 40 mm from the position

of the pinned swimmer within the channel. The different trends correspond to different kinematic viscosities, ν, of the fluids used, produced by dissolving predetermined amounts of sucrose in distilled water. For the least viscous liquid ($\nu = 1 \times 10^{-6}$ m^2 s^{-1}), one observes a maximum in the frequency dependence at ~ 60 Hz suggesting that there is an optimal value for which the induced flow reaches its highest rate. With increase in viscosity, this maximum disappears and the flow speed gradually becomes independent of the frequency of the external field. Figure 5.6b shows the dependence of the flow speed on the amplitude of the applied external magnetic field (at constant frequency of 50 Hz). Generally, the flow speed for the more viscous liquids ($\nu = 4.41 \times 10^{-6}$ m^2 s^{-1}, $\nu = 1.01 \times 10^{-5}$ m^2 s^{-1}, and $\nu = 3.45 \times 10^{-5}$ m^2 s^{-1}) increases when the field strength is increased from 1.0 to 3.0 mT. For the two less viscous liquids ($\nu = 1 \times 10^{-6}$ m^2 s^{-1} and $\nu = 2.48 \times 10^{-6}$ m^2 s^{-1}) the dependence has a maximum at 2.0 mT. In this case, it is observed that for field amplitudes higher than 2.0 mT the motion of the swimmer becomes irregular and unstable leading to a reduction in the flow speed.

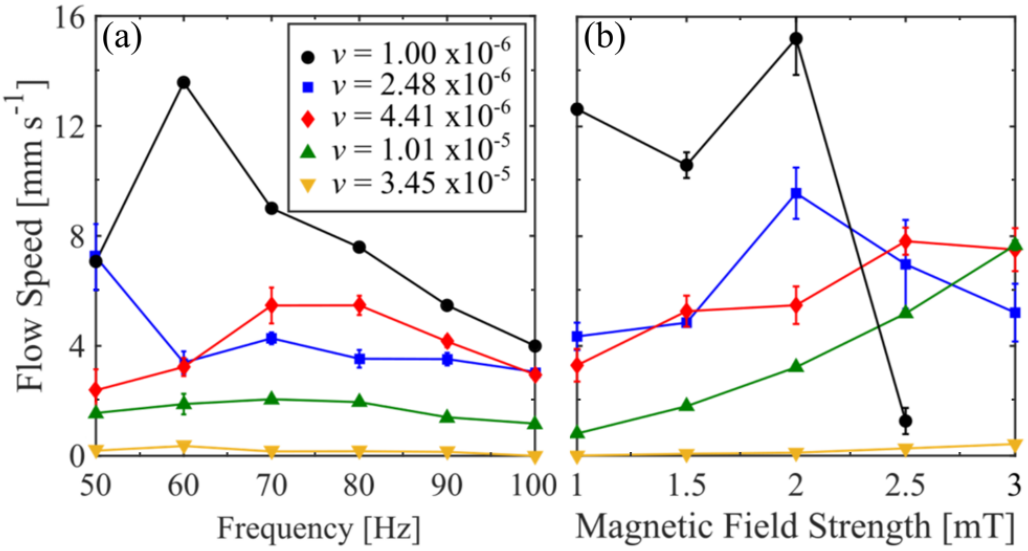

Fig. 5.6 Surface flow speed at different kinematic viscosities in a channel of width 11 mm (a) as a function of field frequency at an amplitude of 1.5 mT, (b) as a function of magnetic field strength at a frequency of 50 Hz. The values of the fluid kinematic viscosity (in m^2 s^{-1}) are given in the insets. The error bars represent the standard deviation from 3 measurements.

Figure 5.6 also shows that the flow speed decreases with the increase in fluid viscosity (apart from the region of instability in Figure 5.5b). However, the flow, although small, is still present and measurable even for the highest viscosity fluid investigated ($\nu = 3.45 \times 10^{-5}$ m^2 s^{-1}, i.e. some 35 times that of water). This mirrors the behaviour of a free two-ferromagnetic particle swimmer previously shown for which the propulsion speed is inversely proportional to the fluid viscosity

Figure 5.7 shows the effect of the channel width on the flow speed. A gradual decrease in the flow speed with increasing channel width is observed, a trend mirroring the free swimmer's propulsion speed (Figure 5.5).

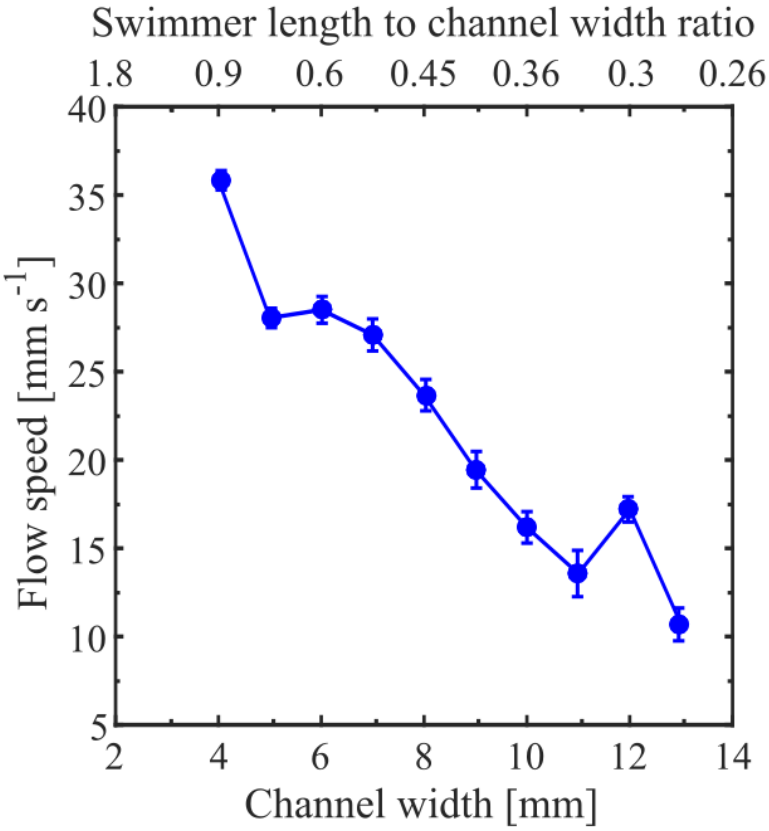

Fig. 5.7 Flow speed as a function of channel width at field strength of 1.5 mT and frequency of 40 Hz. The upper horizontal axis is the ratio between the swimmer's size (3.6 mm) and the channel width.

Further analysis of the behaviour allows the determination of the mean orientation of the pinned swimmer when executing pumping. The mean orientation is shown in Figure 5.8 for different channel widths. For relatively narrow channels of width 4-6 mm (i.e. 0.9-0.6 swimmer length to channel width ratio), confinement of the flow by the walls means that there is a large velocity gradient generating a large viscous drag on the swimmer, which adopts a tilted mean orientation with respect to the channel main axis. For wider channels of width 7-13 mm (0.51-0.28 swimmer length to channel with a ratio), the velocity gradient is lower and the swimmer is able to orient with its axis perpendicular to the channel axis, which is the normal propagation mode of the swimmer at this frequency (Figure 5.4, first panel).

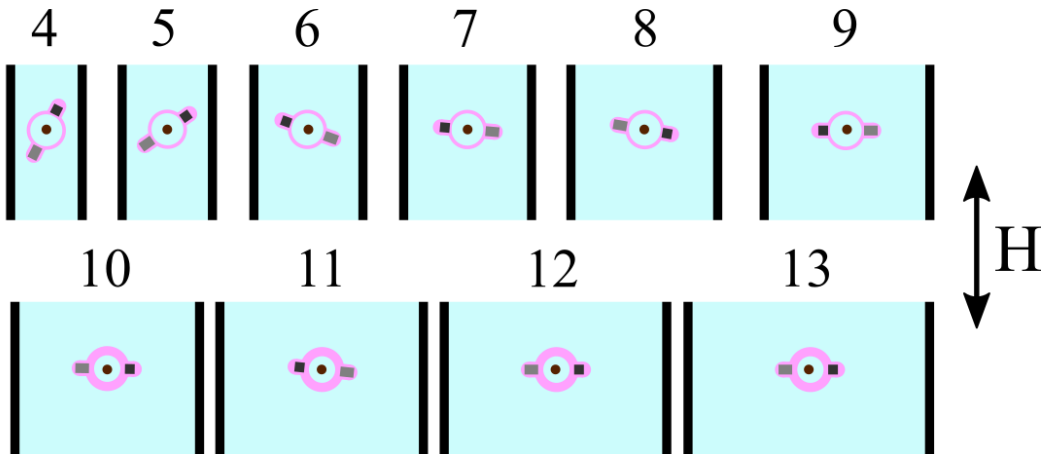

Fig. 5.8 Mean orientation of the pinned swimmer in channels of increasing width once the swimmer reorients when the magnetic field is applied. The magnetic field is aligned along the main axis of the channel and the numbers indicate the width of the channel in mm. Magnetic field parameters: frequency 40 Hz, amplitude 1.5 mT. The direction of flow is downwards.

The final set of experiments with straight channels was aimed at establishing the pumping behaviour of a pinned swimmer as a function of the orientation of the channel with respect to the external magnetic field. Figure 5.9a and Figure 5.9b show the frequency dependencies of the induced flow speeds in two channels of different width (5 mm and 11 mm, respectively) for three orientations of the channel with respect to the external field (0°, 90° and 180°). For the wider channel (11 mm, Figure 5.9b), the trends are similar in the 0° and 180°

orientations (mirror orientations), and show maximums at around 60–70 Hz. The flow in the 90° orientation is slower, and almost stagnant between 50 and 100 Hz.

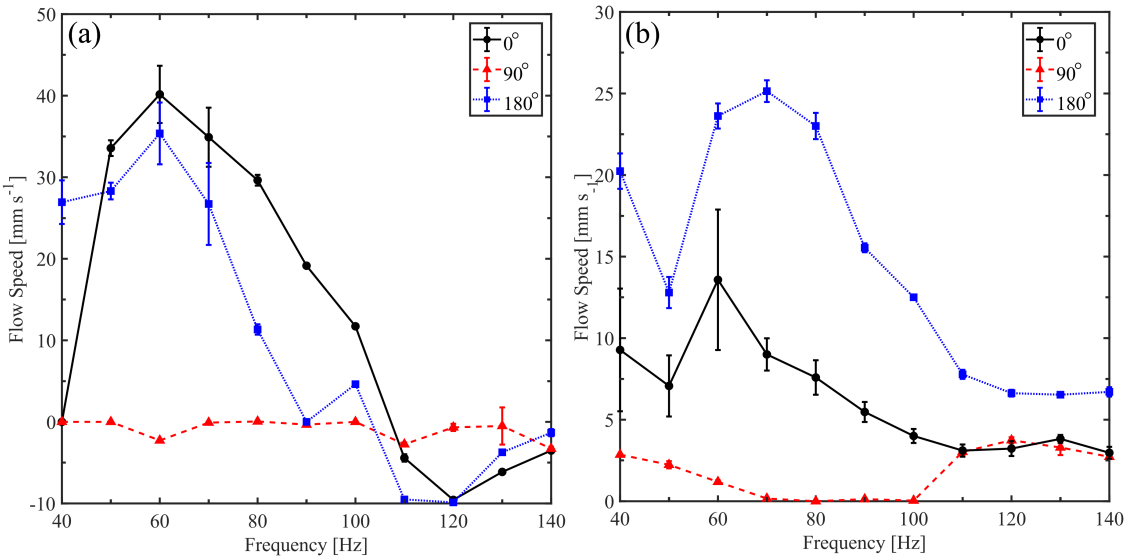

Fig. 5.9 Frequency dependencies of the flow speed at three different orientations between the channel axis and the external magnetic field (0°, 90° and 180°) for (a) channel of width 5 mm and (b) channel of width 11 mm.

The frequency dependencies for the narrower channel (5 mm, Figure 5.9a) show a similar peak around 60 Hz in parallel orientations (0° and 180°), but the flow speeds achieved are higher than those for the wider channel. A prominent feature at this channel width is the reversal of flow direction at higher frequencies between 110 and 140 Hz (note the negative values of the flow speed in Figure 5.9a). In 90° orientation, the flow is stagnant for all frequencies investigated.

The flow patterns at different angles between the channel and the external field are determined by the dynamical behaviour of the pinned swimmer which in principle can be affected by its orientation both with respect to the channel axis and the external field. At angles close to 90° (between the channel and applied field), where the flow is either slow or stagnant, it was observed that the swimmer undergoes rocking motion of large amplitude. When the alignment of the channel is close to parallel to the external field, the

rocking amplitude of the swimmer is much smaller and the induced flow is faster. The mean orientation of the swimmer also depends on the channel width relative to the swimmer's size, as shown in Figure 5.8. Therefore, the structure of the induced flow depends on the interplay between various interactions between the swimmer, field and channel geometry.

In order to clarify the pumping efficiency of the pinned swimmer at different orientations between the channel and the external magnetic field, the speed of the induced fluid flow at intervals of 10° (between 0° and 360°) and 10 Hz (from 40 to 140 Hz) was investigated. The results for the 11 mm channel is presented as a pseudo-colour contour map in Figure 5.10. For lower frequencies, regions of high flow speed are observed at angles close to parallel orientation. Stop-valve behaviour (i.e. stagnant flow) is observed around 90° and 270°. For higher frequencies, the regions of slow or stagnant flow extend over wider range of orientations.

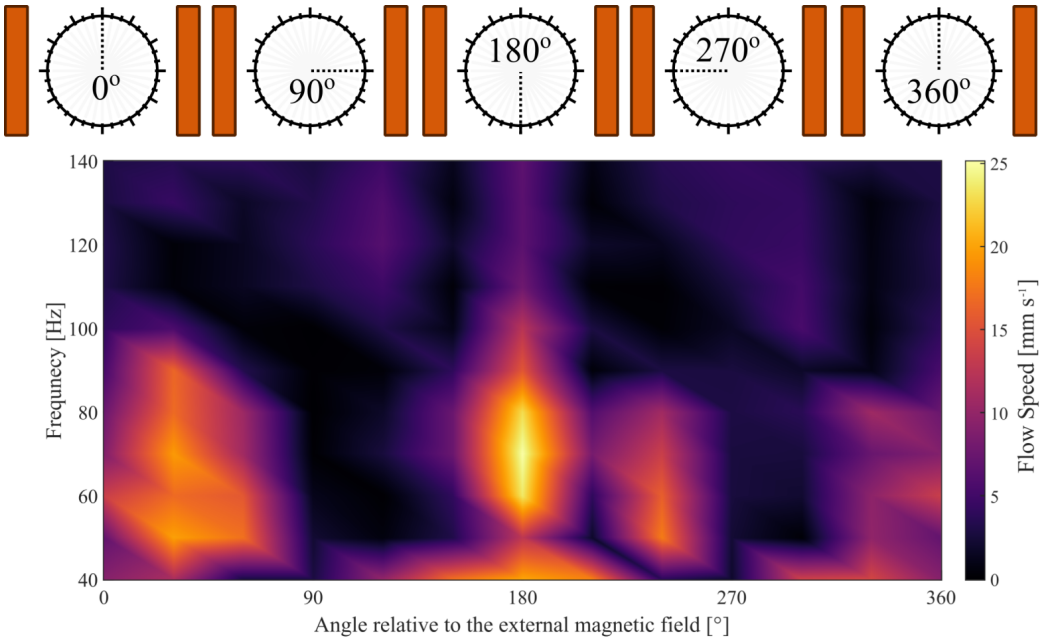

Fig. 5.10 Contour map representing mid-channel flow speed as a function of frequency and channel orientation for the 11 mm channel. The magnetic field amplitude is 1.5 mT.

Together these results illustrate the rich dynamics of the device that can be used to extract useful functionality by varying easily adjustable parameters such as frequency and/or channel orientation.

5.1.3 Tailoring the system for applications

Due to the rich dynamics of this system, it could easily be tailored for a range of applications, depending on the channel geometry. This section is focused on tailoring the channel for possible flow splitter, as well as another system designed to mix a fluid of volume 100 µl.

Pinned swimmer in a cross-shaped channel

The cross-shaped flow structure for a pinned swimmer shown in Figure 5.2 and Figure 5.3 suggests that interesting effects may be expected when the swimmer is actuated near branching channels. Therefore, the flow in a junction mimicking the unrestricted flow structure was explored. A cross-shaped channel of width 10 mm was produced, with the swimmer placed in the centre of the cross. Figure 5.11 shows typical flow patterns for channels oriented at 0°, 10°, 20°, and 30° relative to the applied field (for a magnetic field with frequency 40 Hz and strength 1.5 mT). At 0°, the flow within the channel resembles the cross-shaped structure observed with a swimmer pinned in a Petri dish (Figure 5.2). The fluid is drawn towards the swimmer from the left- and right-hand side channels and ejected in the perpendicular direction. Changing the channel orientation with respect to the field gradually affects the flow and at 30° the flow is directed from the upper left to the upper right channel. However, the two other channels show the formation of vortices, which do not contribute to a net fluid flow. This results in a valve-like regime (two open and two closed branches).

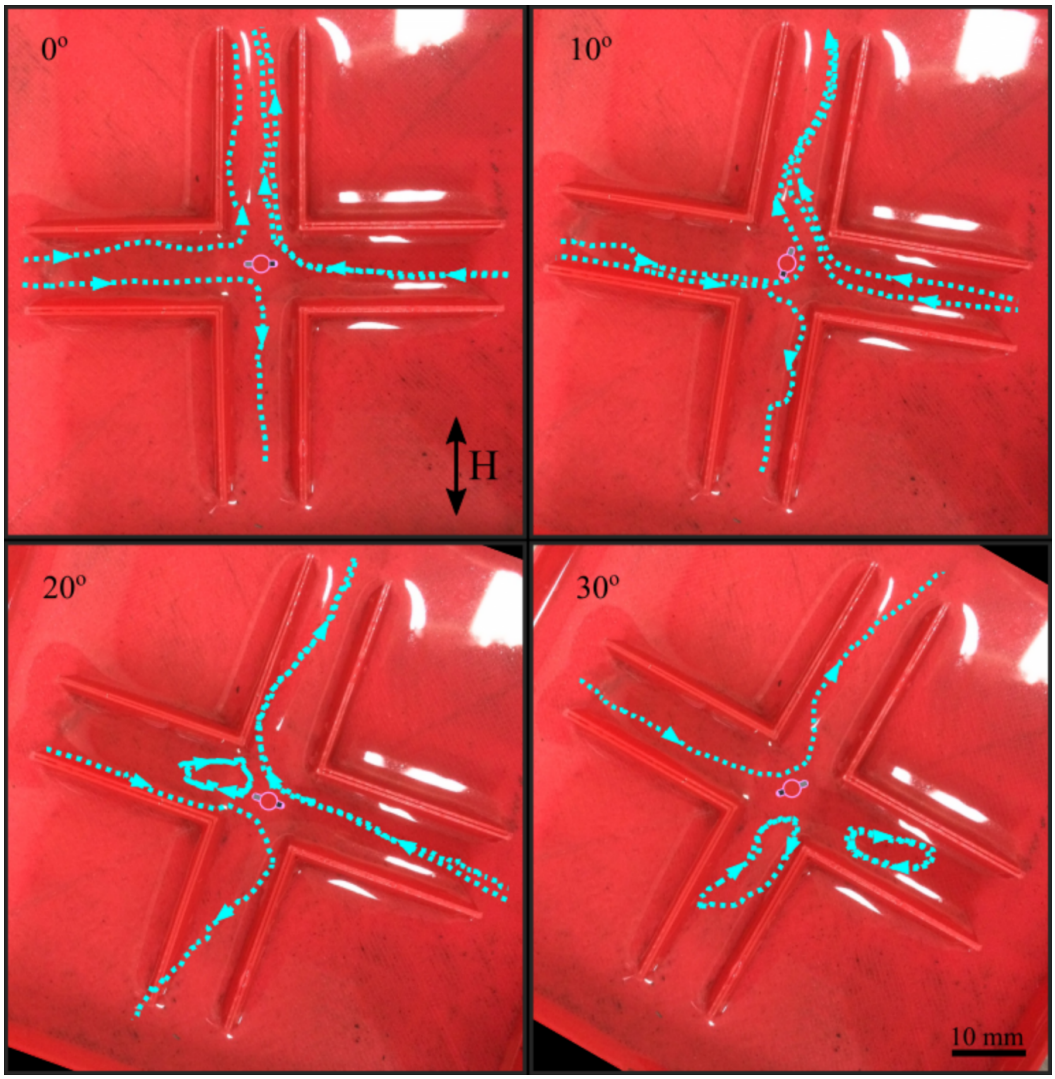

Fig. 5.11 Flow in a cross-shaped channel. The flow lines for four different orientations of the channel relative to the applied magnetic field (0°, 10°, 20°, and 30°) are shown with blue dashed lines and arrows. A schematic diagram of the swimmer is overlaid to show its mean orientation in the centre of the cross. In all orientations, the magnetic field has frequency 40 Hz and strength 1.5 mT.

Pinned swimmer in a Y-shaped channel

The Y-shaped channel was designed to take advantage of the rotation of the flow pattern due to the change in frequency, as seen in Figure 5.3b, with its two arms angled at 30° from the vertical (all arms of the channel had a width of 10 mm, see Figure 5.12), and the swimmer pinned at the centre of the junction. Figure 5.12 shows the change of the fluid flow when the parameters of the external field (frequency and amplitude) are changed without changing the orientation of the channel. At 60 Hz and 2.40 mT (Figure 5.12a), the pinned swimmer directs the flow from the upper right branch towards the bottom branch. Two vortices are formed in the upper left branch; however, they do not generate net fluid flow so this channel is effectively closed. When the frequency and amplitude are adjusted to 130 Hz and 1.38 mT, respectively (Figure 5.12b), the flow is directed from the upper right to the upper left branch, isolating the bottom branch (in which a vortex is observed).

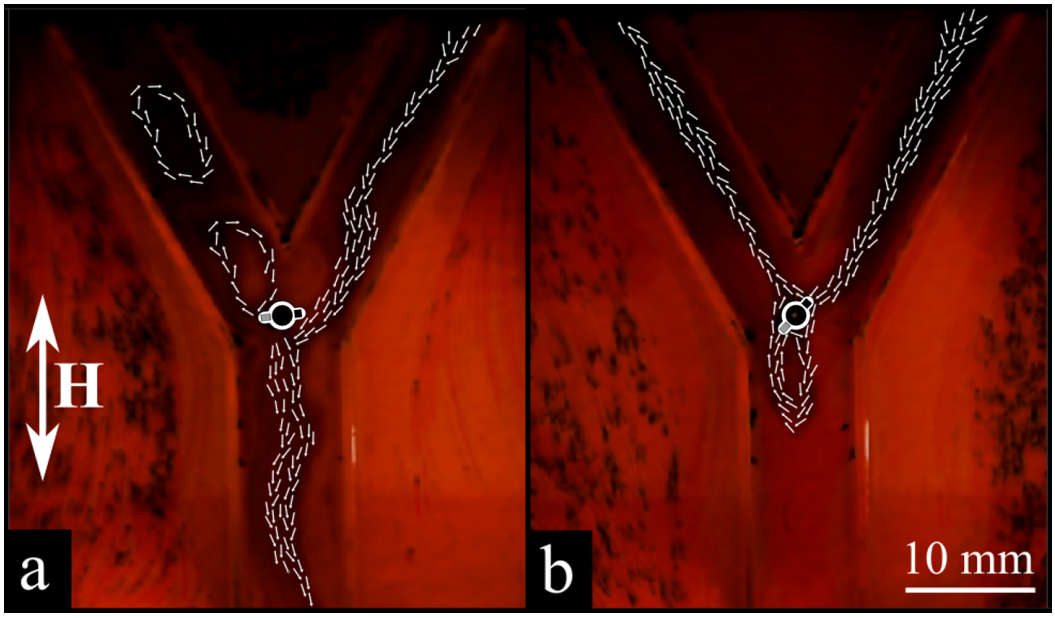

Fig. 5.12 Induced flow with arrows showing the typical flow direction. (a) The direction of the surface flow in the presence of an applied magnetic field of strength 2.40 mT at a frequency of 60 Hz. (b) The direction of the surface flow in the presence of an applied magnetic field of strength 1.38 mT at a frequency of 130 Hz. The schematic of the swimmer shows its orientation in both cases.

A more detailed investigation of the external parameters shows that upon gradual increase of frequency and decrease of amplitude, the two initial vortices in the upper left branch become unstable and part of the flow is directed along this branch. At these intermediate values of the field parameters, the flow from the upper right branch is split between the other two branches. Further increase in frequency and decrease in amplitude causes the flow to be directed entirely towards the upper left branch, effectively closing the bottom branch. These flow patterns are stable and fully reproducible after switching the magnetic field off and on and provide an illustration of the potential for hybrid functionality of the device. With minimal adjustment of the parameters of the external field (without any physical repositioning of the coils or the channel), the device can be used to produce pump- and valve-like functionality as well as serve as a flow splitter. A feedback system could provide automatic adjustment of flow rate and direction.

Pinned swimmer in closed circuits

So far, the demonstrations of fluid pumping have concentrated on walled channels within open dishes. However, many applications require flow generation within a closed system. The final set of experiments presented demonstrates that swimmer-based pumps are also capable of driving circulation in closed circuits. Two such channels were designed which included a well where the swimmer can be positioned using a thin non-magnetic post attached to the bottom of the well (see Figure 5.1c and 5.1d). The first channel was circular with a uniform rectangular cross-section (channel width 2 mm and depth 1.1 mm, with a well for the swimmer of radius 3 mm and depth 1.1 mm) holding $\sim 100\,\mu$l of liquid. The pinned swimmer is capable of driving flow, as seen in Figure 5.13.

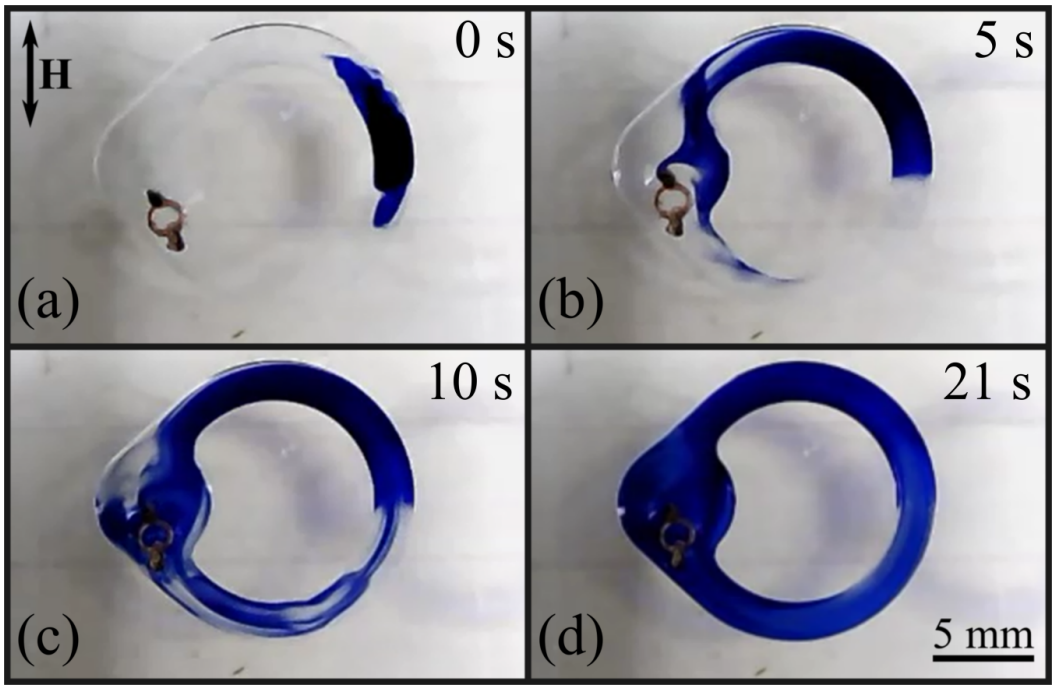

Fig. 5.13 Confined swimmer in a closed loop circular channel. The swimmer is positioned in the left side of the channel in a well and the channel is filled with water. A few drops of ink are placed in the right side of the channel: (a) initial ink distribution; (b) ink distribution at $t = 5$ s; (c) ink distribution $t = 10$ s; (d) ink distribution at $t = 21$ s. The magnetic field has strength 1.5 mT and frequency of 50 Hz.

Figure 5.13 shows four consecutive images of the water-filled channel (100 µl) before and after pumping is activated. Initially, a few drops of ink are placed in the water in the right part of the channel (Figure 5.13a). Shortly after the magnetic field (1.5 mT and 50 Hz) is turned on the swimmer re-orientates and flow is induced in the anticlockwise direction, Figure 5.13e-d.

After 21 seconds of the magnetic field being applied the sample has fully mixed. The speed of this mixing is promising for applications which involve mixing volumes of this size, for example blood plasma analytical tests. The low strength and frequency of the external magnetic field also means that such a system could be made as a portable point-of-care device.

The second design was of a circuit with a non-uniform cross-section. The swimmer well is connected on both sides to 7.2 mm wide and 0.5 mm deep channels, tapering to a 0.5

mm $\times$ 0.5 mm channel on the opposite side (see Figure 5.1c and the inset in Figure 5.14). Even in this case, the swimmer generates flow (Figure 5.14). For this channel, the velocity profile on the surface of the liquid was characterised using a high speed camera attached to a microscope. The resulting velocity profile at 100 Hz and 3.0 mT in the region opposite to the swimmer (where the channel is 0.5 mm $\times$ 0.5 mm) is shown in Figure 5.14. As expected, the velocity profile is approximately parabolic, with a maximal speed of 8.6 ± 0.3 mm s^{-1} at the centre of the channel.

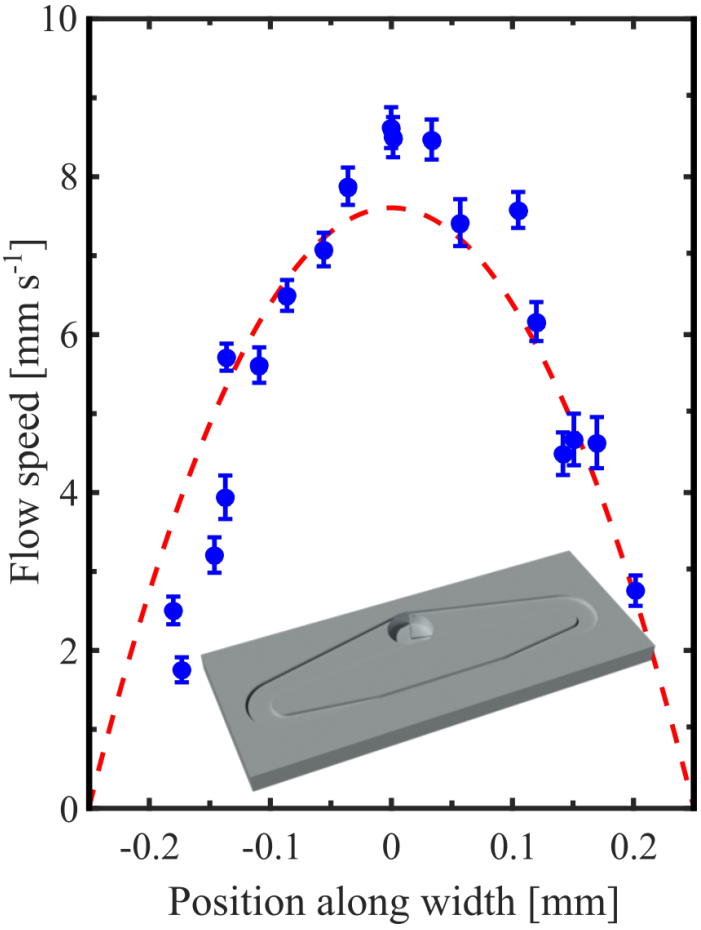

Fig. 5.14 Velocity profile at the surface of the liquid in a closed channel. The red dashed line shows a fitted parabolic function. The velocity profile was measured opposite to the position of the swimmer, where the channel had a cross-section of 0.5 mm $\times$ 0.5 mm. External magnetic field of 100 Hz and 3.0 mT. The inset shows a model of the 3D printed channel.

5.2 Torque driven fluid pumps

In the case of the single ferromagnetic particle swimmer, it is possible to attach one end to the top of an elastic pin. Instead of propelling itself through the fluid, the swimmer now induces a fluid flow. To reduce the size of the system, these torque driven structures could be fabricated into the walls of the channel. This would reduce the amount of passive material (for example the pin) in contact with the fluid. This section will focus on different types of torque driven fluid pumps.

5.2.1 Channel based torque driven fluid pump

A ferromagnetic swimmer attached by one end to a elastic pin (Figure 5.15 inset) will restrict the translational motion, but still allow the beating patterns required to break the time-symmetry. In this configuration, the pinned swimmer rests on the surface of the fluid and the fluid flow it generates can conveniently be investigated. As an example of this application the pinned swimmer (tail length of 7 mm) was attached inside a 3D printed straight channel with width of 5 mm and depth of 10 mm. In this investigation, the external magnetic field is applied perpendicularly to the channel.

Figure 5.15 shows the frequency dependence of the induced flow speeds driven by an actuating magnetic field of 1.5 mT. The figure shows a maximum in flow speed at 30 Hz, then over 40 - 140 Hz a gradual decrease in flow speed between 6 mm s^{-1} and 2 mm s^{-1}. The effectiveness (χ) of the system can be defined as the ratio between the real speed range of a free swimmer and the induced flow speed. When the stable range of the system 40 - 140 Hz was investigated, the effectiveness was found to be $\chi_{7\text{mm}} = 0.31 \pm 0.07$, where the uncertainty is half a standard deviation. The trend seen with his device mimics that seen in Figure 4.24, that the speed decreases with frequency. This is due to the beating of the tail at the higher frequencies not being able to keep in time with the external magnetic field. This is

to be expected as the actuation method and geometries are the same (only differing by the reference frame).

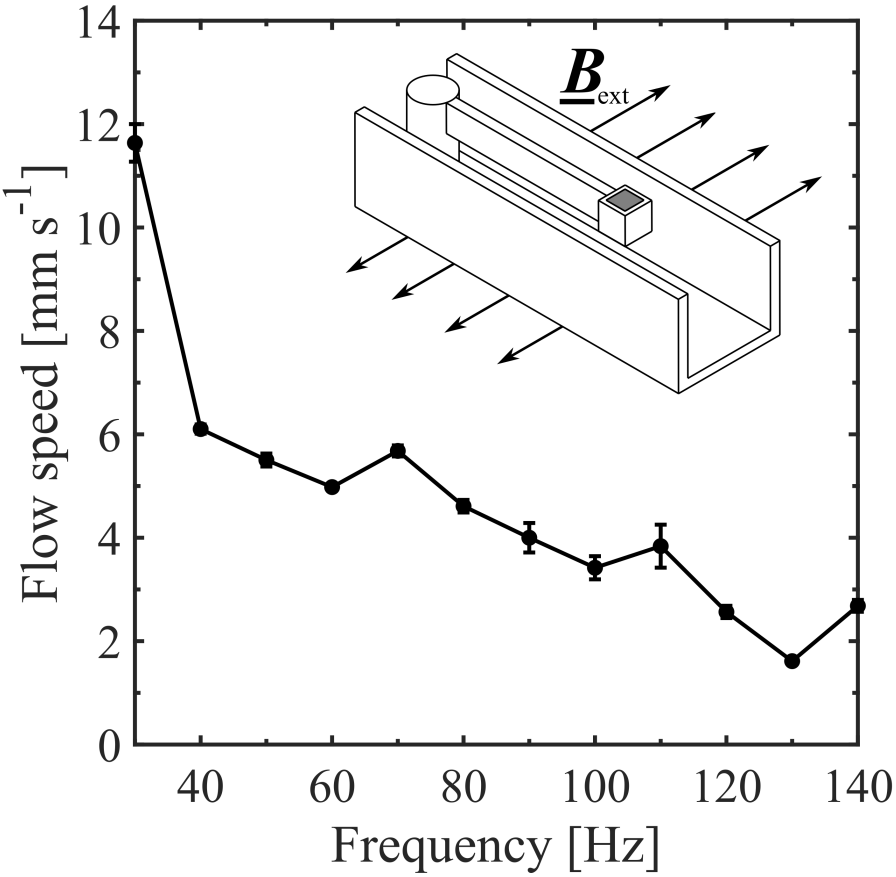

Fig. 5.15 Measured flow speed along the channel as a function of frequency. The inset shows a schematic representation of the single ferromagnetic particle swimmer as a fluid pump. The base of the pin is attached to the base of the channel.

This system shows a stable flow speed over the operating regime of the device. A possible way to improve the effectiveness would be to restrict the translational motion with less effects on the beating pattern. The only concern with such a system is that as the channel width is reduced, the pump could obstruct too much of the channel and the viscous friction will increase, and this may result in a reduced flow rate. This concern could be addressed by scaling the pump with the channel, or incorporating the system into the walls of the channel.

5.2.2 Wall based torque driven fluid pump

This section will focus on the flow induced by a torque driven pump which is incorporated into the wall of a channel. Figure 5.16a shows an Autodesk AutoCAD diagram showing the geometry of the system. The pump system comprises of a hard ferromagnetic particle (NdFeB, 0.5 mm $\times$ 0.5 mm $\times$ 0.5 mm), encapsulated within an elastic tail, similar to the torque driven swimmers previously shown - with the only difference being the curved edges. At the end of the tail, without the magnetic particle, there is an area which can be used to attached the tail to the channel wall. The total length of the pump (tail and head) was $L = 3.8$ mm, the depth was of 0.8 mm and width 0.45 mm. The length chosen is in correspondence to the investigation previously shown on torque driven swimmers. The inverse of the AutoCAD diagram was created and this was used to produce the 3D printed mould. Figure 5.16b shows a photograph of the pump attached (using super glue) to the wall of the channel. Figure 5.16c shows a schematic of the system which can be used to estimate the deflection, w, induced for different magnetic field strengths.

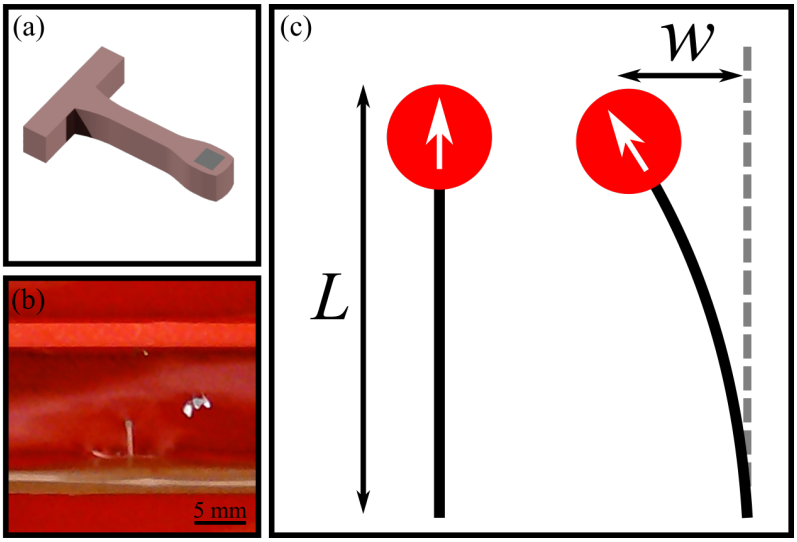

Fig. 5.16 (a) AutoCAD diagram showing the geometry of a torque driven pump attached to a channel wall. (b) Photograph showing a torque driven pump attached to a channel wall. (c) Schematic diagram showing the deflection, w of the pump, as well as the total length $L = 3.8$ mm.

To investigate the induced deflection, the applied force to the pump can be estimated. A simple force-displacement relationship for the bending of an elastic cylindrical beam can be given by

$$\mathbf{F_{disp}} = \left(\frac{3\pi}{64} E \frac{D^4}{L^3}\right) w, \tag{5.1}$$

where E is the Youngs' modulus of the beam (0.001 GPa), $\mathbf{F_{disp}}$ is the bending force, and D is the effective diameter of the beam (0.58 mm). Analysing the videos, the position of the maximum deflection of the end of the pump for each magnetic field strength (at a frequency of 30 Hz) was found. Using the initial position and the maximum deflection position, an estimate of the bending force could be made. The measured deflection and estimated bending force (using equation 5.1) are shown in Table 5.1.

Magnetic field [mT]	Deflection [mm]	Force [mN]
2.5	0.41	45.1 ± 3.9
3.0	0.35	38.5 ± 1.2
3.5	0.41	45.1 ± 3.9
4.0	0.47	51.7 ± 5.1
4.5	0.46	50.6 ± 1.9
5.0	0.49	53.9 ± 2.5
5.5	0.58	63.8 ± 2.7
6.0	0.64	70.4 ± 1.1

Table 5.1 Deflection and bending force for increasing magnetic field strength. The error in the deflection is 0.01 mm from the detect method of the pixels, resulting in the error in the force values.

Table 5.1 clearly shows an increase in deflection for increasing magnetic field strength, and in turn an increase in bending force. This is expected as the induced magnetic torque felt by the NdFeB particle will increase with increasing field strength. The induced flow speed can be investigated, using tracer particles on the surface of the fluid. Figure 5.17 shows the induced flow speed as a function of the magnetic field strength, once again at a frequency

of 30 Hz. To further visualise the deflection the inset on Figure 5.17 shows the increasing deflection for increasing magnetic field strength.

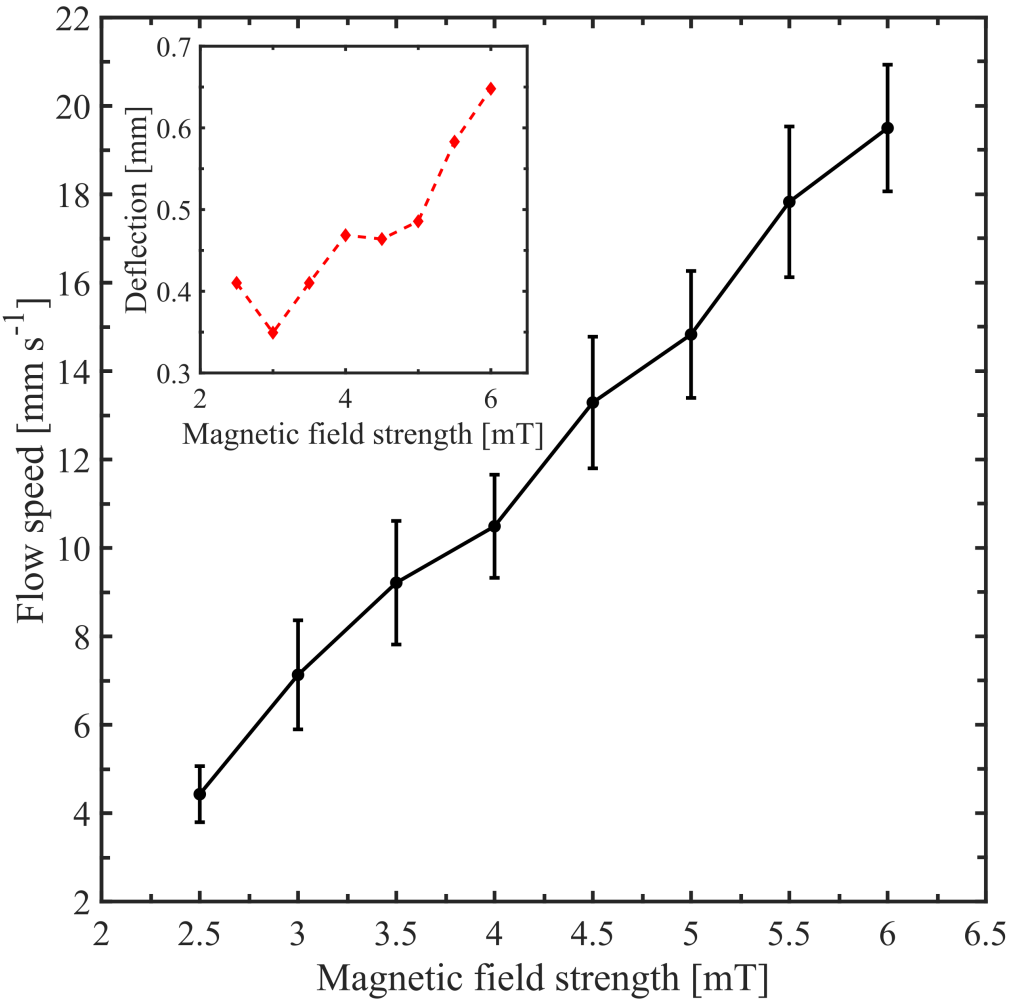

Fig. 5.17 Flow speed as a function magnetic field strength with a frequency of 30 Hz. The inset shows the induced deflection of the pump as a function of the magnetic field strength. The inset shows the deflection, w, of the tail as a function of magnetic field strength, a schematic of this interaction is shown in Figure 5.16c

5.3 Torque driven ferromagnetic membranes

The focus of this section will be magnetically controlled elastic membranes. These systems have seen an increase in interest due to their non-invasive nature [96–98]. Such systems could be attached in various locations along a microchannel, as well as placed on the top surface. These membranes could also be built into the walls of the channels and serve to induce fluid flow.

The work presented will focus on membranes which experience magnetic torques when an external magnetic field is applied. These membranes consist of arrays of magnetic particles and elastic linking structures. The devices are based on the similar swimmer design previously presented where the magnetic torque creates a mechanical torsion and deforms the elastic coupling.

This section will focus on the fabrication and investigation of two different torque driven magnetic membranes. The first membrane is based on the torque driven ferromagnetic swimmer (previously discussed in J.K. Hamilton *et al* [114]), and consists of an array of single particle swimmers. This membrane was attached to the end of a channel and the induced flow inside and outside of the channel was investigated.

The second membrane used the same actuation method - relying on the induced magnetic torque coupling with the mechanical torsion. In this case the membrane consists of a network of magnetic disks, connected with elastic links. Two system were created with this design: the first with all disks magnetised out-of-plane, and the second with a mix of in-plane and out-of-plane magnetisation. The membranes were pinned on the fluid surface and the induced flow was investigated.

5.3.1 Flagella-based magnetic membranes

In this study, properties and external responses of a macro-scaled ferromagnetic membrane is discussed. Experimentally, the membrane was created based on the millimetre-scale torque

driven swimmers and pumps previously discussed. The structure was created with a unit cell containing a flagella structure - mimicking structures observed in nature (shown in Figure 5.18a). The devices were attached to the end of a channel and actuated by manipulating the frequency of a weak oscillating magnetic field (1.5 mT). The induced flow inside and outside of the channel was investigated.

Fabrication of the flagella-based membranes

Experimentally, the flagella-based membrane was composed of a magnetically hard NdFeB cubic particle (0.5 mm $\times$ 0.5 mm $\times$ 0.5 mm). The devices were constructed using a 3D printed mould similar to that of the torque driven ferromagnetic swimmers. To produce a 2 $\times$ 2 unit cell geometry (shown in Figure 5.18a), a mould was designed using Autodesk AutoCAD and 3D printed using a Formlabs Form 2. The magnetically hard ferromagnetic particle was fixed with its anisotropy axis along the tail axis of the unit cell, then the mould was filled with a silicone rubber. After the liquid rubber was cured, the desired tail was produced which also encapsulated the magnetic particle.

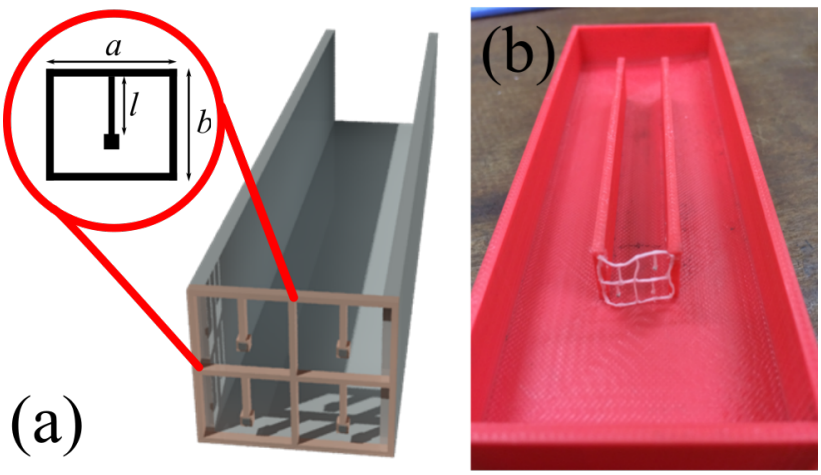

Fig. 5.18 (a) Schematic diagram of a unit cell of the flagella-based membrane, showing the outer dimensions of the cell (a and b), as well as the length of the tail l. (b) Photograph of the 2 x 2 flagella-based membrane attached to the end of a 11 mm wide 3D printed channel.

The dimensions of a unit cell were: $a = 6.8$ mm, $b = 5.8$ mm, $l = 3$ mm, depth = 0.8 mm and width = 0.4 mm. The head around the magnetic particle had dimensions 0.8 mm $\times$ 0.8 mm $\times$ 0.8 mm to ensure full encapsulation of the particle. The length of the tail chosen was 3 mm based on the previous study on single ferromagnetic particle swimmers where the peak in swimming speed was at this length. Figure 5.18b shows the descried membrane (comprising of a 2 $\times$2 array of flagella based swimmers, attached to one end of a channel. The investigated focused on exploring the fluid behaviour induced by the membrane inside and outside of the channel."

Inducing a fluid flow outside the channel

The induced flow of the flagella-based membrane was studied by fixing a 2 $\times$ 2 structure to the end 3D printed channel. The channel had a length of 80 mm and width of 11 mm. The channel was filled with fluid - in this study water - and the device was fully submerged.

The frequency dependence of the induced flow was investigated by applying a fixed field strength of 1.5 mT and varying the frequency between 40 and 140 Hz. Figure 5.19a shows the particle image velocimetry (PIV) results of the generated flow for the flagella-based membrane in the presence of a 1.5 mT external magnetic field and frequencies 40 Hz, 80 Hz, 120 Hz. A key feature observed was two vortices produced outside of the channel for frequencies $>$ 60 Hz. These vortices indicate that a flow is being induced.

Using PIV, the averaged - over 200 frames - flow velocity was observed for different frequencies. Figure 5.19b shows the flow speed generated outside the end of the channel as a function of frequency. The flow speed was shown to gradually increase with increasing frequency and peaked at 120 Hz 6.9 ± 0.2 mm s^{-1}.

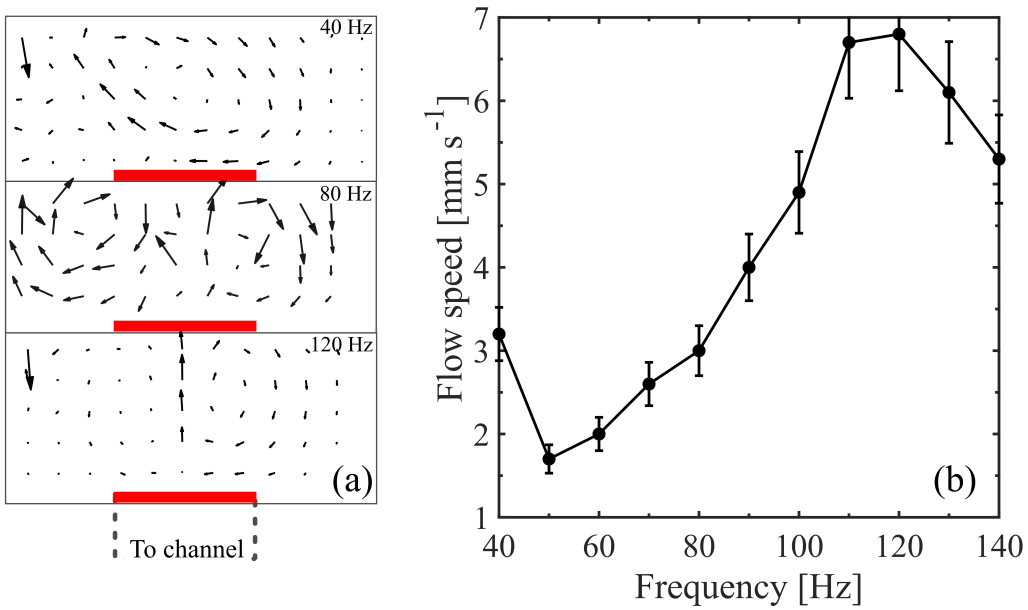

Fig. 5.19 (a) Shows the generated PIV flow fields. The red region indicates the end of the channel, where the membrane is attached. (b) Flow velocity outside the channel as a function of frequency for the flagella-based membrane. The strength of the external magnetic field is kept constant at 1.5 mT.

Inducing a fluid flow inside the channel

Following the investigation outside the channel, the flow of the fluid within the channel was tracked and investigated. Using an external magnetic field of 1.5 mT and frequency 100 Hz the induced surface wave can be observed and tracked.

The speed of propagation of the front of the pulsing wave was tracked using a 2000 FPS camera. Figure 5.20 shows the front speed along the length of the channel. The front speed remains constant ($\sim 450 \pm 92$ mm s^{-1}) between 5 mm (near the membrane) to 40 mm (approximately halfway down the channel). At distances > 50 mm, the front speed starts to fall off, due to the channel exit.

It is clear that the front speed is much larger than the average velocities previously shown from PIV. This is due to the fact the particles do not travel along the front of the induced

wave. Further investigation using tracker particles - and PIV - will need to be conducted to get a full understanding of the induced surface flow down the channel.

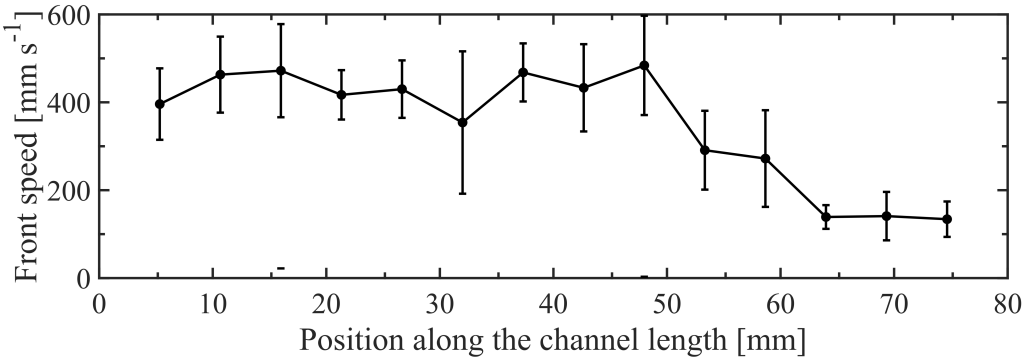

Fig. 5.20 The front speed as a function of distance along the channel. The external magnetic field has strength 1.5 mT and frequency 100 Hz. The membrane is attached at distance = 0 mm.

5.3.2 Disk-based magnetic membranes

Based on the initial idea of the flagella-based membrane, disk-based magnetic membranes were fabricated. They still rely on the induced magnetic torque and mechanical torsion interactions. Two membranes of the same design but with different combinations of magnetic moments were investigated. For both membranes the tilt of the magnetic disks elements due to an external magnetic field were investigated. Also investigated was how manipulating the parameters of the external magnetic field affects the induced fluid flow.

Fabrication of the disk-based magnetic membranes

Using a 3D printed mould magnetic components were fabricated with dimensions: diameter Φ_M = 2.45 mm and depth = 0.8 mm. NdFeB powder (average diameter $< 10\,\mu m$) was added to silicone rubber and mixed (approximately 6% of the total volume). The liquid magnetic rubber was then placed in the mould to create the desired magnetic disks.

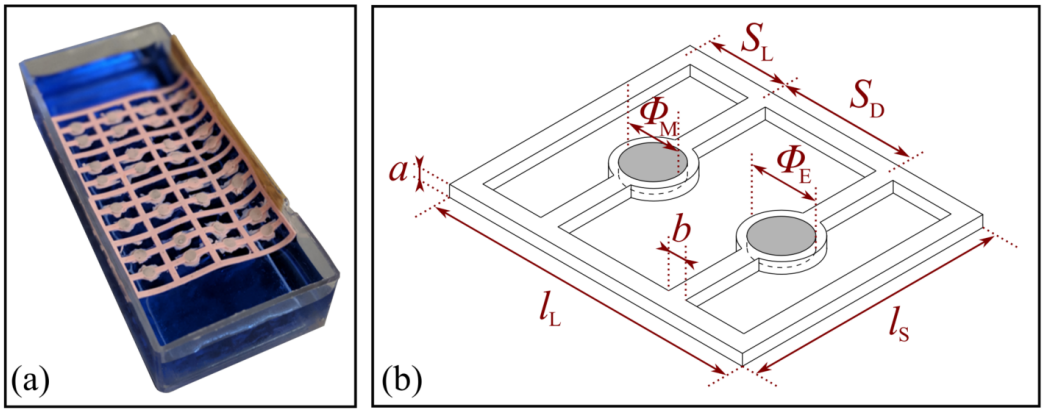

Fig. 5.21 (a) Photograph showing the geometry of the investigated disk-based membrane. (b) Detailed schematic of the fabricated disk-based membrane, showing all dimensions.

The cured magnetic components were magnetised in a Vibrating Sample Magnetometer (VSM) at 1.8 T for 17 minutes to saturate the disks along the major axis of the geometry, resulting in a magnetic moment $m = 1.4 \times 10^{-4}$ A m^2. Once the magnetic components were magnetised they were placed in the mould of the membrane. The dimensions of a unit cell were: link depth a = 0.4 mm, link width b = 1.2 mm, outer long length l_L = 12.8 mm, and outer short length l_S = 9.1 mm. The centre-to-centre separation between the magnetic disk was S_D = 4.0 mm, and the separation between a disk and the side of the unit cell was S_L = 3.8 mm. Non-magnetic liquid silicone rubber was placed in the mould and cured at room temperature. Figure 5.21a shows photograph of a full membrane and schematic diagram of a unit cell (Figure 5.21b). More information regarding the full fabrication can be found in Experimental Methods Chapter.

Investigation of the induced tilt angle

In solid mechanics, torsion is the twisting of an object due to an applied torque τ_{mec}, which can be expressed as

$$\tau_{mec} = \frac{J_T}{l} G\varphi. \tag{5.2}$$

In this case J_T is the torsion constant for a cross-section, l is the length of the object which the torque is being applied over, G is the shear modulus, and φ is the angle of twist (in radians).

The magnetic torque $\boldsymbol{T}_M$ induced by a magnetic moment $\boldsymbol{m}$ in the presence of an external magnetic field $\boldsymbol{B}$

$$\boldsymbol{T}_M = \boldsymbol{m} \times \boldsymbol{B}. \tag{5.3}$$

Using Equation 5.2 and 5.3, a predicted angular dependence on the strength of the external magnetic field can be produced. The predicted dependence is shown with the red dotted line on Figure 5.22. In the case, J_T for a rectangular cross-section with long side length, a and short, b, has been assumed to be

$$J_T \approx ab^3 \left(\frac{1}{3} - 0.21 \frac{b}{a} \left(1 - \frac{b^4}{12a^4} \right) \right). \tag{5.4}$$

Figure 5.22 and Figure 5.23 show the angle of tilt for two cases: when all magnetic disks are magnetised out-of-plane (Figure 5.22) and when in a unit cell, one disk is in-plane and the other is out-of-plane (Figure 5.23). Figure 5.22 shows that the measured data (the error bars show the standard deviation of 30 disks), oscillating in both directions of the external magnetic field fit linearly (blue solid line). The predicted trend (red dotted line) and the measured (blue solid line) fit show an excellent agreement, only with a small shift in the intercept. Such shift is expected due to the presence of the fluid in the experiment, producing a threshold field strength required to overcome the surface tension forces. This effect is not taken into account in the model.

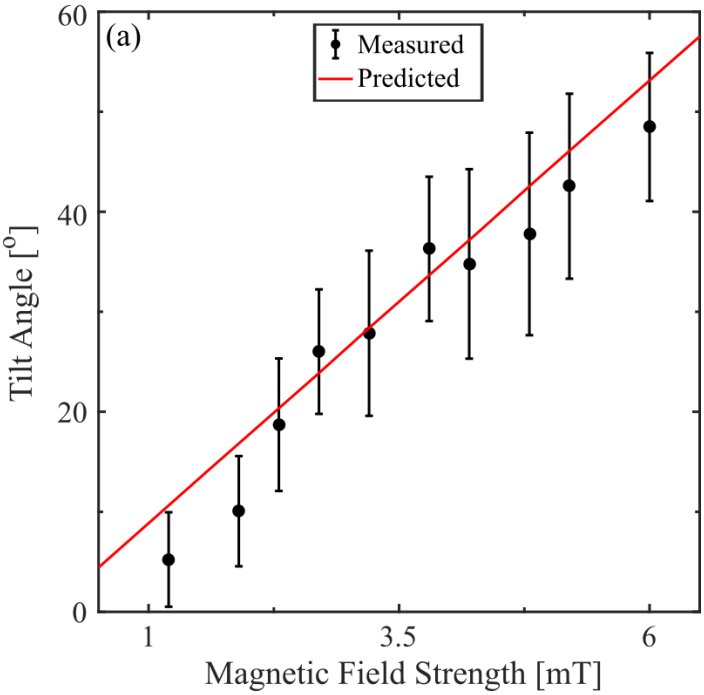

Fig. 5.22 The induced tilt angle as a function of magnetic field strength for a membrane with all disks magnetised out-of-plane. The red dotted line shows the predicted tilt angle for the parameters. The blue solid line shows a linear fit to the measured data.

Figure 5.23 shows the angle of tilt for a membrane with in-plane and out-of-plane magnetised disks. The black circles show the angle of tilt for the out-of-plane disks and the red diamonds show the angle of tilt for the in-plane disks. The error bars show the standard deviation for 24 disks. The figure shows the out-of-plane disks induce similar rotation angles for both directions of the applied magnetic field. The in-plane disks show very different behaviours when the magnetic field is applied in different directions. The solid red line (diamonds) shows that the induced torsion is minimal compared to the $< 90^{\circ}$ rotation of the dotted red line. This difference in the rotation is due to the rest magnetisation orientations of disks in the membrane.

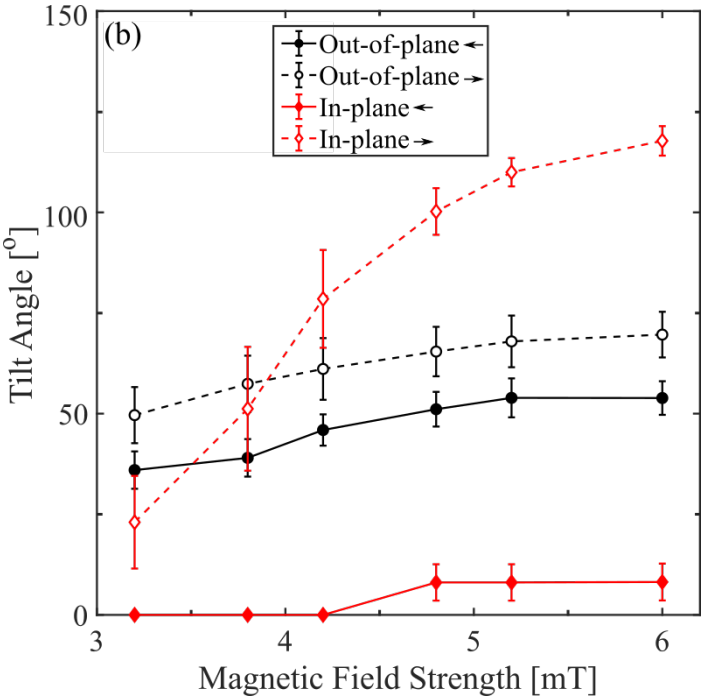

Fig. 5.23 The tilt angle as a function of magnetic field strength for a membrane with a mix of disks magnetised in-plane and out-of-plane. The black data shows the tilt angle for out-of-plane for the magnetic field being applied in each direction. The red data shows the tilt angle for in-plane for the magnetic field being applied in each direction.

In the simplest case, one can take two neighbouring magnetic disks – neglecting net motion of the membranes and investigate if in fact they create a non-reciprocal motion. For the membrane with both disks magnetised out-of-plane the sequence shown in Figure 5.24 over one cycle of the magnetic field is observed. The produced motion is reciprocal in nature, thus not generating a net flow.

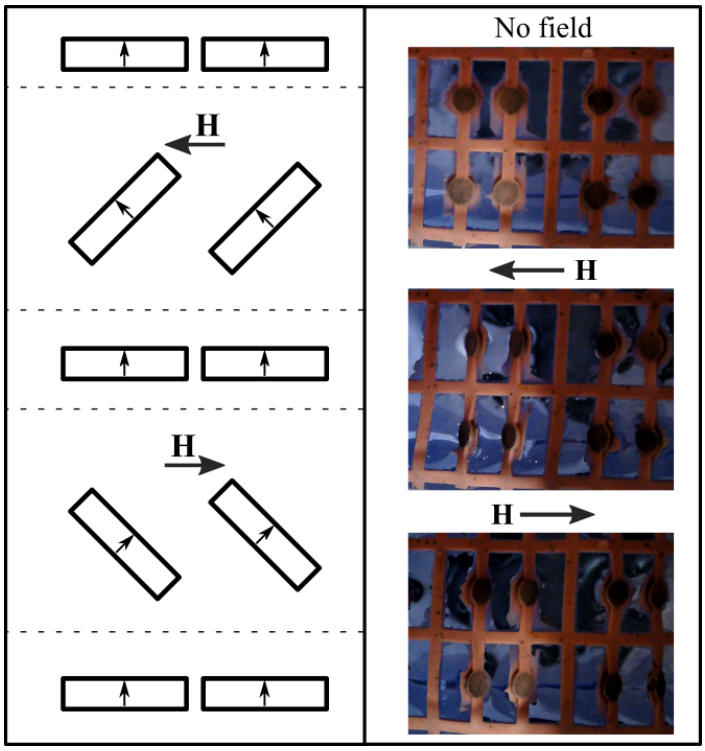

Fig. 5.24 Schematic diagram and photographs visualising the rotation of the a unit cell; with both disks magnetised out-of-plane.

However, when preforming the same analysis on the membrane with disks magnetised in-plane and out-of-plane, the sequence shown in Figure 5.25 is observed. In this case, the motion can be stated as non-reciprocal, thus even in this simplified case, the system would generate a fluid flow at a low Reynolds number.

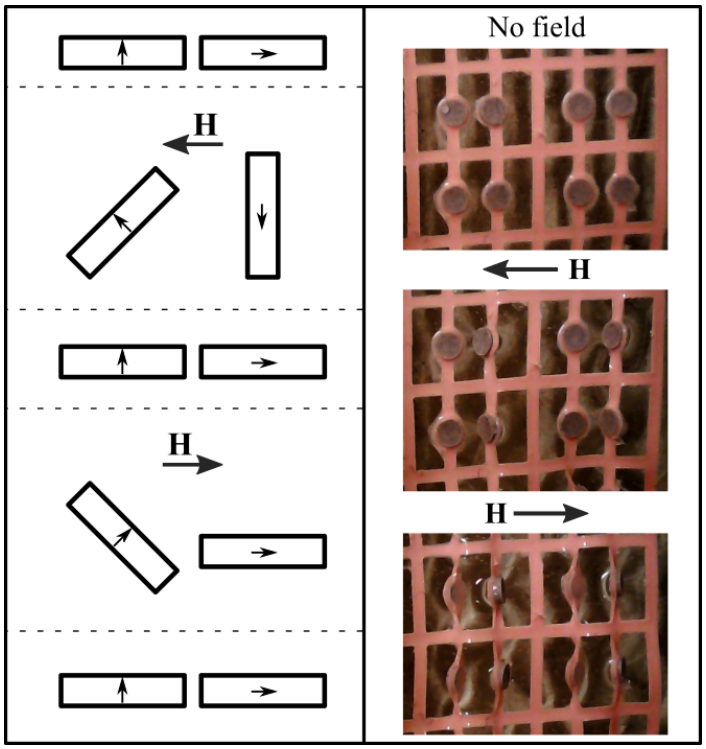

Fig. 5.25 Schematic diagram and photographs visualising the rotation of the a unit cell with one disk magnetised out-of-plane and the other in-plane.

In reality, the systems are not as simple as two tilting disks, as there is a net induced motion of the full membrane, as well as elastic deformations, and surface tension effects. Thus both membranes are able to induce a fluid flow.

Investigation of the induced flow

To investigate the flow induced by the membrane, the induced flow speed as a function of different external parameters, frequency and magnitude of the external magnetic field, was examined. The induce a flow, the membrane was placed on the fluid-air interface and pinned in the centre of a Petri dish, so the membrane is free to rotate if required. Particle image velocimetry (PIV) was used to visualise and analyse the flow.

Figure 5.26 shows the PIV image of the generated flow for an out-of-plane only membrane in the presence of a 1.5 mT field with frequency 40 Hz. The main feature observed is the

four vortices produced around the membrane. The maximum speed of jet of the upper two vortices has a value of $\sim 68 \pm 0.7$ mm s^{-1}, compared to the maximum speed $\sim 26 \pm 0.4$ mm s^{-1} for the jet of the lower two (shown in Figure 5.26). Due to this difference between the jet speeds, if the membrane was free to move on the surface, it would have a preferred direction of propagation. In the case of the pinned membrane, the membrane will induce a preferred direction, creating a net flow.

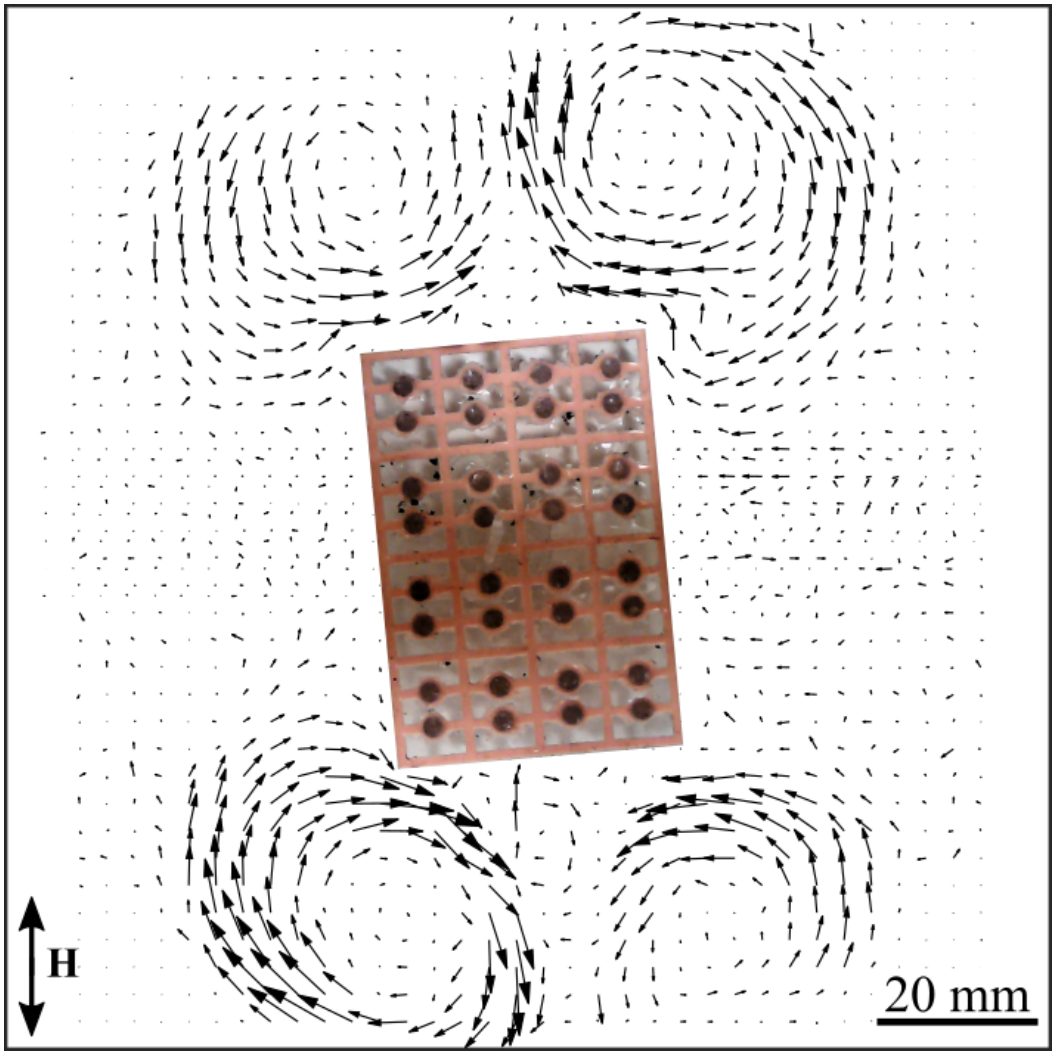

Fig. 5.26 PIV visualisation of the induced flow created by the out-of-plane disk-based membrane in the presence of a 40 Hz, 1.5 mT magnetic field.

Using the information gathered from Figure 5.26, a dependence of flow speed on external parameters can be created, by taking the averaged velocity magnitude of the region around

the two upper vortices. Figure 5.27 (black circles) shows the dependence of flow speed on frequency for the two membranes. Two regimes for the all out-of-plane membrane (< 70 Hz and > 70 Hz) are observed, this is due to the membrane being free to rotate on the surface. At 40 Hz the membrane has the optimum orientation relative to the applied field for the tilting of the magnetic disks (a unit cell parallel to the field). At frequencies between 40 Hz and 80 Hz the membrane is rotating in the field, once the frequency is > 80 Hz, the membrane has rotated 90° producing the second regime.

The motion of the fluid observed in the case of the membrane with in and out-of-plane magnetised disk is a more irregular compared to the previous membrane, but the vortices still occur. Figure 5.27 (red diamond) shows the dependence of the flow speed as a function of frequency. Once again, a peak at 40 Hz is observed, with a second at 70 Hz. The rotation of the membrane in this case is typically at 45° to the applied magnetic field.

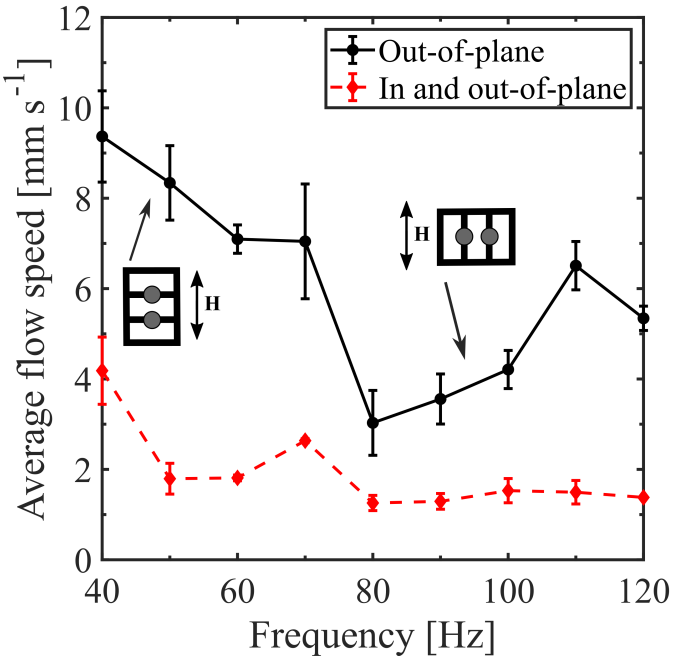

Fig. 5.27 Flow speed as a function of frequency for the out-of-plane (black circle) and in and out-of-plane mixed (red diamond) membranes. Inset shows the orientation of the out-of-plane membrane.

Figure 5.28 shows the flow speed for increasing magnetic field strength for three different frequencies, for the membrane with all out-of-plane magnetic disks. As expected, the flow speed increases with increasing field strength, indicating that the flow speed has a dependence of the angle of tilt (shown in Figure 5.22). At 40 Hz and fields > 2.5 mT, the vortices start to break down, thus the average flow speed plateaus.

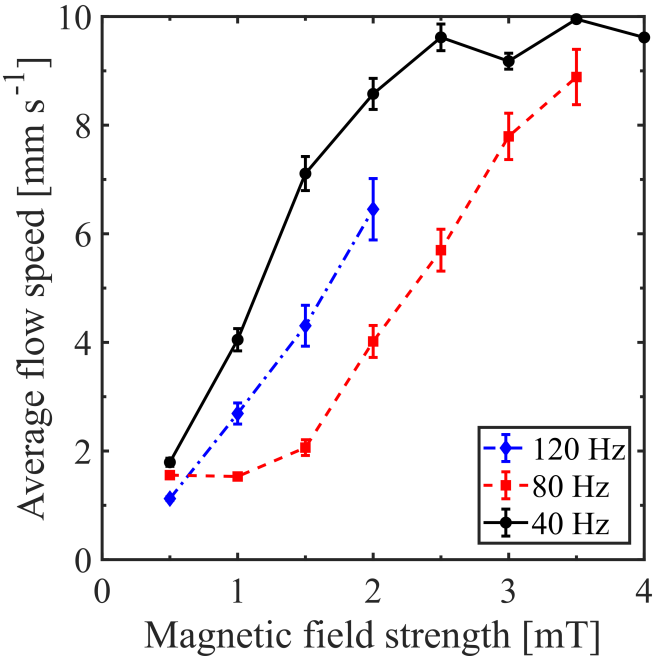

Fig. 5.28 Flow speed as a function of magnetic field strength for 40 Hz (black circles), 80 Hz (red squares) and 120 Hz (blue diamonds), for the out-of-plane membrane.

Figure 5.29 shows a similar dependence for the membrane with both in-plane and out-of-plane magnetic disks - with comparably lower velocities. At high fields ($>$ 3.0 mT) and 40 Hz, both membranes are creating a similar averaged flow speed.

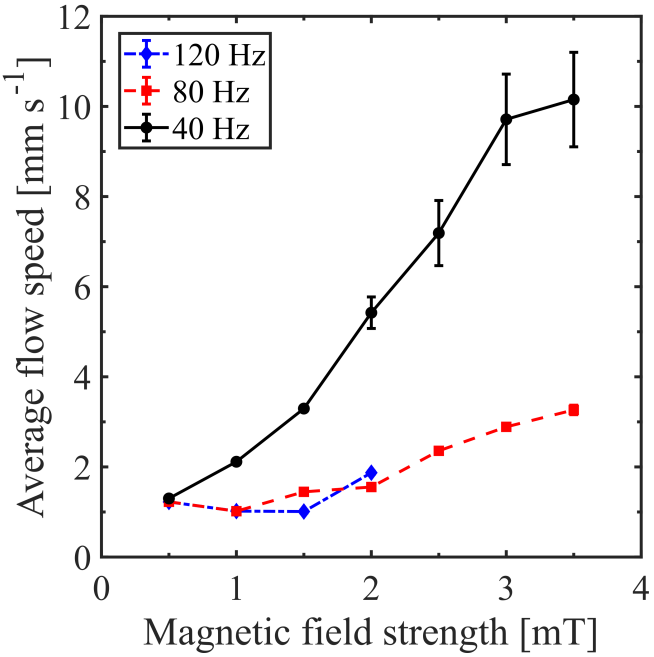

Fig. 5.29 Flow speed as a function of magnetic field strength for 40 Hz (black circles), 80 Hz (red squares) and 120 Hz (blue diamonds), for the disk-based membrane with in-plane and out-of-plane magnetic components.

5.4 Conclusion

A proof of concept was demonstrated for a new class of active microfluidic components and lab-on-a-chip devices of hybrid functionality. The systems were based on the performance of a low Reynolds number swimmer - consisting of a pinned two-ferromagnetic particle swimmer - which, when prevented from translation, is capable of generating flows of different speed, directionality and pattern. These systems could potentially be used as pumps, valves and mixers in microfluidic applications with a number of advantages, particularly for point-of-care technologies where options for flow control are limited due to requirements of portability and low cost. The system lends itself to robust control and can quickly switch between different functionalities (e.g. as a pump, valve, flow splitter or mixer). It is controlled wirelessly through a small number of easily adjustable parameters of the external uniaxial magnetic field, such as frequency and amplitude. The fact that the swimmer is connected by an elastic ring means that it can easily be pinned and prevented from translation without loss of other degrees of freedom necessary for its proper function. This may be difficult to achieve with other swimmers such as the unconnected [130] or helical configurations [18, 131] for which pinning would interfere with the method of propulsion.

Secondly, a torque driven fluid pump system was presented. This system worked on a similar premise to the two-ferromagnetic particle swimmer, by pinning the swimmer in such a way not to affect the beating patterns produced. It was shown that this system was able to induce a stable flow speed over the operating regime of the device. However, the method used to pin the swimmer may be affecting the motion of the swimmer, resulting in the slow flow speed generated compared to the free swimming speeds. It also shown that such systems could be built into the walls of the channel. The induced deflection of the wall based pump was investigated and an estimated bending force was shown to have the similar dependence on the external magnetic field strength as the induced flow speed. A further extension to this work would be to investigate how multiple torque driven pumps would collectively work

together. Such an investigation could shed light on how the separation between the pumps affects the induced flow.

The final section was decided to the investigation of two different magnetically controlled membranes. The first was a 2×2 membrane based on a magnetic flagella-like structure. This macroscopic membrane was attached to the end of a 3D printed channel and submerged in fluid. The dependency of the frequency of the actuating magnetic field on the induce flow speed was investigated. PIV was used to find the flow field velocity out of the channel near the membrane.

The front speed within the channel was also investigated. Both measurements indicate that a flow has been induced due to the active membrane. Further work will have to be to be done on controlling or enhancing the induced flow created by this design.

Using a similar principle, membranes comprising of magnetic disks were fabricated and actuated using an external magnetic field to induce a magnetic torque and in turn a mechanical torsion. Two membranes were investigated: one with all magnetic components magnetised out-of-plane, and the other with a mixture of in and out-of-plane magnetic components in a unit cell. The membranes were actuated using an in-plane uniaxial magnetic field, and the mechanical tilt of the components were investigated, showing excellent agreement with the predicted angles. By manipulating the frequency and amplitude of external magnetic field, the membranes induced a fluid flow. The induced flow was investigated using PIV and a four vortex structure of the flow was shown.

The simple design of these devices is promising for incorporating them into lab-on-a-chip systems. The next step in this work would be to fabricate such structures on a micrometre length scale. One method could be lithographic fabrication for the elastic components and electrodeposition for the magnetic components.

Chapter 6

Collective motion of magnetic systems

This chapter will focus on the collective motion of two different magnetic systems. The first system was based on the rotational collective patterns of an array of ferromagnetic rotors. Under the influence of an external magnetic field, the rotors can create different rotational patterns, analogous to the metachronal wave seen in nature. A metachronal wave is formed from the interaction between neighbouring beating cilia.

The second system will also show a collective motion analogous to a metachronal wave, however, this system comprises of a line of rocking rudders within a channel. The magnetic rudders had different fixed magnetic moments, to induce a phase lag between the rudders.

In recent years, the magnetic colloids have been extensively used in microfluidic devices and applications such as magnetic swimmers [54, 65, 1, 112, 132], magnetic pumps [128, 133, 21, 23], magnetic cilia [91, 134, 135], and particle sorting and segregations [136–139]. When a uniform rotational magnetic field is applied to a ferromagnetic colloidal particle, the colloidal particle experiences torque and rotates together with the field.

Many previous studies achieved their goals of net motion by utilising this rotational motion in investigating ways. For instance, a magnetic colloid rotating close to a wall boundary causes net translational motions [54], and can be delivered to a desired position.

Another example would be a magnetic particle with a helical tail [65] which converts its rotational motion to translational motion with its chiral tail.

The colloid rotation can be used for pumping or mixing fluids but it is not intuitive to achieve net-pumping effect under low Reynolds number regime, because a single rotating unit would just result in a rotlet flow-field, [140], resulting in no net flow.

In previous studies, two approaches have been tested to extract effective pumping from colloid rotation. The first idea is to utilise the wall boundary effect to break the rotational flow symmetry [133, 21, 23]. When a colloid rotates parallel to the wall, the net-pumping effect can be achieved because the flow farther from the wall would be faster than the flow closer to the wall [133].

The second idea is to create an non-reciprocal beating during a rotation cycle [91, 134, 141]. The previously discussed self-assembled magnetic cilia were shown to produce fluid flow, if pathway of effective/recovery strokes are different.

Many of these previous investigations were designed to control a single magnetic unit or to actuate many units in exactly the same manner. For next stage of these magnetic devices, it will be practical if the collective dynamics of the magnetic units could be controlled by only changing the external magnetic field.

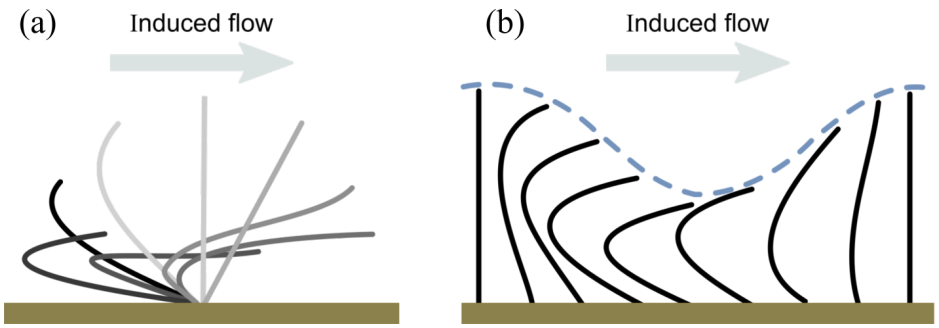

Fig. 6.1 (a) Schematic showing the asymmetric beating pattern of a single cilium. A full cycle is shown from light grey to black. (b) Schematic showing a visualisation of an array of beating cilia producing a metachronal wave.

However, it is not intuitive to achieve different behaviour among the units because all units receive a same signal from outside. It is known that cilia, natural pump, has rich collective dynamics in their beating pattern [142]. Due to the hydrodynamic interactions between the cilia, they beat with a phase lag with their neighbours which is known as the metachronal wave. An example of a single beating cilium and an array of cilia is shown in Figure 6.1. There are only few attempts [134, 135] to control collective dynamics of large number of magnetic units.

6.1 Collective rotational patterns of magnetic rotors

This work was completed in collaboration with Dr. Daiki Matsunaga from the University of Oxford. In this work, the interesting collective rotation/swinging of magnetic rotors that are positioned in a grid structure was investigated. The magnetic rotors are fabricated with 3D printing technology, and the collective motions under actuation of 1D alternating magnetic fields were analysed. By changing parameters, magnetic field strength and grid size, two interesting collective modes of rotors were found: the quarter rotational pattern and stripe swinging pattern. A theoretical model was developed by Dr. Daiki Matsunaga that matched and helped describe the experimental results (shown in Appendix B).

6.1.1 Experimental investigation

The system consisted of $N = N_x N_y$ magnetic rotors with ring geometries (Figure 6.2) positioned in a grid structure, where N_x and N_y is the number of rotors in x- and y-direction respectively. The rotors are fabricated by mixing liquid silicone rubber and NdFeB magnetic powder. The liquid magnetic rubber was then placed in the 3D printed mould and cured at room temperature for 6 hours. The cured magnetic rotors were then placed in a Vibrating Sample Magnetometer (VSM). The VSM ramped the magnetising field up to 1.8 T over 17

minutes to saturate the rotors in-plane along their longer major axis resulting in a magnetic moment $m = 2.2 \times 10^{-4}\text{Am}^2$ at the presence of zero external field. The magnetic hysteresis of a rotor is shown in Figure 6.3. The dimensions of the rotors are shown in Figure 6.2 (inset) and have a depth of 0.9 mm.

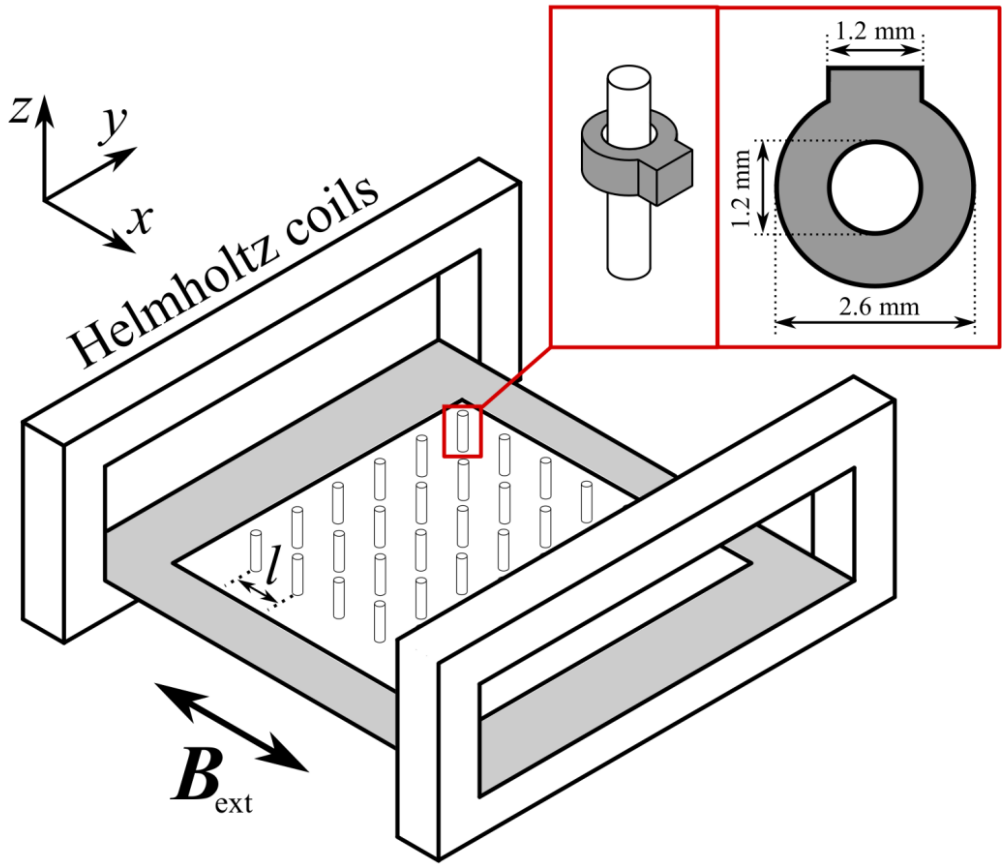

Fig. 6.2 Schematic of the experimental setup, consisting of a Helmholtz coil system, with the 3D printed pin system placed in the centre. The inset shows a rotor placed on a 3D printed pin and its dimensions.

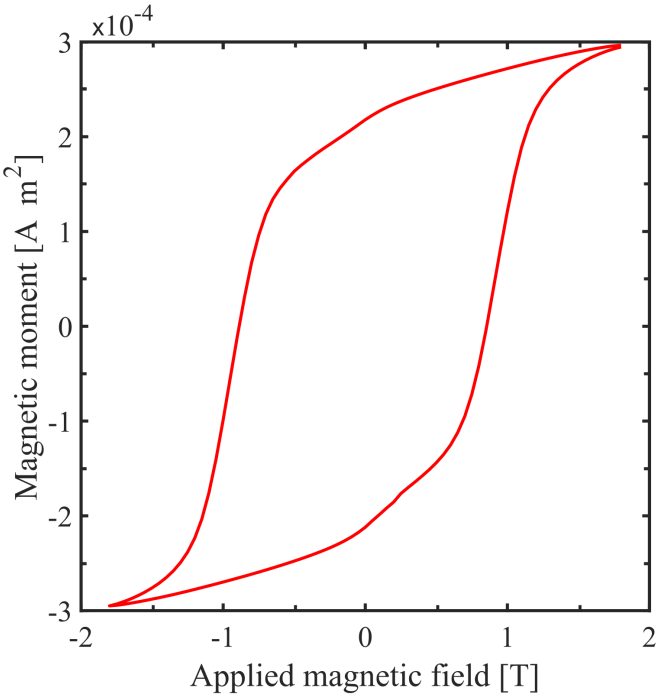

Fig. 6.3 Magnetic hysteresis of a single magnetic rotor used for the collective motion of arrays of identical magnetic structures. At zero external magnetic field the magnetic moment was shown to be $m = 2.2 \times 10^{-4}\mathrm{Am}^2$.

The rotors are placed on the fluid-air interface on 3D printed posts (radius 0.5 mm) separated of a distance l from each other, and glycerol ($> 99.5\%$ pure, viscosity $\eta = 1.4$ Pas) is used as the fluid. The rotors have no translational degree of freedom because of the posts, but can freely rotate under the action of the local magnetic fields.

Similar to previous experiments, a Helmholtz coil system was used to create a uniform magnetic field alternating in x-direction as

$$\boldsymbol{B}_{\mathrm{ext}} = [B\sin(2\pi ft), 0, 0], \tag{6.1}$$

where B is the amplitude and f is the frequency. The coil system is powered by a signal generator and power amplifier to generate the sinusoidal field, and the amplitude and frequency of the field could be manipulated by using the attached computer.

Dimensionless parameters introduced for the rotor system

The rotor behaviour is governed by both magnetic and hydrodynamic interactions with neighbouring rotors. After introducing several simplifications, Dr. Daiki Matsunaga developed a theoretical model that describes the rotational dynamics of the rotors which is discussed later in this section. Based on the model, there are three important dimensionless parameters:

$$\alpha = \frac{Bl^3}{\mu_0 m}, \tag{6.2}$$

$$\beta = \frac{\eta l^3 f}{mB}, \tag{6.3}$$

and the reduced rotor radius $\tilde{a} = a/l$, where a is characteristic size of the rotor.

The parameter α defines the dipole-dipole interaction strength of the rotors compared to the external magnetic field. The second parameter, β defines the relaxation time of the system compared to the external field frequency f. The final parameter is $\tilde{a}$, which defines the contribution of hydrodynamic interactions of rotors compared to magnetic interactions; the hydrodynamic contribution is important for larger $\tilde{a}$.

The hydrodynamic interactions would play an important role if the rotors are close to each other $\tilde{a} \approx 0.5$, because of the lubrication interactions [140]. In the experimental set-up $\tilde{a} = 0.21 - 0.33$ and these interactions would are weak.

Table 6.1 shows the parameters values used in the following experiments. The Reynolds number of this system can be defined as

$$\mathrm{Re} = \frac{a^2 \rho f}{\eta} \approx 10^{-3}, \tag{6.4}$$

and the inertial effect would be negligible due to the small Reynolds number $\mathrm{Re} \ll 1$.

Parameter	Experimental value
characteristic size (radius) of rotors	$a = 1.3$ mm
grid size	$l_1 = 6.3$, $l_2 = 4.0$ mm
magnetic moment of rotors	$m = 2.2 \times 10^{-4}$ Am^2
external magnetic field strength	$B_1 = 6.0$, $B_2 = 1.5$ mT
external magnetic field frequency	$f = 1.0$ Hz
fluid viscosity	$\eta = 1.4$ Pa s
fluid density	$\rho = 1.3 \times 10^3$ kgm^{-3}
Reynolds number	$\mathrm{Re} = 1.57 \times 10^{-3}$
α	$\alpha_1 = 6.0$, $\alpha_2 = 0.4$
β	$\beta_1 = 0.3$, $\beta_2 = 0.3$
$\tilde{a}$	$\tilde{a}_1 = 0.21$, $\tilde{a}_2 = 0.33$

Table 6.1 Experimental values used for the rotor system, as well as the Reynolds number and dimensionless parameters.

Base state conditions under a static magnetic field

Finally, the rotor orientational pattern under static or no magnetic fields conditions is briefly described. For all sets of parameters, the experimental findings and the model are shown.

Figure 6.4a shows a pattern under no magnetic field $B = 0$ ($\alpha = 0$) resulting in the spin ice structure [143, 144] since the rotors try to maximise their angle difference from their neighbour. The pattern is also known as a “two-in, two-out" structure since two arrows face inside while the other two face outside at each grid.

At the other extreme $\alpha \gg 1$, all rotors follow the external magnetic field direction as shown in Figure 6.4c, due to their dipolar interactions being negligible in this condition.

At an intermediate value of $\alpha \approx 1$ ($\alpha = 0.2$ is shown here) shown in Figure 6.4b, there is a small local alignment resulting in a tilting at the corners and edges: the rotors placed left-bottom or right-top show slight tilting towards $+y$, while those in other two corners show tilting towards $-y$.

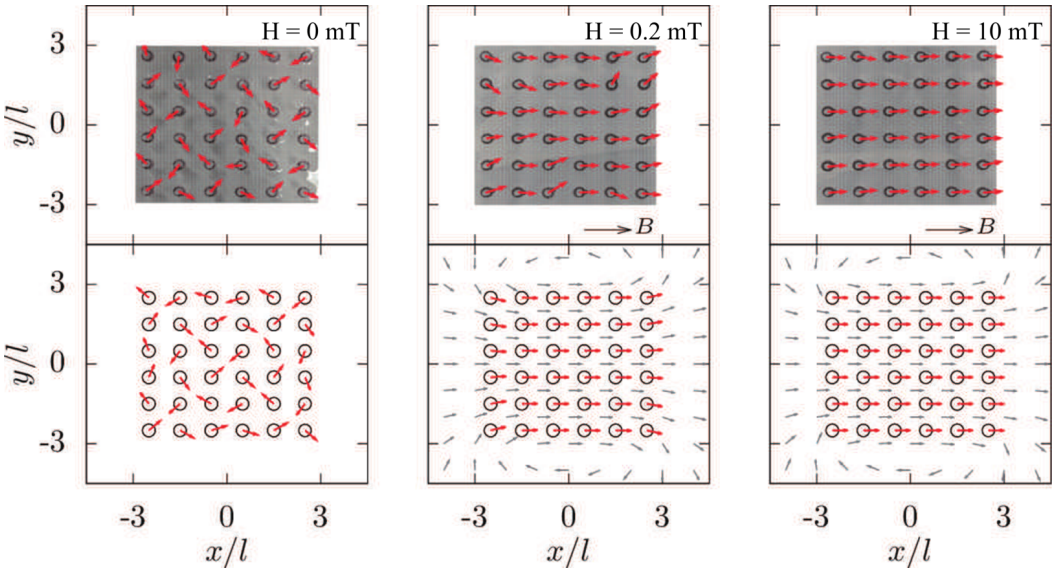

Fig. 6.4 Snapshots of orientational configuration under a static field with (a) $\alpha = 0.0$, (b) 0.2 and (c) 10.0. The external magnetic field is imposed to right. Top row shows results from the experiment while bottom shows the simulation. Red arrows describe the magnetic moment direction of each rotor, in both the model and experiment.

The behaviour of a single rotor

For easy understanding of the system, firstly the simplest rotor behaviour was described: a single rotor under the alternating field. Experiencing the torque exerted from the uniaxial external field, the rotor would swing continuously back-and-forth with a frequency f. The swinging direction would purely depend on the initial angle, and they show upper-swing if the initial $\mathbf{m}$ orientation is pointing $+y$-half while they will show lower-swing for other half. Since the system satisfies small inertia condition $\mathrm{Re} \ll 1$, the rotor would not overshoot during the swinging behaviour and they tend to stay at one side. Therefore, they will never show full-rotation under alternating field at any given parameters α and β.

The collective motions of the rotor arrays under external magnetic field is descried below. Changing the parameters, two different collective modes in this system were found: quarter rotational pattern and stripe swing pattern.

Rotational patterns

As shown in Appendix B, a full phase diagram from the theoretical model for the comprehensive understanding of the system was created. Figure 6.5 shows the phase diagram of the collective rotational patterns. Figure 6.5 shows the rotors form the quarter rotational pattern

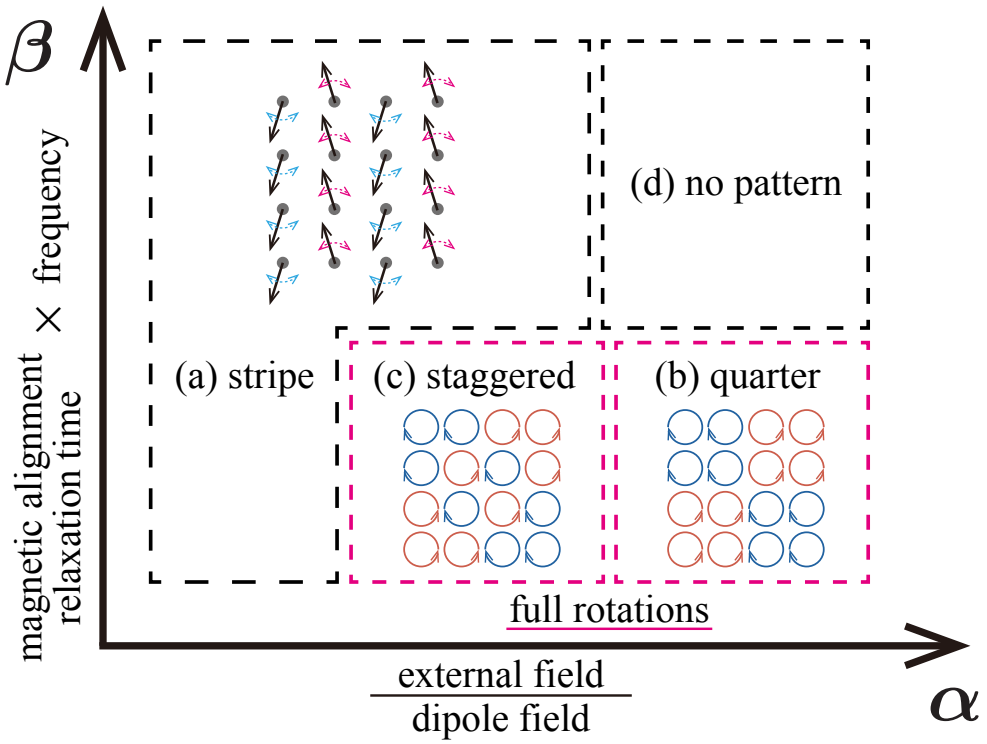

Fig. 6.5 Phase diagram from the simulation in $N_x = N_y = 4$ array. Showing the resulting rotational patterns for different combinations of α and β. Showing 4 regions of interest: (a) the stripe swinging pattern, (b) the quarter rotational pattern, (c) the staggered pattern, and (d) where no pattern is observed.

for large α while they form the stripe swinging pattern for smaller α. In a range between these two states, another interesting set of rotational pattern was observed, which is named “staggered patterns". There are also regions where for given combinations of alpha and beta in which no patterns are observed. The following section show the experimental verification of the existence of the quarter rotational and stripe swinging patterns.

Quarter rotational pattern

Figure 6.6 shows a schematic diagram of the rotational pattern under the one dimensional alternating magnetic field with $\alpha_1 = 6.0$ and $\beta_1 = 0.3$. Interestingly, the rotors have their own preference in the rotating direction depending on the rotor position the rotors located top left and bottom right quarters rotate clockwise, while they rotate anticlockwise for the other two corners. The rotor movements are visualised in Figure 6.6, and there is a clear contrast from a single rotor motion because the rotors are showing full rotation during the cycle.

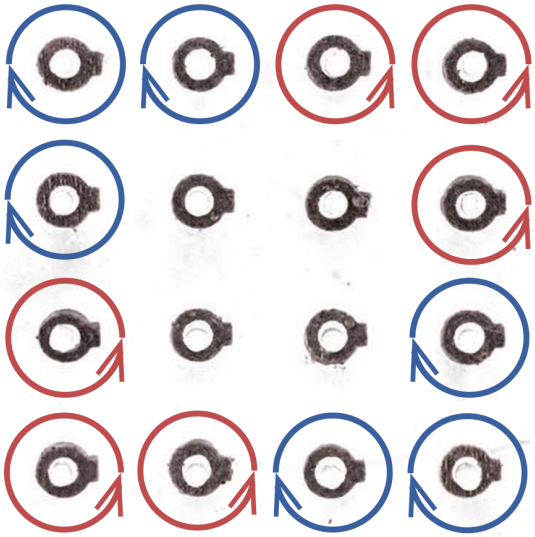

Fig. 6.6 Schematic showing the rotational pattern in the presence of an external magnetic field with $\alpha_1 = 6.0$ and $\beta_1 = 0.3$. The rotors are shown in a 4×4 grid, with the blue arrows showing clockwise rotation and the red arrows showing anticlockwise rotation.

In order to characterise the rotational pattern, the number of rotations during x-directional flipping was counted, and the following parameter was introduced

$$R = \frac{n_+ - n_-}{n_+ + n_-}, \tag{6.5}$$

where n_+ and n_- are number of rotation in $+z$ (anticlockwise) and $-z$ (clockwise) respectively.

Figure 6.7 shows the parameter R for each rotor. Rotors at the corners almost always rotate in the same direction. The rotor motions did not result in a reciprocal motion [4] because the dipolar interactions between rotors break the time reversibility of the system. At the same time, the four central rotors do not have a preferred direction and they typically swing during a cycle.

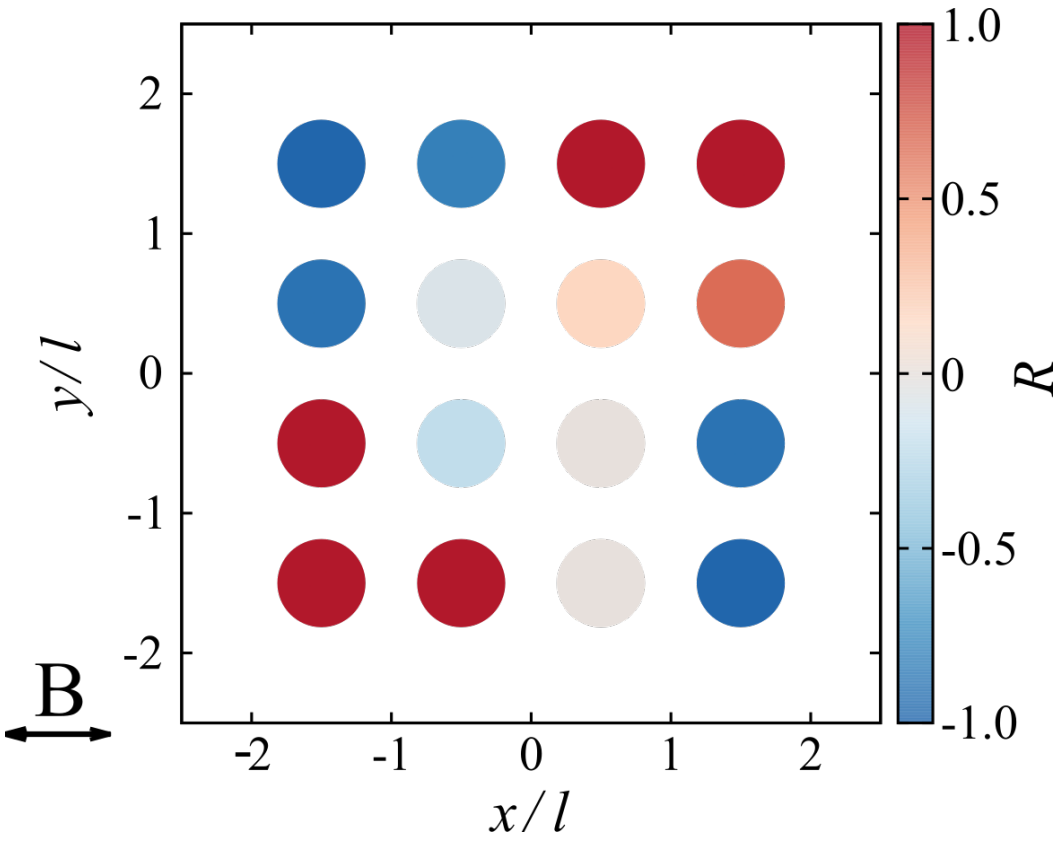

Fig. 6.7 The rotational parameter R of each rotor for a 4×4 rotor array. The circles depict a single rotor, with blue meaning clockwise and red meaning anticlockwise rotation. The observation was based on 25 cycles.

The rotational preference appeared because of the non-uniformity of the magnetic interactions, which is based on the finite system size. For simplicity, consider the situation of flipping the magnetic field suddenly from $+x$ to $-x$ in Figure 6.4b. Before flipping the field, all rotors more or less point $+x$ direction but with a slight tilting due to the local dipolar interactions.

As previously shown, when discussing the base conditions of the rotors, the rotors placed left-bottom or right-top of the system show slight tilting towards $+y$, while those in other two corners show tilting towards $-y$. If the external magnetic field direction switches to $-x$ suddenly, this spatial dependent tilting gives rise to the rotation preference: rotors at left-bottom and right-top corner prefer to rotate anticlockwise because this direction is closer to $-x$ direction (it will be the opposite for other two corners). After giving sufficient time for the system to relax, same preference in the rotation would happen in a flip back ($-x$ to $+x$) because it is purely symmetric from the first flip.

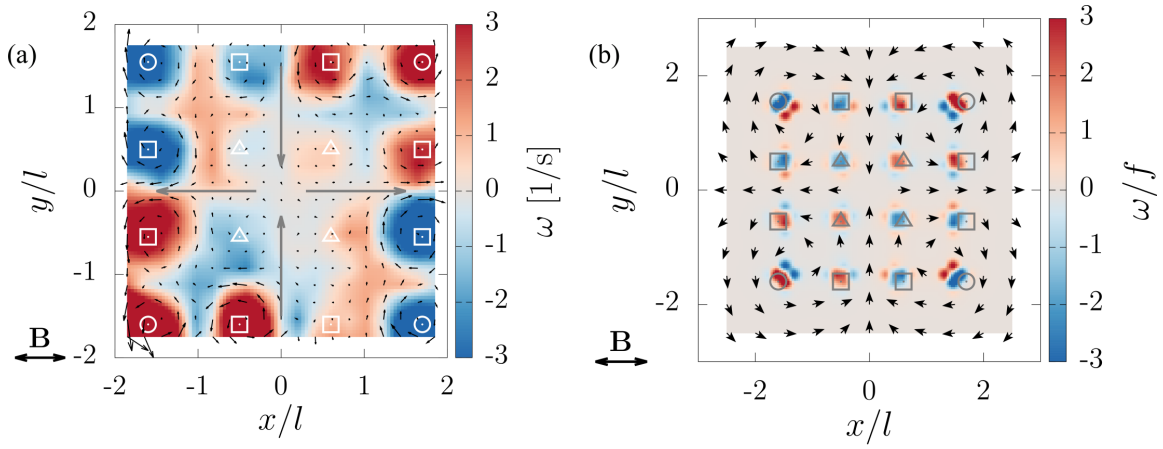

Fig. 6.8 Time-averaged flow field generated by the rotors in (a) experiment ($\alpha_1 = 6.0$ and $\beta_1 = 0.3$) and (b) simulation ($\alpha = 6.0$ and $\beta = 0.03$). The contour shows the vorticity ω strength, the black arrows visualise the local flow field and the large grey arrows show net flow field created by the system. Symbols indicate the rotor position: corners - circles, edges - squares, and centre - triangles.

This is the basic mechanism of the quarter rotational pattern, and this phenomenon stands for small β because the system needs time to catch up to the external field. The collective motion is interesting because rotors behave differently and have their own rotational direction, even though they are identical with one another.

This collective rotational pattern can be used to mix or pump fluid as shown in Figure 6.8a. Due to the quarter rotational pattern, the rotors system pull the fluid into the centre from y-direction and push it out in the x-direction. In other words, the system created dipolar flow field, which can be also seen in a flow generated by stresslets [140].

The dipolar flow field is also seen in our theoretical model presented in Figure 6.8b. The average flow speed through the system was found to be 0.63 ± 0.25 mms^{-1}. This approach of creating dipolar flow field is practical, because the flow field direction can be easily switched by the external magnetic field: the system would pull the fluid into itself from a direction parallel to the external field and push the fluid toward a perpendicular direction.

To investigate the rotational phase of the rotors, the rotors are classified into three categories depending on the position as shown in Figure 6.8a and Figure 6.8b with different symbols. Figure 6.9 shows the time history of vorticity strength $|\omega| = |\nabla \times \mathbf{u}|$ for the three categories and indicates that the corner rotors start to rotate first and the phase propagates towards the centre of the system.

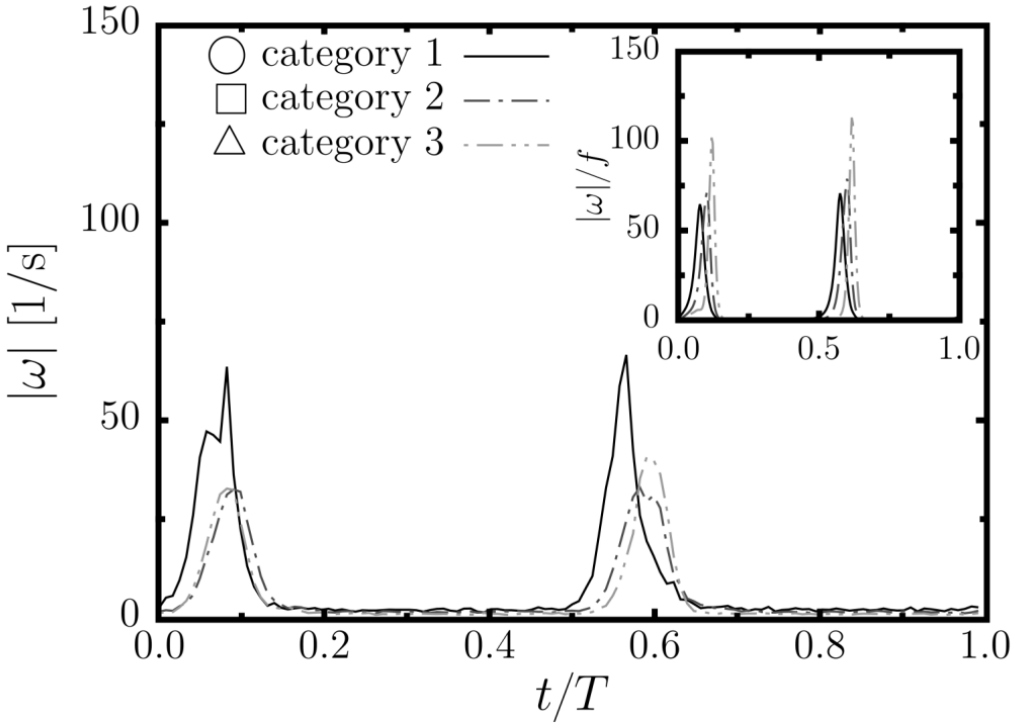

Fig. 6.9 Time history of the vortex strength $|\omega|$ for three categories of rotors, in experiment and simulation (inset). Note $T = 1/f$ is the period.

This phase propagation is also clearly shown in the theoretical model (inset). The phase lag is again due to the finite system size effect. The corner rotors start to rotate first because they have the maximum tilting angle from the external magnetic field as shown in Figure 6.4b, and this variety in the tilting angles gives rise to the phase lag.

An analogy can be drawn between the phase lag observed here and the metachronal wave beating [142]. Previous studies achieved metachronal waves by designing the magnetic units different from one another. This was achieved by different size gradient of the magnetic units [135] or patterning the magnetisation direction differently [145]. The phase lag in this system is different from the previous systems because all the units are identical, and the current method is a new approach of creating phase lag based on the finite system size effect. One of its advantages is production simplicity, since all magnetic elements are the same.

Stripe swinging pattern

If the strength of the external magnetic field B is decreased, which corresponds to decreasing α, the dipolar interactions between the rotors will be dominant. Figure 6.10 shows snapshot of this rotational pattern, and the rotors show back-and-forth swinging instead of full-rotation. This pattern was given the name stripe swinging pattern because the rotors form the y-directional stripe upper-swing (red arrows) and lower-swing (blue arrows). This pattern is clearly different from a single rotor swinging, because the upper-swing/lower-swing is not determined by the initial angle and it is established by the interactions with the neighbours.

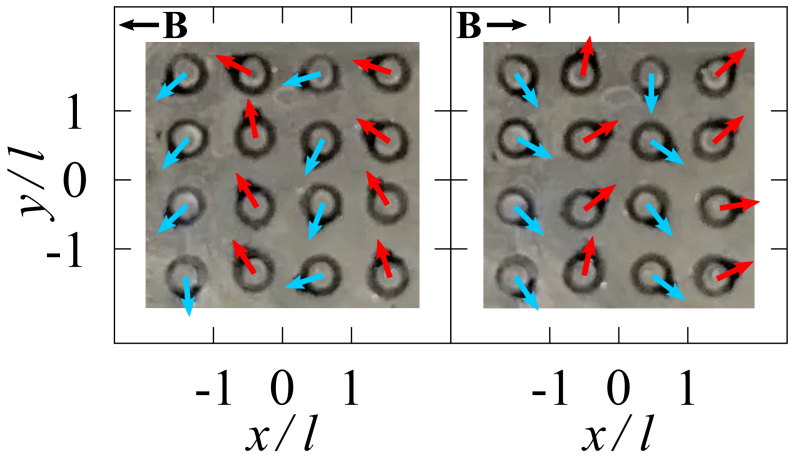

Fig. 6.10 Experimental observation of the stripe swinging pattern for a 4x4 rotor array under $\alpha_2 = 0.4$ and $\beta_2 = 0.3$. The arrows depict the direction of the magnetic moments and the two frames show the moment when the external magnetic field reached $-B$ (left) and $+B$ (right), respectively.

The dynamics can be understood by regarding the pattern as adding small perturbation to the spin ice structure, Figure 6.4a. The spin ice structure intrinsically has the stripe character: in Figure 6.4a, odd-columns from the left are pointing up while even-columns are pointing down. If a small external magnetic field (1.5 mT) is applied, the rotors would form a stripe pattern and swing together back-and-forth. By changing the two parameters α and β in the experiment two different collective patterns develop.

6.2 Magnetically actuated rudders

This section will focus on another collective motion system. However, in this case, the magnetic components are placed within a channel. The magnetic components had a depth similar to the height of that channel. The section is focused on investigating how the magnetisation of the components can affect the collective motion.

6.2.1 Experimental investigation

The main idea of this work was to create a low Reynolds number system similar to that presented with the rotor array, but within a channel. The structures investigated either comprised of a pair of rudders or three rudders in a row. The main parameters investigated were how the magnetisation direction of each rudder affects the induced flow, and also how the separation affects the flow.

The rudders were fabricated using a 3D printed mould. The geometry of the rudder was similar to the rotors previously presented. However, the rudders were symmetric and had a depth of 4 mm. Figure 6.11 shows a schematic diagram and photograph of a rudder. The rudders were made from a mixture of silicone rubber and NdFeB powder. The cured magnetic rudders were then placed in a Vibrating Sample Magnetometer (VSM). The VSM ramped the magnetising field up to 1.8 T over 17 minutes to saturate the rudders.

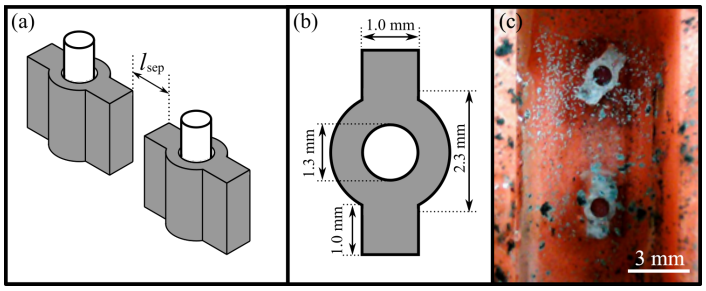

Fig. 6.11 Schematic diagrams and photograph of the magnetically controlled rudders. (a) Schematic showing a pair of rudders pinned on posts with separation l_{sep}. (b) Schematic showing the dimensions of a rudder with depth 4 mm. (c) Photograph of a pair of magnetic rudders, pinned in the bulk of a fluid within a 10 mm channel, tracer particles are placed on the surface.

The magnetisation of the rudders in a pair was different. Taking the in-plane magnetisation of the main axis as 0°, rudders were magnetised with the orientations, θ_{mag}; 0°, 30°, 60°, and 90°. Figure 6.12 shows the different configurations of magnetisation orientation. The difference in magnetisation was introduced to create a phase lag between the rotation of the rudders in a pair. This phase lag was to be an analogue to the metachronal wave of beating cilia.

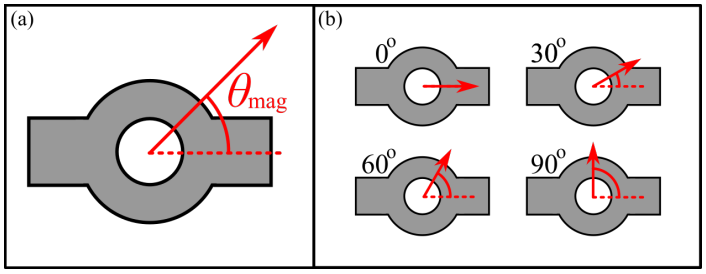

Fig. 6.12 Schematic diagrams showing the magnetisation direction (θ_{mag}) of the magnetically controlled rudders. (a) Shows the angle θ_{mag}. (b) Shows the magnetisation for different rudders: θ_{mag} = 0°, 30°, 60°, and 90°.

The initial investigation involved pinning a pair of rudders at different separations to observe how this affected the induced fluid flow. The separation of the rudders, l_{sep}, ranged from 1 mm to 8 mm. The pairs of rudders investigated were: 0° and 0° (the control), 0° and 30°, and 0° and 60°. The legend on Figure 6.13 helps visualise the rudder pairs. In the case

of the control system, assuming there was no magnetic interaction between the rudders, no net flow would be expected.

The rudders were placed in the bulk of the fluid, however the tracer particles were placed on the surface and tracking using PIV. Once again, the fluid used for the investigation was 99.9% pure glycerol. The magnitude and direction of the induced flow were measured, away from the rudders so the net flow could be observed. The external magnetic field applied had a frequency of 1 Hz, and a strength of 6.0 mT. These magnetic field parameters were selected as in the case of the rotor array, for a full rotation of $\sim 180°$.

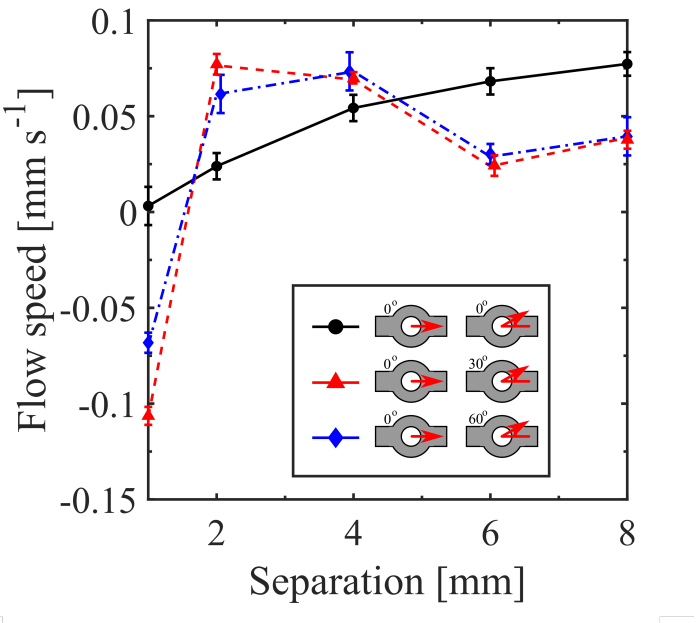

Fig. 6.13 Flow induced by a pair of magnetically actuated rudders, as a function of separation. (a) Induced flow as a function of separation for different magnetic phase: black circles - 0° and 0°, red triangles - 0° and 30°, blue diamonds - 0° and 60°. (b) Shows the maximum flow speed for each separation. The external magnetic field had strength 6.0 mT and frequency 1 Hz. The legend describes the magnetisation of the pairs.

Figure 6.13 shows the induced flow for all systems. The control system (black circles) in fact shows an induced flow. This could be due to the fact that there is a dipolar interaction between the rudders, resulting in a non-reciprocal motion. Thus, the flows generated would be more complex than two rudders beating in phase.

An interesting observation to make is that the flow switches direction. When the separation is 1 mm for all cases - apart from the control - the flow direction is defined as negative. As the separation is increased, typically for each case, the flow direction switches. This effect may be due to the magnetic interaction between the rudders at low separation. However, this is an interesting effect and shows that the flow direction can be controlled by only altering the separation.

The pairs consisting of 0° and 30° (red triangles) and 0° and 60° (blue diamonds), both show similar tends and flow speeds. In both cases, as the separation is increased the flow direction switches, followed by the induced flow slowly decreasing to about zero. This reduction in flow speed is to be expected as the separation is increased, the rudders more like single rocking paddles confined by a reciprocal motion.

To further investigate the rudder system, additional pairs were created. To increase the torque experienced by the rudders, the rudder in a pair which was previously 0° was replaced with a 90° magnetised rudder. In this orientation, the rudders will beat perpendicular to the applied field and channel. The pairs of rudders investigated were: 90° and 0°, 90° and 30°, and 90° and 60°.

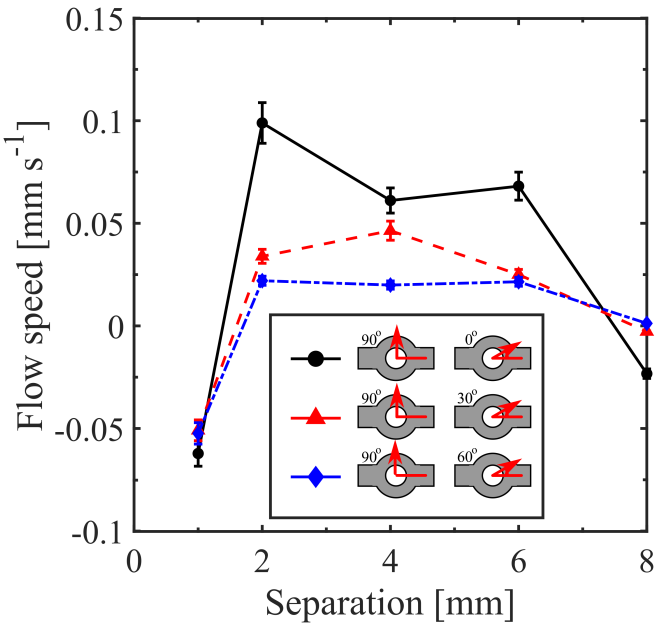

Fig. 6.14 Flow induced by a pair of magnetically actuated rudders, as a function of separation. (a) Induced flow as a function of separation for different magnetic phase: black circles - 90° and 0°, red triangles - 90° and 30°, blue diamonds - 90° and 60°. (b) Shows the maximum flow speed for each separation. The external magnetic field had strength 6.0 mT and frequency 1 Hz. The legend describes the magnetisation of the pairs.

Figure 6.14 shows the induced flow speeds of these pairs of rudders. Similar to the previously shown data, the pairs with the 30° (red triangles) and 60° (blue diamonds) rudders show similar flow speeds and tends. The overall flow speeds in this investigation are lower when compared to that shown in Figure 6.13. However, in Figure 6.14, a third new pair of rudders are shown. This pair consists of 90° and 0° magnetised rudders. This pair (shown as black circles) produced the highest peak value of flow speed (~ 0.1 mm s^{-1}).

The final stage of this investigation involved creating a new rudder system, comprising of three different magnetised rudders. Using the information gather from Figure 6.13, the magnetic phase between the rudders was: 0°, 30°, and 60°. These values were selected due to the tends and flow speeds of two rudder pairs being similar. Figure 6.15 shows the flow

speed dependence of this rudder system. The external magnetic field used was the same as for the previous rudder pairs: strength 6.0 mT and 1 Hz frequency.

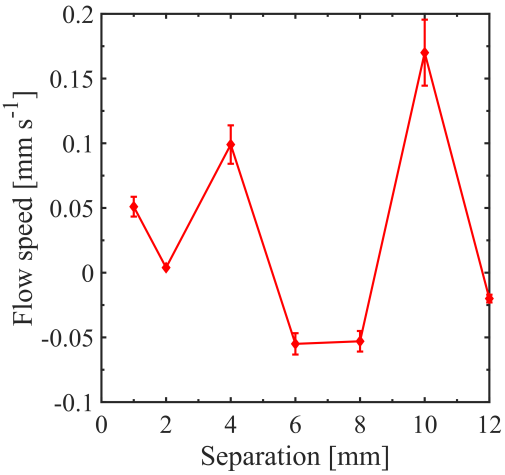

Fig. 6.15 Flow induced by a system of three magnetically actuated rudders, as a function of separation. The magnetic phase between the rudders shown was 0°, 30°, and 60°. The external magnetic field had strength 6.0 mT and frequency 1 Hz.

The maximum flow speed observed with this system was 0.17 ± 0.03 mm s^{-1}, which is comparable to the maximum of the rudder pair system. However, typically the induced flow speeds were lower than that of the rudder pair system. This could be due to the magnetic interactions between the rudders resulting in a negative impact on the induced flow. The flow switched directions multiple times as the separation was increased. The investigation suggests that the three rudder system was not as stable as the rudder pair. A way to improve the system for use in a real microfluidic chip could be to have multiple pairs of rudders. These pairs could be separated from other pairs by a much larger distance to reduce the magnetic interaction between pairs.

6.3 Conclusion

This chapter focused on the presentation of the collective motion of two different magnetic systems. The first system was based on the rotational collective patterns of an array of

ferromagnetic rotors. When arranged in a grid structure and under the influence of an external magnetic field, interesting collective motion was observed. A simple model produced by Dr. Daiki Matsunaga was also presented, to help understand the interactions present in the experiment.

The magnetic rotors are fabricated with 3D printing technology, and the motion of the rotor array was analysed, as well as the fluid flow induced under actuation of 1D alternating magnetic fields. By changing parameters, magnetic field strength and grid size, two interesting collective modes of rotors were found: the quarter rotational pattern and the stripe swinging pattern. In the quarter rotational pattern, rotors at each quarter of the system showed spatial dependent continuous rotation: two corners show clockwise rotation while the other two show anticlockwise rotation. Due to the rotational pattern, the system creates dipolar flow field with a metachronal wave like phase lag of rotations.

When the magnetic dipolar interaction is significant compared to the external field, the rotors showed the stripe swinging pattern. Changing the effectiveness of the dipole-dipole interaction, the system revealed that variety of collective modes can be extracted from a group of magnetic units. The collective modes presented in this work are interesting because rotors behave differently even though they are identical to each other.

The second system shown was a collective motion analogous to a metachronal wave. This system comprised of a line of rocking rudders within a channel. The magnetic rudders had different fixed magnetic moments, to induce a phase lag between the rudders. The dependence of the induced flow on the separation between the pair was investigated - for different pairs of magnetic phases. The most investigating/stable system was the 0°-30° pair. This system produced a maximum flow speed of 0.15 ± 0.04 mm s^{-1}.

Both presented systems can be discussed as an analogy to the metachronal wave observed in nature by beating cilia. Such systems could be used as a controllable microfluidic pumping system, placed in the centre of a junction. Using magnetic components, it was shown

that the phase lag can be controlled to a high degree. Future studies investigations could include creating an all-on-one microfluidic chip containing the microfluidic channels and the magnetic components.

Chapter 7

Future investigations

This chapter will focus on possible future investigations related to the presented work. One possibility discussed in this chapter is the interesting collective swimming patterns of the two-ferromagnetic particle swimmer. Other investigations involve using the two-ferromagnetic particle swimmer for different fluidic applications. One application would be using the two-ferromagnetic particle swimmer to evaluate viscoelastic properties of insoluble monolayers spread on aqueous surfaces. This could be a plausible application due to the changes in the effective viscosity as the packing order of the monolayer increases. Another possible application would be using the closed circuit pump systems as a cell growth environment. The current method of controlled cell growth can be very wasteful in term of nutrients needed for cell growth. The two-ferromagnetic particle pump system could be used to cycle nutrients around a closed circuit microchannel. A similar approach could also be used for mixing blood samples and/or separating red blood cells from the blood plasma.

The final proposed future investigation is focused on the creation of a novel elastic-ferromagnetic membrane. The idea would be to create membranes using the methods of fabrication presented in Chapter 6. In this case, there would be a high control over the magnetic structure of a ribbon-like structure to create efficient microfluidic pump components.

Some preliminary work on these ideas is presented in the following sections to demonstrate the plausibility of the approach.

7.1 Collective swimming behaviour of two-ferromagnetic particle swimmers

This section will focus on the possible investigation involving the interesting swimming behaviour of multiple two-ferromagnetic particle swimmers. Cohort behaviour of swimmers is an interesting topic and has been shown to have beneficial effects on the swimming performance - for example increased swimming speeds [111, 146]. These effects have been found in nature [147–149].

As a proof of concept, Polydimethylsiloxane (PDMS) two-ferromagnetic particle swimmers with the same size and geometry as the previously presented were created.

Fig. 7.1 Sequence of images showing the motion of two PDMS two-ferromagnetic particle swimmers (3.6 mm). The coloured rings are overlaid to distinguish between the two swimmers. The magnetic field applied has a strength of 2.5 mT and frequency of 90 Hz.

When the external magnetic field was applied the behaviour of the swimming is altered compared to a single two-ferromagnetic particle swimmer. Figure 7.1 visualises the motion with a sequence of images. The two-ferromagnetic particle swimmers rotate around each other in the x-y plane, resulting in a net translational motion. The interesting observation of this interaction is that the swimmers are aligned antiparallel with respect to the magnetic particles. This can be observed in the inset of Figure 7.2a. The trajectory of the two swimmers is visualised in Figure 7.2a. It can be seen that initially the swimmers only rotate around each other with a minimal net motion. After a number of cycles, the swimmers establish a

direction of propulsion. Figure 7.2b shows the theoretical trajectories of two-ferromagnetic particle swimmers [111]. Although slightly different, these theoretical trajectories show the interactions affect the trajectories and produce a braiding motion. This behaviour has also previously been predicted by A. Cēbers and M. Ozols [146].

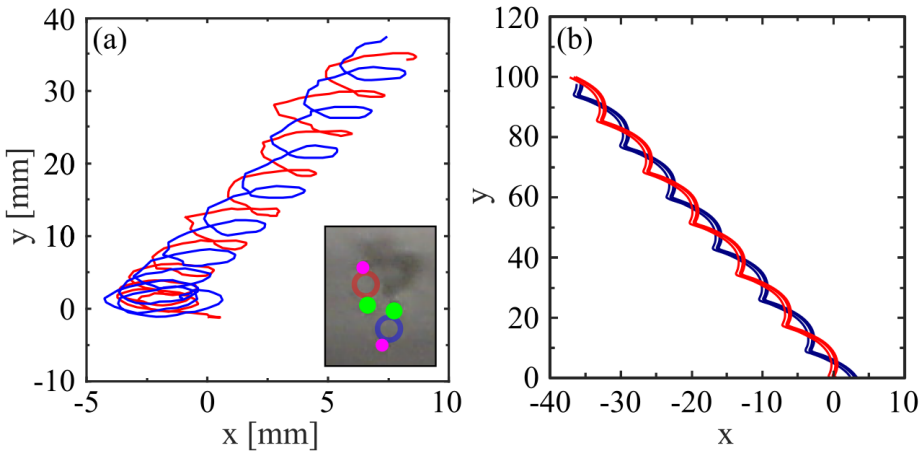

Fig. 7.2 Trajectories of two swimmers in the presence of an external magnetic field. (a) The experimental trajectories when a 2.5 mT and 90 Hz external magnetic field is applied. (b) The theoretical trajectories adapted [111]. The lines depict the evolution of the centre of the link with time. The inset shows the configuration of the two-ferromagnetic particle swimmers. The pink circle indicates a hard ferromagnetic particle and the green circle indicates a soft ferromagnetic particle.

Figure 7.3 compares the swimming speed of a two swimmer system with a single two-ferromagnetic particle swimmers (made from PDMS). It was observed that there was an increase in swimming speed with the two-ferromagnetic particle swimmers due to their interaction. These initial findings indicate that the magnetic and hydrodynamic interactions between multiple swimmers could be beneficial to the swimming capabilities of the two-ferromagnetic particle swimmers.

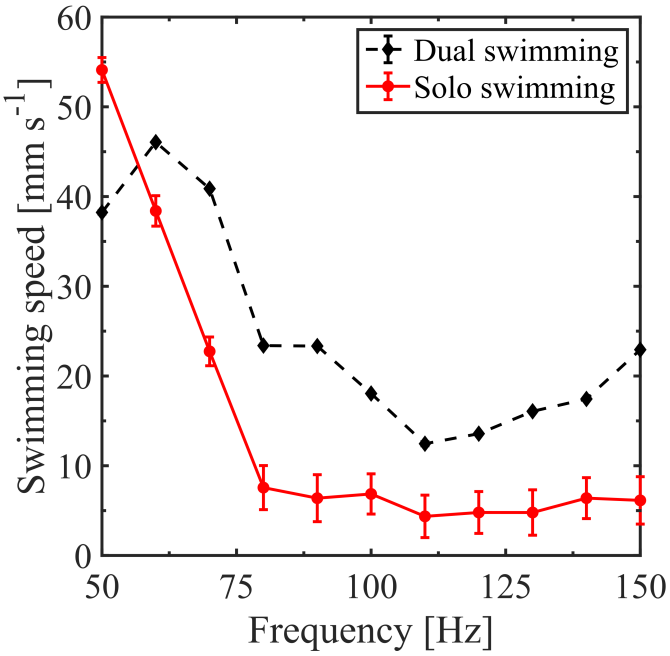

Fig. 7.3 Variation of swimming speed of cohort swimming of two-ferromagnetic particle swimmers with frequency. In the presence of a 2.5 mT external magnetic field.

7.2 Viscoelastic properties of Langmuir monolayers

Lipid molecules are insoluble in water, due to their amphiphilic nature. At an interface, they form monomolecular films that reduce the surface tension [150, 151]. The properties of these lipid monolayers vary with the surface density [152]. For example, a dilute monolayer, can be well described by a two-dimensional gas. As the area per molecule is decreased -

increasing the surface pressure - the monolayer transitions into a new phase, traditionally called the liquid expanded phase. Further compression of the monolayer gives rise to a transition from liquid expanded to a condensed phase. A diagram illustrating the phases is shown in Figure 7.4. Slight differences in the molecular lattice are often accompanied by significant changes in the surface viscosity and elasticity. Thus, the surface viscoelastic properties of lipid monolayers have been an area of active research [153, 154].

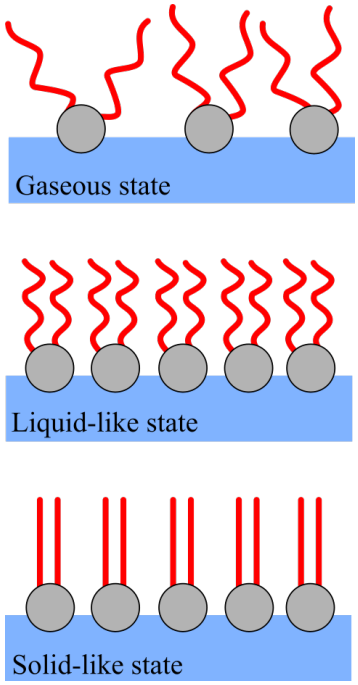

Fig. 7.4 Diagram to visualise the phase changes - gaseous, liquid-like and solid-like states - of a typical lipid monolayer.

The idea is to use a two-ferromagnetic particle swimmer as a reporter of the monolayer viscosity, since the swimmer's propulsion speed depends on the fluid viscosity ($u \propto \omega^{-0.6}\nu^{-1}$). This would result in a less invasive method compared to current techniques to monitor monolayer viscosity, for example torsion pendulums and channel viscometers [155–157]. The method consists on placing a two-ferromagnetic particle swimmer on the surface on the lipid monolayer at a given area per molecule. When the external magnetic field is applied, the two-ferromagnetic particle swimmer will propel with a speed dependent on viscosity.

From the previously presented work on the two-ferromagnetic particle swimmers, it is known that the speed dependency on the viscosity is $\frac{1}{\nu}$. Using the speed of the swimmer in water, one can deduce an effective viscosity for the monolayer. The following preliminary work was to demonstrate if this measurement is sensitive enough to distinguish between different phases of the lipid monolayer.

In collaboration with Dr Bob-Dan Lechner, Dipalmitoylphosphatidylcholine (DPPC) was spread on a water surface to form a monolayer. Figure 7.5 (solid line) shows the pressure-area isotherm for the lipid monolayer recorder using a Langmuir trough. In a separate set of experiments, a smaller Petri dish was mounted between two Helmholtz coils (since the Langmuir trough had a prohibitive large size). It was used to form a monolayer at a particular area per molecule, and a two-ferromagnetic particle swimmer was placed on the water-air interface. The speed of the swimmer was recorded at three different frequencies of the external oscillating magnetic field (70 Hz, 100 Hz and 130 Hz) and an amplitude of 1.5 mT. This measurement was repeated for six different surface concentrations (hence pressures) of lipid, as well as a control measurement with water. The recorded speeds were then used to calculate an effective viscosity using previous dependence and the control (please note that this is not the surface viscosity of the monolayer, but rather an effective quantity equivalent to a bulk viscosity of a fluid in which a submerged swimmer would propel with a given speed). The results are presented in Figure 7.5 (symbols). It is clear from the figure that the effective viscosity closely mirrors the phase behaviour of the lipid monolayer. There is a systematic shift along the area axis of approximately 17 Angstrom^2/molecule. This is due to the fact that the surface concentration of lipid in the Petri dish was changed by adding small amounts of lipid and hence difficult to control (compared to the precise measurements in the Teflon-made Langmuir trough, in which exact areas per molecule are achieved by monolayer compression or expansion).

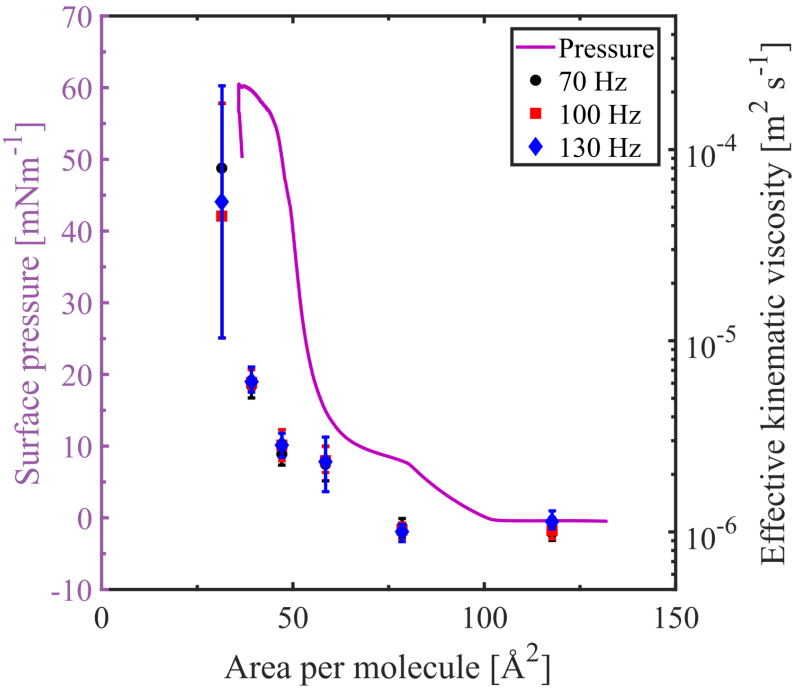

Fig. 7.5 Surface pressure of DPPC lipid monolayer as a function of area per molecule, in comparison with the effective kinematic viscosity, measured using a two-ferromagnetic particle swimmer.

These initial experiments clearly show that the trends are comparable and this gives confidence that this method could be used for to quantify the viscous properties of monolayers. Further work will need to be conducted to better validate this methodology.

7.3 Controlling cell growth within microchannels

This section will focus on another possible application by using the closed circuit pump systems as a cell growth environment. In order to systematically study cells under well-understood environments, a process of cell growth under controlled conditions was developed. This progress is known as cell culture. Many types of cell trapping have been proposed so that the controlled growth can be conducted. Some examples of trapping methods are: laser trapping, chemical trapping, acoustic trapping, magnetic trapping [158]. A popular method

is known as hydrodynamic trapping and involves using microfluidic channels to trap the cells [159].

One of the most commonly used methods involves trapping cells in a 20 µm × 200 µm lateral channels off of a master channel (with an inlet and outlet at each end), and flowing nutrients through the channel [160, 161]. The current method of controlled cell growth can be very wasteful in term of the nutrients needed for the growth. The nutrients in this case are not cycled around the loop-shaped channel, but new nutrients are continually pumped through an inlet and passed through an outlet.

The two-ferromagnetic particle pump system could be used as a method of cycling the nutrients around a closed circuit microchannel. The motivation of this investigation is to create a new microfluidic channel in which a standard 20 µm × 200 µm loop channel (with lateral channels for cell trapping) was attached in a closed circuit to a well with a pump based on a two-ferromagnetic particle swimmer.

A UV mask of a 20 µm × 200 µm channel is typically used to create an epoxy-based negative photoresist (SU-8) mould containing multiple channels. PDMS is poured over the mould to create the channel. The channel would then be cured in an oven for 30 minutes at 100°.

Attempts have been made to produce a prototype of the proposed system. To create the component to hold the swimmer, 3D printed sections were created (Figure 7.6). These sections comprised of a well of diameter 5 mm and depth 1 mm, with two arms to connect to the microchannel with cross-section 1 mm × 0.5 mm. Once printed these components were glued to the epoxy-based mould, to complete the closed circuit channel (Figure 7.7). PDMS was poured over the mould and cured. Once cured, the final channel and a glass microscope slide were oxygen etched, to alter the wettability of the PDMS. A two-ferromagnetic particle swimmer was placed inside the macro-scaled well and when the PDMS channel and glass

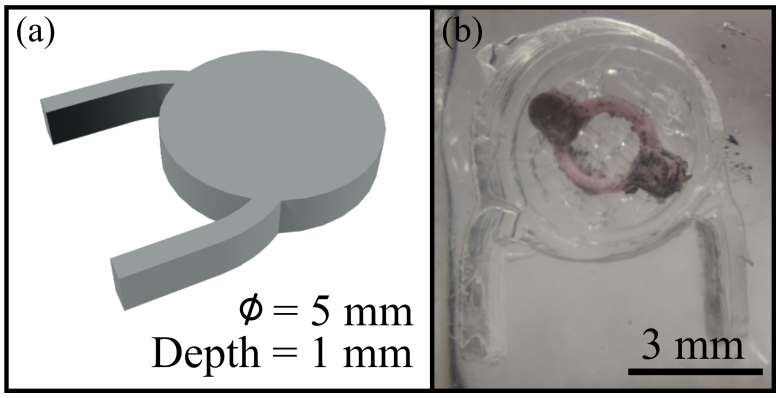

Fig. 7.6 3D representation and photograph of the millimetre scaled section for the cell growth channel. (a) AutoCAD model of the 3D printed section, with diameter 5 mm, depth 1 mm, and width of the arms of 0.5 mm. (b) Photograph of the produced channel with a two-ferromagnetic particle swimmer trapped within the well.

slide were put in contact they fused together. Figure 7.8 shows photographs the final prototype with a trapped swimmer; from the top (Figure 7.8a) and from the bottom (Figure 7.8b).

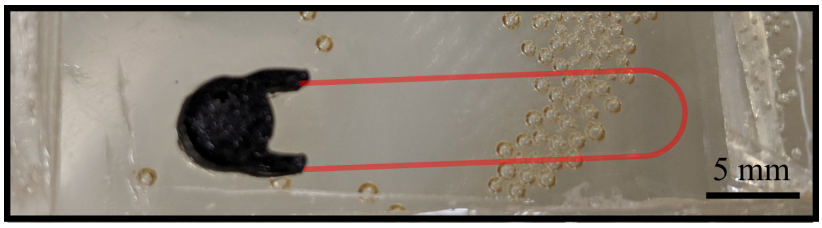

Fig. 7.7 Photograph of the 3D printed section attached to the epoxy-based mould for the cell growth channel. The red overly helps visualise the micro-channel (20 µm × 200 µm).

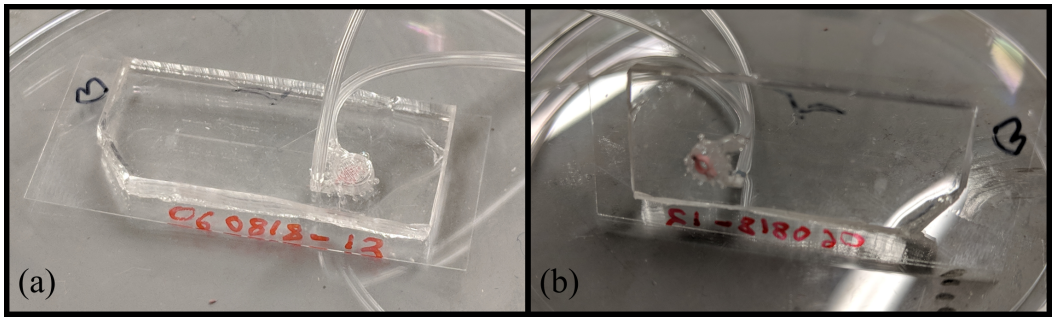

Fig. 7.8 Photographs of the finished prototype of the cell growth channel. (a) Shows a photograph from the top. (b) Shows a photograph from the bottom. The swimmer is shown trapped in the well, and the tubes shows the inlets and outlets.

An inlet and outlet were added to the channel to allow a mixture of 10 µm tracer particles and distilled water (with a concentration of 0.1% of the total volume). When actuated by an external magnetic field no flow was induced. After inspecting the two-ferromagnetic particle swimmer under actuation, it was clear that the swimmer was getting suck and the flow only circles around the well area. Other prototypes were produced and showed similar behaviour.

This cell growth system could be used for an interesting new method to controlled cell growth. However, work will need to be continued to improve the current system. Some of the issues with the current system include: the swimmer getting suck, due to motion in the z-axis, air bubbles trapped within the microchannel, and the transition between the 20 µm channel to the 500 µm arms of the swimmer well.

7.4 Controlling blood plasma separation within channels

Blood plasma is full of various biomarkers, including proteins and metabolites. Medical diagnostics relies on the analysis of these biomarkers. A significant part of the preparation of the plasma samples rely on processes such as filtration or centrifugation in a lab. Such processes can take time to produce a sample and in some cases this can create significant problems.

In recent years, there has been a large interest in creating lab-on-a-chip system for the blood plasma separation. A full review of the field can be found in M. Kersaudy-Kerhoas and E. Sollier [162]. A popular method of cell separation relies on the creation of acoustic standing waves [163, 164]. The motivation for this future investigation would be to create an all-on-one portable pump system to mix and/or separate blood plasma. This system would be based on the closed circuit pumps previously presented. The closed circuit channels were created to hold a volume of 100 µm which is the typical volume needed for a diagnostic test involving blood.

Initially, a sample was created with a mixture of 1 mL of PBS (a buffer solution) with 20 µm of blood. 100 µm of the sample was placed in a closed circuit channel. This very dilute sample was used to test the flow speed induced by the pump. Figure 7.9 shows the induced flow as a function the external magnetic field strength (with a frequency of 80 Hz). The maximum flow speed observed was approximately 2.0 ± 0.1 mm s^{-1}. The flow speed was calculated by tracking the speed of the red blood cells.

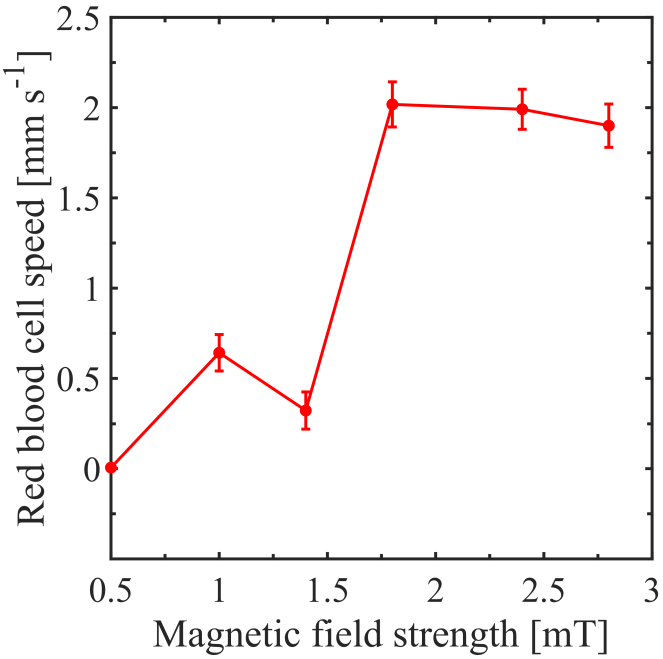

Fig. 7.9 Initial tests to show the speed of red blood cells in a closed circuit channel as a function of magnetic field strength. The flow is induced by a pinned two-ferromagnetic particle swimmer, and actuated by an 80 Hz magnetic field.

The second preliminary investigation involved creating of a more 'realistic' sample, in this case ten-parts PBS to one-part blood. In this experiment, there was no clear flow induced in the channel. However, after observing the channel, area of high (in the arms of the channel) and low (near the swimmer well) concentrations of red blood cells occurred as shown in Figure 7.10.

To further investigate this phenomenon, the experiment was repeated for three different frequencies (50 Hz, 70 Hz, and 90 Hz). These experiments once again showed the collection

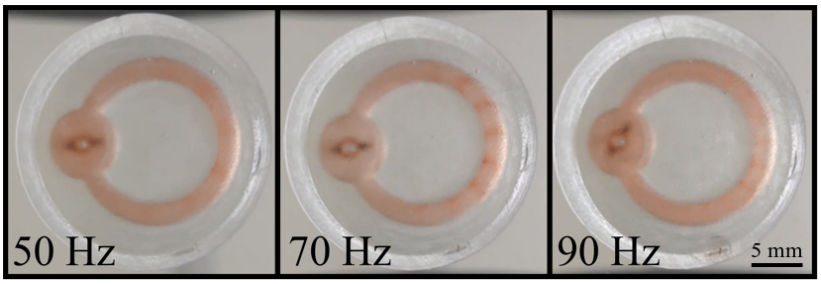

Fig. 7.10 Photographs of the closed circuit channel with a PBS and blood mixture, for different applied frequencies after 2 minutes of actuation. The external magnetic field strength was 1.5 mT for all measurements. There is a clear cell-plasma separation (see the right side of the channel at 70 Hz).

of red blood cells, but with a different number of nodes (Figure 7.10). Due to the differences in the number of nodes, the current hypothesis is that the two-ferromagnetic particle swimmer is creating a standing wave and the blood cells collect in the nodes. A similar method has been used in the past to collect and order cells [163, 164].

To test the concentration of plasma an albumin test was conducted. Samples were taken from different location within the channel: from an arm of the channel (A), from a node (N), and from the swimmer well (SW). Figure 7.11 shows a schematic with the locations as well as the albumin tests. From this crude test, it appears that the location SW contains the most plasma and the location N contains the least. This observation indicates that this method may in fact separate the red blood cells from the plasma.

The samples used for the test had a small volume, so pipetting errors could be large. Larger samples would be needed to further investigate this phenomenon. However, the initial tests show promising results which could be built upon in future investigations. To further show the portability of the system, a small-scale magnetic coil was created (this system is shown in Figure 7.12. This coil created an isolated oscillated magnetic field around the pinned swimmer (rather than across the whole channel). As the area required of the field was only approximately 5 mm, the field could be generated with a current of < 1 A (the power supplied by a standard USB).

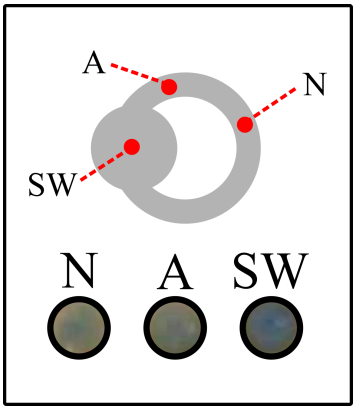

Fig. 7.11 Schematic diagram showing the locations of the samples for the albumin test. The results for the albumin test are also shown for each location. The brighter the colour of the blue, the higher the concentration of plasma in the sample.

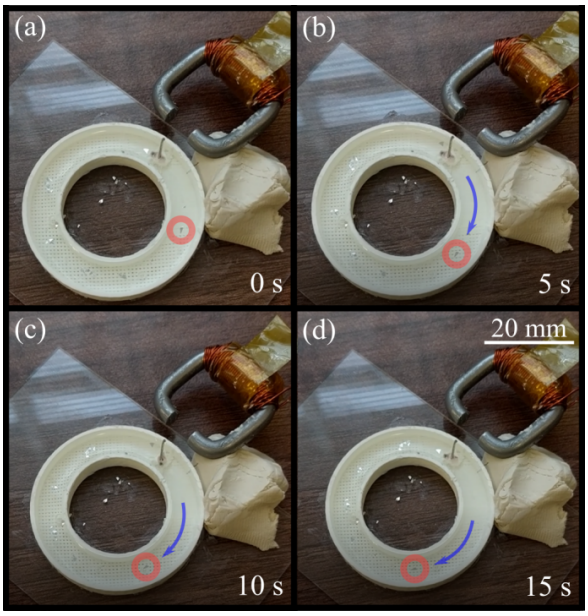

Fig. 7.12 Snapshots of the induced flow from a USB powered oscillating magnetic field. A particle is highlighted to show the net motion. The snapshots show (a) 0 s, (b) 5 s, (c) 10 s, and (d) 15 s.

7.5 Magnetically controlled ribbon-like membranes

To section will focus on a preliminary investigation of ribbon-like membranes. The proposed membranes are a continuation of the torque driven magnetic membranes presented in Chapter 5. An interesting work would be creating soft materials which as a bulk contain magnetic powder [165–169], rather than a material with a mixture of magnetic and non-magnetic materials. By producing these soft materials, the magnetisation profiles can be manipulated to produce interesting effects. Such materials have previously been investigated - to different levels of success - and a review of this field can be found in L. Hines *et al.*[170].

The main focus of this future investigation would be to test freezing the magnetic moments of the structure to produce non-reciprocal motion. In a recent publication by Y. Kim *et al.* [168], they used an in-house build magnetic 3D printer to create elastic materials with different magnetisation. Here, the directions of magnetisation can be controlled by creating a uniform mixture of silicone rubber and NdFeB powder, fixing the structure in the desired geometry and magnetising using the VSM to create a 1.8 T magnetic field.

This concept is similar to that of M. Sitti's group [166, 169]. In their work, they fabricate thin (0.1 mm) sheets of magneto-elastic materials (3.7 mm long). The structure was folded into a ring and magnetised, to produce a single-wavelength harmonic magnetisation profile. By manipulating the external magnetic field – for example between a periodic and rotating **B** – the device was shown to be able to swim through a fluid, crawl, and roll along a hard surface, and even jump over obstacles.

The preliminary data shown here use this simple method of freezing the magnetic moments to create a ribbon-like structure. Figure 7.13a shows a schematic of the membrane, with length 45 mm, width 9 mm, and depth 0.5 mm. The structure also has a small hole towards one end, which allows the membrane to be pinned within a channel. As a simple example, the ribbon-like structure was folded in a concertina shape. The structure was then magnetised as shown in Figure 7.13b, once unfolded the ribbon-like structure will return to

its original shape. Figure 7.13c shows the ribbon-like membrane pinned within a 10 mm wide channel.

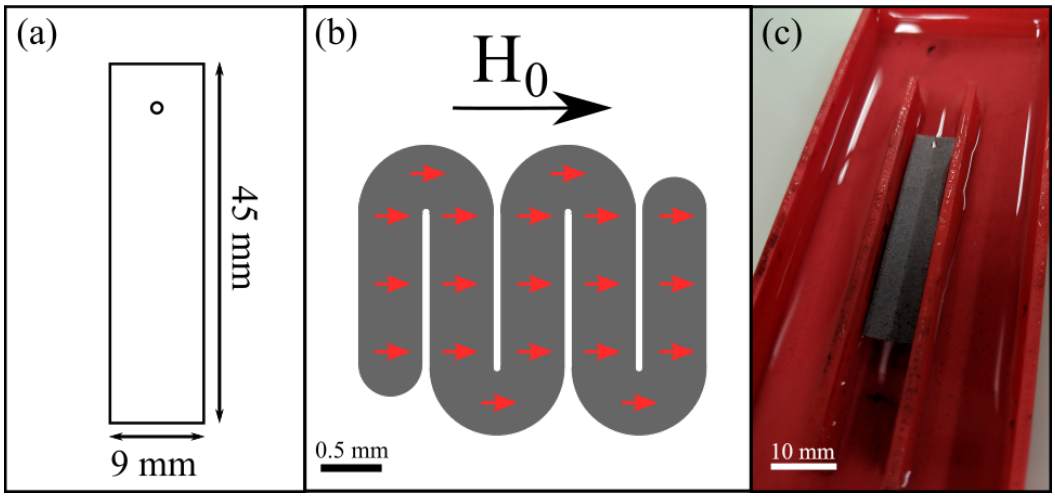

Fig. 7.13 Schematic diagrams and photograph of the ribbon-like membranes. (a) Schematic diagram showing the dimensions of the ribbon-like membrane, with depth 0.5 mm. (b) Schematic diagram to show the magnetisation of the ribbon-like membrane. (c) Photograph of the ribbon-like membrane fixed within a 3D printed channel.

By oscillating the external magnetic field, the structure would actuate and create bending modes. As a proof of concept, the structure was pinned in a 10 mm wide channel, on the air-glycerol interface. The induced flow speed was investigated for increasing magnetic field strength and different frequencies.

Typically, for all frequencies a rise (with similar flow speed) to a peak occurs then the flow speed drops off. For increasing frequency, the peak shifts towards larger magnetic field strengths. The maximum observed flow speed was approximately 0.8 ± 0.1 mm s^{-1}.

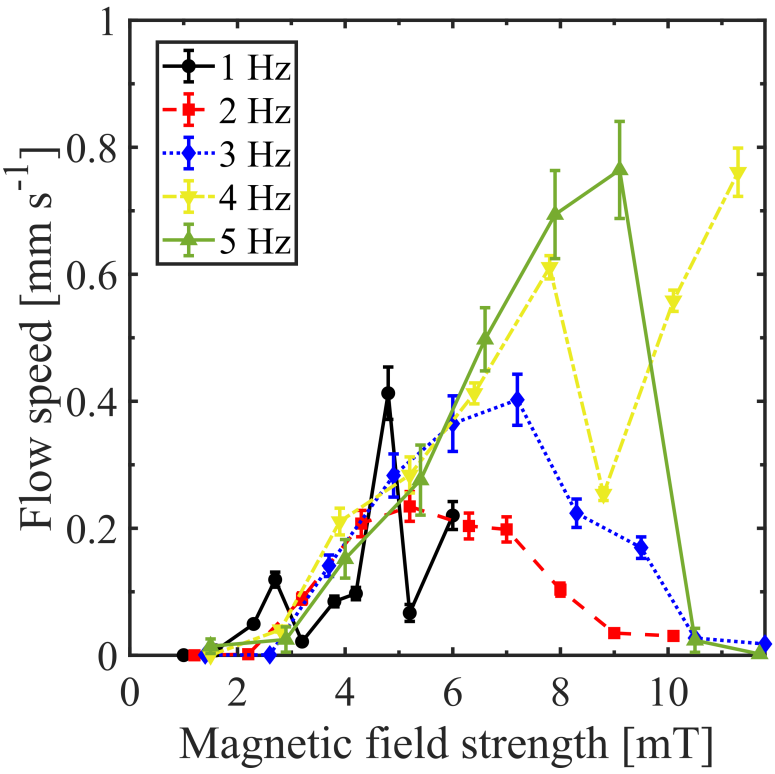

Fig. 7.14 Flow speed induced by the ribbon-like membrane as a function of magnetic field strength. Frequencies: black circle - 1 Hz, red square - 2 Hz, blue diamond - 3 Hz, yellow triangle - 4 Hz, and green triangle - 5 Hz.

Previous work [166, 169] focused on thin sheets of magneto-elastic materials suggested that the swimming speed have the following dependence $v_{\text{swim}} \propto B^2$. In their work, experimentally, they were unable to achieve this dependence, and it was stated that the differences between the predicted dependence and the experimental dependence was due to the surface interactions [166]. However, in the preliminary results with the ribbon placed on the surface shown in Figure 7.14, the induced flow speed – analogous to the swimming speed – was shown to be approximately B^2. One can fit a power law dependence ($v = B^b$) for the region before the plateau. Table 7.1 shows the values of b for different frequencies of the external magnetic field. For all cases, the dependency was shown to be of the order of 2.

Using this method, the magnetisation of the desired structure could easily be controlled. The preliminary data showed that even with a simple geometry the fixed magnetic moments

Frequency [Hz]	Power law fitting, b
2	2.211 ± 0.978
3	1.723 ± 0.573
4	1.916 ± 0.293
5	1.929 ± 0.310

Table 7.1 List of fitted power law dependencies on the external magnetic field strength, for ribbon-like membrane pumps.

- under actuation of an external magnetic field - could induce a flow, and therefore non-reciprocal motion. Such simple elastic-ferromagnetic system could be built into a microfluidic channel and used to induce a flow. This method described could be used for adding magnetic components to the fabrication of PDMS micro channels.

Chapter 8

Conclusions

The initial study in this thesis focused on the fabrication and experimental investigation of magnetically controlled ferromagnetic swimmers. The first type of swimmer shown was a two-ferromagnetic particle swimmer. The system was created to mimic the deformation swimming mechanism seen by eukaryotic cells. This was the first experimental investigation on this system, and the initial investigation focused on the optimisation of the materials used and fabrication. This swimmer was based on a pair of interacting ferromagnetic particles, coupled to an elastic material. Under the actuation of an external magnetic field, it was shown that it had two main swimming regimes: a pendulum regime in which the swimmer rocks on the major axis, and a locomotive regime in which the swimmer propels perpendicularly to the major axis. The swimming performance was investigated, and it was shown that by varying the external magnetic field parameters (amplitude and frequency) as well as a small external bias, the direction of motion and speed could be controlled. The dependence of the average propagation speed on viscosity and frequency were in qualitative agreement with the idealised two-particle pair analytical model.

The second system comprised of a ferromagnetic particle attached to a flexible tail (analogous to a single beating flagellum). This system reacted to an induced torque via an external magnetic field to produce translational motion. The frequency and tail length

response showed that there was an optimum tail length of 4 mm, corresponding to the speed of the propulsion and control of the direction. A analytical model was produced to help understand the modes of translation. The model comprised of three particles, one of which is magnetic, to describe the basic motion of the swimmer in a low Reynolds number regime. This showed a quantitative agreement with experiment, even with the simplified geometry and elastic properties. This investigation helps to understand the behaviour of these magnetically controlled swimmers. Understanding and optimising such systems will help with possible technological applications which require reliable actuation as well as a high degree of control. Not only could these applications include novel drug delivery systems, but microfludic components in lab-on-a-chip devices.

Chapter 5 focused on the converting swimming devices into fluid pumps and mixers. Swimming and pumping in this context are two sides of the same coin because at low Re, both configurations are subject to the scallop theorem. This work initially focused on restricting the transtational degrees of freedom of the swimmers within channels which induces a fluid flow. It was shown that by tailoring the channel geometry and manipulating the external magnetic field parameters, the pumps could switch between different regimes of pumping/mixing. Examples of these regimes include switching the flow direction or creating a valve. This versatility endows the device with varied functionality which, together with the robust remote control and reproducibility, makes it a promising candidate for several applications. The applications which the shown channel geometries could be used for could include, a cell sorting system, or a blood sample mixing system. Chapter 5 later focused on creating membranes – with a mixture of elastic and ferromagnetic components - which rely on magnetic and mechanical torques. These systems hold promise for use as fluid pumps in a less invasive way, for example when attached to the walls or top of a channel.

Chapter 6 focused on creating magnetic systems which rely on the collective motion of multiple components. This chapter was motivated by the metachronal waves observed

by beating cilia. Mimicking nature, arrays of elastic-ferromagnetic mixture components were investigated for different external magnetic field parameters. It was shown that for different combinations of external parameters, as well as separation between the components, that several interesting rotational patterns occurred. A theoretical model was produced by Dr. Daiki Matsunaga (University of Oxford), to predict the possible rotational patterns and net fluid flow. Similar components were also aligned within a channel to investigate the induced flow along a channel. In this case, the magnetisation angle was used to create a phase lag between the components. The separation between the components was found to be an important factor and resulted in different regimes being present. The produced rotational patterns created different fluid flows, including mixing regimes and net pumping regimes.

The final chapter focused on the future investigation and possible extensions to the presented work. The main focus was applications of the two-ferromagnetic particle swimmer. One proposed application was to use the two-ferromagnetic particle swimmer as a novel method of quantifying the viscostiy of monomolecular layers on aqueous surfaces. preliminary results using a dipalmitoylphosphatidylcholine (DPPC) monolayer demonstrated the feasibility of this approach. Other investigations included using the two-ferromagnetic particle swimmer within a closed circuit channel. In this system, the two-ferromagnetic particle swimmer could be used to either mix blood samples with a buffer solution (phosphate-buffered saline, PBS) or separate the red blood cells from the blood plasma. In this configuration the two-ferromagnetic particle swimmer could also be used to control the nutrients used for cell growth in microfluidic channels. Once again, preliminary results were presented showing the viability of these methods.

The final proposed future investigation focused on using mixtures of silicone rubber and NdFeB powder to create complex structures with interesting functionality. The example presented was based on a ribbon-like structure which was magnetised in a concertina shape.

Conclusions

When pinned this strucutre was able to induce a fluid flow along a channel filled with a high viscosity fluid.

Chapter 9

Publications and conferences

9.1 Publications

Here I list all published and submitted papers within my postgraduate study. An asterisk (*) indicates the corresponding author. An obelus (†) indicates that both authors contributed equally.

- Joshua K. Hamilton, Peter G. Petrov, C. Peter Winlove, Andrew D. Gilbert, Matthew T. Bryan, Feodor Y. Ogrin*. Magnetically controlled ferromagnetic swimmers. Scientific Reports, volume 7, 44142, (2017)

- Joshua K. Hamilton*, Matthew T. Bryan, Andrew D. Gilbert, Feodor Y. Ogrin, Thomas O. Myers. A new class of magnetically actuated pumps and valves for microfluidic applications. Scientific Reports, volume 8, 933 (2018)

- Joshua K. Hamilton*, Peter G. Petrov, Andrew D. Gilbert, Feodor Y. Ogrin. Torque driven ferromagnetic swimmers. Physics of Fluids, volume 30, 092001 (2018)

- Matthew T. Bryan*, Jose Garcia-Torres, Elizabeth L. Martin, Joshua K. Hamilton, Carles Calero, Peter G. Petrov, C. Peter Winlove, Ignacio Pagonabarraga, P. Tierno,

Francesc Sagués, Feodor Y. Ogrin. Microscale magneto-elastic composite swimmers at the air-water and water-solid interfaces under a uniaxial field. Physical Review Applied, volume 11, 044019 (2019)

- Joshua K. Hamilton†, Daiki Matsunaga†*, Fanlong Meng, Ramin Golestanian, Feodor Y. Ogrin, and Julia M. Yeomans. Controlling collective (or spatial) rotational pattern of magnetic rotors (Responding to review, Nature Communications)

9.2 Conferences

9.2.1 Organised conferences

- Bio-inspired Magnetic Systems 2018, Exeter, UK (9th - 11th July 2018)

9.2.2 Oral presentations

- Magnetism 2016, Sheffield, UK (4th - 5th April 2016) - "Experimental investigation of magnetically controlled ferromagnetic swimmers"
- Intermag 2017, Dublin, Ireland (24th - 28th April 2017) - "Ferromagnetic swimmer: A microfluidic pump prototype"
- 62nd Annual Conference on Magnetism and Magnetic Materials, Pittsburgh, USA (6th - 10th November 2017) - "Ferromagnetic swimmers - Devices and Applications"
- 70th Annual Meeting of the APS Division of Fluid Dynamics, Denver, USA (19th - 21st November 2017) - "Ferromagnetic swimmers - Devices and Applications"
- Bio-inspired Magnetic Systems 2018, Exeter, UK (9th - 11th July 2018) - "Ferromagnetic Swimmers: Fabrication, Controlled Swimming, and Applications"

9.2.3 Poster presentations

- 5th International Conference on Superconductivity and Magnetism 2016, Fethiye, Turkey (24th - 30th April 2016) - "Experimental investigation of magnetically controlled ferromagnetic swimmers"
- MAST STC Defence Materials Forum, Exeter UK (17th May 2016) - "Experimental control of magnetically actuated ferromagnetic swimmers"
- Magnetism 2017, York, UK (3rd - 4th April 2017) - "Ferromagnetic swimmer: A microfluidic pump prototype"
- Micromotors Summer School, Dresden Germany (14th - 18th August 2017) - "Ferromagnetic swimmer: A microfluidic pump prototype" - Awarded Student Travel Grant
- Magnetism 2018, Manchester, UK (9th - 10th April 2017) - "Ferromagnetic swimmer: fabrication, controlled swimming, and applications"
- 6th International Conference on Superconductivity and Magnetism 2018, Antalya, Turkey (30th April - 4th May 2018) - "Ferromagnetic swimmers - Devices and Applications" - 3rd Best Poster Prize
- International Conference on Magnetism 2018, San Francisco, USA (15th - 20th July 2018) - "Elastic-ferromagnetic swimmers, pumps, and membranes" - Awarded Student Travel Grant

References

[1] F. Y. Ogrin, P. G. Petrov, and C. P. Winlove. Ferromagnetic microswimmers. *Physical Review Letters*, 100(21):218102, 2008.

[2] F. Y. Ogrin, P. G. Petrov, and C. P. Winlove. Ogrin, Petrov, and Winlove Reply:. *Physical Review Letters*, 103(19):199802, 2009.

[3] R. P. Feynman. There's Plenty of Room at the Bottom, 1960.

[4] E. M. Purcell. Life at low Reynolds number. *American Journal of Physics*, 45(1):3–11, 1977.

[5] K. J. Rao, F. Li, L. Meng, H. Zheng, F. Cai, and W. Wang. A Force to Be Reckoned With: A Review of Synthetic Microswimmers Powered by Ultrasound. *Small*, 11(24):2836–2846, 2015.

[6] W. Li, X. Wu, H. Qin, Z. Zhao, and H. Liu. Light-Driven and Light-Guided Microswimmers. *Advanced Functional Materials*, 26(18):3164–3171, 2016.

[7] M. H. Oddy and J. G. Santiago. A method for determining electrophoretic and electroosmotic mobilities using AC and DC electric field particle displacements. *Journal of Colloid and Interface Science*, 269(1):192–204, 2004.

[8] K. Ishiyama, M. Sendoh, A. Yamazaki, and K. I. Arai. Swimming micro-machine driven by magnetic torque. *Sensors and Actuators, A: Physical*, 91(1-2):141–144, 2001.

[9] R. Dreyfus, J. Baudry, M. L. Roper, M. Fermigier, H. A. Stone, and J. Bibette. Microscopic artificial swimmers. *Nature*, 437(7060):862–865, 2005.

[10] A. Ghost and P. Fischer. Controlled propulsion of artificial magnetic nanostructured propellers. *Nano Letters*, 9(6):2243–2245, 2009.

[11] Mariana Medina-Sánchez, Haifeng Xu, and Oliver G Schmidt. Micro- and nanomotors: the new generation of drug carriers. *Therapeutic Delivery*, 9(4):303–316, 2018. PMID: 29540126.

[12] E.M. Haacke, R.W. Brown, M.R. Thompson, and R. Venkatesan. *Magnetic Resonance Imaging: Physical Principles and Sequence Design*. Wiley, 1999.

[13] D.J. Tritton. *Physical Fluid Dynamics*. Oxford Science Publ. Clarendon Press, 1988.

[14] G. G. Stokes. On the theories of the internal friction of fluids in motion, 1845.

[15] D. A. Fletcher and J. A. Theriot. An introduction to cell motility for the physical scientist. *Physical Biology*, 1(1):T1, 2004.

[16] M. Silverman and M. Simon. Flagellar rotation and the mechanism of bacterial motility. *Nature*, 249:73 – 74, 1974.

[17] H. C. Berg. Bacterial behaviour. *Nature*, 254(5499):389–392, 1975.

[18] S. Tottori, L. Zhang, F. Qiu, K. K. Krawczyk, A. Franco-Obregõn, and B. J. Nelson. Magnetic helical micromachines: Fabrication, controlled swimming, and cargo transport. *Advanced Materials*, 24(6):811–816, 2012.

[19] M. Medina-Sánchez, L. Schwarz, A. K. Meyer, F. Hebenstreit, and O. G. Schmidt. Cellular Cargo Delivery: Toward Assisted Fertilization by Sperm-Carrying Micromotors. *Nano letters*, 16(1):555–561, 2015.

[20] F. Martinez-Pedrero and P. Tierno. Magnetic Propulsion of Self-Assembled Colloidal Carpets: Efficient Cargo Transport via a Conveyor-Belt Effect. *Physical Review Applied*, 3(5):1–6, 2015.

[21] S. Maruo, A. Takaura, and Y. Saito. Optically driven micropump with a twin spiral microrotor. *Opt. Express*, 17(21):18525–18532, 2009.

[22] A. R. Shields, B. L. Fiser, B. A. Evans, M. R. Falvo, S. Washburn, and R. Superfine. Biomimetic cilia arrays generate simultaneous pumping and mixing regimes. *Proceedings of the National Academy of Sciences*, 107(36):15670–15675, 2010.

[23] W. T. E. van den Beld, N. L. Cadena, J. Bomer, E. L. de Weerd, L. Abelmann, A. van den Berg, and J. C. T. Eijkel. Bidirectional microfluidic pumping using an array of magnetic janus microspheres rotating around magnetic disks. *Lab Chip*, 15:2872–2878, 2015.

[24] A. Najafi and R. Golestanian. Simple swimmer at low Reynolds number: Three linked spheres. *Physical Review E - Statistical, Nonlinear, and Soft Matter Physics*, 69(6), 2004.

[25] J. E. Avron, O. Kenneth, and D. H. Oaknin. Pushmepullyou: An efficient microswimmer. *New Journal of Physics*, 7:234–243, 2005.

[26] W. F. Paxton, K. C. Kistler, C. C. Olmeda, A.n Sen, S. K. St. Angelo, Y. Cao, T. E. Mallouk, P. E. Lammert, and V. H. Crespi. Catalytic nanomotors: Autonomous movement of striped nanorods. *Journal of the American Chemical Society*, 126(41):13424–13431, 2004.

[27] T. R. Kline, W. F. Paxton, T. E. Mallouk, and A. Sen. Catalytic Nanomotors: Remote-Controlled Autonomous Movement of Striped Metallic Nanorods. *Angewandte Chemie*, 117(5):754–756, 2005.

[28] T. C. Lee, M. Alarcón-Correa, C. Miksch, K. Hahn, J. G. Gibbs, and P. Fischer. Self-propelling nanomotors in the presence of strong Brownian forces. *Nano Letters*, 14(5):2407–2412, 2014.

[29] R. Golestanian, T. B. Liverpool, and A. Ajdari. Propulsion of a molecular machine by asymmetric distribution of reaction products. *Physical Review Letters*, 94(22):1–4, 2005.

[30] J. R. Howse, R. A. L. Jones, A. J. Ryan, T. Gough, R. Vafabakhsh, and R. Golestanian. Self-Motile Colloidal Particles: From Directed Propulsion to Random Walk. *Physical Review Letters*, 99(4):8–11, 2007.

[31] Maria Guix, Sonja M. Weiz, Oliver G. Schmidt, and Mariana Medina-Sánchez. Self-propelled micro/nanoparticle motors. *Particle & Particle Systems Characterization*, 35(2):1700382, 2018.

[32] Yingjie Wu, Xiankun Lin, Zhiguang Wu, Helmuth Möhwald, and Qiang He. Self-propelled polymer multilayer janus capsules for effective drug delivery and light-triggered release. *ACS Applied Materials & Interfaces*, 6(13):10476–10481, 2014.

[33] Xing Ma, Kersten Hahn, and Samuel Sanchez. Catalytic mesoporous janus nanomotors for active cargo delivery. *Journal of the American Chemical Society*, 137(15):4976–4979, 2015.

[34] Wei Gao, Allen Pei, and Joseph Wang. Water-driven micromotors. *ACS Nano*, 6(9):8432–8438, 2012.

[35] Debabrata Patra, Samudra Sengupta, Wentao Duan, Hua Zhang, Ryan Pavlick, and Ayusman Sen. Intelligent, self-powered, drug delivery systems. *Nanoscale*, 5:1273–1283, 2013.

[36] Wei Gao and Joseph Wang. Synthetic micro/nanomotors in drug delivery. *Nanoscale*, 6:10486–10494, 2014.

[37] Ana C. Hortelão, Tania Patiño, Ariadna Perez-Jiménez, Àngel Blanco, and Samuel Sánchez. Enzyme-powered nanobots enhance anticancer drug delivery. *Advanced Functional Materials*, 28(25):1705086, 2017.

[38] Wei Gao, Renfeng Dong, Soracha Thamphiwatana, Jinxing Li, Weiwei Gao, Liangfang Zhang, and Joseph Wang. Artificial micromotors in the mouse's stomach: A step toward in vivo use of synthetic motors. *ACS Nano*, 9(1):117–123, 2015.

[39] Maria Guix, Anne K. Meyer, Britta Koch, and Oliver G. Schmidt. Carbonate-based janus micromotors moving in ultra-light acidic environment generated by hela cells in situ. *Scientific Reports*, 6:21701, 2016.

[40] James R. Baylis, Karen Y.T. Chan, and Christian J. Kastrup. Halting hemorrhage with self-propelling particles and local drug delivery. *Thrombosis Research*, 141:S36 – S39, 2016.

[41] Jinxing Li, Pavimol Angsantikul, Wenjuan Liu, Berta Esteban-Fernández de Ávila, Soracha Thamphiwatana, Mingli Xu, Elodie Sandraz, Xiaolei Wang, Jorge Delezuk, Weiwei Gao, Liangfang Zhang, and Joseph Wang. Micromotors spontaneously neutralize gastric acid for ph-responsive payload release. *Angewandte Chemie International Edition*, 56(8):2156–2161, 2017.

[42] Berta Esteban-Fernández de Ávila, Pavimol Angsantikul, Jinxing Li, Miguel Angel Lopez-Ramirez, Doris E. Ramírez-Herrera, Soracha Thamphiwatana, Chuanrui Chen, Jorge Delezuk, Richard Samakapiruk, Valentin Ramez, Marygorret Obonyo, Liangfang Zhang, and Joseph Wang. Micromotor-enabled active drug delivery for in vivo treatment of stomach infection. *Nature Communications*, 8:272, 2017.

[43] M. C. Ziskin and D. B. Petitti. Epidemiology of human exposure to ultrasound: A critical review. *Ultrasound in Medicine & Biology*, 14(2):91–96, 1988.

[44] E. Litvak, K. R. Foster, and M. H. Repacholi. Health and Safety Implications of Exposure to Electromagnetic Fields in the Frequency Range 300 Hz to 10 MHz. *Bioelectromagnetics*, 23(1):68–82, 2002.

[45] W. Wang, L. A. Castro, M. Hoyos, and T. E. Mallouk. Autonomous motion of metallic microrods propelled by ultrasound. *ACS Nano*, 6(7):6122–6132, 2012.

[46] S. Ahmed, W. Wang, L. O. Mair, R. D. Fraleigh, S. Li, L. A. Castro, M. Hoyos, T. J. Huang, and T. E. Mallouk. Steering acoustically propelled nanowire motors toward cells in a biologically compatible environment using magnetic fields. *Langmuir*, 29(52):16113–16118, 2013.

[47] A. A. Solovev, W. Xi, D. H. Gracias, S. M. Harazim, C. Deneke, S. Sanchez, and O. G. Schmidt. Self-Propelled Nanotools. *ACS Nano*, 6(2):1751–1756, 2012.

[48] M. Camacho-Lopez, H. Finkelmann, P. Palffy-Muhoray, and M. Shelley. Fast liquid-crystal elastomer swims into the dark. *Nature materials*, 3:307–310, 2004.

[49] C. Huang, J. Lv, X. Tian, Y. Wang, Y. Yu, and J. Liu. Miniaturized Swimming Soft Robot with Complex Movement Actuated and Controlled by Remote Light Signals. *Scientific Reports*, 5:17414, 2015.

[50] Stefano Palagi, Andrew G. Mark, Shang Yik Reigh, Kai Melde, Tian Qiu, Hao Zeng, Camilla Parmeggiani, Daniele Martella, Alberto Sanchez-Castillo, Nadia Kapernaum, Frank Giesselmann, Diederik S. Wiersma, Eric Lauga, and Peer Fischer. Structured light enables biomimetic swimming and versatile locomotion of photoresponsive soft microrobots. *Nature Materials*, 15:647, 2016.

[51] S. T. Chang, V. N. Paunov, D. N. Petsev, and O. D. Velev. Remotely powered self-propelling particles and micropumps based on miniature diodes. *Nature materials*, 6:235–240, 2007.

[52] J. Simmchen, J. Katuri, W. E. Uspal, M. N. Popescu, M. Tasinkevych, and S. Sánchez. Topographical pathways guide chemical microswimmers. *Nature Communications*, 7:10598, 2016.

[53] D. J. Griffiths. *Introduction to Electrodynamics*. Pearson, 2008.

[54] P. Tierno, R. Golestanian, I. Pagonabarraga, and F. Sagués. Magnetically actuated colloidal microswimmers. *Journal of Physical Chemistry B*, 112(51):16525–16528, 2008.

[55] F. Martinez-Pedrero, A. Ortiz-Ambriz, I. Pagonabarraga, and P. Tierno. Colloidal Microworms Propelling via a Cooperative Hydrodynamic Conveyor Belt. *Physical Review Letters*, 115(3):1–5, 2015.

[56] F. Martinez-Pedrero, A. Cebers, and P. Tierno. Orientational dynamics of colloidal ribbons self-assembled from microscopic magnetic ellipsoids. *Soft Matter*, 12(16):3688–3695, 2016.

[57] F. Martinez-Pedrero, P. Tierno, T. H. Johansen, and A. V. Straube. Regulating wave front dynamics from the strongly discrete to the continuum limit in magnetically driven colloidal systems. *Scientific reports*, 6:19932, 2016.

[58] M. Sendoh, K. Ishiyama, and K. I. Arai. Fabrication of Magnetic Actuator for Use in a Capsule Endoscope. *IEEE Transactions on Magnetics*, 39(5):3232–3234, 2003.

[59] T. Honda, K. I. Arai, and K. Ishiyama. Micro swimming mechanisms propelled by external magnetic fields. *IEEE Transactions on Magnetics*, 32(5):5085–5087, 1996.

[60] K. Kikuchi, A. Yamazaki, M. Sendoh, K. Ishiyama, and K. I. Arai. Fabrication of a spiral type magnetic micromachine for trailing a wire. *IEEE Transactions on Magnetics*, 41(10):4012–4014, 2005.

[61] A. W. Mahoney, J. C. Sarrazin, E. Bamberg, and J. J. Abbott. Velocity Control with Gravity Compensation for Magnetic Helical Microswimmers. *Advanced Robotics*, 25:1007–1028, 2011.

[62] D. Walker, M. Kübler, K. I. Morozov, P. Fischer, and A. M. Leshansky. Optimal Length of Low Reynolds Number Nanopropellers. *Nano Letters*, 2015.

[63] F. Qiu, S. Fujita, R. Mhanna, L. Zhang, B. R. Simona, and B. J. Nelson. Magnetic Helical Microswimmers Functionalized with Lipoplexes for Targeted Gene Delivery. *Advanced Functional Materials*, 25(11):1666–1671, 2015.

[64] D. J. Bell, S. Leutenegger, K. M. Hammar, L. X. Dong, and B. J. Nelson. Flagella-like propulsion for microrobots using a nanocoil and a rotating electromagnetic field. *Proceedings - IEEE International Conference on Robotics and Automation*, .:1128–1133, 2007.

[65] L. Zhang, J. J. Abbott, L. Dong, K. E. Peyer, B. E. Kratochvil, H. Zhang, C. Bergeles, and B. J. Nelson. Characterizing the swimming properties of artificial bacterial flagella. *Nano Letters*, 9(10):3663–3667, 2009.

[66] Ambarish Ghosh and Peer Fischer. Controlled propulsion of artificial magnetic nanostructured propellers. *Nano Letters*, 9:2243–2245, 2009.

[67] Wei Gao, Xiaomiao Feng, Allen Pei, Christopher R. Kane, Ryan Tam, Camille Hennessy, and Joseph Wang. Bioinspired helical microswimmers based on vascular plants. *Nano Letters*, 14(1):305–310, 2014.

[68] A. Snezhko, I. S. Aranson, and W. K. Kwok. Surface wave assisted self-assembly of multidomain magnetic structures. *Physical Review Letters*, 96(7):1–4, 2006.

[69] A. Snezhko, M. Belkin, I. S. Aranson, and W.-K. Kwok. Self-Assembled Magnetic Surface Swimmers. *Physical Review Letters*, 102(11):118103, 2009.

[70] G. Lumay, N. Obara, F. Weyer, and N. Vandewalle. Self-assembled magnetocapillary swimmers. *Soft Matter*, 9(8):1–6, 2013.

[71] Y. H. Li, H. C. Lin, and C. Y. Chen. Steering of magnetic micro-swimmers. *IEEE Transactions on Magnetics*, 49(7):4120–4123, 2013.

[72] Andreas Kaiser, Alexey Snezhko, and Igor S. Aranson. Flocking ferromagnetic colloids. *Science Advances*, 3(2), 2017.

[73] H. Saotome, T. Okubo, and Y. Ikeda. A novel actuator with Nd-Fe-B magnets swimming in parallel to the magnetic field. *IEEE Transactions on Magnetics*, 38(5):3009–3011, 2002.

[74] W. Gao, S. Sattayasamitsathit, K. M. Manesh, D. Weihs, and J. Wang. Magnetically powered flexible metal nanowire motors. *Journal of the American Chemical Society*, 132(41):14403–14405, 2010.

[75] I. S. M. Khalil, K. Youakim, A. Sanchez, and S. Misra. Magnetic-based motion control of sperm-shaped microrobots using weak oscillating magnetic fields. *IEEE International Conference on Intelligent Robots and Systems*, pages 4686–4691, 2014.

[76] Islam S. M. Khalil, Ahmet Fatih Tabak, Mohamed Abou Seif, Anke Klingner, and Metin Sitti. Controllable switching between planar and helical flagellar swimming of a soft robotic sperm. *PLOS ONE*, 13(11):1–15, 2018.

[77] Anthony K. Au, H. Lai, B. R. Utela, and A. Folch. Microvalves and micropumps for biomems. *Micromachines*, 2(2):179–220, 2011.

[78] J. D. Zahn. *Bio-MEMS Technologies and Applications*. CRC Press, 2007.

[79] M. Koch, N. Harris, R. Maas, A. G. R. Evans, N. M. White, and A. Brunnschweiler. A novel micropump design with thick-film piezoelectric actuation. *Measurement Science and Technology*, 8(1):49, 1997.

[80] M. Koch, N. Harris, A. G. R. Evans, N. M. White, and A. Brunnschweiler. A novel micromachined pump based on thick-film piezoelectric actuation. *Sensors and Actuators A: Physical*, 70(1):98 – 103, 1998.

[81] L. S. Jang, Y. J. Li, S. J. Lin, Y. C. Hsu, W. S. Yao, M. C. Tsai, and C. C. Hou. A stand-alone peristaltic micropump based on piezoelectric actuation. *Biomedical Microdevices*, 9(2):185–194, 2007.

[82] C. H. Wang and G. B. Lee. Pneumatically driven peristaltic micropumps utilizing serpentine-shape channels. *Journal of Micromechanics and Microengineering*, 16(2):341, 2006.

[83] C. W. Huang, S. B. Huang, and G. B. Lee. Pneumatic micropumps with serially connected actuation chambers. *Journal of Micromechanics and Microengineering*, 16(11):2265, 2006.

[84] M. H. Wu, S. B. Huang, Z. Cui, Z. Cui, and G. B. Lee. A high throughput perfusion-based microbioreactor platform integrated with pneumatic micropumps for three-dimensional cell culture. *Biomedical Microdevices*, 10(2):309–319, 2008.

[85] S. Böhm, W. Olthuis, and P. Bergveld. A plastic micropump constructed with conventional techniques and materials. *Sensors and Actuators A: Physical*, 77(3):223 – 228, 1999.

[86] C. Yamahata, C. Lotto, E. Al-Assaf, and M. A. M. Gijs. A pmma valveless micropump using electromagnetic actuation. *Microfluidics and Nanofluidics*, 1(3):197–207, 2005.

[87] M. Shen, C. Yamahata, and M. A. M. Gijs. Miniaturized pmma ball-valve micropump with cylindrical electromagnetic actuator. *Microelectronic Engineering*, 85(5):1104 – 1107, 2008. Proceedings of the Micro- and Nano-Engineering 2007 Conference.

[88] F. Fahrni, M. W. J. Prins, and L. J. van IJzendoorn. Micro-fluidic actuation using magnetic artificial cilia. *Lab on a Chip*, 9(23):3413, 2009.

[89] M. Vilfan, A. Potocnik, B. Kavcic, N. Osterman, I. Poberaj, A. Vilfan, and D. Babic. Self-assembled artificial cilia. *Proceedings of the National Academy of Sciences*, 107(5):1844–1847, 2010.

[90] J. Belardi, N. Schorr, O. Prucker, and J. Rühe. Artificial cilia: Generation of magnetic actuators in microfluidic systems. *Advanced Functional Materials*, 21(17):3314–3320, 2011.

[91] Y. Wang, Y. Gao, H. Wyss, P. Anderson, and J. den Toonder. Out of the cleanroom, self-assembled magnetic artificial cilia. *Lab on a Chip*, 13(17):3360, 2013.

[92] K. S. Ryu, K. Shaikh, E. Goluch, Z. Fan, and C. Liu. Micro magnetic stir-bar mixer integrated with parylene microfluidic channels. *Lab on a chip*, 4(6):608–13, 2004.

[93] T. Sawetzki, S. Rahmouni, C. Bechinger, and D. W. M. Marr. In situ assembly of linked geometrically coupled microdevices. *Proceedings of the National Academy of Sciences of the United States of America*, 105(51):20141–5, 2008.

[94] M. Hagiwara, T. Kawahara, Y. Yamanishi, T. Masuda, L. Feng, and F. Arai. On-chip magnetically actuated robot with ultrasonic vibration for single cell manipulations. *Lab on a Chip*, 11(12):2049, 2011.

[95] M. Hagiwara, T. Kawahara, T. Iijima, and F. Arai. High-Speed Magnetic Microrobot Actuation in a Microfluidic Chip by a Fine V-Groove Surface. *IEEE TRANSACTIONS ON ROBOTICS*, 29(2):363–372, 2013.

[96] F. N. Pirmoradi, J. K. Jackson, H. M. Burt, and M. Chiao. A magnetically controlled MEMS device for drug delivery: design, fabrication, and testing. *Lab on a Chip*, 11(18):3072, 2011.

[97] D. M. Drotlef, P. Blümler, and A. Del Campo. Magnetically actuated patterns for bioinspired reversible adhesion (dry and wet). *Advanced Materials*, 26(5):775–779, 2014.

[98] P. Tseng, J. Lin, K. Owsley, J. Kong, A. Kunze, C. Murray, and D. D. Carlo. Flexible and stretchable micromagnet arrays for tunable biointerfacing. *Advanced Materials*, 27(6):1083–1089, 2015.

[99] M. Asadi. *Beet-Sugar Handbook*. Wiley-Blackwell, 2005.

[100] J. F. Swindells and United States. National Bureau of Standards. *Viscosities of sucrose solutions at various temperatures: tables of recalculated values*. National Bureau of Standards circular. For sale by the Supt. of Docs., U.S. G.P.O., 1958.

[101] R. D. Keane and R. J. Adrian. Optimization of particle image velocimeters. I. Double pulsed systems Optimization of particle image ve I oci m e te rs. Part I: Double pulsed systems. *Meas. Sci. Technol. Meas. Sci. Technol*, 1(1):1202–1215, 1990.

[102] C. E. Willert and M. Gharib. Digital particle image velocimetry. *Experiments in Fluids*, 10(4):181–193, 1991.

[103] R. J. Adrian. Particle-Imaging Techniques for Experimental Fluid Mechanics. *Annual Review of Fluid Mechanics*, 23(1):261–304, 1991.

[104] P. Buchhave. Particle image velocimetry-status and trends. *Experimental Thermal and Fluid Science*, 5(5):586–604, 1992.

[105] W. Thielicke and E. J. Stamhuis. PIVlab – Towards User-friendly, Affordable and Accurate Digital Particle Image Velocimetry in MATLAB. *Journal of Open Research Software*, 2:30, 2014.

[106] W. Thielicke. *The flapping flight of birds: Analysis and application*. PhD thesis, University of Groningen, 2014.

[107] P. Cappuccinelli. *The movement of eukaryotic cells*, pages 59–74. Springer Netherlands, Dordrecht, 1980.

[108] G. Bertotti. *Hysteresis in magnetism*. Academic Press, San Diego, 1998.

[109] L. D. Landau and E. M. Lifshitz. *Fluid mechanics*. Butterworth–Heinemann, 1959.

[110] A. D. Gilbert, F. Y. Ogrin, P. G. Petrov, and C. P. Winlove. Theory of ferromagnetic microswimmers. *Quarterly Journal of Mechanics and Applied Mathematics*, 64(3):239–263, 2011.

[111] A. D. Gilbert, F. Y. Ogrin, P. G. Petrov, and C. P. Winlove. Motion and mixing for multiple ferromagnetic microswimmers. *European Physical Journal E*, 34(11):121–130, 2011.

[112] J. K. Hamilton, P. G. Petrov, C. P. Winlove, A. D. Gilbert, M. T. Bryan, and F. Y. Ogrin. Magnetically controlled ferromagnetic swimmers. *Scientific Reports*, 7(October 2016):44142, 2017.

[113] H. Allag, J Yonnet, and M. E. H. Latreche. 3D analytical calculation of forces between linear Halbach-type permanent-magnet arrays. *ELECTROMOTION, Jul 2009, Lille, France*, pages 1–6, 2009.

[114] J. K. Hamilton, A. D. Gilbert, P. G. Petrov, and F. Y. Ogrin. Torque driven ferromagnetic swimmers. *Physics of Fluids*, 30(9):092001, 2018.

[115] A. Cebers and I. Javaitis. Dynamics of a flexible magnetic chain in a rotating magnetic field. *Physical Review E - Statistical, Nonlinear, and Soft Matter Physics*, 69(2 1):1–7, 2004.

[116] T. S. Yu, E. Lauga, and A. E. Hosoi. Experimental investigations of elastic tail propulsion at low Reynolds number. *Physics of Fluids*, 18(9):2–6, 2006.

[117] O. S. Pak, W. Gao, J. Wang, and E. Lauga. High-speed propulsion of flexible nanowire motors: Theory and experiments. *Soft Matter*, 7(18):8169–8181, 2011.

[118] W. Gao, D. Kagan, O. S. Pak, C. Clawson, S. Campuzano, E. Chuluun-Erdene, E. Shipton, E. E. Fullerton, L. Zhang, E. Lauga, and J. Wang. Cargo-towing fuel-free magnetic nanoswimmers for targeted drug delivery. *Small*, 8(3):460–467, 2012.

[119] R. Livanovičs and A. Cebers. Magnetic dipole with a flexible tail as a self-propelling microdevice. *Physical Review E - Statistical, Nonlinear, and Soft Matter Physics*, 85(4):5–9, 2012.

[120] H. Gadêlha. On the optimal shape of magnetic swimmers. *Regular and Chaotic Dynamics*, 18(1-2):75–84, 2013.

[121] J. Espinosa-Garcia, E. Lauga, and R. Zenit. Fluid elasticity increases the locomotion of flexible swimmers. *Physics of Fluids*, 25(3), 2013.

[122] I. S. M. Khalil, H. C. Dijkslag, L. Abelmann, and S. Misra. MagnetoSperm: A microrobot that navigates using weak magnetic fields. *Applied Physics Letters*, 104(22), 2014.

[123] A. Cebers and K. Erglis. Flexible Magnetic Filaments and their Applications. *Advanced Functional Materials*, 26(22):3783–3795, 2016.

[124] F. Box, E. Han, C. R. Tipton, and T. Mullin. On the motion of linked spheres in a Stokes flow. *Experiments in Fluids*, 58(4):1–10, 2017.

[125] C. P. Lowe. Dynamics of filaments: modelling the dynamics of driven microfilaments. *Philosophical Transactions of the Royal Society B: Biological Sciences*, 358(1437):1543–1550, 2003.

[126] M.T. Bryan, J. Garcia-Torres, E.L. Martin, J.K. Hamilton, C. Calero, P.G. Petrov, C.P. Winlove, I. Pagonabarraga, P. Tierno, F. Sagués, and F.Y. Ogrin. Microscale magneto-elastic composite swimmers at the air-water and water-solid interfaces under a uniaxial field. *Phys. Rev. Applied*, 11:044019, Apr 2019.

[127] D. E. Nikitopoulos and A. Maha. *Bio-MEMS Technologies and Applications*. CRC Press, 2007.

[128] J. K. Hamilton, M. T. Bryan, A. D. Gilbert, F. Y. Ogrin, and T. O. Myers. A new class of magnetically actuated pumps and valves for microfluidic applications. *Scientific Reports*, 8(1):933, 2018.

[129] M. T. Bryan, S. R. Shelley, M. J. Parish, P. G. Petrov, C. P. Winlove, A. D. Gilbert, and F. Y. Ogrin. Emergent propagation modes of ferromagnetic swimmers in constrained geometries. *Journal of Applied Physics*, 121(7):073901, 2017.

[130] M. Leoni, J. Kotar, B. Bassetti, P. Cicuta, and M. C. Lagomarsino. A basic swimmer at low Reynolds number. *Soft Matter*, 5(2):472–476, 2009.

[131] Y. Ding, F. Qiu, X. Casadevall i Solvas, F. W. Y. Chiu, B. J. Nelson, and A. De Mello. Microfluidic-based droplet and cell manipulations using artificial bacterial flagella. *Micromachines*, 7(2):1–13, 2016.

[132] Kathrin E. Peyer, Li Zhang, and Bradley J. Nelson. Bio-inspired magnetic swimming microrobots for biomedical applications. *Nanoscale*, 5(4):1259–1272, 2013.

[133] J. Leach, H. Mushfique, R. di Leonardo, M. Padgett, and J. Cooper. An optically driven pump for microfluidics. *Lab Chip*, 6:735–739, 2006.

[134] N. Coq, A. Bricard, F. D. Delapierre, L. Malaquin, O. du Roure, M. Fermigier, and D. Bartolo. Collective beating of artificial microcilia. *Phys. Rev. Lett.*, 107:014501, 2011.

[135] S. Hanasoge, P. J. Hesketh, and A. Alexeev. Metachronal motion of artificial magnetic cilia. *Soft Matter*, pages –, 2018.

[136] M. Hejazian, W. Li, and N. T. Nguyen. Lab on a chip for continuous-flow magnetic cell separation. *Lab Chip*, 15:959–970, 2015.

[137] R. Zhou, F. Bai, and C. Wang. Magnetic separation of microparticles by shape. *Lab Chip*, 17:401–406, 2017.

[138] D. Matsunaga, F. Meng, A. Zöttl, R. Golestanian, and J. M. Yeomans. Focusing and sorting of ellipsoidal magnetic particles in microchannels. *Phys. Rev. Lett.*, 119:198002, 2017.

[139] D. Matsunaga, , A. Zöttl, F. Meng, R. Golestanian, and J. M. Yeomans. Focusing and sorting of ellipsoidal magnetic particles in microchannels. *IMA J. Appl. Math.*, 2018.

[140] S. Kim and J. S. Karrila. *Microhydrodynamics - Principles and Selected Applicaitons*. Dover Publications, Inc., 1991.

[141] E. M. Gauger, M. T. Downton, and H. Stark. Fluid transport at low reynolds number with magnetically actuated artificial cilia. *The European Physical Journal E*, 28(2):231–242, 2009.

[142] R. Golestanian, J. M. Yeomans, and N. Uchida. Hydrodynamic synchronization at low reynolds number. *Soft Matter*, 7:3074–3082, 2011.

[143] S. T. Bramwell and M. J. P. Gingras. Spin ice state in frustrated magnetic pyrochlore materials. *Science*, 294(5546):1495–1501, 2001.

[144] C. Castelnovo, R. Moessner, and S. L. Sondhi. Magnetic monopoles in spin ice. *Nature*, 451:42, 2008.

[145] F. Tsumori, R. Marume, A. Saijou, K. Kudo, T. Osada, and H. Miura. Metachronal wave of artificial cilia array actuated by applied magnetic field. *Japanese Journal of Applied Physics*, 55(6S1):06GP19, 2016.

[146] A. Cēbers and M. Ozols. Dynamics of an active magnetic particle in a rotating magnetic field. *Phys. Rev. E*, 73:021505, 2006.

[147] N. C. Darnton, L. Turner, S. Rojevsky, and H. C. Berg. Dynamics of Bacterial Swarming. *Biophysical Journal*, 98(10):2082–2090, 2010.

[148] D. B. Kearns. REVIEWS A field guide to bacterial swarming motility. *Nature*, 8(9):634–644, 2010.

[149] T. Vicsek and A. Zafeiris. Collective motion. *Physics Reports*, 517(3-4):71–140, 2012.

[150] V. M. Kaganer, H. Möhwald, and P. Dutta. Structure and phase transitions in langmuir monolayers. *Rev. Mod. Phys.*, 71:779–819, 1999.

[151] R. Wüstneck, J. Perez-Gil, N. Wüstneck, A. Cruz, V.B. Fainerman, and U. Pison. Interfacial properties of pulmonary surfactant layers. *Advances in Colloid and Interface Science*, 117(1):33 – 58, 2005. A Collection of Papers from the International Workshop on Bubble and Drop Interfaces, Genoa, Italy, 25-28 April, 2004.

[152] I. Langmuir. The constitution and fundamental properties of solids and liquids. ii. liquids.1. *Journal of the American Chemical Society*, 39(9):1848–1906, 1917.

[153] C. Alonso and J. A. Zasadzinski. A brief review of the relationships between monolayer viscosity, phase behavior, surface pressure, and temperature using a simple monolayer viscometer. *The Journal of Physical Chemistry B*, 110(44):22185–22191, 2006. PMID: 17078656.

[154] S. Ghazvini, B. Ricke, J. A. Zasadzinski, and P. Dhar. Monitoring phases and phase transitions in phosphatidylethanolamine monolayers using active interfacial microrheology. *Soft Matter*, 11:3313–3321, 2015.

[155] W. D. Harkins and R. J. Myers. Viscosity of Monomolecular Films. *Nature*, 140:465, 1937.

[156] R. J. Myers and W. D. Harkins. The viscosity (or fluidity) of liquid or plastic monomolecular films. *The Journal of Chemical Physics*, 5(7):601–603, 1937.

[157] D. L. Koch and G. Subramanian. Collective hydrodynamics of swimming microorganisms: Living fluids. *Annual Review of Fluid Mechanics*, 43(1):637–659, 2011.

[158] Robert M. Johann. Cell trapping in microfluidic chips. *Analytical and Bioanalytical Chemistry*, 385(3):408–412, Jun 2006.

[159] H-M Wu, T-A Lee, P-L Ko, H-J Chiang, C-C Peng, and Y-C Tung. Review of microfluidic cell culture devices for the control of gaseous microenvironments in vitro. *Journal of Micromechanics and Microengineering*, 28(4):043001, 2018.

[160] Ping Wang, Lydia Robert, James Pelletier, Wei Lien Dang, Francois Taddei, Andrew Wright, and Suckjoon Jun. Robust growth of escherichia coli. *Current Biology*, 20(12):1099 – 1103, 2010.

[161] Rosemary A. Bamford, Ashley Smith, Jeremy Metz, Georgina Glover, Richard W. Titball, and Stefano Pagliara. Investigating the physiology of viable but non-culturable bacteria by microfluidics and time-lapse microscopy. *BMC Biology*, 15, 2017.

[162] M. Kersaudy-Kerhoas and E. Sollier. Micro-scale blood plasma separation: from acoustophoresis to egg-beaters. *Lab on a Chip*, 13(17):3323, 2013.

[163] P. Mishra, M. Hill, and P. Glynne-Jones. Deformation of red blood cells using acoustic radiation forces. *Biomicrofluidics*, 8(3):1–11, 2014.

[164] C. W. Shields IV, C. D. Reyes, and G. P. López. Microfluidic cell sorting: a review of the advances in the separation of cells from debulking to rare cell isolation. *Lab Chip*, 15:1230–1249, 2015.

[165] J. Kim, S. E. Chung, S. E. Choi, H. Lee, J. Kim, and S. Kwon. Programming magnetic anisotropy in polymeric microactuators. *Nature Materials*, 10(10):747–752, 2011.

[166] E. Diller, J. Zhuang, G. Zhan Lum, M. R. Edwards, and M. Sitti. Continuously distributed magnetization profile for millimeter-scale elastomeric undulatory swimming. *Applied Physics Letters*, 104(17), 2014.

[167] S. R. Mishra, M. D. Dickey, O. D. Velev, and J. B. Tracy. Selective and directional actuation of elastomer films using chained magnetic nanoparticles. *Nanoscale*, 8(3):1309–1313, 2016.

[168] Y. Kim, H. Yuk, R. Zhao, S. A. Chester, and X. Zhao. Printing ferromagnetic domains for untethered fast-transorming soft materials - Supplementary Information. *Nature*, 558(7709AB):1–7, 2018.

[169] W. Hu, G. Z. Lum, M. Mastrangeli, and M. Sitti. Small-scale soft-bodied robot with multimodal locomotion. *Nature*, 554(7690):81–85, 2018.

[170] L. Hines, K. Petersen, G. Z. Lum, and M. Sitti. Soft Actuators for Small-Scale Robotics. *Advanced Materials*, 29(13), 2017.

[171] J. Happel and H. Brenner. *Low Reynolds number hydrodynamics*. Kluwer, Dordrecht, 1983.

Chapter 10

Appendix A

10.1 Three particle theoretical model

To elucidate the swimmer mechanism shown in Chapter 4, Section 2, a minimal theoretical model was developed where three spherical particles labelled by $j = 1, 2, 3$, were connected via elastic filaments, as depicted in Figure 10.1.

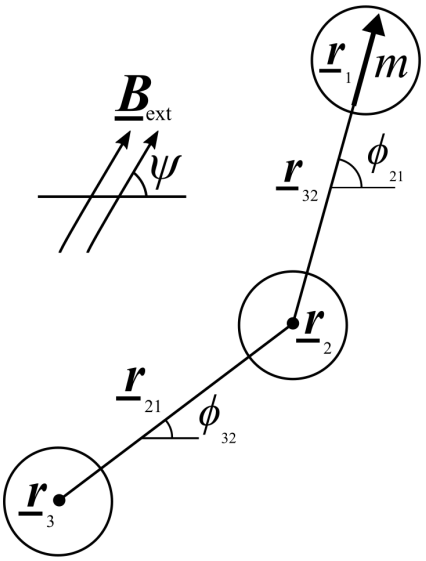

Fig. 10.1 Geometrical configuration of the modelled torque driven ferromagnetic swimmer. The model comprises of three particles - one of which is ferromagnetically hard, elastically coupled together. The external magnetic field is also shown.

The particles had radii R_j and were centred at $\boldsymbol{r}_j(t) = (x_j(t), y_j(t))$; the centre of reaction [171] were $\boldsymbol{X} = (X, Y)$ given by

$$\boldsymbol{X} \sum_j R_j = \sum_j R_j \boldsymbol{r}_j.$$

Setting $\boldsymbol{r}_{jk} = \boldsymbol{r}_k - \boldsymbol{r}_j$, $r_{jk} = |\boldsymbol{r}_{jk}|$, $\hat{\boldsymbol{r}}_{jk} = r_{jk}^{-1} \boldsymbol{r}_{jk}$, and letting ϕ_{jk} be the angle between $\boldsymbol{r}_{jk}$ and the x-axis. The motion of a particle is described by

$$\xi_j \ddot{\boldsymbol{r}}_j = \boldsymbol{F}_{\text{spring},j} + \boldsymbol{F}_{\text{bend},j} + \boldsymbol{F}_{\text{ext},j} + \boldsymbol{F}_{\text{fluid},j}, \tag{10.1}$$

with masses ξ_j taken to be sufficiently small that the motion is in an inertia-free Stokes regime (the results are insensitive to the values of ξ_j in the limit $\xi_j \to 0$). The following forces are derived from potentials, the elastic forces can be written as

$$V_{\text{spring}} = \tfrac{1}{2} k (r_{21} - l_0)^2 + \tfrac{1}{2} k (r_{32} - l_0)^2,$$

where l_0 is each filament's natural length and k is a spring constant. A force is imposed resisting bending motion of the three particle configuration, derived from the potential

$$V_{\text{bend}} = -\ell \cos(\phi_{21} - \phi_{32}).$$

Since $\cos \varepsilon = 1 - \varepsilon^2/2 + \cdots$, this is quadratic for small angle, but being periodic in the angle does not result in numerical problems if an angle jumps by 2π in the simulations.

The external magnetic field $\boldsymbol{B}_{\text{ext}}$ drives the swimmer directly through a potential term, on magnetic particle $j = 1$

$$V_{\text{ext}} = -\boldsymbol{m} \cdot \boldsymbol{B}_{\text{ext}} = -m B_{\text{ext}} b(t) \cos(\phi_{21} - \psi(t)),$$

where the field has magnitude $B_{\text{ext}}b(t)$ and angle $\psi(t)$ to the x-axis. Here B_{ext} is a constant and $b(t)$ and $\psi(t)$ are dimensionless. The field is taken to be purely back-and-forth along a single axis - the y-axis

$$\boldsymbol{B}_{\text{ext}} = B_{\text{ext}}(0, \sin\omega t). \tag{10.2}$$

Provided that the radii $R_j \ll l_0$, the length of the connecting filaments, the force on each particle from the surrounding fluid may be written as expansions that include Stokes drag and the leading order fluid interaction term [171, 109]

$$\boldsymbol{F}_{\text{fluid},j} = \boldsymbol{F}_{\text{drag},j} + \boldsymbol{F}_{\text{interact},j} = -6\pi\mu R_j \dot{\boldsymbol{r}}_j + \sum_k \frac{9\pi}{2}\frac{\mu R_j R_k}{r_{jk}}(\hat{\boldsymbol{r}}_{jk}\hat{\boldsymbol{r}}_{jk} + I)\cdot\dot{\boldsymbol{r}}_k, \tag{10.3}$$

where I is the identity matrix. Here and below the term when $j = k$ is excluded, without comment. These are the leading terms in an expansion in the small parameter $\varepsilon = R/l_0 \ll 1$ where $R = \frac{1}{3}(R_1 + R_2 + R_3)$ is the average particle radius, say. At this level of approximation the motion of the centre of reaction is given by

$$6\pi\mu\Big(\sum_j R_j\Big)\dot{\boldsymbol{X}} = \sum_j \boldsymbol{F}_{\text{interact},j} = \sum_{j,k}\frac{9\pi}{2}\frac{\mu R_j R_k}{r_{jk}}(\hat{\boldsymbol{r}}_{jk}\hat{\boldsymbol{r}}_{jk} + I)\cdot\dot{\boldsymbol{r}}_k. \tag{10.4}$$

The parameters introduced are $\{\xi_j, R_j, k, l_0, \ell, m, B_{\text{ext}}, \omega, \mu\}$ and it is convenient to define length, time and mass scales via

$$l_0 = \mathscr{L}, \quad \omega^{-1} = \mathscr{T}, \quad \ell l_0^{-2}\omega^{-2} = \mathscr{M},$$

as well as dimensionless parameters, similar to the ones previously discussed [110]

$$\varepsilon = \frac{R}{\mathscr{L}}, \quad \varpi = \varepsilon\frac{\mathscr{L}\mathscr{T}}{\mathscr{M}}6\pi\mu = \frac{\omega l_0^2 R}{\ell}6\pi\mu,$$
$$A_{\text{ext}} = mB_{\text{ext}}\frac{\mathscr{T}^2}{\mathscr{M}\mathscr{L}^2} = \frac{mB_{\text{ext}}}{\ell}.$$

Note that the quantity A_{ext} is sometimes called the magnetoelastic number. The following experimental parameter values are used for simulations,

Parameter	Value
R	1.25×10^{-3} m
k	1.67×10^{-2} N m^{-1}
l_0	5×10^{-3} m
$\ell = kl_0^2$	4.2×10^{-7} J
m	1.2×10^{-4} A m^2
B_{ext}	3×10^{-3} T
ω	$100 \times 2\pi$ s^{-1}
μ	1×10^{-3} Pa s

Table 10.1 Experimental parameter values for the torque driven ferromagnetic swimmer.

yielding the following scales and dimensionless parameters

$$\mathscr{L} = 5 \times 10^{-3} \text{ m}, \ \mathscr{T} = 1.6 \times 10^{-3} \text{ s}, \ \mathscr{M} = 4.2 \times 10^{-8} \text{ kg},$$

$$\varepsilon = 0.25, \quad \varpi = 0.89, \quad A_{\text{ext}} = 0.86,$$

however, it should noted that the idealised model is only expected to allow qualitative comparison with the experiments, due to significant different in geometry.

In the approximate model, the swimmer's particles are located at $(l_0, 0)$, $(0, 0)$ and $(-l_0, 0)$ for $j = 1, 2, 3$, respectively. The equations of motion are linearised for small displacements, neglecting any fluid interaction forces. The framework is easily generalised to any radii particles and number. However, for simplicity the following assumptions were made: the driving magnetic field to be given by Equation 10.2, zero inertia - $\xi_j = 0$, and the particles having radius $R_j = R$. The linearised equations only involve the transverse displacements y_j

and take the form

$$6\pi\mu R\dot{\boldsymbol{y}} = \ell l_0^{-2} M\boldsymbol{y} + mB_{\text{ext}} l_0^{-1} \sin\omega t\, \boldsymbol{w},$$
$$M = \begin{pmatrix} -1 & 2 & -1 \\ 2 & -4 & 2 \\ -1 & 2 & -1 \end{pmatrix}, \quad \boldsymbol{w} = \begin{pmatrix} 1 \\ -1 \\ 0 \end{pmatrix}, \quad \boldsymbol{y} = \begin{pmatrix} y_1 \\ y_2 \\ y_3 \end{pmatrix}.$$

A harmonic can be extracted by setting $\boldsymbol{y} = l_0\hat{\boldsymbol{y}}e^{i\omega t} + \text{c.c.}$. The factor l_0 makes the vector $\hat{\boldsymbol{y}}$ dimensionless and the governing equations then become

$$i\varpi\,\hat{\boldsymbol{y}} = M\hat{\boldsymbol{y}} - \tfrac{1}{2}iA_{\text{ext}}\,\boldsymbol{w}. \tag{10.5}$$

This can be inverted to give $\hat{\boldsymbol{y}}$, giving the balance between elastic forces, Stokes drag and magnetic driving, but excluding fluid interactions in Equation 10.3 - in other words the *internal motion* of the swimmer.

The actual swimming speed is given at leading order by substituting the internal motion into the Equation 10.4 for the centre of reaction. The leading order in perturbation theory is given by the quadratic terms and the average speed in the x-direction is then

$$\dot{X} = \tfrac{1}{4}Rl_0^{-2}\,\langle \boldsymbol{y}^T N\dot{\boldsymbol{y}}\rangle, \quad N = \begin{pmatrix} 0 & 1 & \frac{1}{4} \\ -1 & 0 & 1 \\ -\frac{1}{4} & -1 & 0 \end{pmatrix}, \tag{10.6}$$

where the angled brackets denote a time average. This becomes

$$\dot{X} = \tfrac{1}{2}i\varepsilon l_0\omega\,\hat{\boldsymbol{y}}^{*T} N\hat{\boldsymbol{y}}, \tag{10.7}$$

noting that $l_0\omega = \mathscr{L}/\mathscr{T}$ are the units of speed in the non-dimensionalisation, the motion of the swimmer is measured in units of link length per cycle, multiplied by ε reflecting the fact that it is the weak fluid interactions that are key to motion of the centre of reaction.

Although a similar system is easily written down for any number of particles, the advantage of dealing with just three is that the problem may be solved analytically. The matrix M has eigenvectors $\boldsymbol{v}_1 = (1,1,1)^T$ eigenvalue $\lambda_1 = 0$ (a translation mode), $\boldsymbol{v}_2 = (1,0,-1)^T$, $\lambda_2 = 0$ (a rotation mode) and $\boldsymbol{v}_3 = (1,-2,1)^T$, $\lambda_3 = -6$ (a bending mode). The magnetic driving excites the latter two since $\boldsymbol{w} = \frac{1}{2}\boldsymbol{v}_2 + \frac{1}{2}\boldsymbol{v}_3$ and then the solution to Equation 10.5 can be expressed as

$$\hat{\boldsymbol{y}} = -\tfrac{1}{4}A_{\text{ext}}[\varpi^{-1}\boldsymbol{v}_2 + (\varpi - 6i)^{-1}\boldsymbol{v}_3]. \tag{10.8}$$

Driving at least two modes is crucial for swimming at this regime. Now $\boldsymbol{v}_2^T N \boldsymbol{v}_3 = -\boldsymbol{v}_3^T N \boldsymbol{v}_2 = -7/2$ and thus after a short calculation, the swimmer's speed can be obtained from Equation 10.7 as

$$\frac{\dot{X}}{l_0\omega} = \varepsilon \frac{21A_{\text{ext}}^2}{16\varpi(\varpi^2+36)}. \tag{10.9}$$

The velocity here is normalised in terms of body length per radian of the magnetic field cycle. It is worth noting that when $\varpi \to 0$, the RHS of the expression diverges. This divergence is unphysical, however in reality the linearisation would break down at this limit.

It is worth mentioning the motion of the swimmer. A swimmer needs to excite two distinct modes to break the symmetry of motion. In this case, the translational mode $\boldsymbol{v}_1$ cannot be excited externally as there is no net force on the swimmer. For a model three-particle biological swimmer (without any external torques or forces), the second mode $\boldsymbol{v}_2$ also could not be generated and only $\boldsymbol{v}_3$ could be, leading to precisely a scallop type motion and no swimming. A point being raised here is that the external field provides torques on the swimmer and allows a three-particle swimmer to work. Although these remarks are for idealised multi-particle swimmers, they are also relevant to more realistic geometry.

The theory developed above gives an approximation to the swimming speed as

$$\dot{X} = \varepsilon l_0 \omega \frac{21 A_{\text{ext}}^2}{16\varpi(\varpi^2+36)} \simeq 2.4 \times 10^{-2}\ \text{m s}^{-1}. \tag{10.10}$$

Figure 10.2a shows the motion of the swimmer using the parameter values in Table 10.1 with no fluid interactions between particles. The symmetry breaking on the motion in one cycle is shown by figure of eight trace of each particle. Once the fluid interactions are turned on in the simulation, the swimmer now propels itself through the fluid (Figure 10.2b), as seen in a series of snap-shots in Figure 10.3.

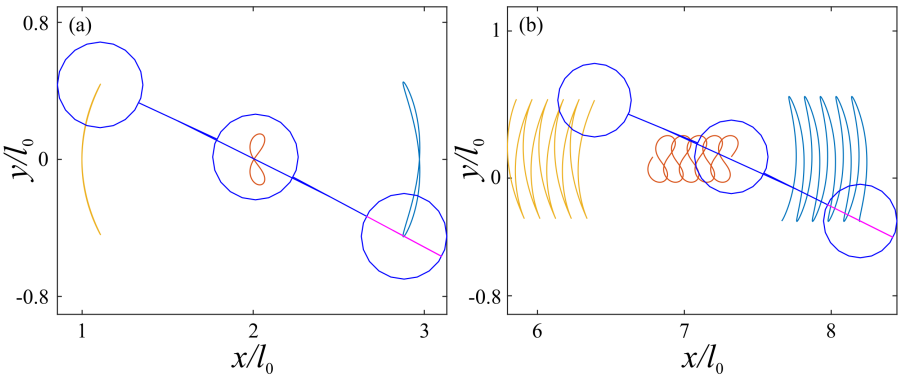

Fig. 10.2 (a) The motion of the swimmer without fluid interactions, to visualise how time-reversibility is broken. (b) The overall motion of the modelled swimmer with fluid interactions.

Figure 10.4 shows the frequency dependence of the swimming speed when A_{ext} takes the above value (solid red line) and when it is reduced to 20% in 20% intervals. For all values of A_{ext} the simulated velocities show a peak for low frequencies ($\varpi \lessapprox 1$).

Figure 10.5 shows the dependency of the number of linked particles on the swimming speed. The investigation ranges from $n = 2$ to $n = 8$, for different values of the frequency. For all cases, a rise to a peak ($\approx n = 3$) occurs before a steady decrease in speed. This is in agreement with results for flexible-tailed swimmers, Figure 7 of R. Livanovičs *et al.*[119] which shows similar peaks in velocity as a function of swimmer length. For frequencies

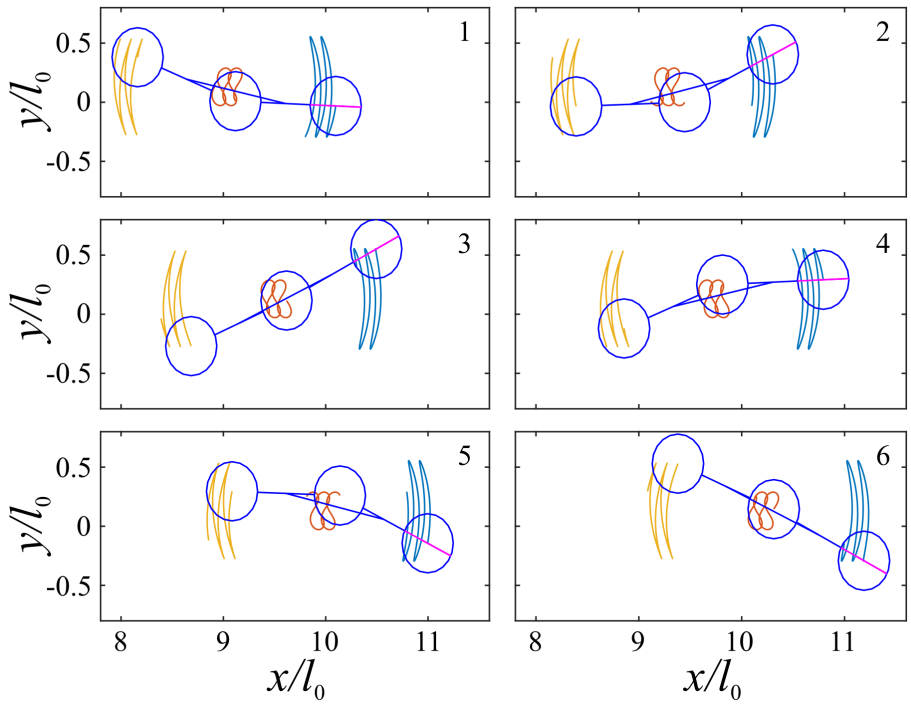

Fig. 10.3 A series of snap-shots showing the motion of the modelled three-particle swimmer, with each panel separated by $2\frac{1}{6}$ cycles of the external field. The sequence reads as labelled.

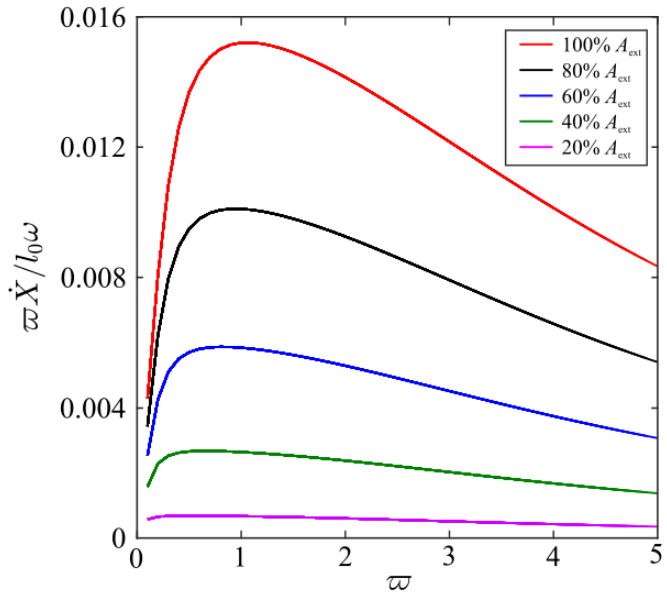

Fig. 10.4 Scaled non-dimensional speed as a function of frequency for different values of A_{ext}. 100% A_{ext} - red line, 80% A_{ext} - black line, 60% A_{ext} - blue line, 40% A_{ext} - green line, and 20% A_{ext} - pink line.

where $\varpi \leq 0.4$, a peak at $n = 4$ is observed, and as the frequencies increases ($\varpi \geq 0.6$), the maximum shifts towards $n = 3$.

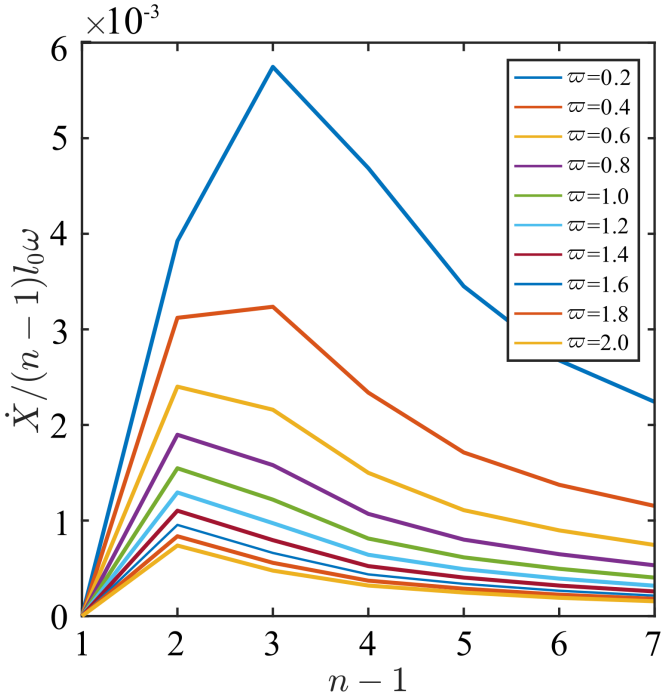

Fig. 10.5 Scaled non-dimensional speed as a function of number of linked particles for different dimensionless frequencies, with $\varepsilon = 0.1$. The frequencies are shown in the legend.

Chapter 11

Appendix B

11.1 The theoretical model of magnetic rotors

The following two simplifications were introduced and a theoretical model was developed by Dr. Daiki Matsunaga to accompany the experimental work shown in Chapter 6, Section 1. Firstly, it was assumed that a rotor is a flat disk with radius a that can freely rotate. The second simplification was to ignore that the rotors are located at liquid-air interface, and consider that rotors are submerged in a fluid with a viscosity η and a density ρ.

The governing equation

A rotor has magnetic moment $\boldsymbol{m} = \{m\cos\theta, m\sin\theta, 0\}$ where θ is the angle of the magnetic moment, and the rotational motion are governed by the magnetic and hydrodynamic interactions. The rotor i would feel a magnetic torque from both the external magnetic field as well as the neighbouring rotors. An expression for this magnetic torque is given by

$$T_i = \left\{ \boldsymbol{m}_i \times \left(\boldsymbol{B}_{\text{ext}} + \frac{\mu_0}{4\pi} \sum_{j \neq i}^{N} \frac{3(\boldsymbol{m}_j \cdot \boldsymbol{n}_{ij})\boldsymbol{n}_{ij} - \boldsymbol{m}_j}{r_{ij}^3} \right) \right\}_z , \tag{11.1}$$

where $\boldsymbol{r}_i$ is the position vector of a rotor i, $\boldsymbol{r}_{ij} = \boldsymbol{r}_j - \boldsymbol{r}_i$, $r_{ij} = |\boldsymbol{r}_{ij}|$, $\boldsymbol{n}_{ij} = \boldsymbol{r}_{ij}/r_{ij}$ and a subscript z denotes the z component.

The first term gives the torque from the external magnetic field $\boldsymbol{B}_{\text{ext}}$, while the second term describes the torque given by the dipolar interactions between the rotors. If the effect of the first order hydrodynamic coupling of the torques are taken into account, the angular velocity of a rotor i is given by

$$\omega_i = \frac{d\theta_i}{dt} = \frac{T_i}{8\pi\eta a^3} - \frac{1}{16\pi\eta}\sum_{j\neq i}^{N}\frac{T_j}{r_{ij}^3}. \tag{11.2}$$

The coefficient for the first term $8\pi\eta a^3$ is a friction constant for the rotation of a sphere, while the second term is responsible for the rotational velocity resulting from the rotation of the other particles [140]. Since there is a negative sign in the second term, rotors try to make neighbour particle rotate in the opposite direction. Although the hydrodynamic interactions would play an important role if the rotors are in the touching distance due to the lubrication interactions [140], the interaction is not important in this set-up due to relatively small particle size $\tilde{a}$. Considering the rotor as a point torque, the flow velocity $\boldsymbol{v}$ at position $\boldsymbol{x}$ can be expressed by a summation of rotlets as

$$\boldsymbol{v}(\boldsymbol{x}) = \frac{1}{8\pi\eta}\sum_{i}^{N}\left\{\frac{1}{R^3}\boldsymbol{T}(\boldsymbol{r_i})\times\boldsymbol{R}(\boldsymbol{x},\boldsymbol{r}_i)\right\}, \tag{11.3}$$

where $\boldsymbol{R} = \boldsymbol{x} - \boldsymbol{r}_i$ and $R = |\boldsymbol{R}|$.

In the simulation, equations (11.1) and (11.2) were calculated for each rotor to analyse the rotational dynamics of the rotor. The initial orientation $\theta(t=0)$ of the rotors are given at random, and the orientations are updated with the 1st-order Euler method with a time step $f\Delta t = 1.0\times10^{-3}$. The dimensionless parameter $\tilde{a} = 0.2$ is kept constant for all simulations.

Phase diagram

Finally, a full phase diagram from the theoretical model for the comprehensive understanding of the system was created. Figure 11.1 shows the phase diagram of the collective rotational patterns. Note that the experiment and model are not exactly matching because of the simplifications introduced in the model.

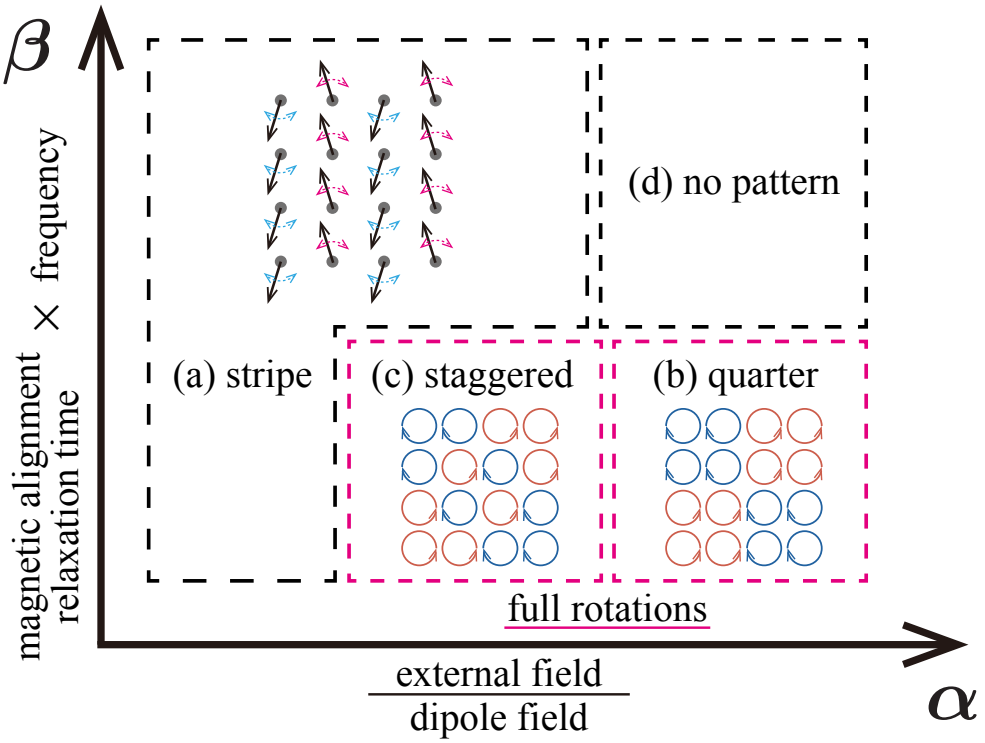

Fig. 11.1 Phase diagram from the simulation in $N_x = N_y = 4$ array. Showing the resulting rotational patterns for different combinations of α and β. Showing 4 regions of interest: (a) the stripe swinging pattern, (b) the quarter rotational pattern, (c) the staggered pattern, and (d) where no pattern is observed.

Figure 11.1 shows the rotors form the quarter rotational pattern for large α while they form the stripe swinging pattern for smaller α, which is qualitatively the same as shown in the experiment. In a range between these two states, another interesting set of rotational pattern was observed, which is named “staggered patterns", as shown in Figure 11.2. There were two main staggered patterns observed, the staggered patterns are slight variations of the quarter rotational and stripe swinging patterns. The first staggered pattern shown in Figure

11.2a is the “staggered stripe swinging pattern" where half of the pattern is shifted along. The “staggered quarter rotational pattern" shows a similar rotational pattern to the standard quarter rotational pattern, however the centre rotors have reversed chirality.

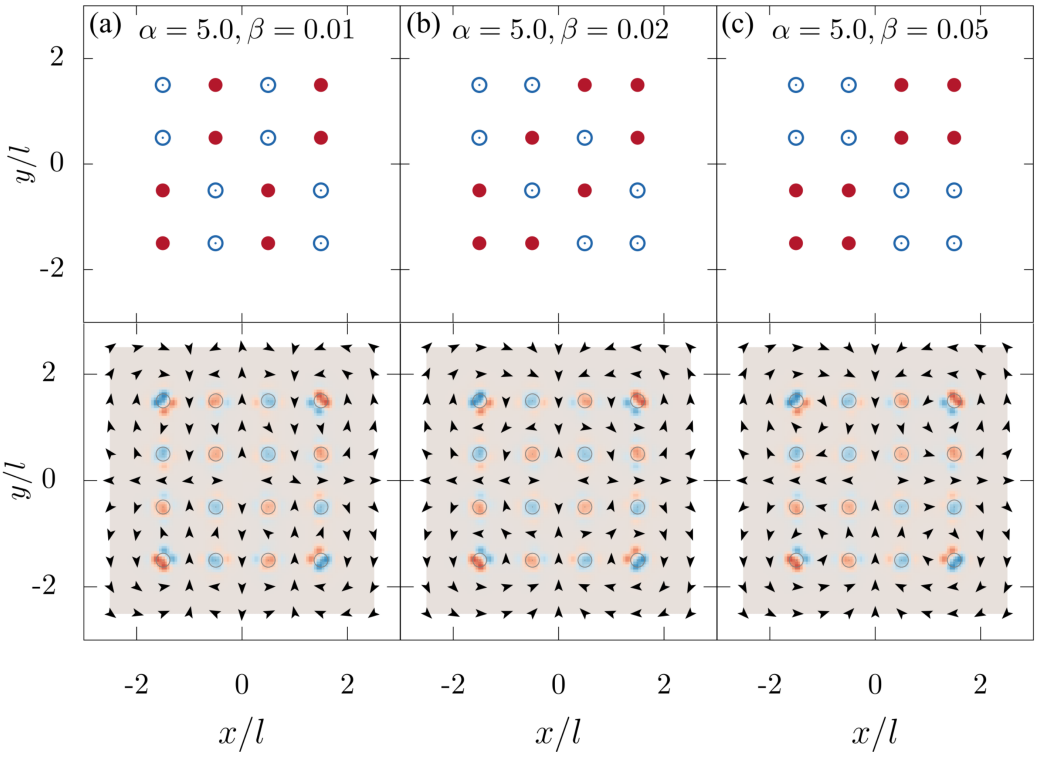

Fig. 11.2 Rotational patterns for three different combinations of α and β; red describe anticlockwise rotation while blue describes clockwise rotation. Bottom row shows generated flow field from the rotational patterns.

As a result, the flow field is not purely dipolar (Figure 11.2c bottom) as seen in the quarter rotation pattern, but more complex (Figure 11.2 bottom). These patterns might be useful because different rotational patterns could allow access different length scales of mixing.

Although attempts were made to observe these staggered patterns in the experiment, such patterns could not be reproduced due to fabrication imperfections. Adding small noise to the rotor position (even $0.05l$ deviation from the grid structure) in the simulation resulted in failure to reproduce the same result (data not shown). Therefore, it was concluded that a perfect grid structure is required for reproducing these patterns in the experiment.